UNIVERSITY OF CALIFORNIA

Los Angeles

Biomaterials to Enhance T Cell Therapies

A dissertation submitted in partial satisfaction of the

requirements for the degree Doctor of Philosophy

in Bioengineering

by

Fatemeh Sadat Majedi

2020

ABSTRACT OF THE DISSERTATION

Biomaterials to Enhance T Cell Therapies

by

Fatemeh Sadat Majedi

Doctor of Philosophy in Bioengineering

University of California, Los Angeles, 2020

Professor Dino Di Carlo, Co-Chair

Professor Louis S. Bouchard, Co-Chair

Despite recent successes in cancer immunotherapies that emphasize its high therapeutic potency in treating patients with progressive tumors, significant challenges, including insufficient activation and eventual exhaustion of effector T cells as well as suppression of their effector responses in the tumor microenvironment; and inadequate ability to expand tumor-specific T cell *ex vivo* hinder the potential of T cell therapies, especially in solid tumors. Most of the current immunotherapy approaches aim to facilitate T cells to fight tumors and provoke their infiltration. Some of the commonly used strategies include blocking inhibitory receptors such as anti PD-1 and anti-CTLA-4 while others include evoking cytotoxic T lymphocyte (CTL) responses such as chimeric antigen receptor (CAR)-T cell therapies and adoptive cell transfer (ACT) approaches. Despite their revolutionary approaches for hematopoietic cancers, potency of these methods and the need for expanding tumor-specific T cells is a need not yet satisfactorily met for solid tumor

therapy. Additionally, one of the major flaws associated with checkpoint inhibitor therapies (CPI) and chemokine therapies such as IL-2 or IL-12 that hampers their clinical translation is their administration route and all the immune-related adverse events that are affiliated with it. The other matter in these systems is that the rate of release of cytokines is not well controlled. We have shown here that the rate at which cytokines are delivered to CD8+ T cells impacts their differentiation and effector functionality. To tackle the issues related to ACT and improve *ex vivo* activation and expansion of tumor-reactive T cells several groups have developed antigen-presenting cell (APC) mimetic biomaterials that has proven to be far more potent in the polyclonal expansion of T cells compared to the commercial Dynabeads. Yet they lack the ability to manipulate tumor microenvironment so that it favors formation of tumor fighting T cells. In this thesis, we studied the impact of combining mechanical, oscillatory movements provided by an orbital shaker with soft, biocompatible, artificial APCs (aAPCs) of various sizes and amounts of antigen. We showed these aAPCs allow for testing the strength of signal delivered to T cells and enabled us to confirm that that absolute amounts of antigen engaged by the T cell are more important for activation than the density of antigen. We also found that when our aAPCs interact with T cells in the context of an oscillatory mechanoenvironment, they roughly double antigenic signal strength as compared to conventional, static culture. Combining these effects, our aAPCs significantly outperformed the commonly used Dynabeads.

Moreover, mechanical stiffness of the niche in which T cells home and face antigens makes a difference on their fate which is a missing piece in most of the *in vivo* studies. We show that T cells can recognize forces arising from the mechanical rigidity of the microenvironment. We fabricated 3D scaffold matrices with mechanical stiffness tuned to the range 4 to 40 kPa and engineered them to be microporous, independently of stiffness. We cultured T cells and antigen

presenting cells within the matrices and studied T cell activation by flow cytometry and live-cell imaging. We found that there was an augmentation of T-cell activation, proliferation, and migration speed in the context of mechanically stiffer 3D matrices as compared to softer materials. These results show that T cells can sense their 3D mechanical environment and alter both their potential for activation and their effector responses in different mechanical environments. A 3D scaffold of tunable stiffness and consistent porosity offers a biomaterial advancement for both translational applications and reductionist studies on the impact of tissue microenvironmental factors on cellular behavior.

Another major challenge that cold tumors face is poor infiltration of effector T cells and a high ratio of T regulatory cells (Tregs) to effector CD8+ T cells. Transforming growth factor β (TGF- β) is known to be the key factor in the induction of T regs from helper T cells drawn to the tumor, which then promotes cancer growth and metastasis. TGF-β also potently inhibits cytotoxic T cells in the tumor microenvironment and has, therefore, become an exciting target in the enhancement of immunotherapy. However, systemic TGF-β inhibition in preclinical models has shown major adverse effects on the cardiovascular, gastrointestinal, and skeletal systems, owing to the pleiotropic effects that TGF-β plays across the body.

Eventually, we focused our attempts on developing a platform that holds the key to solve the above-mentioned challenges by offering a “synthetic lymph node” niche proximally to the tumor for supporting transferred T cells while enhancing their infiltration and cytotoxic capabilities. Our implantable, porous synthetic lymph node serves as a home for the recruitment of endogenous tumor resident T cells and serves them with the activation clues while juicing them up with necessary cytokines/chemokines at controlled rates. The mechanical stiffness of our biomaterial is optimized to mimic that of lymph nodes. We believe the provided niche offers a home to T cells

either for ACT purposes or for tumor resident T cells to get the required training against tumor cells and facilitates their fight by increasing their number via proliferation signals and blocking the formation of suppressor T cells locally. This flexible platform holds high promises for localized immunomodulation and treatment of cancer.

The dissertation of Fatemeh Sadat Majedi is approved.

Steven J. Bensinger

Manish J. Butte

Song Li

Louis S. Bouchard, Committee Co-Chair

Dino Di Carlo, Committee Co-Chair

University of California, Los Angeles

2020

Dedicated to the brightest mind I have ever met, my handsome husband,

Mahdi Hasani; who is the light of every minute of my life.

And to my Mom and Dad, Gity Abbasi and Mir Naser Majedi, whose unconditional love and prayers led to every success in my life.

TABLE OF CONTENTS

LIST OF FIGURES

LIST OF TABLES

ACKNOWLEDGEMENTS

The journey of my PhD has not been a solo one. I owe this thesis and everything that I have ever accomplished to God who has never stopped to care for me and then to my mentors who led every step of the way. My journey started by joining Dr. Bouchard's lab to whom I owe my every achievement during the last five years of my PhD at UCLA. His unconditional and non-stop support has warmed my heart and encouraged me to do more and never stop dreaming and trying to make them happen. I have been the luckiest graduate student to have such a full support and trust at every stage. Every single day of this journey started for me with a deep appreciation of his support and all I hoped was to be worthy of this opportunity. I would like to thank Dr. Michael Lake, a very passionate scientist who was amongst my first mentors in Dr. Bouchard's lab.

Then this journey led us to search for a T cell expert where we were introduced to Dr. Bensinger. A bright, energetic, and passionate professor who accepted us with open arms and opened the doors of immunology to me. I deeply thank him and the kind, passionate and knowledgeable postdoc in his lab, Dr. Yoko Kidani who mentored me on how to obtain and work with primary cells.

One of my dreams was to design a T cell training gym and to study the effect of applying frequent forces on T cells in terms of engineering their functions. It was at this point where I met Dr. Manish Butte. I shall never forget the first time that I attended his talk and the excitement that filled my mind on that day. I don't think so far, I have ever been that excited by any talk as much as Manish's talk on that day. He was telling the story of my dreams and I just couldn't believe it. From that day on this collaboration started and he took me in his lab as his student. There is no amount of

appreciation for the kind of mentorship that Manish provides. If I took one step, he took ten! He has this everlasting urge for science that is exemplary and inspires everyone around him. I have been truly blessed to have the opportunity of having such mentors during my PhD. I want to give a special thanks to Dr. Tim Thauland, the project scientist in Manish's lab whose depth of knowledge has never ceased to amaze me and majority of what I know about T cells is thanks to him.

I would also like to convey my gratitude to my dissertation committee members: Dr. Dino Di Carlo and Dr. Song Li for being so cooperative and helpful. Their comments on my research provided me with valuable ideas for the continual of my work.

I want to thank my dearest friend Eta Atolia who has been most supportive and helpful, both scientifically and socially. I want to thank my friend and our amazing lab manager who is the best in the world, Chanti Bun. I want to thank Dr. Jennifer Aron, our postdoc, who has the most vivid spirit and is always so supportive and positive. I would like to thank Mattew Miller, Humza Khan and Dr. Kevin Meng, Cher Zhang for all their helps and kindness. I truly felt that I belonged to this family of Butte lab as we shared so many great moments together both in lab and outside. I would like to specially thank Dr. Reihaneh Haghniaz for all her help and support with lyophilization and mechanical testing. She was always there for me with such open arms. I would like to thank my friend Hamed Nilchi for all his unconditional help and support.

I would also like to thank Dr. Timothy Deming for the wonderful class that he taught on bioconjugate chemistry which I learned a lot from it and has been most useful for my research. I believe his course aided me in shaping the ideas for my research.

I would also like to thank Dr. Philippe Renaud and his group, for introducing me to, and ultimately grounding my work in the world of microfluidics. I like to thank Dr. Melody Swartz who was the first that introduced me to the world of immunoengineering and immunotherapy. Meeting her truly changed the path of my research to a better one. I would like to thank my previous instructors who paved the way for me to get to where I am today: Drs. Zahabi, Sebti, Maftoon, Rezaee, Razavi, Feili, Soleimani, Seyedmir, Majd, Ansari, Arabzadeh, Abotalebi, Shokrgozar, Emami, Solati, Kordestani, Mir Zadeh, Gharib Zadeh, Mohammadi, and Keshvari. I would also like to thank our SAO, Anne-Marie who was most helpful with all my needs.

I want to give a most special thanks to my mom who has been a mother and father to me and has devoted every single minute of her life to my advancement. No amount of appreciation comes even close to enough considering all the sacrifices she made for me. I owe my whole life to her and nothing would have been possible without her. I devote this thesis to my dad who was a great doctor but I wasn't lucky enough to have him in my life and lost him too soon. I hope that my work has made him proud. I like to thank my grandfather and grandmother, Morad Hossein and Ahoo, for their unconditional love and support. They were the angels and guardian of my life. I would love to thank my aunt Nikoo who was like a mother to me. My uncles Abedin, whom I lost while being away doing my PhD studies and is my biggest regret as he truly filled my father's place for me all those years. I want to thank my other uncles, Mohammad and Fereidoon who were like my big brothers to me and my nieces Ghazal, Afra and Soheil who are my true sisters and brother. I would love to thank my mother and father in-laws, Farideh, Mohammad Hossein, and my sister- in-laws who are my best friends Zahra and Fatemeh for all their kind supports and patience.

I would like to thank my best and truest friend Sara for being there for me the whole time. I sincerely appreciate her encouragement and willingness to help me in numerous ways. She is the best friend I could have ever dreamed of.

I would like to thank Sergey Mareninov for all the lyophilization services that was a key step in all my experiments. I would like to thank him for all his great comments and helps which were truly valuable. I like to thank Dr. Martin Phillips for his passionate mentorship and help with characterization analysis.

Eventually, I want to express my deepest thanks and love to my friend, colleague, mentor, and husband, Mahdi who has been with me at every step. I have had a 24/7 professor right beside me. From the minute that I met him till forever his brilliance and burning flame to explore the boundaries of science has been most inspirational for me. I have been the luckiest girl to have the honor of living with such a beautiful mind. May God always leads our way…

VITA

2015-2020	Graduate Student Researcher, Prof. Louis Bouchard and Prof. Manish Butte Department of Bioengineering, UCLA
2020	New Venture Fellow, UCLA Technology Transfer Office
2015	Multiyear Fellowship UCLA Bioengineering
2013	3rd-Place Winner of Young Khwarizmi Award in Fundamental Research Ministry of Science, Research & Technology, Tehran, Iran
2010-2012	M.Eng. in Bioengineering and Biotechnology Swiss Federal Institute of Technology (EPFL) Lausanne, Switzerland
2009-2011	M.Sc. in Biomedical Engineering (Biomaterials) Amirkabir University of Technology, Tehran, Iran
2005-2009	B.Sc. in Biomedical Engineering (Biomaterials) Amirkabir University of Technology, Tehran, Iran

Selected Publications

Journal Articles

1) **Majedi F.S.,** Hasani-Sadrabadi M.M., Thauland T.J., Li S., Bouchard L.S., Butte M.J.,* T-cell activation is modulated by the 3D mechanical microenvironment. *Biomaterials* 252 (2020) 120058.

2) Meng K.P., **Majedi F.S.,** Thauland T.J., Butte M.J.,* Mechanosensing through YAP controls T cell activation and metabolism. *Journal of Experimental Medicine* 217 (2020) e20200053.

3) Hasani-Sadrabadi M.M., **Majedi F.S.,** Miller M., Thauland T.J., Bouchard L.S., Li S.*, Butte M.J.* Augmenting T-cell Responses to Tumors by In Situ Nanomanufacturing. *Materials Horizons*. 7 (2020) 3028-3033.

4) **Majedi F.S.,** Hasani-Sadrabadi M.M., Thauland T.J., Li S., Bouchard L.S., Butte M.J.,* Augmentation of T-Cell Activation by Oscillatory Forces and Engineered Antigen-Presenting Cells. *Nano Letters*. 19 (2019) 6945-6954.

5) **Majedi F.S.,** Hasani-Sadrabadi M.M., Kidani Y., Thauland T.J., Moshaverinia A., Butte M.J.*, Bensinger S.J.*, Bouchard L.S.* Cytokine secreting microparticles engineer the fate and the effector functions of T cells. *Advanced Materials*. 30 (2018) 1703178.

6) Hasani-Sadrabadi M.M., **Majedi F.S.,** Bensinger S.J., Wu B., Bouchard L.S.*, Weiss P.S.*, Moshaverinia A.* Mechanobiological Mimicry of Helper T Lymphocytes to Evaluate Cell-Biomaterial Cross-Talk. *Advanced Materials*. 30 (2018) 1706780.

7) Hasani-Sadrabadi M.M., Karimkhani V., **Majedi F.S.,** VanDersarl J.J., Dashtimoghadam E., Afshar-Taromi F., Mirzadeh H., Jacob K.I., Bertsch A., Renaud, P.,* Stadler F. J.,* Kim I.* Microfluidic-Assisted Self-Assembly of Complex Dendritic Polyethylene Drug Delivery Nanocapsules. *Advanced Materials* 26 (2014) 3118–3123.

8) **Majedi F.S.,** Hasani-Sadrabadi M.M., VanDersarl J.J.,* Mokarram N., Hojjati Emami S., Dashtimoghadam E., Bertsch A., Renaud, P.* On-Chip Fabrication of Paclitaxel Loaded Chitosan Nanoparticles for Cancer Therapeutics. *Advanced Functional Materials*. 24 (2014) 432-441.

Chapter 1.

Background

Despite the many efforts during the past decades at eradicating cancer, the latter still remains a leading cause of death globally. Many advances have been made towards cancer therapy and improving lives of the patients. Chemotherapy remains the most common and well-stablished treatment despite all the unwanted side effects.[1] Researchers later introduced the idea of recruiting one's own immune system to fight cancer, paving the way for the emergence of cancer immunotherapy.[2] The multifaceted idea of immunomodulation includes any agent that either suppresses or activates the immune system. Amongst the many approaches introduced over the years, chimeric antigen receptor (CAR) T cell therapies and immune checkpoint blockade therapies have shown promise for liquid cancers. One of the major advantages of cancer immunotherapy compared to chemotherapy, which affects both healthy and cancerous cells, is the ability to modulate immune cells specifically. This results in fewer side effects. Conventional chemotherapy, on the other hand, is cytotoxic towards the normal cells. Despite the promising advantages of immunotherapy over conventional chemotherapy, systemic administration of immunomodulatory agents through bolus injection has shown unwanted side effects due to the disturbance of homeostasis in off-target tissues. Leveraging the fact that most immune-related events are two-party interactions between antigen presenting cells (APCs) and T cells, scientists have tried to modify either party. For example, several efforts have been focused towards modulation of dendritic cells (DCs) as a major player in the APC families, where they are responsible for sampling tumor antigens and presenting them to T cells in the form of major histocompatibility complex (MHC).[3] This process will then trigger the migration of T cells to tumor sites where they recognize the presented antigens on tumor surfaces. Cytokine-releasing cascades typically follow as a result. Other types of immune cells such as B cells or natural killer

(NK) cells have also been the subject of much research as a means to modulate the immune system.[4]

From the first report on using NK cells for immunotherapy in the 1970s till now, this field has emerged to be very promising for adaptive immunotherapy.[5] NK cells are considered to be the first line of defense against cancer. In addition to their key role in innate immunity they also play a crucial role in adaptive immunity *via* cytokine secretion and retaining of immune memories.[6] In contrast to T cells NK cells render the ability to eliminate tumor cells without prior sensitization. For NK cells to get activated and perform their tumor-killing activities, NK cell-activating receptors against tumor ligands must be presented to them. In patients with cancer these ligands are mostly downregulated which makes NK cell therapies less efficient.[7] One of the promising approaches has shown to be ex vivo expansion and activation of NK cells to boost their potency against immunosuppressive tumors. NK cell therapies have been categorized as either autologous or allogenic where in the autologous category cells are collected from the patient, expanded *ex vivo* and reinfused in the patient. While the source of cells in the allogenic category comes from a donor other than the patient. Difficulties and challenges are associated with each category. For example, the purification and sufficient expansion of NK cells is both very time consuming and expensive. On the other hand, this method is vulnerable to resistant tumor cells and tumor targeting in these cases is a big issue which allows for those tumor cells to escape the NK surveillance and grow. Moreover, tumor microenvironment especially in the case of solid tumors makes it very hard for immune cells to penetrate. To overcome some of these obstacles different approaches have been explored. Addition of immune stimulants to boost the tumor killing effects and provide synergistic effects, *ex vivo* expansion, or genetical modification of NK cells to make them more potent are amongst the steps that have been taken to improve NK cell therapies.

B cells have also been studied as immunotherapy targets. In addition to their role as antibody producers, they have shown to have immune-regulatory roles and serve as very potent antigen

presenting cells to mediate and induce specific T cell responses. The CD40L/CD40 signaling pathway is known to be the most important stimulant of antigen presentation in B cells. There have been several preclinical reports on effective anti-tumoral immunity via CD40 activated B cell cancer immunotherapy. Moreover, there have been reports on applications of B cells as cancer vaccines. Though, there are some contradictory reports on tumor-infiltrating B cells where some studies suggest their tumor progressing role while others correlate their role with improved tumor clearance.[8] In general, the role of B cells in tumor clearance in not very clear yet and more studies are being conducted in this area.

As mentioned before, another promising and rapidly growing immunotherapy approach is adoptive cell transfer (ACT) where patient's own immune cells are collected, processed *ex vivo*, and transferred back to their body to clear the tumor. Several kinds of ACT have been introduced but amongst them CAR T cell therapies have advanced furthest in clinic. Remarkable improvements have been recorded in cancer patients who received CAR T cell therapy but mostly in the case of liquid tumors. Main players in this therapy, as it comes from its name, are T cells. T cell's crucial role in orchestrating immune responses makes them the main target for most immunotherapy approaches. In the case of CAR T cell therapies patient's T cells are purified from their blood *ex vivo* and then transfected with a virus to genetically engineer the T cells so they express CAR receptors on their surface. These CARs allow T cells then recognize and attack to a specific protein on tumor cells. The next step is the expansion of these transfected T cells followed by their reinfusion to the blood. Challenges such as these extremely expensive and time-consuming processes of purification, transfection, and expansion are the hurdles that CAR T cell therapy faces in liquid tumors and for solid tumors there still is no FDA approved CAR T therapy.

Another way to enhance T cell-APC interaction is to alter T cell function in the tumor microenvironment. There have been multiple reports on cancer vaccines, immune check point blockade therapies such as anti-PD-1 and anti-CTLA-4 claiming to boost T cell function, as well as CAR-T cell therapies.[9,10] Check point inhibitor therapies in general have shown some promising

results on solid tumors. One of the major duties of our immune system is to tell between "self" and foreign cells. Upon making this decision T cells will then decide to pass or attack a cell. T cells do so by using check points. These immune checkpoints are molecules on immune cells that upon their activation or blockade immune responses will be blocked or induced. One of the many strategies that cancer cells use to stealth is to use these checkpoints and trick the immune system to count them as self cells. To find a way around this one approach that researchers have taken is the administration of drugs that inhibit those checkpoints and allow for immune cells to perform at their full potency. One of the most common checkpoints is the PD-1 protein on T cells which acts as a break on T cells and hold them from attacking normal cells. This process happens when PD-1 attaches to its ligand on a normal cell called PD-L1 and that cell will not be attacked. Cancer cells also express this PD-L1. So, one approach has been to administer drugs that either block the PD-1 or its ligand so cancer cells get recognized by T cells and eventually get eliminated. Another well-known checkpoint protein is CTLA-4 which again its blockade results in induction of killing cascade in T cells. The major issue with these therapies is that Systemic administration of these therapeutic agents through blood circulation results in their unwanted accumulation in off target tissues followed by adverse side effects. In this regard, few attempts have been made towards making the deliveries more localized to limit therapies to the tumor site rather than affecting the whole body. One innovative approach towards more localized therapy has been the nanogels with T cell targeting capabilities that deliver cytokine only to T cells.[11]These nanogels act as backpacks for T cells with continuous release of chemokines. However, as T cells traffic through the body the continual release risks systemic exposure of all organs to those chemokines which will again results in unwanted side effects. Another novel report towards making drug deliveries more targeted is fusion of Collagen-binding domains to cytokines that are more specific to T cells such as IL-12 to improve their efficacy and prolong their release in the tumor microenvironment.[12] Though, like many other systemic drug deliveries the intravenous (IV) injection in this case especially puts patients with cardiovascular disease at risk. Additionally, there have been some

reports on DC mediated cancer vaccines which has shown some promising results in clinical studies.[13] On the other hand, therapies that seek to improve T cell's functionality such as checkpoint blockade therapies have also shown promising results in some cancers such as urotherial carcinoma, hepatocellular carcinoma and few others.[14,15] Though, again limitations such as severe side effects still remains to block their clinical translation. Moreover, the idea of CAR T cell therapy in which patient's own T cell would be genetically modified *ex vivo* and then infused back to patient has received lots of attention recently but yet issues such as the high cost, potential side effects, and long processing times challenge their clinical application. In order to address many of the abovementioned issues and mainly to avoid side effects, several biomaterial platforms have been developed with the idea of localizing treatments to the tumor site to allow for overcoming the off-target issues.[3,16,17] Moreover, in the area of cancer vaccines there have been improvements using nanomaterials to encourage lymph node targeting and DC presentation to enhance cellular and humoral responses.[16,18]

It is critical to consider that in the design of nanomaterials or bioimplants is most important to find the best combination of degradability, and surface area for optimal therapeutic outcomes. The structure and pore size of implantable scaffolds directly affects the kinetics of release of their cargo while the choice of biomaterials themselves impacts the degradation properties. Many designs and materials have been tested so far for optimization of cytotoxic T cell responses. Overall local bioimplants with tunable kinetics of release and degradation can be very favorable platforms for cancer immunotherapies.[19] Moreover, compared to nanomaterials bioimplants offer better platforms for combinatorial therapies.[20,21] Additionally, bioimplants have shown to be promising for adaptive cell transfer in terms of improving the survival and proliferation of transferred T cells.[22,23] To date, one major class of biomaterials that have been most investigated are nanomaterials and nanoparticles in particular. These controlled release platforms have been studied for a long time in terms of optimizing their circulation, targeting,

loading efficiency, and release kinetics to improve cancer therapies.[19,24,25] Nano- and micro-particles have been designed to serve different purposes in cancer treatment.[26–28] Since they offer a very tunable platform, research groups have tried to tailor their size, surface chemistry, material composition, pharmacokinetics and pharmacodynamics to match their desired goals. Some of the offered nanoparticle systems have proven to be potent based on the preclinical data on limited solid tumors with high enhanced permeation and retention (EPR) effect. Though these approaches highly depend on the vasculature state of the tumor[29] and limits the size of the particle to be in a certain range that makes passive targeting possible. Other groups have tried to tailor particles so that they mostly target lymph nodes for vaccination purposes.[30] Another interesting area that particulate systems can be useful for is to steer lineage specification and favoring lymphocytes towards a more cytotoxic population or pursuing memory formation in T cells. Spatiotemporal control over secretion of certain cytokines can result in skewing T cell populations toward desired outcomes. Since cytotoxic T cells are endowed with the potency to kill, and helper CD4+ T cells provide secretion of necessary cytokines to clear cancer and modulate aberrant responses, controlled manipulation of these population can be very helpful for cancer immunotherapy purposes. Another area that has recently been the focus of many researches is developing better antigen presenting platforms using particulate systems. These platforms have been offered in different formats such as microparticles,[31] or nanorods.[17] Improving in vitro T cell expansion platforms via better antigen presentation has high clinical relevance and application.

Many of the ACT therapies are limited by poor ex vivo expansion of functional T cells. As a result, many efforts has been put in to mimicking natural APCS. To perform a successful T cell priming and activation three signal are required: T cell receptor engagement (anti-CD3), co-stimulation signal (anti-CD28), and pro-survival signals. An efficient artificial antigen presenting platform should be able to provide all these signals for T cells for a successful polyclonal expansion. Currently commercially available Dynabeads offer the anti-CD3/28 signal for better *ex vivo* clinical expansion of T cells though there is no control over the strength of the signal they

provide due to the fixed conjugation density of antibodies. Additionally, those particles can only be used *in vitro* due to their non-degradable polystyrene core. To offer a more natural presentation of those signals lipid coating on the surface of nanoparticle or nanorods have been offered to add fluidity to antigen presentation which has proven to be two to ten folds more potent in the polyclonal expansion of T cells compared to the commercial Dynabeads.[17] Also, biodegradable materials such as Alginate or mesoporouse silica (MES) have been used to enable *in vivo* applications, as well. Designing a modular platform allows for deeper understanding of the effect of signal strength and antigen density on better T cell expansion. To this end research groups have designed nanopatterned antigen arrays comprising a planar lipid bilayer and have shown that the number of antigens on the surface are more important than their surface density, with a density of 90–140 pMHC/μm, yielding maximal stimulation.[32]

Another aspect that is known to play a key role in T cell activation is biophysical cues. Immune cells can sense and respond to biophysical cues - from dynamic forces to spatial features - during their development, activation, differentiation and expansion. These biophysical signals regulate a variety of immune cell functions such as leukocyte extravasation, macrophage polarization, T cell selection and T cell activation. Recent studies have advanced our understanding on immune responses to biophysical cues and the underlying mechanisms of mechanotransduction, which provides rational basis for the design and development of immune-modulatory therapeutics. Accumulative evidence suggests that biophysical cues, in addition to biochemical signals, play an important role in modulating immune cells functions. Understanding the importance of mechanical and environmental cues on immunemodulation has led to the emerge of new avenue for engineering of biomaterials that can result in better immunotherapy platforms. Several studies have shown that T cell receptors are mechano-sensitive and triggering TCR-APC interaction requires mechanical forces.[33] Parallel to this several reports has proven the importance of both the strength of activation signals (amount of conjugated antibodies on the surface) that T cells receive along with the nature and frequency of the forces that are transferred

between T cell and APC in the process of T cell activation. These findings have mostly been possible *via* biomaterial platforms that allow for modulation of these factors so that the underlying cellular mechanism can be followed. To trigger TCR activation via pMHC mechanical forces, mostly pulling forces, are generated by T cells through a series of oscillatory pulling movements. Thus, platforms that offer exogenous control over the force being applied on T cells can open the door to biomedical applications of mechanically activated T cells.

When T cells recognize their cognate antigen on the surface of antigen presenting cells (APCs), they form a complex three-dimensional structure known as the immune synapse (IS).[34] The IS, which facilitates communication between T cells and APCs via receptor-ligand interactions, is critical for T-cell activation, and constitutes a platform for the delivery of effector molecules (e.g. the contents of cytolytic granules). At the molecular level, receptor-ligand interactions at the IS trigger a series of signaling cascades. These TCR-proximal signals initiate transcriptional programs controlling T-cell proliferation, differentiation, and effector function.

The actin cytoskeleton, in particular, is critical for T-cell biology, and pharmacological disruption of F-actin severely cripples T-cell motility, IS formation, and T-cell activation.[35] While cytoskeletal rearrangement is crucial for IS formation, the state of the cytoskeleton prior to T cell-APC conjugation is also important. Ken et al. have previously shown that naive T cells are mechanically stiffer than activated effector T cells.[33] This difference in stiffness allows the more pliable effector T cells to form larger IS with APCs upon initial triggering, increasing the number of receptor-ligand interactions and enhancing activation. Thus, the T-cell cytoskeleton acts as a layer of regulation, allowing effector cells to sensitively respond to APCs. The stiffness of the antigen presenting surface that T cells interact with also plays a role in activation. Experiments examining the interaction of T cells with stimulatory 2D surfaces of varying stiffnesses have demonstrated that relatively stiffer surfaces provide a stronger stimulus.[36–41] Elastic moduli around 15–20 kPa enable maximal spreading of T cells and optimal activation optimal

activation.[42] The cytotoxicity of T cells is also affected by substrate stiffness.[43] All these experiments have been performed in 2D, i.e., on surfaces.

While the mechanical properties of the T cell and the antigen presenting surface have been investigated, the effect of the mechanical properties of the 3D microenvironment on actin-dependent T-cell functions such as motility, IS formation, and activation has barely been examined.[44] The properties of 3D scaffolds can be manipulated by altering the density of polymers and crosslinkers. As cells migrate through scaffolds, they interact with functional groups that act as ligands for cell surface receptors, presented by the polymer. Thus, increasing polymer density results in a concomitant increase in ligand density and a decrease in mesh size, which alters cell-polymer interactions. On the other hand, keeping polymer content constant and varying the crosslinker density also alters the mesh size of the gel, which directly impacts molecular diffusion and cell motility.[45] While stiffness and ligand density can be modulated independently of polymer content with some synthetic polymers, the direct relationship between crosslinker density and mesh size has made it difficult at best to relate cell behavior to pure stiffness. Fortunately, in the case of the biodegradable polymer alginate gelation is induced by calcium ions. Due to the formation of G-blocks that provide pockets for calcium entrapment, the stiffness of the gel can be altered by varying the concentration of calcium ions without altering the ligand density or pore size.[3] As a result Alginate platforms make great candidates for manipulation of mechanical stiffness and as a results IS formation and T cell activation and cytokine secretion without changing the pore size. This can be another variable to tune T cell's cytotoxic function in tumor microenvironment.

Another major challenge that cold tumors face is poor infiltration of effector T cells and a high ratio of T regulatory cells (Tregs) to effector CD8+ T cells. Transforming growth factor b (TGF-b) is known to be the key factor in the induction of T regs from helper T cells drawn to the tumor, which then promotes cancer growth and metastasis. TGF-β also potently inhibits cytotoxic

T cells in the tumor microenvironment[46] and has, therefore, become an exciting target in the enhancement of immunotherapy.[47] However, systemic TGF-β inhibition in preclinical models has shown major adverse effects on the cardiovascular, gastrointestinal, and skeletal systems, owing to the pleiotropic effects that TGF-β plays across the body.[48] The release of TGF-β inhibitors by injected nanoliposomes was shown to reduce metastases[49] but did not show a local impact in regulatory T cells.

Scope and Aims of Current Research

In this thesis we aimed to address some of the abovementioned issues by first designing platforms that can improve in vitro differentiation (Chapter 2), activation, and expansion (**Chapter 3** and **4**) and then offering an implantable microporous, 3D platform for *in vivo* recruitment and education of endogenous T cells local to the tumor microenvironment (**Chapter 5**). To facilitate T-cell activation and differentiation in vitro, we have developed core–shell microparticles for sustained delivery of cytokines (**Chapter 2**). These particles are enriched by heparin to enable a steady release of interleukin-2 (IL-2), the major T-cell growth factor, over 10+ d. The controlled delivery of cytokines is used to steer lineage specification of cultured T-cells. This approach enabled differentiation of T-cells into central memory and effector memory subsets. In chapter 3, we studied the impact of combining mechanical, oscillatory movements provided by an orbital shaker with soft, biocompatible, artificial APCs (aAPCs) of various sizes and amounts of antigen. We showed that these aAPCs allow for testing the strength of signal delivered to T cells, and enabled us to confirm that that absolute amounts of antigen engaged by the T cell are more important for activation than the density of antigen. We also found that when our aAPCs interact with T cells in the context of an oscillatory mechanoenvironment, they roughly double antigenic signal strength, compared to conventional, static culture. Combining these effects, our aAPCs significantly outperformed the commonly used Dynabeads. We finally demonstrated that tuning the signal strength down to a submaximal "sweet spot" allows for robust

expansion of induced regulatory T cells. Then due the fact that T cells can recognize forces arising from the mechanical rigidity of the microenvironment, we fabricated 3D scaffold matrices with mechanical stiffness tuned to the range 4–40 kPa and engineered them to be microporous, independently of stiffness (**Chapter 4**). We cultured T cells and antigen presenting cells within the matrices and studied T-cell activation by flow cytometry and live-cell imaging. We found that there was an augmentation of T-cell activation, proliferation, and migration speed in the context of mechanically stiffer 3D matrices as compared to softer materials. Our results showed that T cells can sense their 3D mechanical environment and alter both their potential for activation and their effector responses in different mechanical environments. Our 3D scaffold of tunable stiffness and consistent microporosity offers a biomaterial advancement for both translational applications and reductionist studies on the impact of tissue microenvironmental factors on cellular behavior. Eventually in **chapter 5**, we focused our attempts on developing a platform that holds the key to solve the above-mentioned challenges by offering a "synthetic lymph node" niche proximally to the tumor for supporting transferred T cells while enhancing their infiltration and cytotoxic capabilities. We proposed an implantable, porous synthetic lymph node that can offer a home for the recruitment of endogenous tumor resident T cells and serves them with the activation clues while juicing them up with necessary cytokines/chemokines at controlled rates. The mechanical stiffness of our biomaterial is optimized to mimic that of lymph nodes. To deal with the issue related to abundance of regulatory T cells in the tumor microenvironment we have embedded TGFβi releasing nanoparticles within our platform. We believe the provided niche offers a home to T cells either for ACT purposes or for tumor resident T cells to get the required training against tumor cells and facilitates their fight by increasing their number via proliferation signals and blocking the formation of suppressor T cells locally. This flexible platform holds high promises for localized immunomodulation and treatment of cancer.

Reference

1 Hanahan D, Weinberg RA. Hallmarks of cancer: The next generation. *Cell* 2011. https://doi.org/10.1016/j.cell.2011.02.013.

2 Khalil DN, Smith EL, Brentjens RJ, Wolchok JD. The future of cancer treatment: Immunomodulation, CARs and combination immunotherapy. *Nat Rev Clin Oncol* 2016. https://doi.org/10.1038/nrclinonc.2016.25.

3 Gu L, Mooney DJ. Biomaterials and emerging anticancer therapeutics: Engineering the microenvironment. *Nat Rev Cancer* 2016. https://doi.org/10.1038/nrc.2015.3.

4 Rydyznski C, Daniels KA, Karmele EP, Brooks TR, Mahl SE, Moran MT, *et al.* Generation of cellular immune memory and B-cell immunity is impaired by natural killer cells. *Nat Commun* 2015. https://doi.org/10.1038/ncomms7375.

5 Cheent K, Khakoo SI. Natural killer cells: Integrating diversity with function. *Immunology* 2009. https://doi.org/10.1111/j.1365-2567.2009.03045.x.

6 Wang F, Lau JKC, Yu J. The role of natural killer cell in gastrointestinal cancer: killer or helper. *Oncogene* 2020. https://doi.org/10.1038/s41388-020-01561-z.

7 Meyer-Monard S, Passweg J, Siegler U, Kalberer C, Koehl U, Rovó A, *et al.* Clinical-grade purification of natural killer cells in haploidentical hematopoietic stem cell transplantation. *Transfusion* 2009. https://doi.org/10.1111/j.1537-2995.2008.01969.x.

8 Helmink BA, Reddy SM, Gao J, Zhang S, Basar R, Thakur R, *et al.* B cells and tertiary lymphoid structures promote immunotherapy response. *Nature* 2020. https://doi.org/10.1038/s41586-019-1922-8.

9 Waldman AD, Fritz JM, Lenardo MJ. A guide to cancer immunotherapy: from T cell basic science to clinical practice. *Nat Rev Immunol* 2020. https://doi.org/10.1038/s41577-020-0306-5.

10 Hollingsworth RE, Jansen K. Turning the corner on therapeutic cancer vaccines. *Npj Vaccines* 2019. https://doi.org/10.1038/s41541-019-0103-y.

11 Tang L, Zheng Y, Melo MB, Mabardi L, Castaño AP, Xie YQ, *et al.* Enhancing T cell therapy through TCR-signaling-responsive nanoparticle drug delivery. *Nat Biotechnol* 2018. https://doi.org/10.1038/nbt.4181.

12 Mansurov A, Ishihara J, Hosseinchi P, Potin L, Marchell TM, Ishihara A, *et al.* Collagen-binding IL-12 enhances tumour inflammation and drives the complete remission of established immunologically cold mouse tumours. *Nat Biomed Eng* 2020. https://doi.org/10.1038/s41551-020-0549-2.

13 Melero I, Gaudernack G, Gerritsen W, Huber C, Parmiani G, Scholl S, *et al.* Therapeutic vaccines for cancer: An overview of clinical trials. *Nat Rev Clin Oncol* 2014. https://doi.org/10.1038/nrclinonc.2014.111.

14 Teng F, Meng X, Kong L, Yu J. Progress and challenges of predictive biomarkers of anti PD-1/PD-L1 immunotherapy: A systematic review. *Cancer Lett* 2018. https://doi.org/10.1016/j.canlet.2017.11.014.

15 La Thangue NB, Kerr DJ. Predictive biomarkers: A paradigm shift towards personalized cancer medicine. *Nat Rev Clin Oncol* 2011. https://doi.org/10.1038/nrclinonc.2011.121.

16 Wang H, Mooney DJ. Biomaterial-assisted targeted modulation of immune cells in cancer treatment. *Nat Mater* 2018. https://doi.org/10.1038/s41563-018-0147-9.

17 Cheung AS, Zhang DKY, Koshy ST, Mooney DJ. Scaffolds that mimic antigen-presenting cells enable ex vivo expansion of primary T cells. *Nat Biotechnol* 2018. https://doi.org/10.1038/nbt.4047.

18 Koshy ST, Mooney DJ. Biomaterials for enhancing anti-cancer immunity. *Curr Opin Biotechnol* 2016. https://doi.org/10.1016/j.copbio.2016.02.001.

19 Sepantafar M, Maheronnaghsh R, Mohammadi H, Radmanesh F, Hasani-sadrabadi MM, Ebrahimi M, *et al.* Engineered Hydrogels in Cancer Therapy and Diagnosis. *Trends Biotechnol* 2017;**35**:. https://doi.org/10.1016/j.tibtech.2017.06.015.

20 Lu X, Horner JW, Paul E, Shang X, Troncoso P, Deng P, *et al.* Effective combinatorial immunotherapy for castration-resistant prostate cancer. *Nature* 2017. https://doi.org/10.1038/nature21676.

21 Chen Q, Xu L, Liang C, Wang C, Peng R, Liu Z. Photothermal therapy with immune-adjuvant nanoparticles together with checkpoint blockade for effective cancer immunotherapy. *Nat Commun* 2016. https://doi.org/10.1038/ncomms13193.

22 Smith TT, Moffett HF, Stephan SB, Opel CF, Dumigan AG, Jiang X, *et al.* Biopolymers codelivering engineered T cells and STING agonists can eliminate heterogeneous tumors. *J Clin Invest* 2017;**127**:2176–91. https://doi.org/10.1172/JCI87624.

23 Stephan SB, Taber AM, Jileaeva I, Pegues EP, Sentman CL, Stephan MT. Biopolymer implants enhance the efficacy of adoptive T-cell therapy. *Nat Biotechnol* 2015. https://doi.org/10.1038/nbt.3104.

24 Cho K, Wang X, Nie S, Chen Z, Shin DM. Therapeutic nanoparticles for drug delivery in cancer. *Clin Cancer Res* 2008. https://doi.org/10.1158/1078-0432.CCR-07-1441.

25 Sun T, Zhang YS, Pang B, Hyun DC, Yang M, Xia Y. Engineered nanoparticles for drug delivery in cancer therapy. *Angew Chemie - Int Ed* 2014. https://doi.org/10.1002/anie.201403036.

26 Bertrand N, Wu J, Xu X, Kamaly N, Farokhzad OC. Cancer nanotechnology: The impact of passive and active targeting in the era of modern cancer biology. *Adv Drug Deliv Rev* 2014. https://doi.org/10.1016/j.addr.2013.11.009.

27 Ferrari M. Cancer nanotechnology: Opportunities and challenges. *Nat Rev Cancer* 2005. https://doi.org/10.1038/nrc1566.

28 Nie S, Xing Y, Kim GJ, Simons JW. Nanotechnology applications in cancer. *Annu Rev Biomed Eng* 2007. https://doi.org/10.1146/annurev.bioeng.9.060906.152025.

29 Jain RK, Stylianopoulos T. Delivering nanomedicine to solid tumors. *Nat Rev Clin Oncol* 2010. https://doi.org/10.1038/nrclinonc.2010.139.

30 Liu H, Moynihan KD, Zheng Y, Szeto GL, Li A V., Huang B, *et al*. Structure-based programming of lymph-node targeting in molecular vaccines. *Nature* 2014. https://doi.org/10.1038/nature12978.

31 Hasani-Sadrabadi MM, Majedi FS, Bensinger SJ, Wu BM, Bouchard LS, Weiss PS, *et al*. Mechanobiological Mimicry of Helper T Lymphocytes to Evaluate Cell–Biomaterials Crosstalk. *Adv Mater* 2018;**30**:1–10. https://doi.org/10.1002/adma.201706780.

32 Majedi FS, Hasani-Sadrabadi MM, Thauland TJ, Li S, Bouchard L-S, Butte MJ. Augmentation of T-Cell Activation by Oscillatory Forces and Engineered Antigen-Presenting Cells. *Nano Lett* 2019;**19**:. https://doi.org/10.1021/acs.nanolett.9b02252.

33 Thauland TJ, Hu KH, Bruce MA, Butte MJ. Cytoskeletal adaptivity regulates T cell receptor signaling. *Sci Signal* 2017;**3737**:1–11.

34 Dustin ML. Visualization of cell-cell interaction contacts: Synapses and kinapses. *Self Nonself* 2011;**2**:85–97. https://doi.org/10.4161/self.2.2.17931.

35 Burkhardt JK, Carrizosa E, Shaffer MH. The actin cytoskeleton in T cell activation. *Annu*

Rev Immunol 2008;**26**:233–59. https://doi.org/10.1146/annurev.immunol.26.021607.090347.

36 Judokusumo E, Tabdanov E, Kumari S, Dustin ML, Kam LC. Mechanosensing in T lymphocyte activation. *Biophys J* 2012;**102**:L5-7.

37 O'Connor RS, Hao X, Shen K, Bashour K, Akimova T, Hancock WW, *et al.* Substrate rigidity regulates human T cell activation and proliferation. *J Immunol* 2012;**189**:1330–9.

38 Tabdanov E, Gondarenko S, Kumari S, Liapis A, Dustin ML, Sheetz MP, *et al.* Micropatterning of TCR and LFA-1 ligands reveals complementary effects on cytoskeleton mechanics in T cells. *Integr Biol (Camb)* 2015;**7**:1272–84. https://doi.org/10.1039/c5ib00032g.

39 Husson J, Chemin K, Bohineust A, Hivroz C, Henry N. Force generation upon T cell receptor engagement. *PLoS One* 2011;**6**:e19680.

40 Hui KL, Balagopalan L, Samelson LE, Upadhyaya A. Cytoskeletal forces during signaling activation in Jurkat T-cells. *Mol Biol Cell* 2015;**26**:685–95. https://doi.org/10.1091/mbc.E14-03-0830.

41 Saitakis M, Dogniaux S, Goudot C, Bufi N, Asnacios S, Maurin M, *et al.* Different TCR-induced T lymphocyte responses are potentiated by stiffness with variable sensitivity. *Elife* 2017;**6**:e23190.

42 Wahl A, Dinet C, Dillard P, Nassereddine A, Puech P-H, Limozin L, *et al.* Biphasic mechanosensitivity of T cell receptor-mediated spreading of lymphocytes. *Proc Natl Acad Sci U S A* 2019:1–6. https://doi.org/10.1073/pnas.1811516116.

43 Basu R, Whitlock BM, Husson J, Le Floc'h A, Jin W, Oyler-Yaniv A, *et al.* Cytotoxic T Cells Use Mechanical Force to Potentiate Target Cell Killing. *Cell* 2016;**165**:100–10. https://doi.org/10.1016/j.cell.2016.01.021.

44 Majedi FS, Hasani-Sadrabadi MM, Thauland TJ, Li S, Bouchard LS, Butte MJ. T-cell activation is modulated by the 3D mechanical microenvironment. *Biomaterials* 2020. https://doi.org/10.1016/j.biomaterials.2020.120058.

45 Vining KH, Mooney DJ. Mechanical forces direct stem cell behaviour in development and regeneration. *Nat Rev Mol Cell Biol* 2017;**18**:728–42. https://doi.org/10.1038/nrm.2017.108.

46 Chen ML, Pittet MJ, Gorelik L, Flavell RA, Weissleder R, Von Boehmer H, *et al.* Regulatory T cells suppress tumor-specific CD8 T cell cytotoxicity through TGF-β signals in vivo. *Proc Natl Acad Sci U S A* 2005. https://doi.org/10.1073/pnas.0408197102.

47 Batlle E, Massagué J. Transforming Growth Factor-β Signaling in Immunity and Cancer. *Immunity* 2019. https://doi.org/10.1016/j.immuni.2019.03.024.

48 Kelly M Credill AJS. Nonclinical Safety Evaluation of a Transforming Growth Factor β Receptor I Kinase Inhibitor in Fischer 344 Rats and Beagle Dogs. *J Clin Toxicol* 2014. https://doi.org/10.4172/2161-0495.196.

49 Park J, Wrzesinski SH, Stern E, Look M, Criscione J, Ragheb R, *et al.* Combination delivery of TGF-β inhibitor and IL-2 by nanoscale liposomal polymeric gels enhances tumour immunotherapy. *Nat Mater* 2012. https://doi.org/10.1038/nmat3355.

Chapter 2.

Cytokine Secreting Microparticles Engineer the Fate and the Effector Functions of T-Cells [1]

Abstract.

T-cell immunotherapy is a promising approach for cancer, infection, and autoimmune diseases. However, significant challenges hamper its therapeutic potential, including insufficient activation, delivery and clonal expansion of T cells into the tumor environment. To facilitate T-cell activation and differentiation *in vitro*, we developed core-shell microparticles for sustained delivery of cytokines. These particles were enriched by heparin to enable a steady release of interleukin-2 (IL-2), the major T-cell growth factor, over 10+ days. The controlled delivery of cytokines was used to steer lineage specification of cultured T-cells. This approach enables differentiation of T-cells into central memory and effector memory subsets. We showed that the sustained release of stromal cell-derived factor 1α (SDF-1α) could accelerate T-cell migration. We demonstrated that CD4+ T-cells could be induced to high concentrations of regulatory T-cells through controlled release of IL-2 and TGF-β. We found that CD8+ T-cells that received IL-2 from microparticles were more likely to gain effector functions as compared with traditional administration of IL-2. Culture of T-cells within 3D scaffolds that contain IL-2-secreting microparticles enhanced proliferation as compared with traditional, 2D approaches. This yield a new method to control the fate of T-cells and ultimately, to new strategies for immune therapy.

[1] This Chapter is published as: Majedi F.S., Hasani M.M., Kidani Y., Thauland T.J., Moshaverinia A., Butte M.J., Bensinger S.J., Bouchard L.S. Cytokine secreting microparticles engineer the fate and the effector functions of T cells. *Advanced Materials*. 30 (2018) 1703178.

2.1. Introduction

In this work, we developed biocompatible microparticles that delivered a variety of cytokines that influence the proliferation and differentiation of cultured, primary T cells. Augmentation and engineering of immune responses have major applications in combating cancers, and enriching regulatory immune cells has potential roles in suppressing transplant rejection and in mitigating autoimmune and allergic diseases. There are a number of challenges to adoptive T cell therapies [1,2], especially in skewing bulk cultures of T cells towards desired outcomes. Both cytotoxic (CD8+) T cells, endowed with the ability to kill, and helper (CD4+) T cells, endowed with the dedicated production of cytokines, are needed for clearing cancers and modulating aberrant responses. Controlled manipulation of these populations will be key to successful immunotherapies.

A number of groups have developed polymeric carriers, such as microparticles, liposomes, or micelles for delivering biomolecules.[3,4] Such particles have be used to modulate the immune system by delivering antigens, vaccines, adjuvants, and drugs.[5] While the focus of prior work has mainly been on enhancing stability or solubility of the delivered molecules, little has been done on sustained release and its impact on therapeutic efficacy compared to burst release.[6-8] Here we demonstrate enhancements over traditional approaches due to controlled release of cytokines to T cells.

Tuning the effector functions of T cells requires the presence of cytokines during activation. Certain cytokines, such as IL-2, enhance proliferation and affect the balance of effector *vs*. memory cytotoxic T-cell differentiation.[9] The "strength" of IL-2 signals plays a crucial role in facilitating the acquisition of effector phenotypes in CD8+ T-cells.[9] However, few studies have been carried out to investigate the effect of engineered administration of this cytokine.[10-12] In undifferentiated CD4+ T cells, IL-2 can act in synergy with TGF-beta to promote the generation of induced regulatory T cells.[13]

In this study, polymeric particulate systems loaded with cytokines were designed to exhibit tunable release profiles. Alginate and heparin, natural biopolymers, were chosen for our platform to encapsulate IL-2 due to their biocompatibility and facile gelation *via* calcium ions.[14] Traditional methods for the formation of polymeric microparticles such as microemulsions have been gradually replaced by microfluidic approaches[15,16] because of the better control over particle size and distribution (narrower polydispersity). Here we employed a T-shaped droplet generator to form our polymeric microparticles at desired sizes. A protective shell of chitosan with desired thickness was applied to tune the rate of IL-2 release. To assess the potential for activation in a 3D environment and the effect of extended provision of cytokines, lymphocytes were seeded into bioengineered scaffolds imbued with cytokine release. Our data show that the tuning of release of cytokines can be used to regulate the suppressive and cytotoxic potentials of T cells.

2.2. Results and Discussion

To form microparticles, we used a microfluidic device featuring a droplet generator (**Fig. 2.1a**). Using a hydrophobic sheath fluid of mineral oil+ Span 8%, we generated Alginate-Heparin (Alg-Hep) microparticles comprising various concentrations of polymer from 0.5 to 5 wt%/v (as shown in **Fig. 2.1b**, and a well-controlled micromixer (**Fig. 2.1c**). The flow ratios were tuned to make spherical Alg-Hep microdroplets of different diameters from 400 nm to 30 μm (**Fig. 2.1d**). To achieve complete gelation of the resulting particles, they were stored in $CaCl_2$ solution with different Ca^{++} concentrations (50-200 mM) for 40 min [Materials and methods are available as supplementary materials]. Tuning the mesh size as an indicator for nanoscale porosity of the particles can affect the release rate of the entrapped proteins. To calculate the mesh sizes, we measured the swelling ratio of the microparticles. Calculations were done based on the Flory–Rehner method.[17] Estimated mesh size values of the Alg-Hep microparticles as a function of calcium ion and polymer concentrations are shown in **Fig. 2.1e**. Higher cross-linking densities

resulted in microparticles with smaller mesh sizes. These results show that a variety of particle and mesh sizes were achieved in our work.

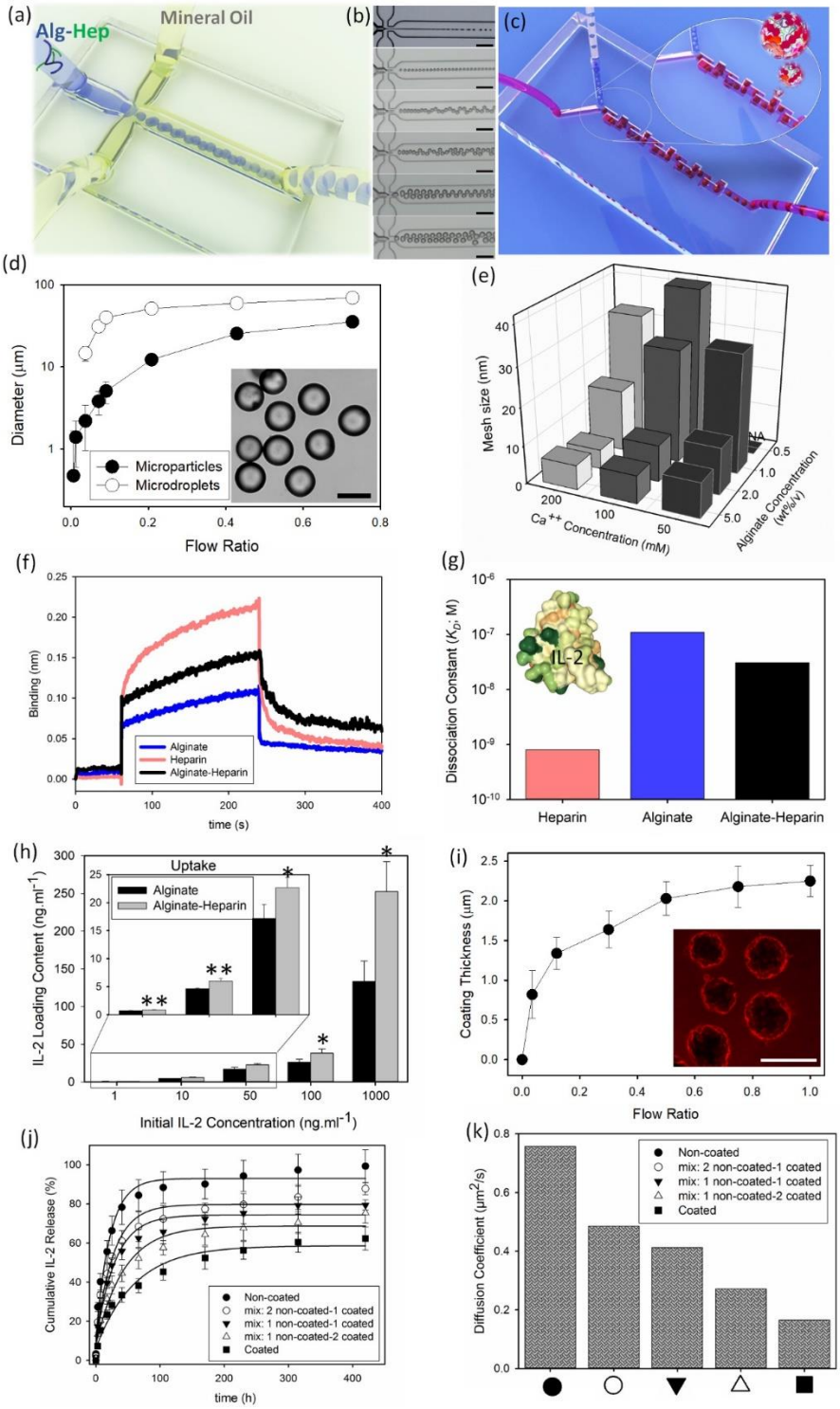

Figure 2.1. Microfluidic generation and coating of Alginate-Heparin (Alg-Hep) microparticles for controlled release of IL-2. (a) Schematic representation of a microfluidic droplet generator device, that is applied to form (Alg-Hep) microparticles *via* sheath hydrophobic flows. (b) Diameter of Alg-Hep microparticles (1 wt%/v) is controlled by changing the volumetric flow rate ratio of aqueous to oil phase (○). Equilibrium diameter of microparticles as characterized after gelation process at calcium ion bath (●). Inset: microscopy image of a typical batch of Alg-Hep particles formed at flow ratio of 0.45. (c) Microscopic images of Alg-Hep microdroplets formed at different flow ratios resulting in different sizes from 400 nm to 30 μm. (d) Schematic illustration of the serpentine micromixer used to coat Alg-Hep particles with Chitosan layer. (e) Quantification of mesh size analysis of microparticles as a function of calcium ion and Alg-Hep concentrations. (f) Bio-layer Interferometry sensorgrams showing the binding kinetic of IL-2 to alginate, heparin, and Alg-Hep functionalized surfaces. (g) Calculated dissociation constants ($K_D = k_{off}/k_{on}$) based on the curve fittings for IL-2 bindings at various concentrations of 5-200 nM; Inset is the 3D representation of IL-2 (PDB ID: 1M47; colored based on hydrophobicity). (h) Interleukin-2 (IL-2) binding efficiency of Alginate and Alg-Hep microparticles at various initial concentrations of IL-2 after 12 h of incubation. The presented data are expressed as average ± SD. The results were analyzed using unpaired t-tests. NA: We could not make particles from 0.5% alginate and 50 mM calcium. (i) Microfluidic tuning of coating thickness *via* changing the flow ratio between Alg-Hep particles and Chitosan polymers. Inset: Fluorescence images of RITC-labeled Chitosan coated Alg-Hep particles. IL-2 release kinetic of microfluidic-synthesized microparticles prepared from different precursor formulations in PBS at 37°C (j) and calculated diffusion coefficients of studied microparticles (k).

To enhance cytokine binding, we modified the alginate biopolymer with heparin. To incorporate heparin into alginate structure, activated carboxylic acid groups on heparin chains were covalently reacted with diamine-modified alginate through an aqueous carbodiimide reaction. We examined the relationship between the initial amount of heparin and the final conjugated value and found that our process saturated at 1.5 nmol of heparin per mg alginate (see Supporting Information, **Fig.2.2**). The intrinsic affinity of IL-2 to heparin has been reported before.[18-20] To measure the binding of IL-2 to alginate, heparin, and Alg-Hep functionalized surfaces, we employed real-time bio-layer interferometry (BLI) (**Fig. 2.1h**). We found that Alg-Hep and IL-2 undergo a high affinity interaction (K_D = 30.6 nM) compared to the unmodified

alginate (110 nM) (**Fig. 2.1f**). These results show that our heparin-modified particles improved the binding of IL-2 over alginate particles alone.

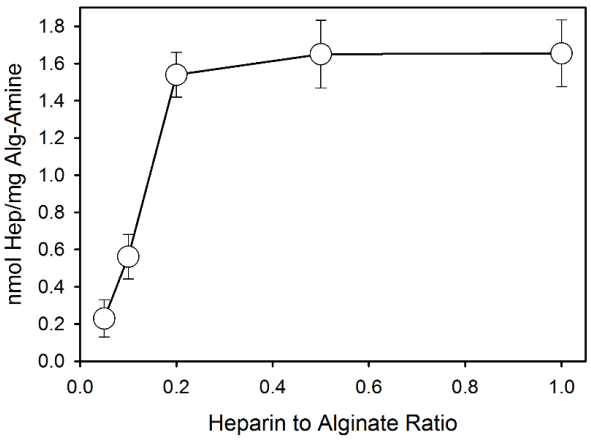

Figure 2.2. Degree of heparinization of alginate with varying amount of initial added heparin content to the reaction.

To assess the amount of IL-2 we could bind to our particles, they were incubated with different concentrations of IL-2 (1-1000 ng/mL) for 12 h at 37 °C and after washing, microparticles were dissolved and the amount of released IL-2 was measured using ELISA. As shown in **Fig. 2.1g**, the presence of heparin significantly enhanced the IL-2 loading content and efficiency (**Fig. 2.3**) of the microparticles.

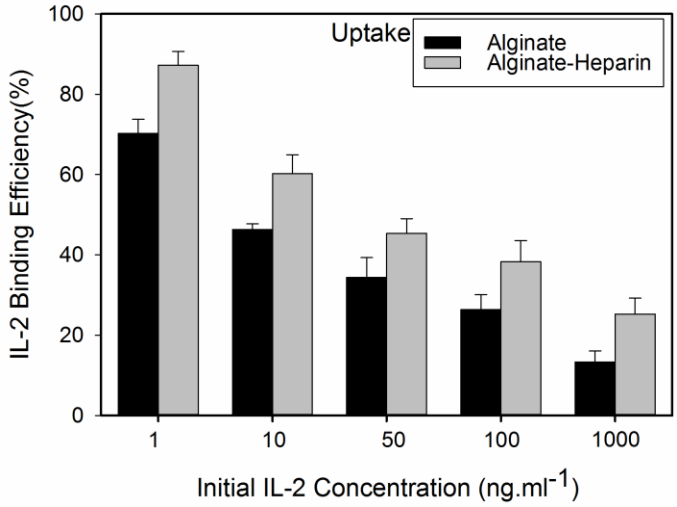

Figure 2.3. IL-2 binding efficiency of alginate and Alg-Hep microparticles at various initial concentration of IL-2 which loaded to particles *via* uptake method. The presented data are expressed as average ± SD.

The IL-2 binding efficiency of alginate and Alg-Hep microparticles was also evaluated when designated amounts of IL-2 (1-100 ng/ml) were mixed with alginate prior to microfluidic droplet formation and subsequent washing steps (see **Fig. 2.4**). To assess whether there was a size dependence to the loading, we tested the binding efficiency of Alg-Hep particles sized 1-35 μm. We found a modest relationship of IL-2 loading to the particle size using both loading methods (**Fig. 2.5**). These results show that large amounts of IL-2 can be integrated into our particles.

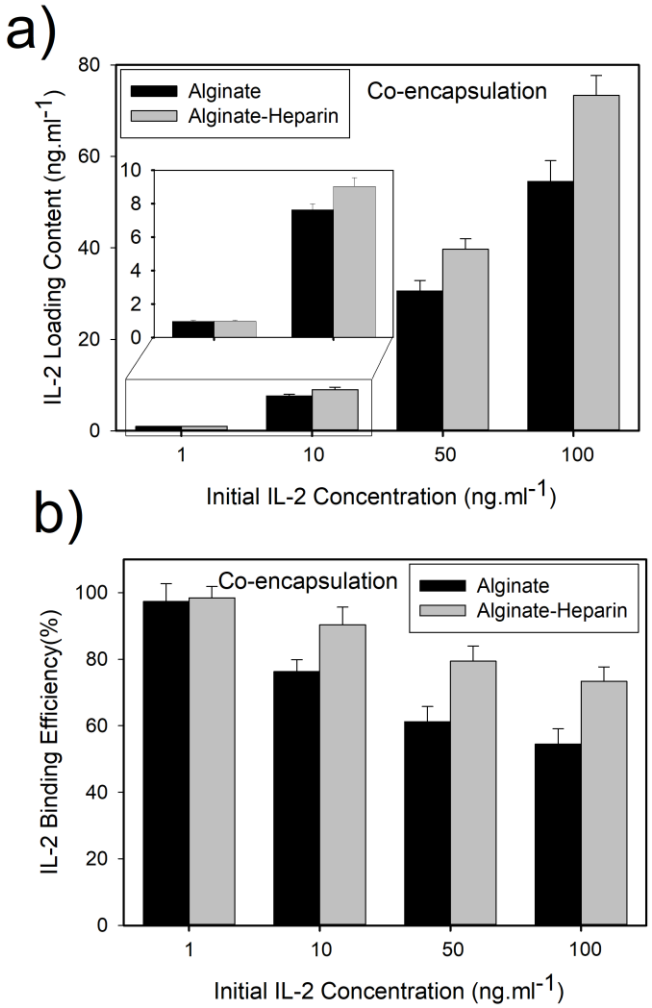

Figure 2.4. IL-2 loading content (a) and binding efficiency (b) of alginate and Alg-Hep microparticles at various initial concentration of IL-2 which co-encapsulated during the particle formation. The presented data are expressed as average ± SD.

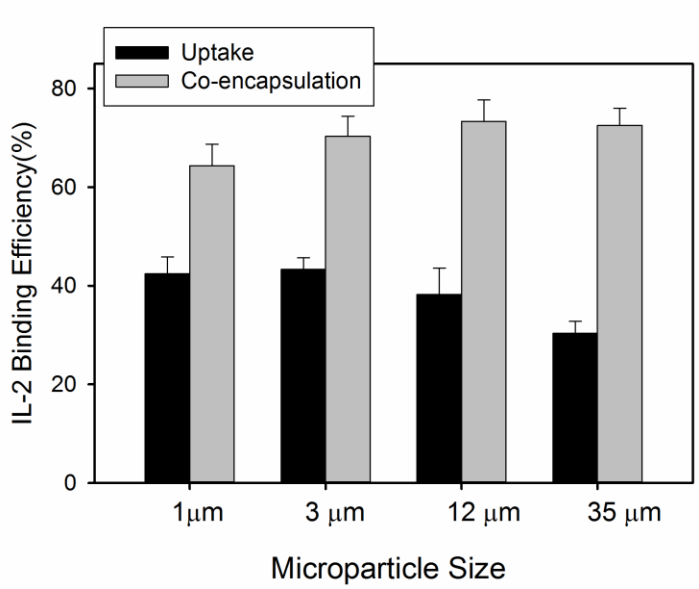

Figure 2.5. Effect of microparticle size on IL-2 binding efficiency of Alg-Hep microparticles at initial IL-2 concentration of 100 ng/ml which was studied through particles that uptake IL-2 after their formation or IL-2 was co-encapsulated within them during their formation procedure. The presented data are expressed as average ± SD.

To control the timing of the release of IL-2 from the particles, we sought to coat the alginate-heparin particles with a layer ("shell") of chitosan. We prepared a microfluidic device that controls residence time of particles and thus allows for increasing amounts of coating over time. In the second microfluidic device (serpentine micromixer; **Fig. 2.1d**), mixing and laminar flows are the predominant mechanisms of mass transfer, where the coating process mainly occurs at the microscale and is controlled through manipulation of the residence time.[21] The serpentine micromixer was designed using a 3D printing and structure-removal approach[22] (see Supporting Information, **Fig. 2.6**). By controlling the flow rate, and thus residence time, of particles in this device, we coated them with varying amounts of chitosan. To assess the thickness of chitosan, we coated with chitosan-RITC with various residence times and measured the resulting thickness of the chitosan shell by fluorescence microscopy (**Fig. 2.1e**). These results show that our microfluidic device could successfully coat alginate-heparin particles with chitosan.

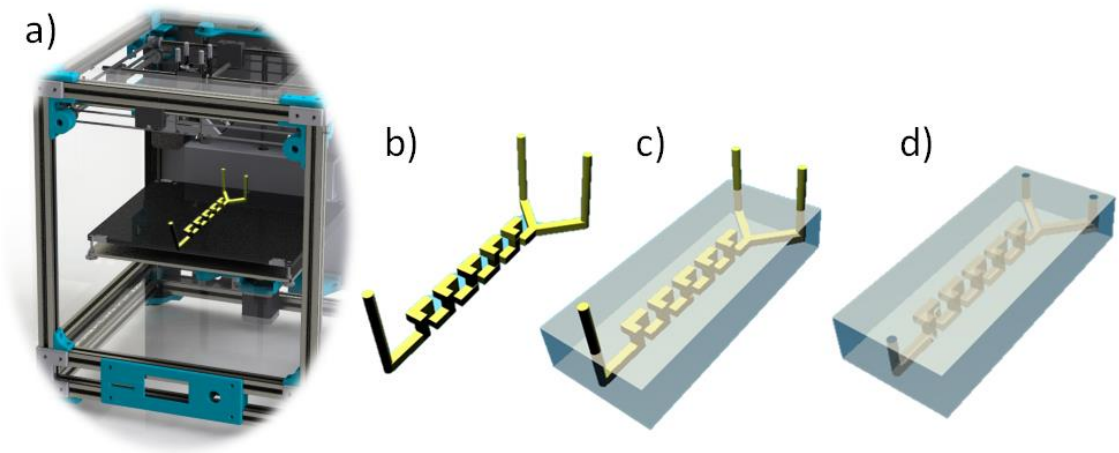

Figure 2.6. Schematic representation of 3D printed and structure removal method that is used to prepare a micromixer platform for coating of Alg-Hep particles includes: (a) 3D printing of mold, (b) PDMS casting and (c) dissolution of ABS filaments to provide microchannels inside PDMS (d).

To assess the effect of chitosan coating on the timing of release of IL-2, we measured the release of IL-2 from Alg-Hep microparticles in the presence or absence of chitosan layer sequentially over 18 days. We found that release of IL-2 from chitosan-coated microparticles was slower than from non-coated ones. By mixing coated and non-coated particles we could tune the release profile of IL-2 (**Fig. 2.1j**). This tuning capability over the microscale release of IL-2, and its diffusion coefficient (**Fig. 2.1k**) under different applied conditions were also investigated. To estimate the diffusion coefficient of IL-2 out of the particles, we examined the initial linear part of the plots (**Fig. 2.7**) and employed Fick's law [Equation (1)]:[23]

$$\frac{M_t}{M_\infty} = 6\left(\frac{Dt}{\pi R^2}\right)^{1/2} \qquad (1)$$

where M_t/M_∞ represents the fraction of released drug at time t, D is the diffusion coefficient of IL-2 molecules and R is the radius of the particles (6.1 μm). The calculated diffusion coefficients are shown in **Fig. 2.1k**. These results show that chitosan-coated particles have lower diffusion

coefficients than non-coated ones, which is desirable for controlling the release of cytokines over time.

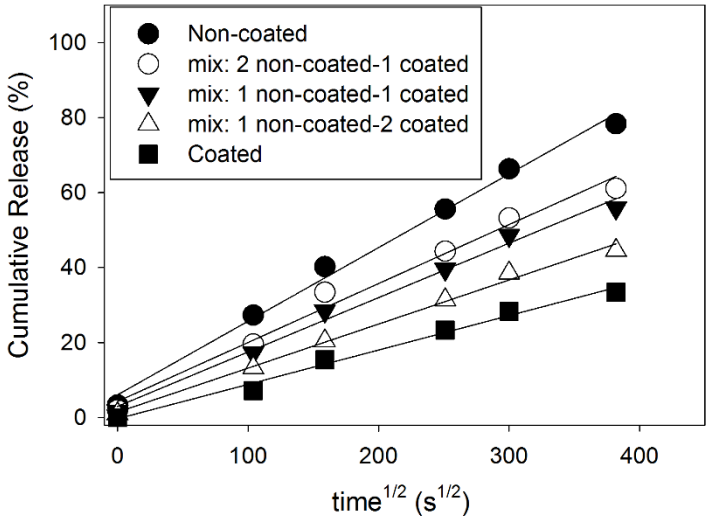

Figure 2.7. *In vitro* release profile of IL-2 from microfluidic Alg-Hep –based microparticles in PBS at 37°C.

Strength of IL-2 signals impacts the cytolytic functionality of CD8+ T cells

To test whether application of IL-2 could improve cytotoxic T-cell activation, we employed our particles in the activation of CD8+ T-cells. Different microparticles with similar loading efficiencies were synthesized and loaded with IL-2. Purified naïve CD8+ T-cells were activated with anti-CD3 and anti-CD28 as described in Methods. After two days, cells were re-plated with different types/ratios of particles (**Fig. 2.8a**).

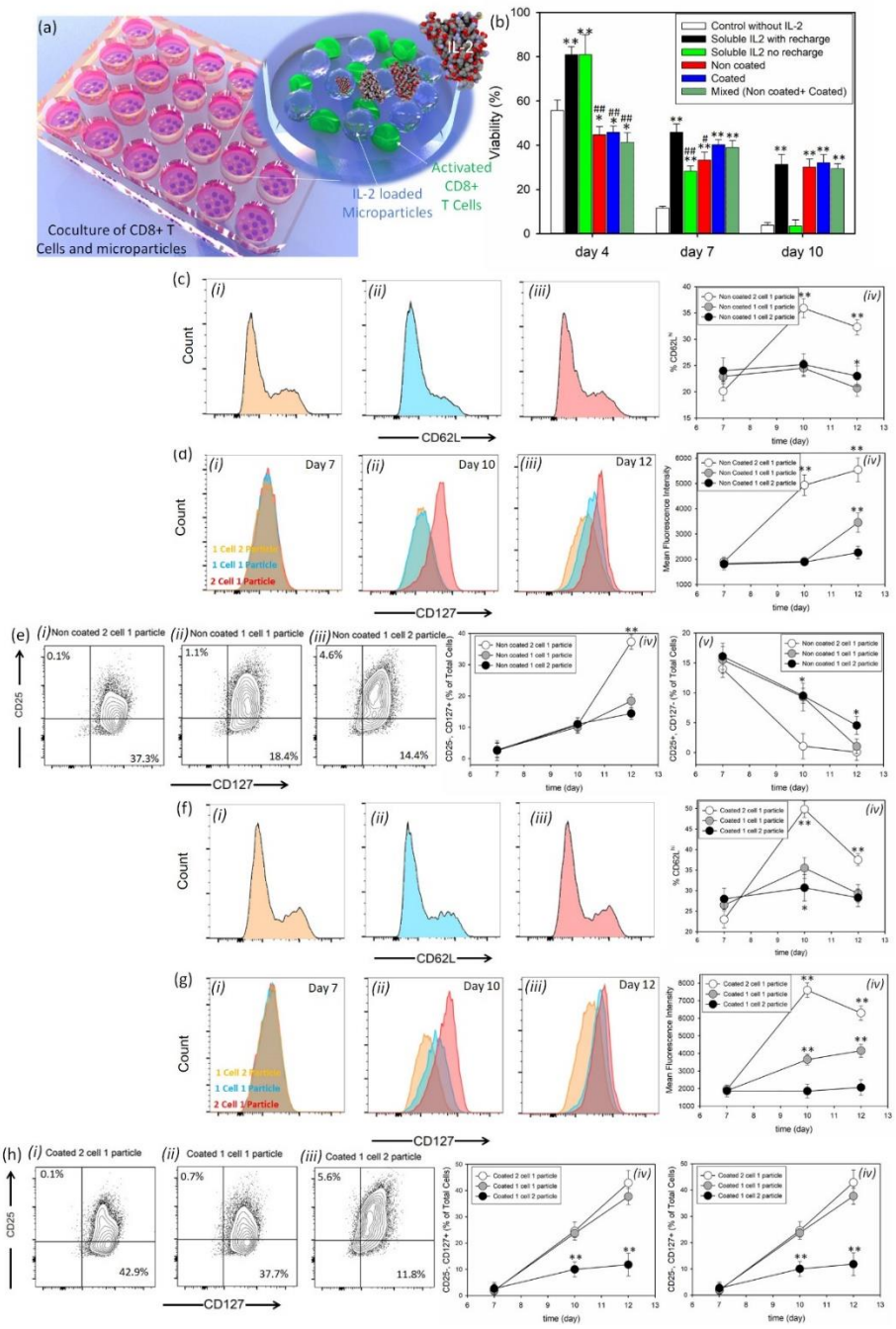

Figure 2.8. Role of interleukin-2 presentation on differentiation of cytotoxic T-cells. (a) Schematic representation of CD8+ T-cells and microparticles co-culture. (b) Effects of IL-2 release on viability of CD8+ T-cells. All data are presented as average ± SD. The results were analyzed using unpaired t-tests. For all of the tests, the threshold was set to $p < 0.05$ for "statistically significant" and $p < 0.01$ was for "statistically very significant". The thresholds $^{*}p < 0.05$ and $^{**}p < 0.01$ were obtained between each group and the control group without IL-2 treatment (negative control). On the other hand, $^{\#}p < 0.05$ and $^{\#\#}p < 0.01$ are between each

treatment and the cells treated by IL-2, with recharge (positive control). (c) Kinetics of CD62L expression when purified naïve CD8+ T-cells were stained with antibodies against CD62L *ex vivo*, and after priming for two days with anti-CD3 + anti-CD28 (day 2). Histograms are representative of day 12 marker expression on cells after treatment with one non-coated particle per two cells (i), one particle per cell (ii), and two particles per cell (iii) as IL-2 releasing agents. (iv) The MFI of CD62L expression during the treatment. (d) Regulation of IL-7Ra (CD127) re-expression after priming in three different ratios of cell to particle at day 7 (i), 10 (ii), and 12 (iii) and MFI of cells in these conditions over time (iv). (e) Flow cytometric analysis of IL-2Ra and IL-7Ra co-expression when treated with non-coated microparticles at particle: cell ratios of (i) 1:2, (ii) 1:1, and (iii) 2:1. Percentage of cells that fall in the category of memory T-cells (CD 25^-, $CD127^+$) (iv), or effector cells ($CD25^+$, $CD127^-$) (v) in three different IL-2 concentrations over time. (f) Kinetics of CD62L expression after incubation of activated $CD8^+$ T-cells with coated microparticles stained with antibodies against CD62L *ex vivo* at particle: cell ratios of 1:2 (i), 1:1 (ii), and 2:1 (iii). Histograms are representative of day 12 marker expression. (iv) The MFI of CD62L staining is shown. (g) The regulation of IL-7Ra (CD127) re-expression after priming in three different ratios of cells to coated particles at day 7 (i), 10 (ii), and 12 (iii) and MFI of cells in these conditions over time (iv). (h) Analysis of IL-2Ra and IL-7Ra co-expression when treated with non-coated microparticles at three different ratios of (i) 1:2, (ii) 1:1, and (iii) 2:1 to the cells. Percentage of cells that fall in the category of memory T-cells (CD 25^-, $CD127^+$) (iv), or effector cells ($CD25^+$, $CD127^-$) (v) in three different IL-2 concentrations over time is represented. In (c)-(h) the presented data are expressed as average ± SD. The results were analyzed using unpaired t-tests.

To first ensure that the particles were not toxic, we evaluated the viability of CD8+ T cells after 12 and 48 h of co-culture with non-coated and coated particles and saw that even at very high ratios of particle (coated or non-coated) to cells (100:1) the cellular viability was more than 79% after 48 h of culture (**Fig. 2.9**). This confirmed the non-toxicity of the particles. IL-2 is critical to support T-cell survival and proliferation. Without addition of IL-2 in culture, cell viability decreased dramatically over a few days (**Fig. 2.8b**, white bars). We compared the viability of T cells in the presence of particles versus two conditions: first, refreshing media and IL-2 approximately every two days (**Fig. 2.8b,** black bars); and second, supplied with IL-2 only at the beginning of experiment and then fresh media was changed every two days (**Fig. 2.8b,** green bars). We found that CD8+ T-cell viability was comparable when employing IL-2 releasing

particles (coated, uncoated, and mixed) as when frequently refreshing soluble IL-2 (**Fig. 2.8b**). This result demonstrates that sustained release of IL-2 from our particles could sustain the viability of T cells over 10 days.

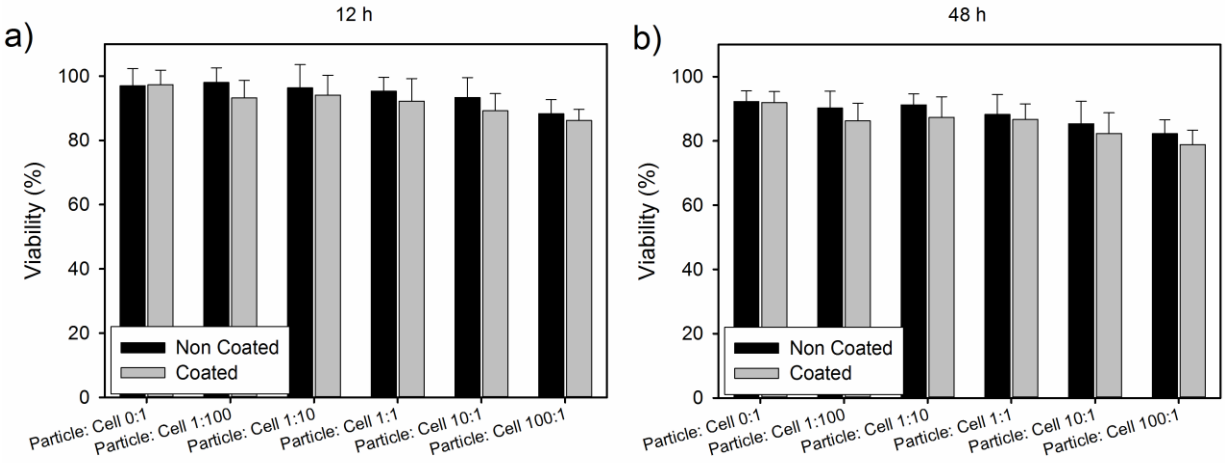

Figure 2.9. Cell viability evaluation of non-coated and coated particles at different ratio to cells after 12 (a) and 48 h (b) of co-culturing with CD8+ T-cells and in absence of IL-2. The presented data are expressed as average ± SD.

To distinguish the effect of IL-2 signal strength versus its rate of elaboration from the beads, we studied the differentiation of CD8+ T cells upon fixing the microparticle type and adjusted the ratio of particles to cells. Activated CD8+ T cells downregulate the IL-7 receptor alpha (CD127), upregulate the IL2 receptor alpha (CD25), and cleave the extracellular domain of CD62L. To this end, experiments were done under three different conditions where we had an equal number of cells and particles at the beginning of the experiment; the number of particles was twice the number of cells or vice-versa. At different time points during a 12-day period, cells were harvested and stained against certain cell surface markers known to be associated with effector or memory cell phenotypes. Up/down regulation of CD62L, CD127, CD25, CD44, and CCR7 proteins on cell surface were monitored by flow cytometry over time, and we showed that the presence of microparticles did not interfere with staining for FACS (**Fig. 2.10**).

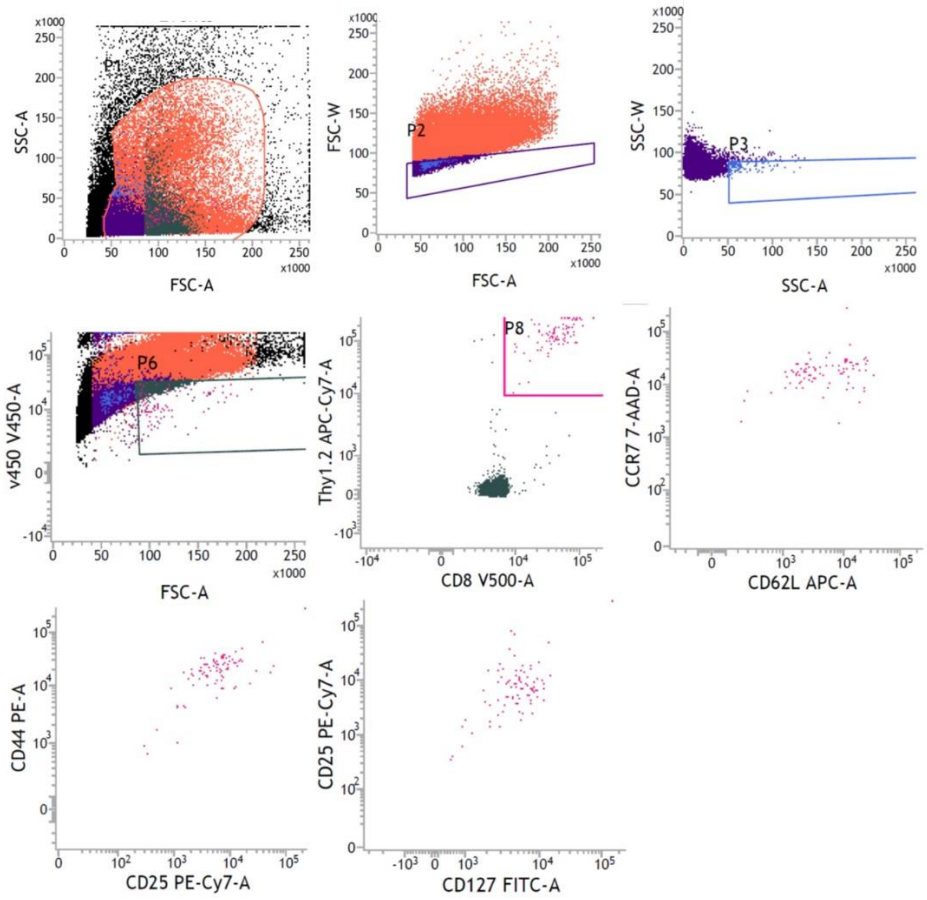

Figure. 2.10. Flow cytometry results of microparticles in the absence of T-cells. The results confirm there is a negligible level of particles staining.

We found that after seven days in culture with the particles, CD8+ T cells in the wells with a 1:2 ratio of non-coated particles:cells (experiencing stronger IL-2 signals) showed the proportion of cells that were $CD62L^{hi}$ was 32.3% whereas the cells exposed to 1:1 or 1:2 ratios of cells:particles showed only 20.7% and 23.0% $CD62L^{hi}$, respectively (**Fig. 2.8c)**. Similarly, we saw the high ratio cells showed more downregulation of CD127 than the ones exposed to a lower ratio of particles (**Fig. 2.8d)**. In addition, we saw that the high ratio cells showed more upregulation of CD25 than the ones exposed to a lower ratio of particles (**Fig. 2.8e)**. These results show that higher exposure to IL-2 signal induced more effector-like phenotypes ($CD62L^{lo}$, $CD127^{lo}$, $CD25^{hi}$), whereas cells exposed to lower IL-2 became a central memory-like phenotype ($CD62L^{hi}$, $CD127^{hi}$, $CD25^{lo}$).

The same set of evaluations was performed on CD8+ cells cultured with different ratios of coated particles. These cells experienced the same overall dosage of IL-2 comparable to their non-coated compartments but the coating reduced the rate of IL-2 release. For the activation markers chosen, the general pattern of responses that the CD8 T cells showed was similar (**Fig. 2.8f, g,h)**. Thus, the number of particles was the dominant factor in activation and differentiation. Our results suggest that the ratio of IL-2 secreting particles to cells drives a major impact in CD8+ T cell differentiation.

The rate at which IL-2 is administered to CD8+ T-cells can tune the ratio of central memory T-cells (TCM) to effector memory T-cells (TEM)

Memory T-cells are classified according to heterogeneity of surface marker expression, effector functions, and homing tissue compatibility. TEMs provide immediate protection while TCMs are responsible for the generation of additional effector cells [17]. Whether these two subsets behave differently in terms of cytolytic activity or which of them holds higher promise for further applications is unclear.[24-26] All activated T cells and memory T cells, even quiescent, show an upregulation and splicing change of CD44, which facilitates rapid extravasation into inflammatory sites through interaction with hyaluronan.[27] The regulation of the chemokine receptor CCR7 as an essential surface marker for migration of T-cells into peripheral lymph nodes is well established.[28] CCR7 expression is a key factor in distinguishing TCMs from TEMs.[24] Generally, TCMs are considered CCR7+CD44^{hi} CD62L^{hi} cells while TEMs are considered CCR7-CD44^{hi} CD62L^{low} cells.

To assess whether the rate of administration of IL-2 impacts cell fate, we monitored the differentiation of CD8+ T cells under conditions where the release profiles were different but the ratios of particle to cells was held constant. We found that after10 days, CD8+ T cells cultured with coated particles at 1:1 ratio (cell: particle) showed the proportion of cells that were CD62L^{hi} was 35.5 % whereas the cells cultured with non-coated particles showed 10% less CD62L^{hi} cells

(**Fig. 2.8 c-v and Fig. 2.8 f iv)**. In culture with coated particles at 1:1 cell: particle ratio, the CD8+ T cells showed a CCR7 MFI of 14000 whereas the cells exposed to non-coated particles showed a MFI of 10800 (**Fig. 2.11d)**. All T cells showed the $CD44^{hi}$ marker of memory cells; it would be expected that recently activated, effector T cells down-regulate CD44 by day 5 to 6 after activation in the absence of ongoing antigen signal.[29] These results show that coated particles favor the formation of a central memory phenotype. (**Fig. 2.11a-ii**, **iv**, **Fig. 2.11c-ii**, **iv**, **Fig. 2.11e-ii**, **iv**), while culture with non-coated particles favored the formation of a more effector memory phenotype (**Fig. 2.11a-i**, **iii**, **Fig. 2.11c-i**, **iii**, **Fig. 2.11e-i**, **iii**).

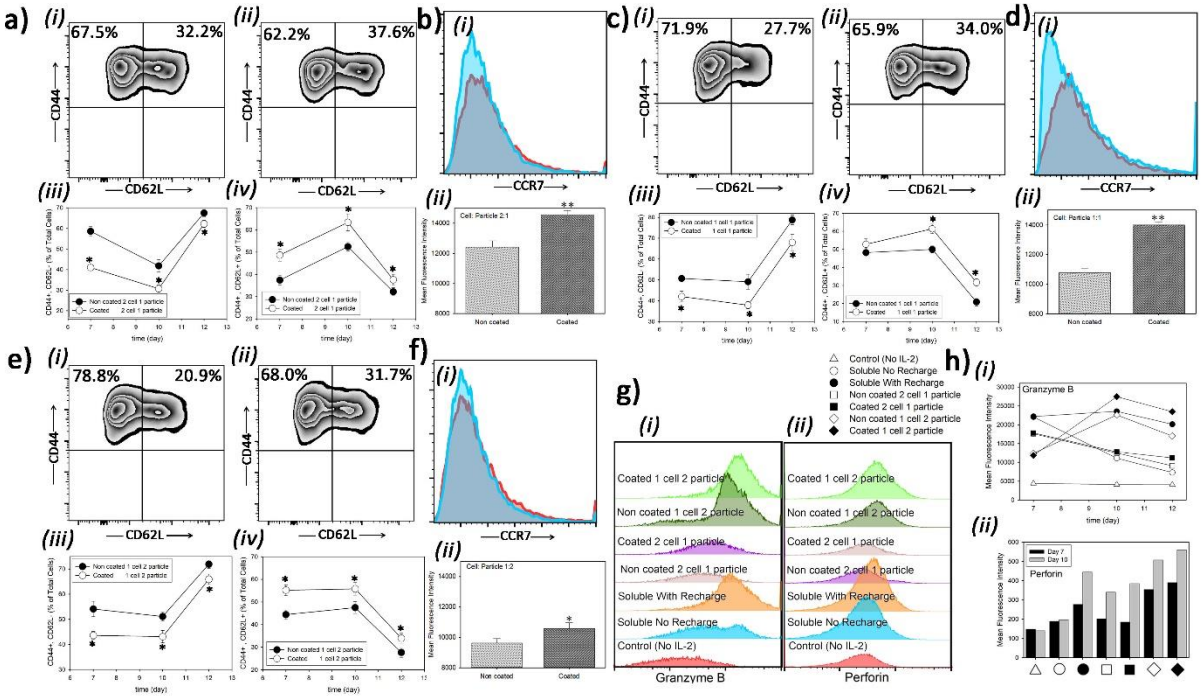

Figure 2.11. Different profiles of IL-2 administration to CD8+ T-cells impacts differentiation of them to central or effector memory cells. (a) Flow cytometric analysis of CD44 and CD62L co-expression at 2 cells per particle (a i-iv), 1 particle per cell (c i-iv), and 2 particles per cell ((e) i-iv). (i) non-coated particles or (ii) coated particles in each set (day 12). Percentage of effector cells ($CD44^{+}CD62L^{-}$) in each case (iii) or memory ($CD44^{+}CD62L^{+}$) phenotype (iv). Histograms of CCR7 expression of memory subset of cells, (b),(d), and (f), when cells are treated with non-coated particles (i) or coated (ii) particles and their MFIs (iii) at day 12. (g), (h) Flow cytometric analysis of granzyme B (i) and perforin (ii) expressions as a function of

treatment modality and time. The presented data are expressed as average ± SD. The results were statistically analyzed using unpaired t-tests.

We attempted to further tune the release profile by mixing coated and non-coated particles (**Fig. 2.1j**). We cultured CD8+ T cells with a constant ratio of one particle per cell but employed coated, non-coated and three different mixtures of un/coated particles (**Fig. 2.12**). Down-regulation of CD127 was correlated with the rate of IL-2 release. This result adds to our conclusion that the rate of IL-2 exposure (as well as the dose) to activated T cells can skew the outcome of their differentiation.

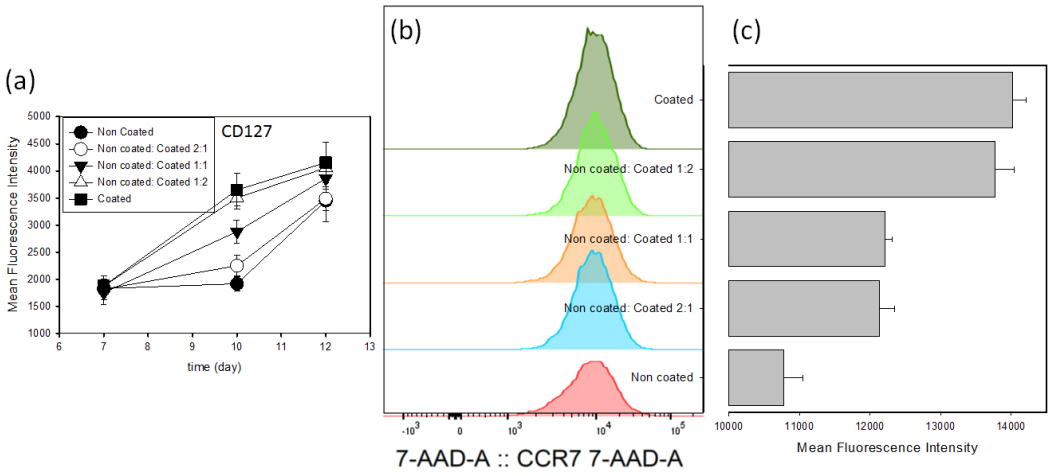

Figure 2.12. (a) Regulation of IL-7Ra (CD127) re-expression after priming in three different cell-to-particle ratios at day 7, 10, and 12. (b) Histograms of CCR7 expression of memory cells subset when cells are treated with designated mixtures of coated vs non-coated particles. The corresponding MFIs are shown in (c). The presented data are expressed as average ± SD.

During CD8+ T-cell activation, these cells induce expression of proteins such as the pore forming perforin and the protease granzyme B that are critical for their cytotoxic function.[9] In activated cells, different expression levels of each protein has been correlated to development of effector or memory CTLs.[30-32] Here we sought to understand if different kinetics of IL-2 administration affected the expression of perforin and granzyme B. Naïve CD8+ T cells were cultured on anti-CD3 anti-CD28 for three days and then moved to a non-stimulatory well that contained IL-2 in the media. Naïve T-cells expressed a minimal amount of perforin and very little

granzyme B (data not shown). Granzyme B expression was higher when IL-2 was "recharged" into the culture media every other day as compared to a single load of IL-2 at the start (**Fig. 2.11g**). We found even higher granzyme expression in culture conditions where there was a high ratio of particles to cells. (**Fig. 2.11h (i)**). Perforin expression levels were higher with stronger and sustained IL-2 signals compared to low IL-2 or when IL-2 was not renewed (**Fig. 2.11h (ii)**). These results show that cytotoxic T cell effect functions can be intensified over conventional approaches by providing IL-2 from microparticles.

Our microparticle platform has a broad capability to deliver a multitude of cytokines and growth factors. The electrostatic charge of heparin should allow for a broad set of proteins to be captured based on their isoelectric point. For example, we expected to easily load into our microparticles positively charged proteins like stromal cell-derived factor 1 (SDF-1α; pI: 9.9), transforming growth factor beta (TGF-β; pI: 8.5), and interferon gamma protein (IFN-γ; pI; 9.5). We performed loading experiments with these cytokines at 50 ng/mL and measured binding efficiency (**Fig. 2.13a**). We found excellent loading, with improved loading in the heparin-coated particles as compared to alginate alone. As shown, this platform has limited functionality for absorbing proteins that have negative charge at neutral pH like tumor necrosis factor alpha (TNF-α; pI; 6.4).

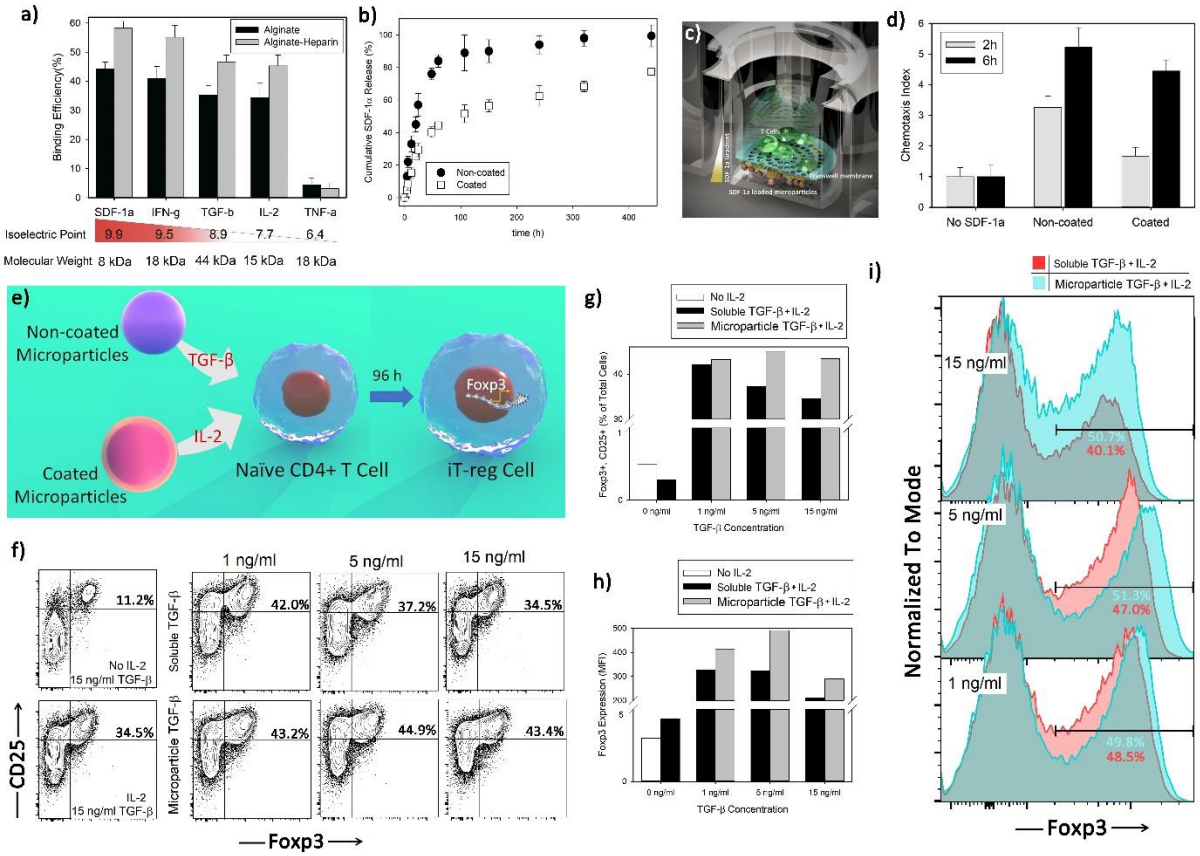

Figure 2.13. Engineered microparticles can deliver other signals beside IL-2. (a) Binding capacity of alginate-heparin microparticles was evaluated after incubating them with various cytokines at constant concentration of 50 ng/ml for 12 h at 4°C and under continuous, gentle shaking. (b) Release profile of SDF-1α cytokine from non/- coated Alg-Hep microparticles at 37°C. SDF-1α releasing microparticles (in the bottom of the well) generate a sustained gradient to recruit local T-cells as schematically illustrated in (c). (d) Quantification of relative T-cell's migration (Chemotactic index) for active T-cells after 2 h of co-culture with non-coated Alg-Hep microparticles at different initial loadings. The presented data are expressed as average ± SD. (e) Sustain release of TGF-β mediates development of induced regulatory T-cells (iT-reg cells). (f-i) Flow cytometric analysis of iT-reg development was assessed and judged by Foxp3 and CD25 co-expression after co-culture of naïve CD4+ T-cells with anti-CD3 and anti-CD28 for four days. The indicated range of TGF-β concentrations were applied either in a soluble format or via non-coated microparticles at the same time as activation signal. All the samples contained IL-2 releasing coated microparticles that delivered 20 U/ml IL-2 during treatment. The control experiments ((f) left panels) were also performed to show the effect of IL-2 presence in the constant concentration of TGF-β (15 ng/ml).

To study the impact on migration of naïve and activated T-cells, we employed alginate-heparin particles to encapsulate stromal cell-derived factor 1 (SDF-1α). Based on binding kinetics data (**Fig. 2.14**), heparin incorporation enhanced SDF-1α interaction with the alginate matrix. The sustained release of SDF-1α could also be controlled by a protective shell similar to the one proposed for IL-2 (**Fig. 2.13b**) or it can be tuned based on the initial loading content of the cytokine (**Fig. 2.14c-d**). We measured migration of T cells using a standard transwell based technique where SDF-1α particles were placed below the transwell and T cells were placed above. T cells were allowed to migrate in response to the eluted chemotactic gradient established across the Transwell. T cells were counted on both sides of the transwell and their chemotactic index calculated. We found that the particles significantly enhanced the chemotaxis of T cells across the transwell (**Fig. 2.13c-d**). This result shows that chemokine-secreting particles can be used to direct the migration of T cells.

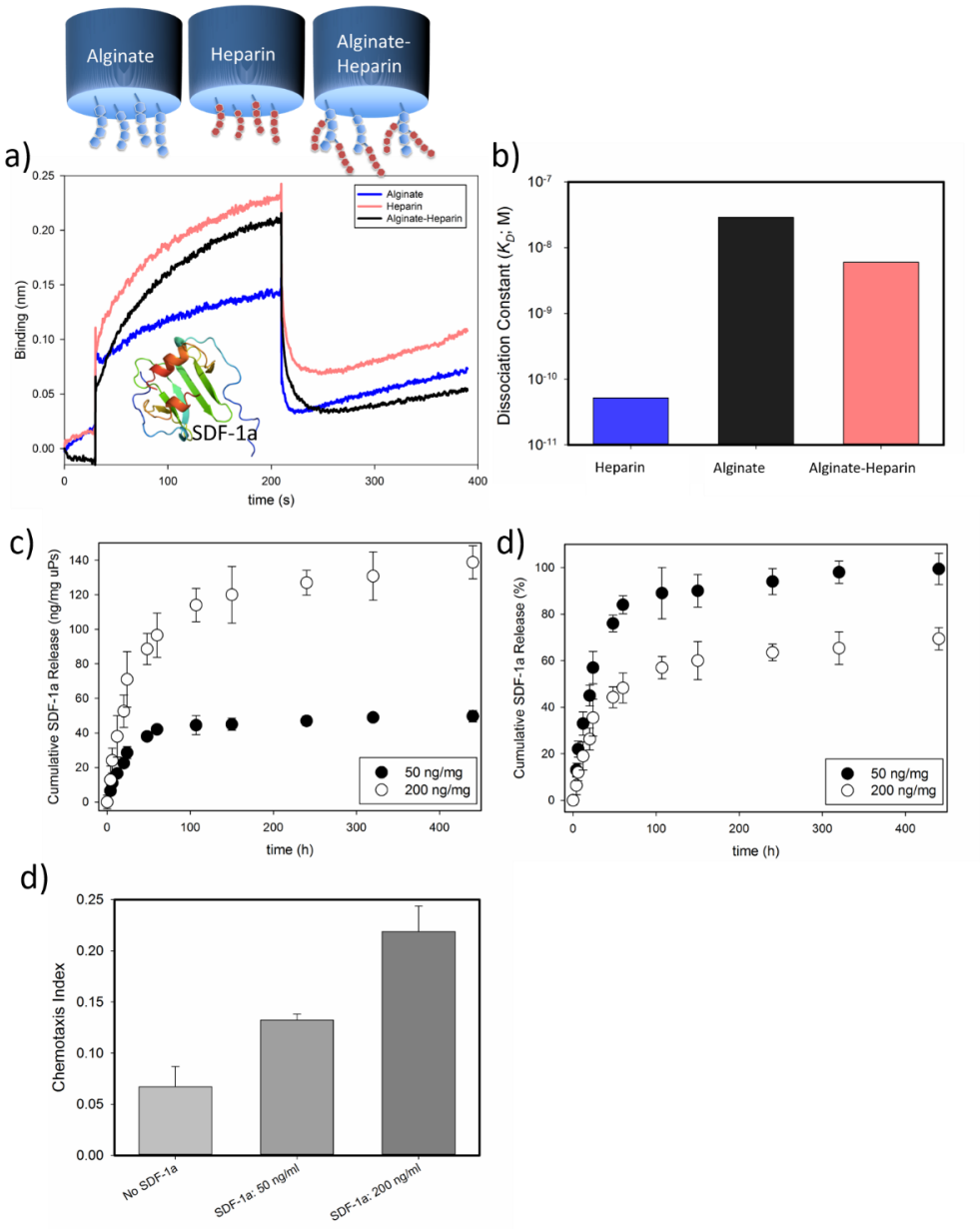

Figure 2.14. (a) Binding kinetic of SDF-1a cytokine (100 nM) to alginate, heparin, and Alg-Hep functionalized surfaces. (b) Calculated dissociation constants (K_D). Release profile of SDF-1a cytokine from non-coated Alg-Hep microparticles into a PBS solution at 37°C at different initial loading of 50 and 200 ng/ml as presented by cumulative released amount (c) and percentage (d). (e) Quantification of relative T-cells migration (Chemotactic index) for naïve and active T-cells after 2 h of culturing with non-coated Alg-Hep microparticles at different initial loading. The presented data are expressed as average ± SD.

We tested the ability of our microparticles to secrete TGF-β, a well-known growth factor

that induces differentiation of naïve T cells into induced regulatory T cells (i-Treg). Tregs express the transcription factor Foxp3 and play antigen-specific suppressive roles in a variety of autoimmune diseases including type 1 diabetes.[33] To evaluate the ability of our particles to generate i-Tregs, we loaded Alg-Hep particles with TGF-β that released at three different concentrations (1 ng/mL, 5 ng/mL, and 15 ng/mL). We cultured rigorously naïve CD4+ T cells with anti-CD3 and anti-CD28 for four days in the wells containing the Alg-Hep particles loaded with TGF-β at different concentrations and compared them to the soluble (no particles) counterparts at identical concentrations. The expression of Foxp3 was measured by flow cytometry (**Fig. 2.13h, i**). In all of the conditions, either when TGF-β were manually added in the beginning of experiment or delivered using the particles, coated particles were added to deliver IL-2 (20 U/ml) to the cells. To show the importance of the role that IL-2 plays in making i-Tregs, for soluble TGF-β at the concentration of 15 ng/ml, we did the measurements in both the absence and presence of IL-2 (**Fig. 2.13f** left panels). Interestingly, in the presence of IL-2, Foxp3 expression was approximately 3-fold greater compared to TGF-β only conditions with no addition of IL-2. In all concentrations of TGF-β as provided by the particles, Foxp3 expression was high (50%+). On the other hand, we found that at very high soluble concentrations of TGF-β, Foxp3 expression plateaued and was even slightly suppressed (**Fig. 2.13g**). Furthermore, the MFI of Foxp3 directly relates to the suppressive capacity of the regulatory T cells.[34] We found that the MFI of Foxp3 was highest when using particles to deliver TGF-β (**Fig. 2.13h**). These results show that induced regulatory T cells can be potently generated by the use of microparticles that secrete TGF-β and IL-2.

It has been reported that the inflammatory cytokines IFN-γ and TNF-α can inhibit differentiation and cause apoptosis of stem cells.[35-37] Here we tested whether the sustained release of IFN-γ from microparticles could affect the fate of human bone marrow mesenchymal stem cells (hBMMSCs). We measured apoptosis using flow cytometry after 7 d of co-culture with stem cells

and particles. We found that 30% of stem cells showed evidence of apoptosis when cultured with IFN-γ releasing coated/non-coated microparticles after one week. In comparison, particles lacking IFN-γ showed only 5% apoptosis (**Fig. 2.15**). These results show that particles can release IFN-γ that influences stem cell survival.

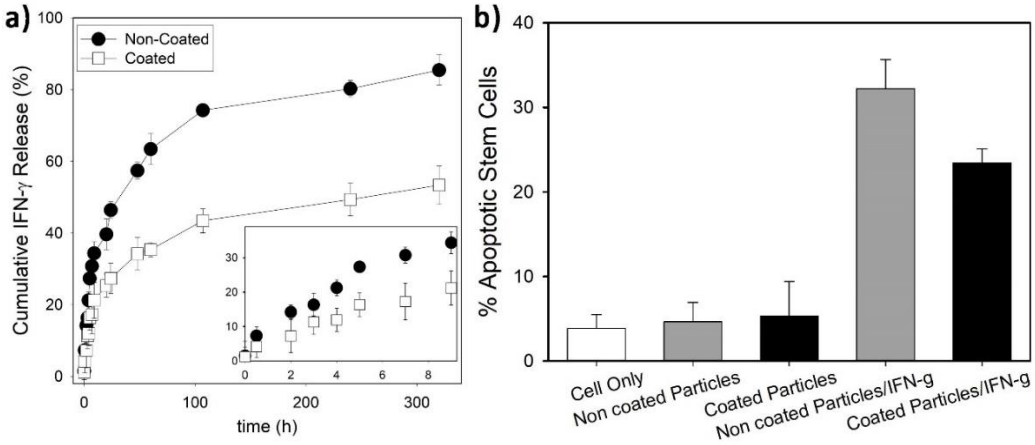

Figure 2.15. (a) Cumulative release of IFN-γ Pro-inflammatory cytokines at 37 °C. (b) Apoptosis of hBMMSCs in the presence of IFN-γ-loaded microparticles after a week of co-culturing, as tested using Annexin V-FITC apoptosis detection kit.

3D culture environments boost the effect

We sought to investigate the combination of secreted cytokines and 3D culture versus 2D culture in driving T cell proliferation and differentiation (**Fig. 2.16a**). We prepared a series of alginate-based scaffolds in the presence or absence of IL-2-carrying microparticles. These 3D environments can mimic the *in vivo* context encountered by activated lymphocytes and give a better idea of the effects of spatiotemporal variables on cellular fate.[38] SEM images of alginate-RGD scaffolds demonstrated their highly porous microstructure with an average pore size of 65±4 μm (**Fig. 2.16b**), which is ample space for mobility of T cells. To turn the scaffold into a more favorable material for cell trafficking, RGD modification was performed (see Methods). IL-2 was delivered to the cells either *via* soluble administration or through embedded particles. To assess proliferation, the number of T cells inside and outside the scaffold was measured after 10 days of

culture (**Fig. 2.16c**).

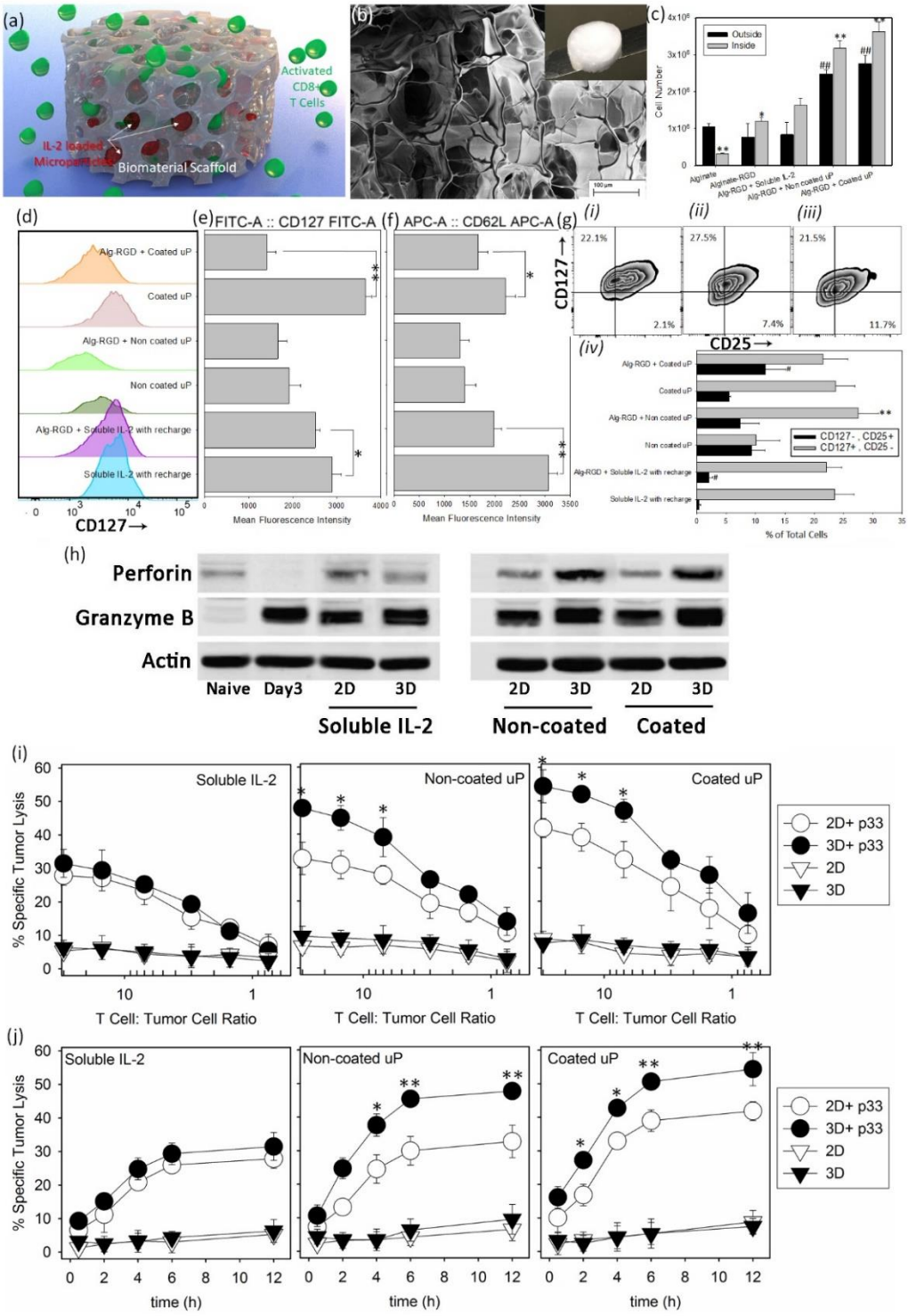

Figure 2.16. Performance boost from encapsulation in scaffold. (a) Schematic representation of scaffold approach to deliver pre-activated T-cells and IL-2 loaded

microparticles. (b) Electron microscopy image of the prepared alginate-RGD scaffold. Scale bar: 100 μm; Inset: Macroscopic image of a freeze-dried scaffold. (c) Number of cells inside and outside the scaffolds 10 days after incorporation of T-cells into the scaffold and in absence or presence of IL-2 (soluble administration or released by microparticles). The presented data are expressed as average ± SD. The results were statistically analyzed using unpaired t-tests. $^{*}p < 0.05$ and $^{**}p < 0.01$ are between numbers of cells inside each scaffold and the control alginate-RGD scaffold with soluble IL-2 (positive control). $^{\#}p < 0.05$ and $^{\#\#}p < 0.01$ are between number of cells outside each scaffold and the control alginate-RGD scaffold with soluble IL-2 (positive control). (d) Regulation of IL-7Ra (CD127) re-expression after 10 days of treatment in presence or absence of scaffold and MFI of cells in these conditions (e). (f) The quantification (MFI) of CD62L expression after 10 days of treatment. $^{*}p < 0.05$ and $^{**}p < 0.01$ are between the samples treated with and without using the alginate-RGD scaffold. (g) Flow cytometric analysis of co-expression of IL-2Ra and IL-7Ra for scaffold-based treatment with soluble IL-2 (i), non-coated (ii) and coated (iii) microparticles at constant ratio of one particle per cell. Quantitative evaluation of the percentage of cells that fall in the category of memory T-cells (CD 25 $^{-}$, CD127 $^{+}$) *vs.* effector cells ($CD25^{+}$, $CD127^{-}$) after 10 days of treatment in different conditions (iv). $^{**}p < 0.01$ is between the samples treated with and without using the alginate-RGD scaffold; $CD25^{+}$, $CD127^{-}$ group. $^{\#}p < 0.05$ is between the samples treated with and without using the alginate-RGD scaffold; CD 25 $^{-}$, CD127 $^{+}$ group at day 10. (h) CD8+ T cells were MACS-purified, FACS-sorted, and cocultured with soluble IL-2 or IL-2 loaded microparticles in 2D or 3D cultures for 10 days. Western blot analysis show levels of perforin and granzyme B. β-actin was used as loading control. (i) Chromium (^{51}Cr) release assays comparing antigen (p33)-specific (circles) and non-specific (triangle) cytotoxicity of treated T-cells with different methods in 2D (empty circles) *vs.* 3D (filled circles) cultures after 12 h in the indicated T-cells to tumor cells ratios. (j) Kinetics of cytotoxic activity of p33-specific T-cells after treatment with soluble IL-2, non-coated, and coated IL-2-loaded microparticles in 2D (empty circles) and in 3D alginate-RGD scaffold (filled circles). Cytotoxic activity of spleen-derived, *in vitro* treated, CD8+ T-cells was analyzed using chromium assay. Specific tumor lysis was determined at the indicated time points (30 min, 2h, 4h, 6h, and 12 h) of incubation. Cytotoxic activity was examined at four different ratios (30:1, 7:1, 3:1, and 0.75:1) of treated T-cells to tumor cells. The data are presented as average ± SD of five independent samples. The presented data are expressed as average ± SD. The results are analyzed using unpaired t-tests. In (h) and (j) p33-treated and non-treated T-cells are significantly different ($p<0.001$).

To test if RGD modification alone made the scaffold more favorable for cells to propagate, we measured the number of T cells proliferating in alginate scaffolds versus alginate+RGD. We found a four-fold increase in the number of cells within the RGD-bearing scaffold. To assess the impact of stimulatory signals on proliferation, IL-2 was either recharged manually at the concentration of 100 U/mL (about 7 ng/mL) or IL-2 was released from coated and non-coated particles. We loaded the particles such that the total amount of IL-2 released from the one-particle-per-cell condition was the same as the soluble 100 U/mL condition. Our results show a significant increase in both the total number of cells and the number of cells in/outside the scaffold in particle-enriched scaffolds compared to the manual administration of soluble IL-2. These findings prove that particulate delivery of IL-2 is superior to soluble IL-2 in 3D structures. For a better clarification of the effect of 3D culture, the same surface markers, CD62L, CD127, and CD25 of each set of cells were compared to their 2D culture compartments (**Fig. 2.16d-g**) alongside their MFIs. We tested if release of IL-2 from the plain alginate scaffold, without particles, could provide a similar effect as the IL-2 particles. We found that in absence of particles it is not possible to provide sustain IL-2 release (**Fig. 2.17**), and treatment of the T-cells in such a scaffold failed to improve the number of memory or effector T-cells over time.

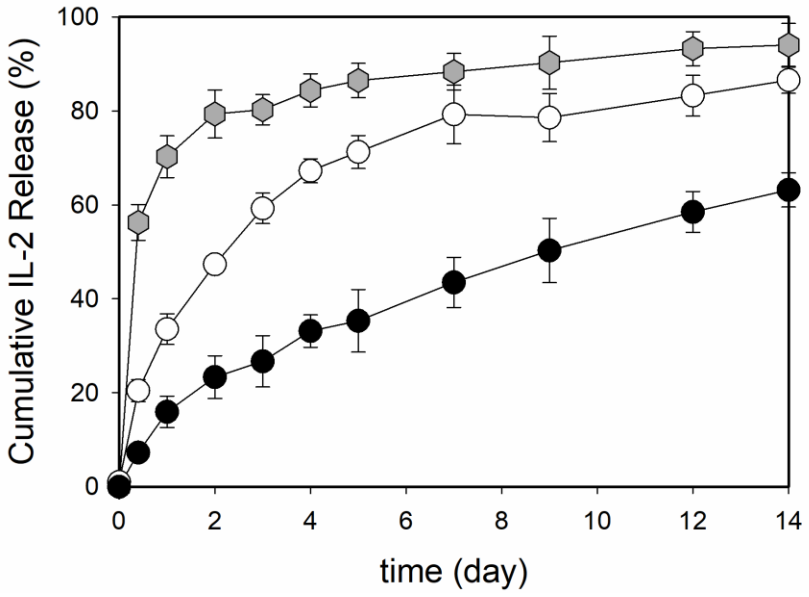

Figure 2.17. IL-2 release kinetic from alginate-based scaffold after encapsulation of free IL-2 (gray hexagon), IL-2 loaded microparticles without (open circles) and with (filled circles) coating in PBS at 37°C. The presented data are expressed as average ± SD.

The differences between the released amounts were statistically very significant ($p < 0.01$). Here we also evaluated the effect of 3D culture on expression of perforin and granzyme B after 10 days of culturing in alginate-RGD scaffolds. We found that both molecules were significantly induced in 3D culture and to a higher degree when particles were used to provide IL-2 (**Fig. 2.16h**). Taken together, these data show the advantage of culturing CD8 T cells in a supportive 3D microenvironment coupled with IL-2 secretion from microparticles.

To further assess the functionality of CD8+ T-cells activated in a 3D environment, we tested the *in vitro* cytotoxicity of T cells using the standard chromium (^{51}Cr) release assays. The cells were first stimulated with p33 antigen to test the antigen specific cytotoxicity at different ratios of T-cells to tumor cells. All treated cells showed specific lysis of p33-coated target tumor cells ($p<0001$). CD8+ T cells cultured initially within a 3D scaffold and in presence of IL-2 secreting microparticles exhibited stronger cytolytic potential compared to the T cells that were

co-cultured with microparticles in 2D. We also evaluated the kinetics of gaining cytotoxic activity of spleen-derived p33-specific T cells after treatment with soluble IL-2, non-coated, and coated IL-2-loaded microparticles in 2D or 3D-alginate-RGD scaffolds (**Fig. 2.16j**). T cells treated with coated particles (i.e., that had slower IL-2 release), both in 2D and 3D, demonstrated faster cytotoxicity compared to those cultured with non-coated particles or that received soluble administration of IL-2 (**Fig. 2.16j**, **Fig. 2.18-20**). This effect was enhanced in the 3D environment as compared with 2D. These results show that 3D culture of cytotoxic T cells in conjunction with IL-2-bearing microparticles produces a potent system for anti-tumor activity.

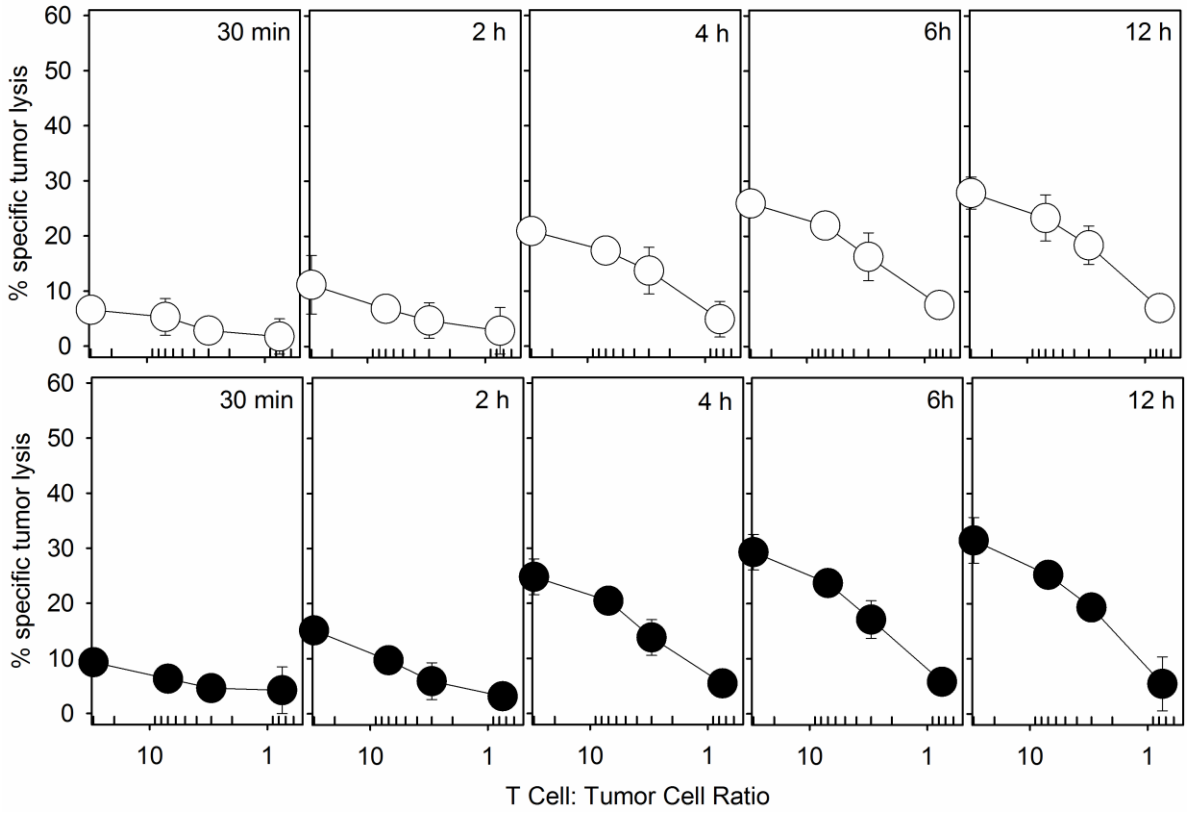

Figure 2.18. Kinetics of cytotoxic activity of p33-specific T-cells after treatment with soluble IL-2 in 2D (upper panels; empty circles) and in the 3D alginate-RGD scaffold (lower panels; filled circles). Cytotoxic activity of spleen-derived, *in vitro* treated CD8+ T-cells was analyzed using chromium assay. Specific tumor lysis was determined at the indicated time points (30 min, 2 h, 4 h, 6 h, and 12 h) of incubation. Cytotoxic activity was examined at four different ratios (30:1, 7:1,

3:1, and 0.75:1) of treated T-cells to tumor cells. The data are presented as average ± SD of five independent samples. The presented data are expressed as average ± SD.

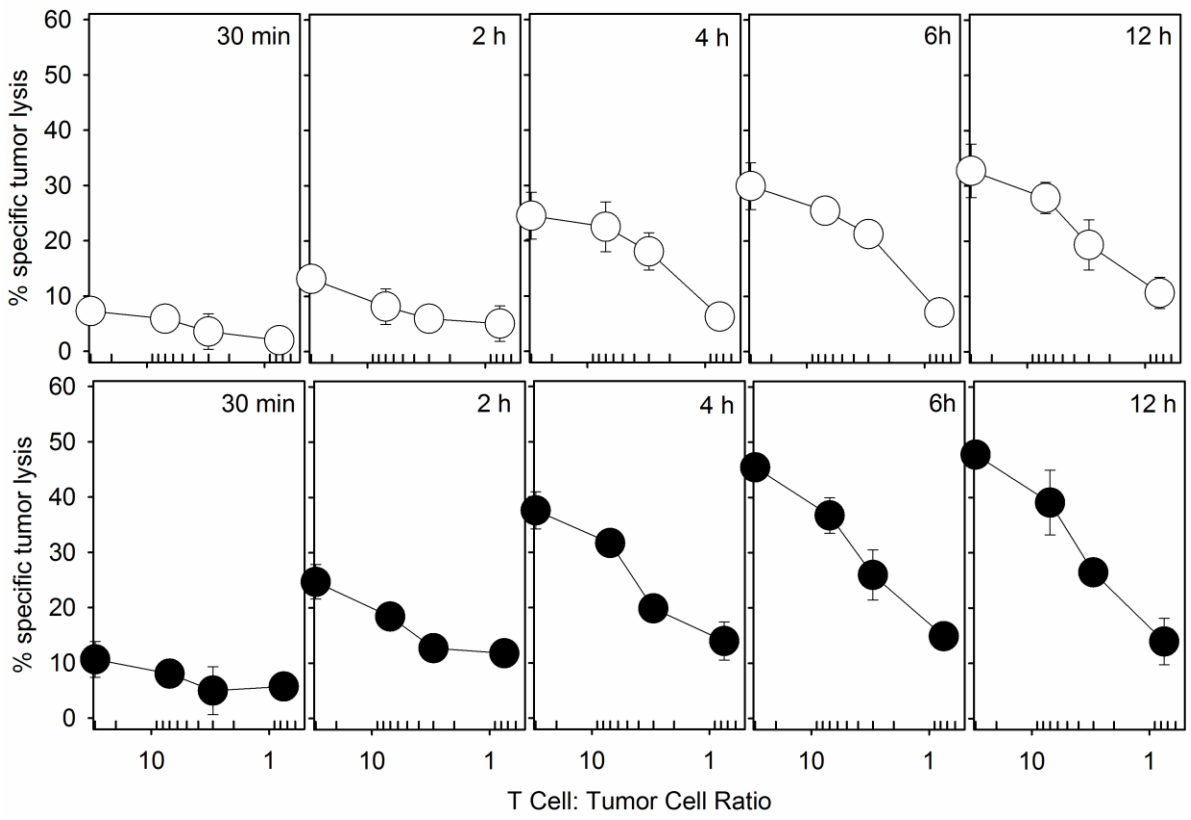

Figure 2.19. Kinetics of cytotoxic activity of p33-specific T-cells after treatment with non-coated IL-2 loaded microparticles in 2D (upper panels; empty circles) and in the 3D alginate-RGD scaffold (lower panels; filled circles). Cytotoxic activity of spleen-derived, *in vitro* treated CD8+ T-cells was analyzed using chromium assay. Specific tumor lysis was determined at the indicated time points (30 min, 2 h, 4 h, 6 h, and 12 h) of incubation. Cytotoxic activity was examined at four different ratios (30:1, 7:1, 3:1, and 0.75:1) of treated T-cells to tumor cells. The data are presented as average ± SD of five independent samples. The presented data are expressed as average ± SD.

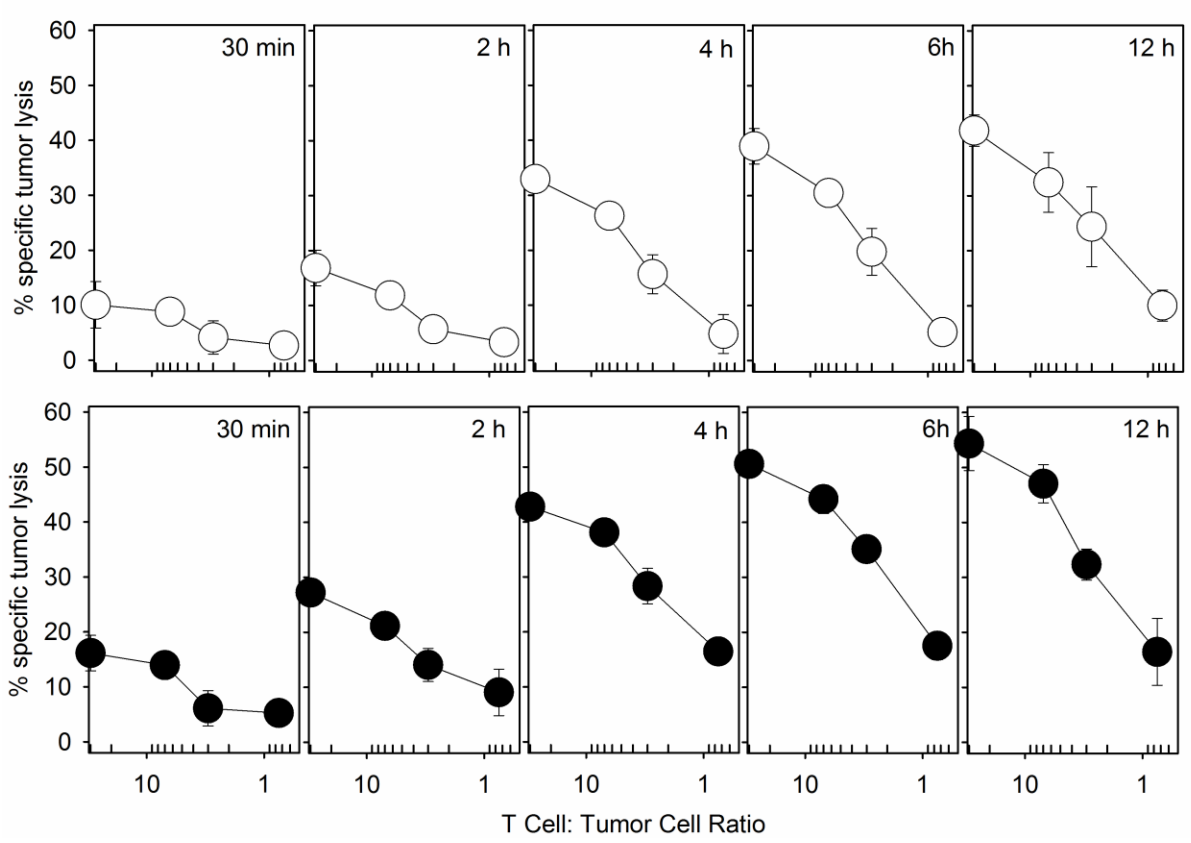

Figure 2.20. Kinetics of cytotoxic activity of p33-specific T-cells after treatment with coated IL-2 loaded microparticles in 2D (upper panels; empty circles) and in 3D alginate-RGD scaffold (lower panels; filled circles). Cytotoxic activity of spleen-derived, in vitro treated CD8+ T-cells was analyzed using chromium assay. Specific tumor lysis was determined at the indicated time points (30 min, 2 h, 4 h, 6 h, and 12 h) of incubation. Cytotoxic activity was examined at four different ratios (30:1, 7:1, 3:1, and 0.75:1) of treated T-cells to tumor cells. The data are presented as average ± SD of five independent samples. The presented data are expressed as average ± SD.

2.3. Conclusion

In this paper, cytokines released from microparticles were shown to skew the activation, differentiation, proliferation, and effector responses of T cells. This new capability is easily adaptable to influence the behaviors of other immune cells, including NK cells and B cells. The scaffold demonstrated here could be engineered to release chemoattractants such as SDF-1α to enhance recruitment of T cells into a tumor site or could release TGF-beta to promote suppression

of tissue specific autoimmunity.

2.4. Materials and Methods

Unless noted otherwise, all chemicals were purchased from Sigma-Aldrich, Inc. (St. Louis, MO). All glassware was cleaned overnight using concentrated sulfuric acid and then thoroughly rinsed with Milli-Q water. All the other cell culture reagents, solutions, and dishes were obtained from Thermo Fisher Scientific (Waltham, MA) except indicated otherwise. Alginate (Mw ≈250 kDa, high G blocks; Novamatrix UP MVG, FMC Biopolymer, Rockland, Maine) was first oxidized using sodium periodate (2%), overnight at room temperature, the reaction was quenched by drop-wise addition of ethylene glycol (Sigma) for 45 min. The sample was then dialyzed (MWCO 3.5 kDa) against deionized water for 3 d followed by lyophilization. Alginate-heparin (Alg-Hep) conjugation was done according to a previously published protocol. Briefly, alginate and heparin were dissolved separately in MES buffer (0.05 M, pH 5.4) in a concentration of 20 mg/ml overnight at room temperature. Carboxylic acid groups of alginates were activated using EDC and NHS at a fixed molar ratio of 0.6 to 1 for 10 minutes before addition of ethylenediamine (EDA, 31 mM) and running the reaction for 4 h under vigorous stirring at room temperature. This solution was then mixed with EDC/NHS activated heparin and allowed to react for 24 h with gentle stirring at room temperature. The resulting polymer conjugate was dialyzed (SpectraPor dialysis membrane MWCO: 8-14kDa; Spectrum Laboratories, Inc., Rancho Dominguez, CA) against 1M NaCl for a day followed by ultrapure water for an additional two days. The solution was then concentrated, lyophilized and kept at -20°C before further use. The amount of conjugated Heparin was determined using a toluidine blue assay reported by Hinrichs *et al.*[39]

A glass hydrophobic microfluidic droplet junction chip (channel depth of 100 μm; Dolomite Microfluidics, Charlestown, MA) was utilized to make monodispersed Alginate-Heparin (Alg-Hep) microparticles. Alg-Hep solution (1% w/v) was used as the inner aqueous phase.

Mineral oil containing 10 wt% surfactant Span 80 was used as the continuous phase. Flow rates of 5 and 12 μL.min^{-1} were applied using two syringe pumps (Fusion 200, Chemyx, Stafford, TX) for the Alginate and oil flows, respectively. Images were taken at various time points using a Leica DMIL inverted microscope. The formed particles were collected in a bath of calcium ions (100 mM $CaCl_2$) and left at room temperature for 30 min for ionic crosslinking. The microgels were extensively washed with 10 mM NaCl solution and centrifuged (15,000 rpm for 10 min) twice before further use.

We also designed a second microfluidic platform using 3D printing and structure-removal [13] to control the coating of alginate-heparin microparticles. The acrylonitrile butadiene styrene (ABS) filament was extruded through a 400 μm nozzle using Flashforge Creator Pro Dual Extrusion 3D Printer (Rowland Heights, CA) to form the desired 3D shape. The ABS-based 3D structure was then immersed in a degassed solution of polydimethylsiloxane (PDMS, resin:curing agent ratio of 10:1; Sylgard 184; Dow Corning Corp., Auburn MI). The PDMS was then cured for 4 h at 65°C; the structure was immersed in acetone for several days to dissolve the ABS filaments. After dissolving the template, the channels were cleaned with acetone injection and air-dried. The resulting serpentine micromixer consisted of one inlet for pre-made Alg-Hep microparticles and one for the aqueous solution of chitosan polymer (0.7 wt%, pH 6.1) plus an outlet. The rhodamine-conjugated chitosan (RITC-Chitosan) coating was also performed to evaluate the coating efficiency and the thickness of the formed layer using fluorescent microscopy.

Binding kinetic of the studied cytokines, Interlukine-2 (IL-2; BRB Preclinical Repository, NCI, NIH, Frederick, MD, USA) and stromal cell-derived factor 1α (SDF-1α; Abcam, Cambridge, MA), with alginate, heparin and alginate-heparin surfaces were estimated using biolayer interferometry with a BLItz (Pall ForteBio LLC; Fremont, CA) device. The alginate, heparin and alginate-heparin polymers were immobilized onto Amine-functionalized biosensor tips using EDC/NHS chemistry. The concentration of reactants has been adjusted to have an approximate

number of 2×10^6 molecules per chip. Different dilutions of IL-2 and SDF-1α samples, 20, 40, 60, 100, 140, and 200 nM, in HEPES buffer (10 mM HEPES, 150 mM NaCl, 3 mM EDTA, pH 7.4) were used for kinetic studies. Data analysis was performed with Fortebio Data Analysis software using a 1:1 binding model and global fitting analysis to report k_{on}, k_{off} and K_D values for the different surfaces.

To prepare IL-2 loaded Alg-Hep microparticles, our microparticles were incubated with cytokine in PBS buffer containing bovine serum albumin (BSA; 0.1 %w/v) and were gently shaken overnight at 4°C. The microparticles were then centrifuged and washed several times to remove unabsorbed cytokines. The concentration of IL-2 in the removed supernatant was measured using enzyme-linked immunosorbant assay (ELISA) to estimate the binding capacity of microparticles. Differences in uptake values after the coating process were also evaluated and were on the order of 12-23% depending on the mixing time. Initial loadings were optimized to provide the same loading content for the non-coated particles.

To study the *in vitro* release profile, cytokine-loaded Alg-Hep microparticles were dispersed in PBS (pH 7.4) and 500 µL of microsphere dispersion were placed in Eppendorf tubes, gently shaken, and incubated at 37 °C. At predetermined time points, samples were collected using centrifugation and the supernatant were replaced with an equivalent volume of fresh PBS solution. The concentration of released cytokine from microparticles was determined using a human IL-2 ELISA Kit.

For scaffolds preparation, the oxidized alginate (as described before) solution in MES (150 mM MES, 250 mM NaCl, pH 6.5) was covalently conjugated to the RGD peptide (GGGGRGDGS; GenScript USA Inc., Piscataway, NJ) using carbodiimide chemistry (NHS/EDC). After 24 h of reaction the solution was again dialyzed (MWCO 20 kDa) and lyophilized. The solution of 2% w/v alginate-RGD in PBS was mixed with 2×10^6 microparticles (IL-2 loaded) and at 60°C. The cross-linking was initiated by the addition of calcium chloride solution (20 mM) to the alginate-

RGD/microparticle mixture while mixing. The mixture was poured in a pre-made PDMS mold, frozen at -80 °C, lyophilized for 3 d, and stored at 4 °C before cellular studies.

Scanning electron microscopy (SEM) was used to observe the cross-sectional microstructure of the alginate-RGD scaffolds. Lyophilized scaffolds were freeze-fractured (using liquid nitrogen) to expose a cross-section. The scaffold specimens were imaged without further coating using a ZEISS Supra 40VP scanning electron microscope (Carl Zeiss Microscopy GmbH, Jena, Germany). The pore sizes were calculated from SEM images by evaluating at least 40 pores using the ImageJ program (National Institutes of Health, Bethesda, MD).

Mice, cell culture and reagents: Five- to eight-week-old wild type mice were purchased from University of California, Los Angeles (UCLA) and maintained in pathogen free facilities at UCLA. All experiments on mice and cells collected from mice were performed in strict accordance with UCLA policy on humane and ethical treatment of animals. Cells were cultured in IMDM supplemented with 10% heat inactivated FBS, 100 U/ml penicillin, 100 µg/ml streptomycin, 50 uM 2-ME. Total T-cells or CD8+ T-cells were purified using a negative enrichment kits (Affymetrix eBioscience).

For *in vitro* activation of CD8+ T-cells, cells were cultured at the concentration of 1x10e6/ml in 96-well plates coated with 5 µg/ml of anti-CD3 (2C11; Bio X Cell) in combination with 2 µg/ml of soluble anti-CD28 (37.51; Bio X Cell) or 100 IU/ml of human IL-2.[40] After three days, cells were re-plated in 24 well plates at the concentration of 0.25 x10e6/ml with IL-2 or IL-2 containing particles. Particles were counted after about 20 times dilution and *via* hemocytometer before co-culture with T-cells. We prepared plain Alg-Hep, chitosan-coated Alg-Hep, and a mixture of both of these IL-2 containing particles. Each type of particle was added to the cells at the particle to cell ratios of 2:1, 1:1, or 1:2.

To seed mouse CD8+ T-cells on alginate-based scaffolds, 250 µl of cell suspension (8×10^6 cells/ml) was seeded on top of each lyophilized scaffold in a 48-well tissue culture plate. Then, the well plate was shaken at 150 rpm using an orbital microplate shaker (MS3, IKA) for 20 min in

a 37°C incubator to help cells infiltrate the biomaterials. At the end of the culture period, T-cells were recovered from alginate-based scaffolds using dissolving buffer (55 mM sodium citrate, 30 mM EDTA, 0.15 M NaCl). The cells were then centrifuged and the number of viable cells in each culture were determined using dual-fluorescence viability assay by AO and PI.

For flow cytometry analysis, antibodies to mouse CD8 (53-6.7), CD25 (PC61.5), CD44 (IM7), Thy1.2 (53-2.1), IL-7R (CD127), CCR7, CD62L, perforin Monoclonal Antibody (eBioOMAK-D), PE, Alexa Fluor® 647 anti-human/mouse granzyme B (GB11), Alexa Fluor® 647 anti-mouse/rat/human FOXP3 and CD16/CD32 (FC block) were purchased from eBioscience (San Diego, CA), BioLegend (San Diego, CA), or BD Biosciences (San Diego, CA). Propidium iodide (PI) and acridine orange (AO) were purchased from Calbiochem. Cells were analyzed on FACSVerse using FlowJo software (Treestar, Ashland, OR).

To analyze perforin and granzyme B expressions after treatment in 2D or 3D cultures using Western blot, T-cells were lysed using protein extraction buffer (Bio-Rad, Irvine, CA). The extracted proteins were then fractionated in 10% sodium dodecyl sulfate-polyacrylamide gels (PAGE) and electrophoretically transferred to a nitrocellulose membrane (Bio-Rad). The membranes were then incubated with antibodies against perforin and granzyme B as well as β-actin which was used as the housekeeping protein.

To perform stem cell cytotoxicity test, 5×10^5 human bone marrow mesenchymal stem cells (hBMMSCs) were cultured in a six-well plate in a regular stem cell medium. Recombinant mouse Interferon gamma protein (IFN-γ; Abcam) was loaded within the coated and non-coated microparticles and co-cultured with the stem cells at the ratio of 1:1 particle: cell. After seven days of coculturing relative number of apoptotic cells was evaluated using Annexin V-PE Apoptosis Detection Kit (BD Bioscience).

For iT-reg formation experiments CD4+ T-cells were purified from mouse spleen by EasySep immunomagnetic negative selection (Stem Cell Technologies). Cells were then activated

on anti-CD3e antibody (8 mg/ml) coated plates with the anti-CD28 antibody (2 mg/ml) supplemented medium. At the same time TGF-β at different concentrations, either in a soluble format or via TGF-β loaded particles were added to the media. All the conditions expect for two of the controls were supplied with IL-2 loaded (20 U/ml) particles. After four days regulatory T-cells were removed from wells coated with anti-CD3e and stained with antibodies for flow cytometry analysis.

Five- to 10-wk-old TCR transgenic 318 mice were used for *in vitro* cytotoxicity assay and were kept under specific pathogen-free conditions, according to institutional guidelines. EL-4 thymoma cells (H-2b, Thy-1.2; ATCC® TIB-39) were cultured in Dulbecco's medium that contained 5% FCS and glutamine and penicillin/streptomycin was added to it.

A total of 4 $\times 10^6$ cells/ml spleen cells from 318 TCR transgenic mice and p33 peptide was added to 1 mM final concentration. After 48 h, CD8+ T-cells were purified by negative selection, as mentioned before. Then 250 µl of cell suspension (8×10^6 cells/ml) was seeded on top of each lyophilized scaffold in a 48-well tissue culture plate. Then, the well plate was shaken at 150 rpm using an orbital microplate shaker for 20 min in a 37°C incubator to help cells infiltrate the biomaterials. At the end of the culture period, T-cells were recovered from alginate-based scaffolds using dissolving buffer (55 mM sodium citrate, 30 mM EDTA, 0.15 M NaCl). Finally, a total of 5 $\times 10^6$ transgenic T-cells/well in a volume of 1ml were counted and serially diluted up to six times (T-Cell: tumor cell= 30:1, 15:1, 7:1, 3:1, 1.5:1, 0.75:1) in MEM supplemented with 2% FCS. Specific cytotoxicity of the dilutions were then determined in a standard ^{51}Cr release assay, as described elsewhere.[41] EL4 cells were coated with peptide p33 at a concentration of 10^{-6} M and were labeled in a total volume of 300 µl with 250 µCi ^{51}Cr for 2 h at 37°C on a rocking platform. The resulting labeled cells were washed three times, and 10^4 cells were added to the effector cells in a final volume of 200 µl. After a 0.5, 2 h, 4 h, 6 h, or 12-h incubation at 37°C, 60 µl of the supernatants was harvested and counted with a gamma counter (PerkinElmer, Richmond, CA).

2.5. References

1 Klebanoff, C. A., Gattinoni, L. & Restifo, N. P. CD8+ T-cell memory in tumor immunology and immunotherapy. *Immunological reviews* **211**, 214-224 (2006).

2 June, C. H., Riddell, S. R. & Schumacher, T. N. Adoptive cellular therapy: a race to the finish line. *Science translational medicine* **7**, 280ps287-280ps287 (2015).

3 Yoo, J.-W., Irvine, D. J., Discher, D. E. & Mitragotri, S. Bio-inspired, bioengineered and biomimetic drug delivery carriers. *Nature reviews Drug discovery* **10**, 521 (2011).

4 Langer, R. New methods of drug delivery. *Science* **249**, 1527-1533, (1990).

5 Moon, J. J., Huang, B. & Irvine, D. J. Engineering nano-and microparticles to tune immunity. *Advanced materials* **24**, 3724-3746 (2012).

6 Li, J. & Mooney, D. J. Designing hydrogels for controlled drug delivery. **1**, 16071, (2016).

7 Wang, Y. & Kohane, D. S. External triggering and triggered targeting strategies for drug delivery. **2**, 17020, doi:10.1038/natrevmats.2017.20 (2017).

8 Tibbitt, M. W., Dahlman, J. E. & Langer, R. Emerging Frontiers in Drug Delivery. *Journal of the American Chemical Society* **138**, 704-717, doi:10.1021/jacs.5b09974 (2016).

9 Pipkin, M. E. *et al.* Interleukin-2 and inflammation induce distinct transcriptional programs that promote the differentiation of effector cytolytic T cells. *Immunity* **32**, 79-90 (2010).

10 Steenblock, E. R., Fadel, T., Labowsky, M., Pober, J. S. & Fahmy, T. M. An artificial antigen-presenting cell with paracrine delivery of IL-2 impacts the magnitude and direction of the T cell response. *Journal of Biological Chemistry* **286**, 34883-34892 (2011).

11 Özbaş-Turan, S., Akbuğa, J. & Aral, C. Controlled release of interleukin-2 from chitosan microspheres. *Journal of pharmaceutical sciences* **91**, 1245-1251 (2002).

12 Jhunjhunwala, S. *et al.* Controlled release formulations of IL-2, TGF-β1 and rapamycin for the induction of regulatory T cells. *Journal of controlled release* **159**, 78-84 (2012).

13 Chen, W. *et al.* Conversion of peripheral CD4+ CD25− naive T cells to CD4+ CD25+ regulatory T cells by TGF-β induction of transcription factor Foxp3. *Journal of Experimental Medicine* **198**, 1875-1886 (2003).

14 Gu, L. & Mooney, D. J. Biomaterials and emerging anticancer therapeutics: engineering the microenvironment. *Nature Reviews Cancer* **16**, 56 (2016).

15 Zhao, X. *et al.* Injectable Stem Cell-Laden Photocrosslinkable Microspheres Fabricated Using Microfluidics for Rapid Generation of Osteogenic Tissue Constructs. *Advanced Functional Materials* **26**, 2809-2819 (2016).

16 Bazban-Shotorbani, S., Dashtimoghadam, E., Karkhaneh, A., Hasani-Sadrabadi, M. M. & Jacob, K. I. Microfluidic directed synthesis of alginate nanogels with tunable pore size for efficient protein delivery. *Langmuir* **32**, 4996-5003 (2016).

17 Sperling, L. H. *Introduction to physical polymer science*. (John Wiley & Sons, 2005).

18 Hasan, M., Najjam, S., Gordon, M. Y., Gibbs, R. V. & Rider, C. C. IL-12 is a heparin-binding cytokine. *The Journal of Immunology* **162**, 1064-1070 (1999).

19 Najjam, S. *et al.* Further characterization of the binding of human recombinant interleukin 2 to heparin and identification of putative binding sites. *Glycobiology* **8**, 509-516 (1998).

20 Najjam, S., Gibbs, R. V., Gordon, M. Y. & Rider, C. C. Characterization of human recombinant interleukin 2 binding to heparin and heparan sulfate using an ELISA approach. *Cytokine* **9**, 1013-1022 (1997).

21 Hasani-Sadrabadi, M. M. *et al.* Microfluidic manipulation of core/shell nanoparticles for oral delivery of chemotherapeutics: a new treatment approach for colorectal cancer. *Advanced Materials* **28**, 4134-4141 (2016).

22 Saggiomo, V. & Velders, A. H. Simple 3D printed scaffold-removal method for the fabrication of intricate microfluidic devices. *Advanced Science* **2** (2015).

23 Majedi, F. S. *et al.* On-chip fabrication of paclitaxel-loaded chitosan nanoparticles for cancer therapeutics. *Advanced Functional Materials* **24**, 432-441 (2014).

24 Sallusto, F., Lenig, D., Förster, R., Lipp, M. & Lanzavecchia, A. Two subsets of memory T lymphocytes with distinct homing potentials and effector functions. *Nature* **401**, 708-712 (1999).

25 Wherry, E. J. *et al.* Lineage relationship and protective immunity of memory CD8 T cell subsets. *Nature immunology* **4**, 225-234 (2003).

26 Masopust, D., Vezys, V., Marzo, A. L. & Lefrançois, L. Preferential localization of effector memory cells in nonlymphoid tissue. *Science* **291**, 2413-2417 (2001).

27 Kuipers, H. F. *et al.* Hyaluronan synthesis is necessary for autoreactive T-cell trafficking, activation, and Th1 polarization. *Proceedings of the National Academy of Sciences* **113**, 1339-1344 (2016).

28 Baars, P. A. *et al.* Properties of murine CD8+ CD27–T cells. *European journal of immunology* **35**, 3131-3141 (2005).

29 Kaech, S. M. & Ahmed, R. Memory CD8+ T cell differentiation: initial antigen encounter triggers a developmental program in naïve cells. **2**, 415, (2001).

30 Bannard, O., Kraman, M. & Fearon, D. T. Secondary replicative function of CD8+ T cells that had developed an effector phenotype. *Science* **323**, 505-509 (2009).

31 Harrington, L. E., Janowski, K. M., Oliver, J. R., Zajac, A. J. & Weaver, C. T. Memory CD4 T cells emerge from effector T-cell progenitors. *Nature* **452**, 356-362 (2008).

32 Opferman, J. T., Ober, B. T. & Ashton-Rickardt, P. G. Linear differentiation of cytotoxic effectors into memory T lymphocytes. *Science* **283**, 1745-1748 (1999).

33 Francisco, L. M. *et al.* PD-L1 regulates the development, maintenance, and function of induced regulatory T cells. *Journal of Experimental Medicine* **206**, 3015-3029 (2009).

34 Wan, Y. Y. & Flavell, R. A. Regulatory T-cell functions are subverted and converted owing to attenuated Foxp3 expression. *Nature* **445**, 766-770, (2007).

35 Liu, Y. *et al.* Mesenchymal stem cell-based tissue regeneration is governed by recipient T lymphocytes via IFN-[gamma] and TNF-[alpha]. *Nature medicine* **17**, 1594-1601 (2011).

36 Akiyama, K. *et al.* Mesenchymal-stem-cell-induced immunoregulation involves FAS-ligand-/FAS-mediated T cell apoptosis. *Cell stem cell* **10**, 544-555 (2012).

37 Ansari, S. *et al.* Hydrogel elasticity and microarchitecture regulate dental-derived mesenchymal stem cell-host immune system cross-talk. *Acta Biomaterialia* **60**, 181-189, doi:https://doi.org/10.1016/j.actbio.2017.07.017 (2017).

38 Stephan, S. B. *et al.* Biopolymer implants enhance the efficacy of adoptive T-cell therapy. *Nature biotechnology* **33**, 97-101 (2015).

39 Hinrichs, W., Ten Hoopen, H., Wissink, M., Engbers, G. & Feijen, J. Design of a new type of coating for the controlled release of heparin. *Journal of controlled release* **45**, 163-176 (1997).

40 Kidani, Y. *et al.* Sterol regulatory element–binding proteins are essential for the metabolic programming of effector T cells and adaptive immunity. *Nature immunology* **14**, 489-499 (2013).

41 Hany, M. *et al.* Anti-viral protection and prevention of lymphocytic choriomeningitis or of the local footpad swelling reaction in mice by immunization with vaccinia-recombinant virus expressing LCMV-WE nucleoprotein or glycoprotein. *European journal of immunology* **19**, 417-424 (1989).

Chapter 3.

Augmentation of T-Cell Activation by Oscillatory Forces and Engineered Antigen-Presenting Cells [2]

Abstract

Activation of T cells by antigen presenting cells (APCs) initiates their proliferation, cytokine production, and killing of infected or cancerous cells. We and others have shown that T-cell receptors require mechanical forces for triggering, and these forces arise during interaction of T cells with APCs. Efficient activation of T cells *in vitro* is necessary for clinical applications. In this paper, we studied the impact of combining mechanical, oscillatory movements provided by an orbital shaker with soft, biocompatible, artificial APCs (aAPCs) of various sizes and amounts of antigen. We showed these aAPCs allow for testing the strength of signal delivered to T cells and enabled us to confirm that that absolute amounts of antigen engaged by the T cell are more important for activation than the density of antigen. We also found that when our aAPCs interact with T cells in the context of an oscillatory mechanoenvironment, they roughly double antigenic signal strength as compared to conventional, static culture. Combining these effects, our aAPCs significantly outperformed the commonly used Dynabeads. We finally demonstrated that tuning down signal strength to a sub-maximal "sweet spot" allows for robust expansion of induced regulatory T cells. In conclusion, augmenting engineered aAPCs with mechanical forces offers a novel approach for tuning of T-cell activation and differentiation.

[2] This Chapter is published as: Majedi F.S., Hasani M.M., Thauland T.J., Li S., Bouchard L.S., Butte M.J., Augmentation of T-Cell Activation by Oscillatory Forces and Engineered Antigen-Presenting Cells. *Nano Letters*. 19 (2019) 6945-6954.

3.1. Introduction

T lymphocytes circulate throughout the body and coordinate the immune response against pathogens by recognizing their proteome as foreign. Activation of T cells begins by T-cell receptors (TCRs) engaging with antigenic peptides proffered by the major histocompatibility complex (p-MHC) of antigen presenting cells (APC). Triggering of the TCR by pMHC requires a mechanical force that pulls upon the TCR.[1,2] Those pulling forces are at least partially generated by the T cells themselves through a series of oscillatory pulling movements.[3] We have previously shown that these forces can be provided by an exogenous source, for example, ligands tethered to the cantilever of an atomic force microscope.[3] Those experiments entailed contact with a single T cell at a time, and thus did not allow for scaling the application of forces toward the large numbers of T cells needed for industrial, clinical purposes. In this paper, we investigated if provision of exogenous forces *in vitro* could augment the force-based triggering of TCRs in a large number of T cells. A positive outcome could open the door to biomedical applications of mechanically activated T cells.

Ex vivo cultivation of T cells is important for manufacturing cellular therapies, such as CAR-T cells. Therefore, the optimization of approaches for polyclonal T-cell cultivation is clinically important.[4] In the activation of T cells for biomedical engineering applications, such T cells are commonly cultured with beads coated with stimulatory antibodies, or artificial antigen presenting cells (aAPCs). A number of groups have developed aAPCs using micro- and nanotechnology approaches, developing particles that can be co-cultured with T cells or engineered surfaces that offer stimulatory signals[5]. In this work, we compared our particles with Dynabeads, which are the most popular, commercial aAPC, comprising a rigid, polystyrene shell roughly the size of resting T cells (4-5 μm diameter) around a superparamagnetic particle, and coated with stimulatory antibodies.

The key to T-cell activation is offering simulation to the TCR, either in the form of pMHC or by using antibodies that trigger the CD3 chains of the TCR complex. Naïve T cells also require costimulation of the CD28 receptor for complete activation, and so antibodies that cross-link and activate CD28 are almost always included in the formulation of aAPCs. The amount of antibodies provided by the aAPC is proportionate to their cost, and so many approaches have attempted to identify and minimize the amount of signal needed. T cells stimulated on a nanopatterned antigen array comprising a planar lipid bilayer showed that the number of antigens on a surface is more important than their surface density, with a density of 90–140 pMHC/μm^2 yielding maximal stimulation.[6] Nanoarrays formed by block copolymer micellar nanolithography (BCML)

functionalized with gold nanoparticles found a plateau of maximal response when the distance between antibodies was 60 nm or less.[7] Because surface curvature may also contribute to T-cell activation,[8,9] it is difficult to extrapolate antigen amounts from experiments done on planar surfaces.

To measure the effect of strength of stimulatory signals on T-cell activation, we fabricated aAPC particles and conjugated anti-CD3 and anti-CD28 antibodies at different densities. To test the effect of various degrees of curvature and different surface areas of contact with T cells, our aAPCs comprised spheres of different sizes. To test whether an external mechanical stimulus upon the TCR could promote activation, we also engaged an oscillatory movement to the aAPCs. Overall, we found conditions that dramatically improved activation beyond conventional, Dynabead-based stimulation. In another example, we chose aAPC conditions that offered a "sweet spot" of signaling to maximize the production of induced regulatory T cells (iTreg), the development of which is actually hindered by high levels of stimulation. The particles were also endowed with the ability to secrete cytokines to further promote iTreg development. These examples show that provision of an oscillatory mechanoenvironment coupled with aAPCs of tunable size/curvature, signal density, and cytokine section offer the possibility to fruitfully engineer T cells for a variety of clinical and experimental needs.

3.2. Design considerations

An important design consideration was to endow the particles with the ability to be easily separated from cells during modification, washing steps, and especially after co-culture. Our solution to this problem was to make the beads magnetic by embedding superparamagnetic iron oxide nanoparticles (SPIONs) during their microfluidic synthesis. The processing conditions were tuned to encapsulate around 2.8 ± 0.3 Vol% SPIONs per particle (**Table 3.1**), which was identified in pilot work to be sufficient for magnetic separation.

Table 3.1. Evaluation of super paramagnetic iron oxide nanoparticles inside the alginate microparticles

	Diameter (nm)	**Volume (nm^3)**	**Relative Volume**	**SPION Weight Content**	**Average Number of SPIONs per**	**Volume fraction of SPIONs (vol %)**	**Distribution Density (nm-3)**
Particle 3	307	1.5×10^7	1	0.25	5.65	2.43	3.73×10^7

Particle 2	824	2.9×10^{8}	19.3	0.33	126.39	2.82	4.31×10^{7}
Particle 1	4540	4.9×10^{10}	3234.1	0.36	22934.98	3.06	4.68×10^{7}

Our polymeric, microparticle aAPCs are composed of alginate, which is ionically crosslinked by addition of divalent cations such as calcium. Ionic crosslinking of alginate provides sufficient working stability; however, we saw irreversible changes (hysteresis) in particle morphology during pilot magnetic separation and traction experiments. To overcome this issue, we used our recently developed combinatorial crosslinking technique which provided both chemical and physical crosslinking.[10]

During our experiments we adjusted the number of aAPCs so as to provide a constant activation surface area of 9.5×10^{7} μm^2 per 1.5×10^{6} T cells (**Table 3.2**). This calculation was equivalent to the surface area of Dynabeads in co-culturing one Dynabead per one primary T cell, the manufacturer's recommendation. This adjustment allowed us to then appropriately consider the impacts of particle size and antigen density on T-cell activation (**Table 3.3**) and also compare our aAPCs to the conventional approach.

Table 3.2. Relative numbers of microparticles used in co-culture experiments

	Diameter (nm)	**Surface Area / Particle (μm^2)**	**Total Required Surface Area (μm^2)**	**Number of Particles to Provide 1 Particle: 1 Cell**	**Relative Number of Particles**
Particle 1	4.5	63.62	9.5×10^{7}	1.5×10^{6}	1
Particle 2	0.8	2.01	9.5×10^{7}	4.7×10^{7}	31.64
Particle 3	0.3	0.28	9.5×10^{7}	3.4×10^{8}	225
Dynabead	4.5	63.62	9.5×10^{7}	1.5×10^{6}	1

Table 3.3. Antibody (protein) used to coat microparticles

	Diameter (μm)	Surface area (μm²)	Required total protein per particle (fg)	Number particles per test*	Total aCD3 (μg)	Total aCD28 μg)	Particle Stock Concentration (#/mL)	Required # of particles
Particle 1	4.5	63.62	795.19	1.5×10^6	1.19	0.30	150×10^6	1.5×10^6
Particle 2	0.8	2.01	25.13	51.9×10^6	1.30	0.33	25×10^9	1.6×10^9
Particle 3	0.3	0.28	3.53	193.7×10^6	0.68	0.17	220×10^9	44×10^9

*: per 1.5×10^6 T cell

3.3. Results and Discussion

To develop our artificial APCs, we utilized a microfluidic droplet generator that encapsulates alginate polymer and magnetic nanoparticles (**Fig. 3.1A**). A constant fraction of crosslinker (4-arm PEG hydrazide) was mixed with the alginate polymer in the main channel. During droplet formation, we encapsulated within our beads magnetic nanoparticles that were 100 nm-diameter, carboxylated SPIONs. The microfluidic approach produced a homogeneous collection of particles, as verified by dynamic light scattering (**Fig. 3.1C**). To tune the size of particles ranging from 150 nm to 10 μm, we varied the ratio of central to sheath flow (**Fig. 3.1B**). To employ a broad range of particle sizes in our experiments (over one order of magnitude), we selected three sizes of particles with average radii of 307 nm ("0.3"), 824 nm ("0.8"), and 4,540 nm ("4.5 μm") (**Fig. 3.1C**). In pilot work, we found that nanoparticles of diameters in the range 50-250 nm could not be fully separated from one another or from T cells due to partial internalization or trapping on the rough cell surface, whereas particles larger than 300 nm could be separated from cells with >95% efficiency (not shown). The resulting alginate particles were

then collected in a bath of 200 mM $CaCl_2$, followed by a ~40 min incubation to reach complete gelation. Eventually particles were subjected to overnight chemical crosslinking though the hydrazine linker. Excess calcium and crosslinker were removed by serial washing with phosphate buffered saline. The mechanical stiffness of these aAPC microparticles was measured by nanoindentation and found to be 14.6 kPa (**Fig. 3.1D**), a substrate stiffness that allowed for maximal spreading of T cells.[11]

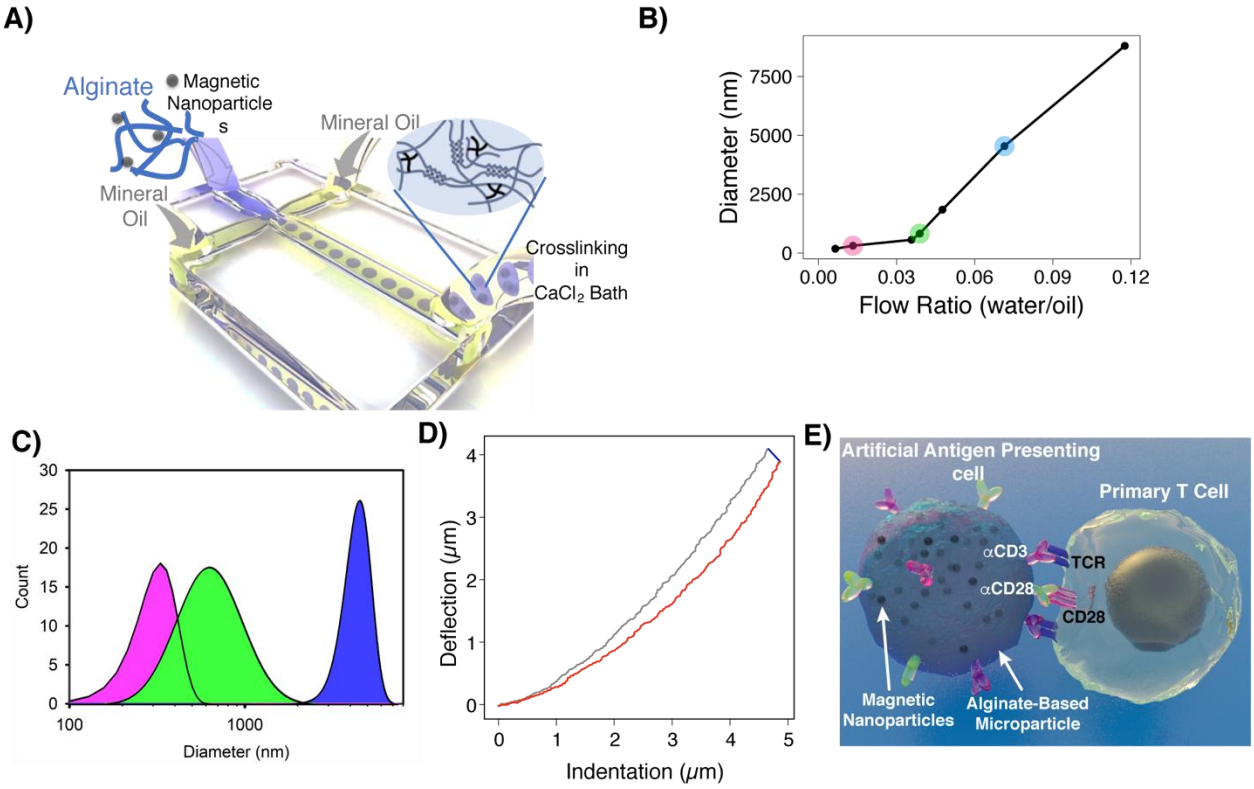

F)

	Diameter (μm)	αCD3-αCD28 per particle (fg)			Protein Density (#/um²)			Spacing between Antibodies (nm)			SPIONs Volume Fraction (vol. %)
		0.01	*0.1*	*1*	*0.01*	*0.1*	*1*	*0.01*	*0.1*	*1*	
Particle 1	4.5	6.6	57.9	591.1	25.1	219.2	2237.4	504.1	170.4	53.3	2.4
Particle 2	0.8	0.3	2.4	23.1	36.4	289.6	2770.5	418.2	148.3	47.9	2.8
Particle 3	0.3	0.04	0.3	3.6	37.9	290.4	3067.7	410.1	148.1	45.6	3.1

Figure 3.1. (A) Schematic representation of microfluidic generation of alginate nano-/microparticles encapsulating magnetic nanoparticles. **(B)** Size distribution analysis of prepared microparticles at different flow rates. **(C)** Size distribution analysis of selected particles (0.3, 0.8, 4.5 μm). **(D)** Nanoindentation to assess the elastic modulus (red, indentation; gray, retraction). **(E)** Schematic representation of proposed interactions between artificial antigen presenting cells and primary T cells. **(F)** Summary of physical characteristics of prepared library of particles to present broad range of antigens on their surfaces.

We next conjugated stimulatory antibodies to the surface of the microparticles. The carboxylic groups of alginate provide a versatile platform for antibody conjugation. Using NHS/EDC chemistry, we conjugated anti-CD3 and anti-CD28 antibodies (see Methods) and washed away excess antibodies and quenching unreacted groups through repeated washing with phosphate buffered saline solution containing 0.5% w/v BSA. To characterize the conjugation of antibodies, we imaged them by confocal microscopy and found that over 80% of antibodies were conjugated to the outside the particles (**Fig. 3.2**).

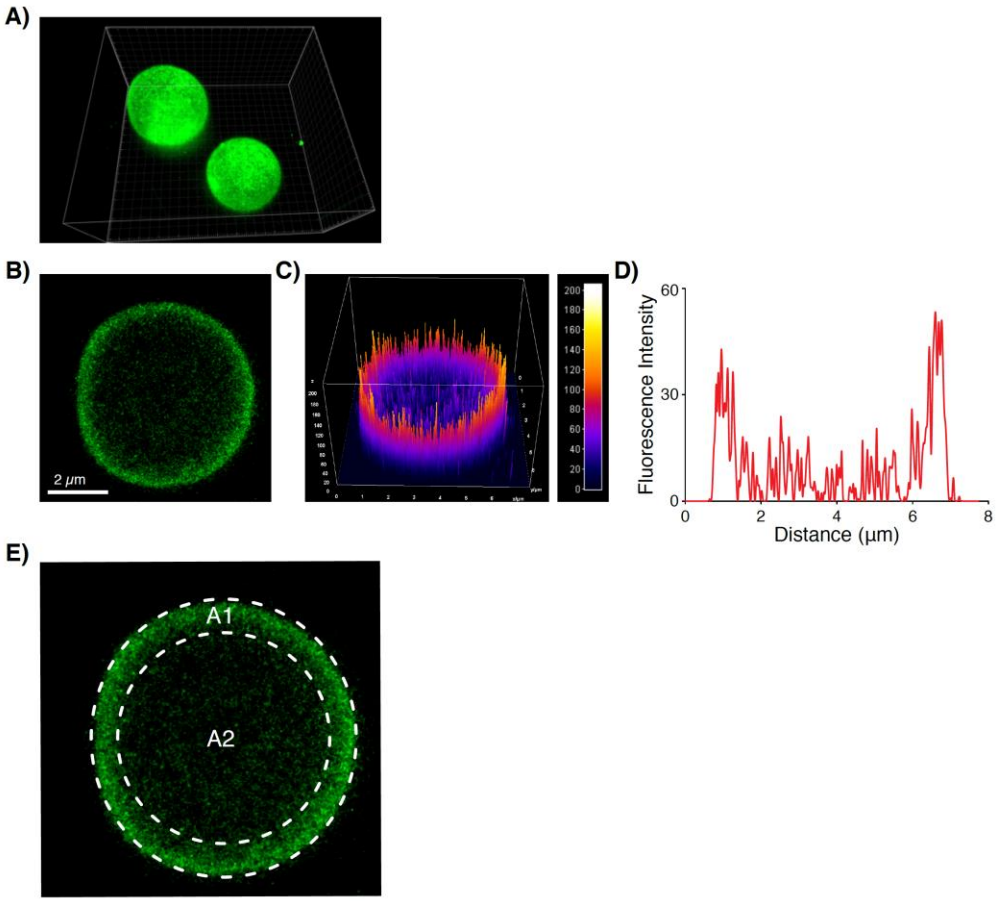

Figure 3.2. Distribution of antibodies conjugated to the microparticles. **A**) confocal micrograph of microparticles coated with fluorescent anti-CD3 antibody. **B**) single slice through the equator of one of the particles. **C**) false color image showing the intensity of fluorescence in the equatorial plane. **D**) Quantification of fluorescence intensity in the equatorial plane. **E**) The equatorial plane was divided into two equal areas ("shells") of 10.2 μm² and compared. On average, the outer shell shows 80.6% of the global integrated fluorescence intensity (n=20). The outer shell has an average pixel intensity of 37.1 while the inner shell has an average of 5.0.

Based on pilot experiments, we chose three different densities of antibodies, representing 10-fold dilutions, to coat beads representing high ("1"), medium ("0.1"), and low ("0.01") amounts of antigenic signaling. An average of 2,692 ± 420, 266 ± 41, and 33 ± 7 antibody molecules per square micrometer were immobilized as high, medium, and low conjugation densities, respectively (**Fig. 3.1F**). For comparison, a theoretical limit of ~12,732 antibodies could be packed into a square micrometer, assuming an antibody has a ~5 nm radius.[12] Thus, what we call a "high" labeling density in this article corresponds to approximately 21% of the theoretical limit. The size of the interface between T cells and antigen presenting cells (**Fig. 3.1E**) varies based on cytoskeletal state of the T cell,[13] with most contacts falling in the range 5-25 μm^2. If one assumes an area of 10 μm^2 for a typical immune synapse, the large particles (2.25 μm radius) would offer a hemispheric area of ~32 μm^2, so that an immune synapse-sized 10 μm^2 would engage ~⅓ of the hemisphere and would engage ~22K antibodies (high density conjugation), 2,192 antibodies (medium), or 251 antibodies (low). For the medium-sized particles (0.3 μm radius) a hemispheric immune synapse offers ~1 μm^2 area and 2,785, 291, and 36 molecules, at these respective conjugation densities (high, medium, low). For the smallest particles (0.15 μm radius), a hemispheric immune synapse would engage 433, 41, and 5 molecules, respectively. The experimentally observed minimum amount of signaling needed to activate a T cell ranges from a 1-4 engaged TCRs[14,15]. Thus, in all cases, the number of T-cell receptors our particles can engage in the immune synapse should be exceed that minimum.

To assess the impact of external, gentle mechanical stimulation on co-cultures of T cells with aAPCs we used an orbital shaker to deliver a continuous oscillatory movement of either ~250 rpm rotational speed ("dynamic") or switched off ("static") (**Fig. 3.3A**). The impact of the aAPCs on T cells were compared with that of the popular, commercially available CD3/CD28 T-cell expansion beads (Dynabeads from Life Technologies). Primary T cells were obtained from spleens of wild-type mice, enriched by negative magnetic-bead selection, and cultured with aAPCs under either static or dynamic conditions.

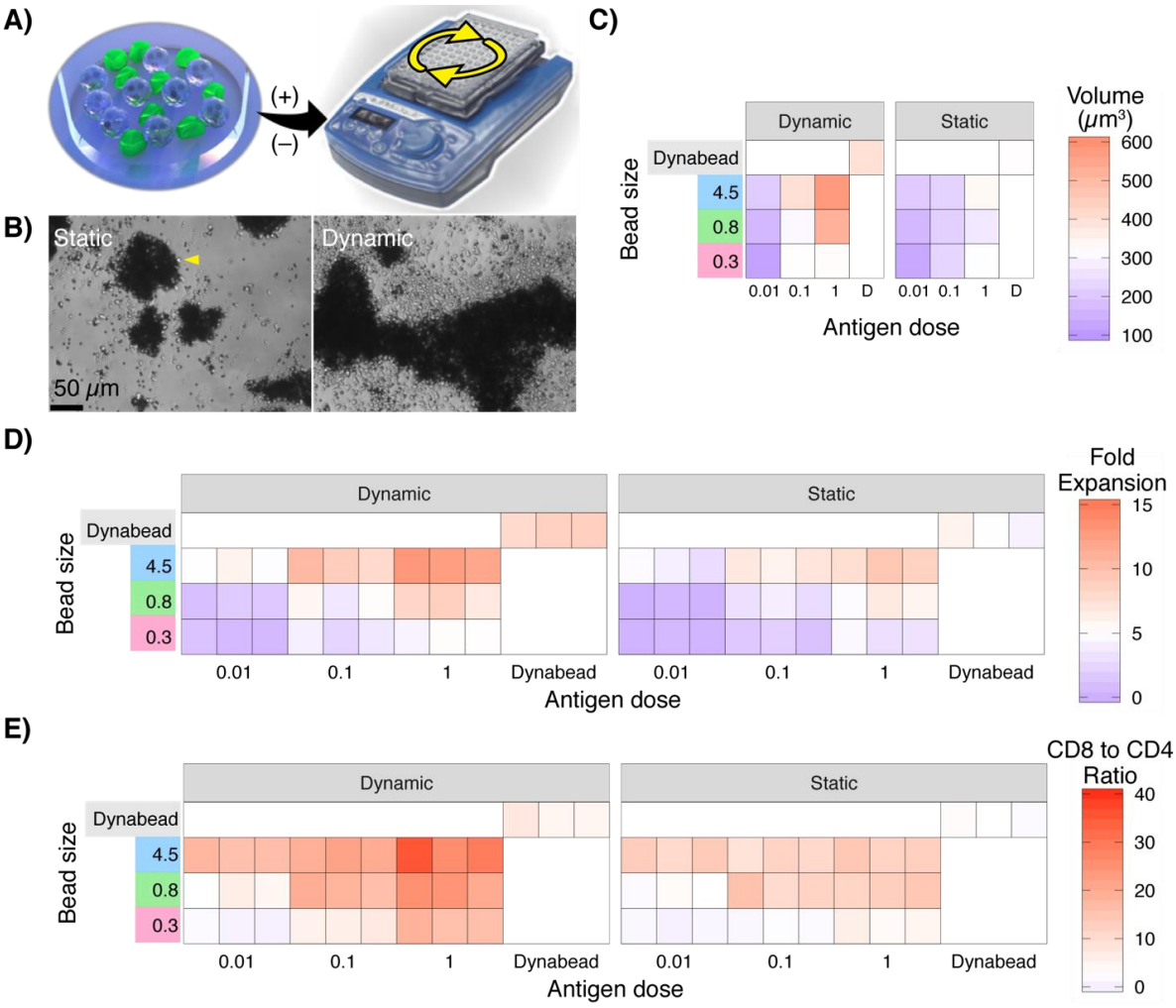

Figure 3.3. (**A**) Particles and T cells were co-cultured under static and dynamic conditions. (**B**) Representative brightfield microscopy images of formed clusters by primary mouse T cells cultured with 5 μm aAPCs at a constant dose (1:1 particle/ T cell ratio) under static and dynamic (mechanical oscillation) cultures. Scale bars, 50 μm. (**C**) The mean volumes of T cells activated and expanded using various formulations of particles, as indicated. (**D**) Expansion of primary mouse CD4+ T cells by varying the antigen dose, particle size or the culture conditions after four days. (**E**) FACS quantification of CD8-to-CD4 ratio of T cells cultured with varying formulations of particles compared to Dynabeads. The starting ratio for all conditions was 0.5.

By day 2 or 3 of culture, polyclonal, primary mouse T cells formed large clusters with the beads. The clusters were obviously larger in the dynamic culture than in static culture (**Fig. 3.3B**). The T cells were separated from the beads and imaged by 3D confocal microscopy to assess their growth. Cell volume was quantified since the volume changes as a cell grows, proliferates, or differentiates. Cell volume can also change in response to external physical cues.[16] We found that cell growth was larger in dynamic culture versus static culture across all particle sizes and conjugation densities (**Fig. 3.3C**, statistical comparisons in **Fig. 3.4A**). The average volume of T

cells co-cultured with Dynabeads in static conditions (n=22) was 321 ± 26 μm³ (mean ± 95% CI), which represents an average diameter of 8.5 ± 0.34 μm. The largest cells were those resulting from co-culture with 4.5 μm particles at the highest density of ligands, which had average volume of 580 ± 74 μm³, corresponding to a diameter of 10.3 ± 0.82 μm (n=25).

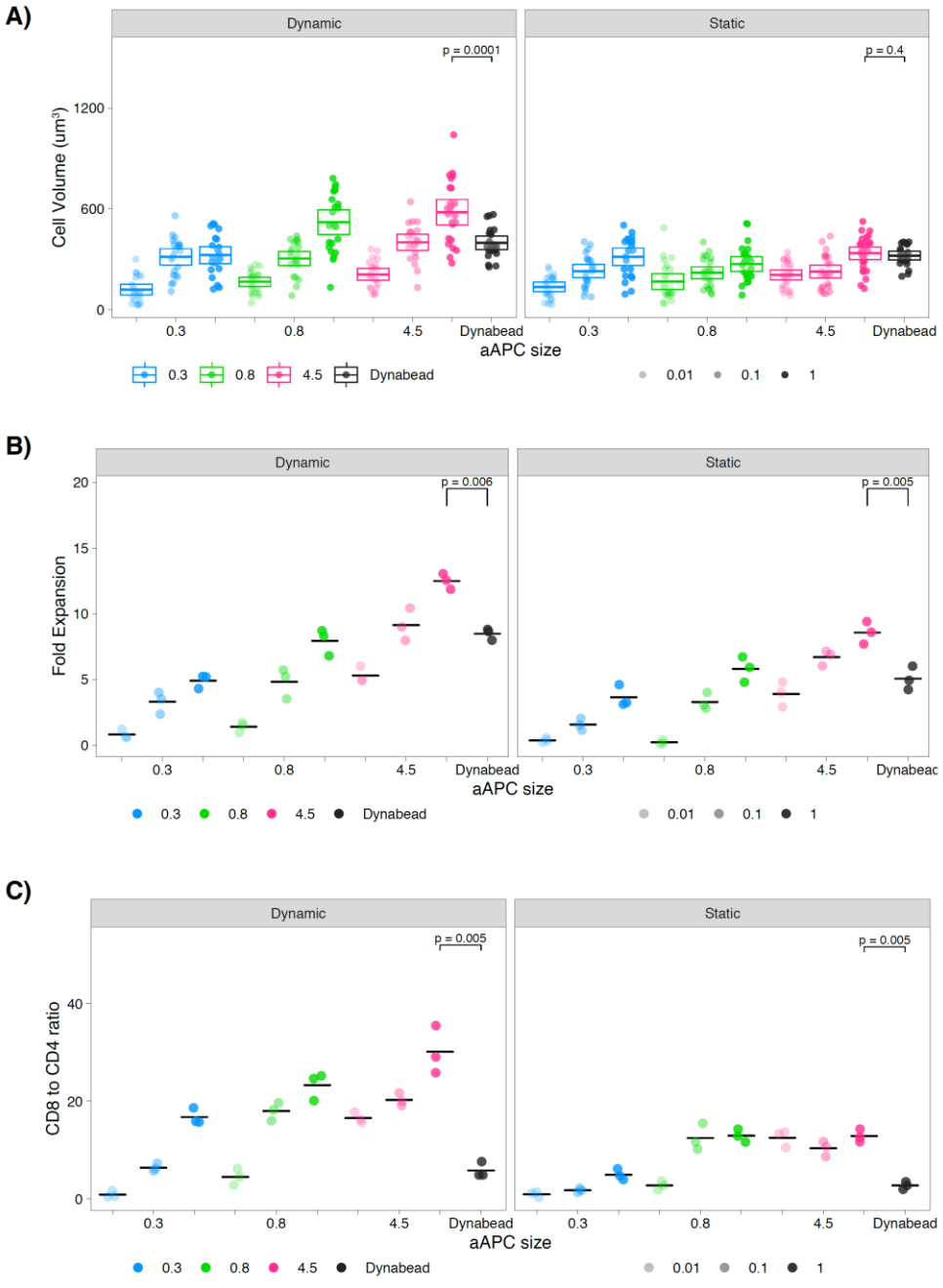

Figure 3.4, accompanies Fig. 3.3C-E. Activation of T cells resulting in **A**) cellular enlargement; **B**) fold expansion in cell numbers; and **C**) change in the CD8 to CD4 ratio (starting

ratio was 0.5). Each dot represents an independent experiment. Horizontal line shows bootstrapped mean. Comparisons are made by permutation testing (see Methods).

To assess their proliferative response, we counted T cells after 3 days of co-culture with the various particles. In all conditions, dynamic culture resulted in significantly higher expansion of T cells than static culture (**Fig. 3.3D**, statistical comparisons in **Fig. 3.4B**). The average fold expansion of T cells co-cultured with Dynabeads in static conditions (n=3) was 5 +/- 1.8 (mean +/- 95% CI) fold. T cells proliferated much more in culture with our mechanically soft particles of the same size and antibody loading as Dynabeads than with Dynabeads, suggesting that the softer mechanics of our aAPC offers an additional stimulus for activation and proliferation (8.6 ± 1.8-fold expansion, $p = 0.006$ compared to static Dynabeads). The largest expansion of T cell count was observed under conditions where T cells were cultured in oscillating conditions with our 4.5 μm particles at the high density of stimulatory antibodies, resulting in an increase of 12.5 ± 1.2 fold ($p = 0.004$ compared to static Dynabeads). Averaging across all particle sizes and antigen doses, mechanical oscillation increased the proliferation of the cells by 2.0- fold compared to static culture (ANOVA considering movement, size, and dose; movement $p = 1.5 \times 10^{-12}$).

In general, cytotoxic CD8+ T cells have a higher proliferative capacity than CD4+ T cells. Cytotoxic T cells have important applications in engineered cancer immunotherapies. We assessed the ability of these particles to promote cytotoxic T cell expansion by monitoring the CD8-to-CD4 T-cell ratio during proliferation. We separately purified CD4+ T cells and CD8+ T cells from mice, then mixed them to achieve the physiological ratio of one CD8+ T cell to two CD4+ T cells. We co-cultured T cells with particles as above, and after 5 days, we measured the ratio of CD8 to CD4 T cells by flow cytometry (**Fig. 3.3E**, statistical comparisons in **Fig. 3.4C**). The average CD8-to-CD4 ratio of T cells co-cultured with Dynabeads in static conditions (n=3) was 2.75 ± 1.5 (mean ± 95% CI). The largest increase in the cellular ratio was observed in the condition where T cells were cultured with 4.5 μm particles with the highest density of ligands, resulting in a CD8 to CD4 ratio of 30.1 ± 9.8 ($p = 0.005$ compared to static Dynabeads). Averaging across all particle sizes and antigen doses, mechanical oscillation increased the CD8 to CD4 ratio of the cells 2.1-fold compared to static culture (ANOVA considering movement, size, and dose; movement $p < 10^{-16}$).

We noted that the larger particles resulted in more expansion, and especially CD8 expansion, of the T cells than the smaller particles, even though the density of antibodies across the beads of different sizes was almost identical (**Fig. 3.1E**) (ANOVA considering size $p < 2 \times 10^{-}$

[16]). This result suggests that the immune synapse integrates the aggregate number of molecular signals across the interface, rather than the density of antigenic ligands.

We further examined the proliferative responses of T cells upon stimulation with our aAPCs by using a dye-dilution approach to follow the proliferation pattern. Sequential generations of daughter cells result in roughly two-fold dilution of the fluorescent signal (**Fig. 3.5A**). The percentage of T cells that underwent proliferation when co-cultured with Dynabeads in static conditions (n=3) was 91.0 ± 5.8% (mean +/- 95% CI) (**Fig. 3.5B**, statistical comparisons in **Fig. 3.6A**). The maximum proliferation was observed under the condition where T cells were cultured with 4.5 μm particles with dynamic oscillations at the highest density of antibodies, resulting in proliferation of 98.8 ± 1.9% ($p = 0.005$ compared with static Dynabeads). Averaging across all particle sizes and antigen doses, mechanical oscillation increased the percentage of T cells that underwent proliferation by 1.72- fold compared to static culture (ANOVA considering movement, size, and dose; movement $p = 0.011$). To measure not just whether the cells divided but also how many times they divided, we also calculated the division index, the average number of cell divisions that a T cell in the original population underwent (the average includes cells that never divided at all) (**Fig. 3.6B**). Because not all cells proliferated, we also compared the proliferation index, the average number of divisions for just the responding population (**Figure S3C**). These show that the maximum number of divisions was observed under the condition where T cells were cultured with 4.5 μm particles at the highest density of antibodies.

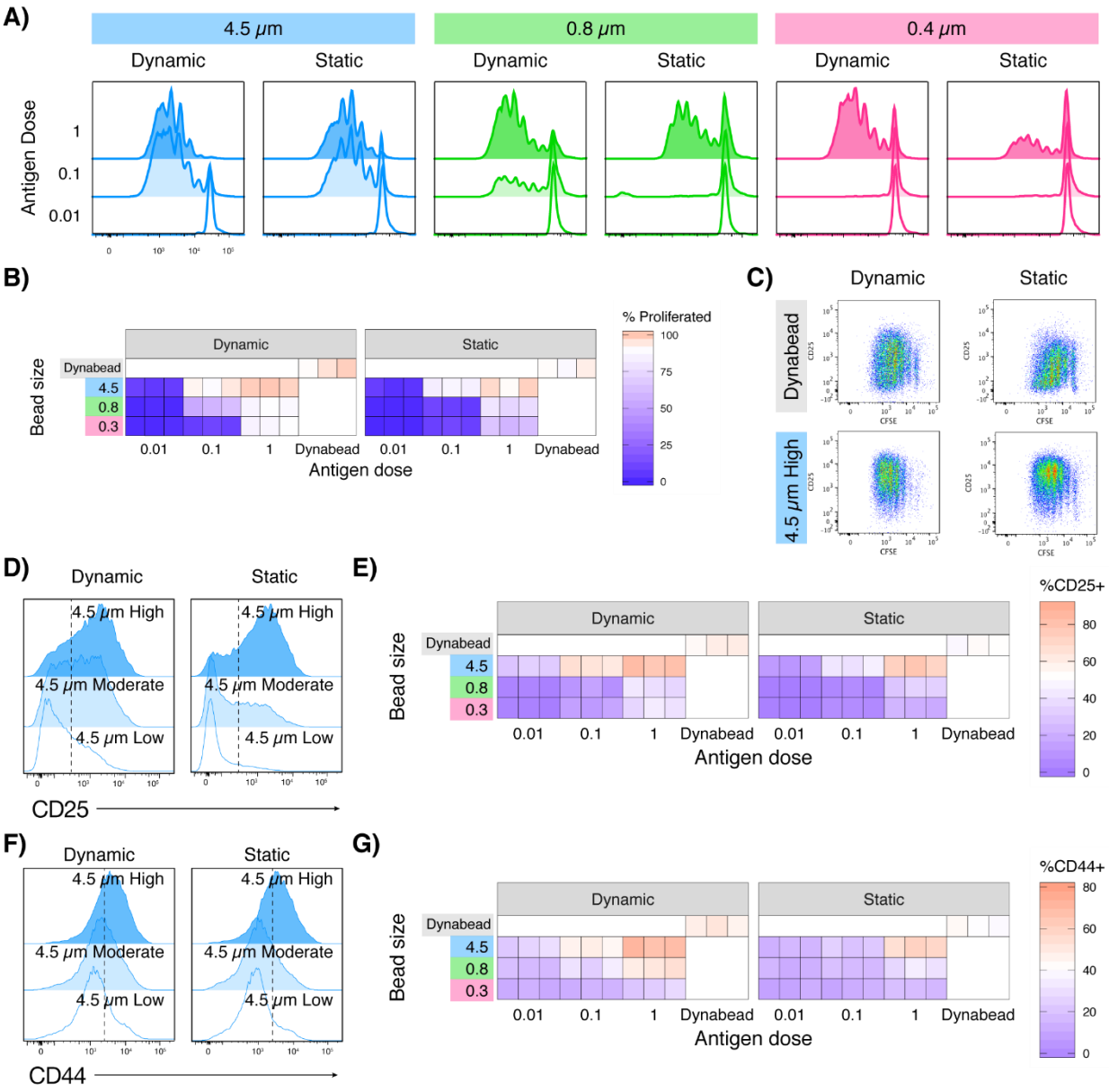

Figure 3.5. Proliferation and activation analyses of CD4⁺ T cells cultured under static or dynamic conditions in the presence of varying formulation of particles. (**A**) Flow cytometry histograms CFSE dilution and (**B**) Percentage of proliferated T cells three days after co-culturing with different formulation of engineered particles. (**C**) (**D**) CD25 expression histograms after 24 h of co-culturing of primary naïve CD4+ T cells with 5 µm microparticles presenting various surface density of antibodies under static or dynamic culture. (**E**) Percentage of CD25+ T cells 24 h after activation with various formulation of particles or Dynabeads. (**F**) CD44 expression histograms after 24 h of co-culturing of primary naïve CD4+ T cells with 5 um microparticles presenting various surface density of antibodies under static or dynamic culture. (**G**) Percentage of CD44+ T cells 24 h after activation with various formulation of particles or Dynabeads.

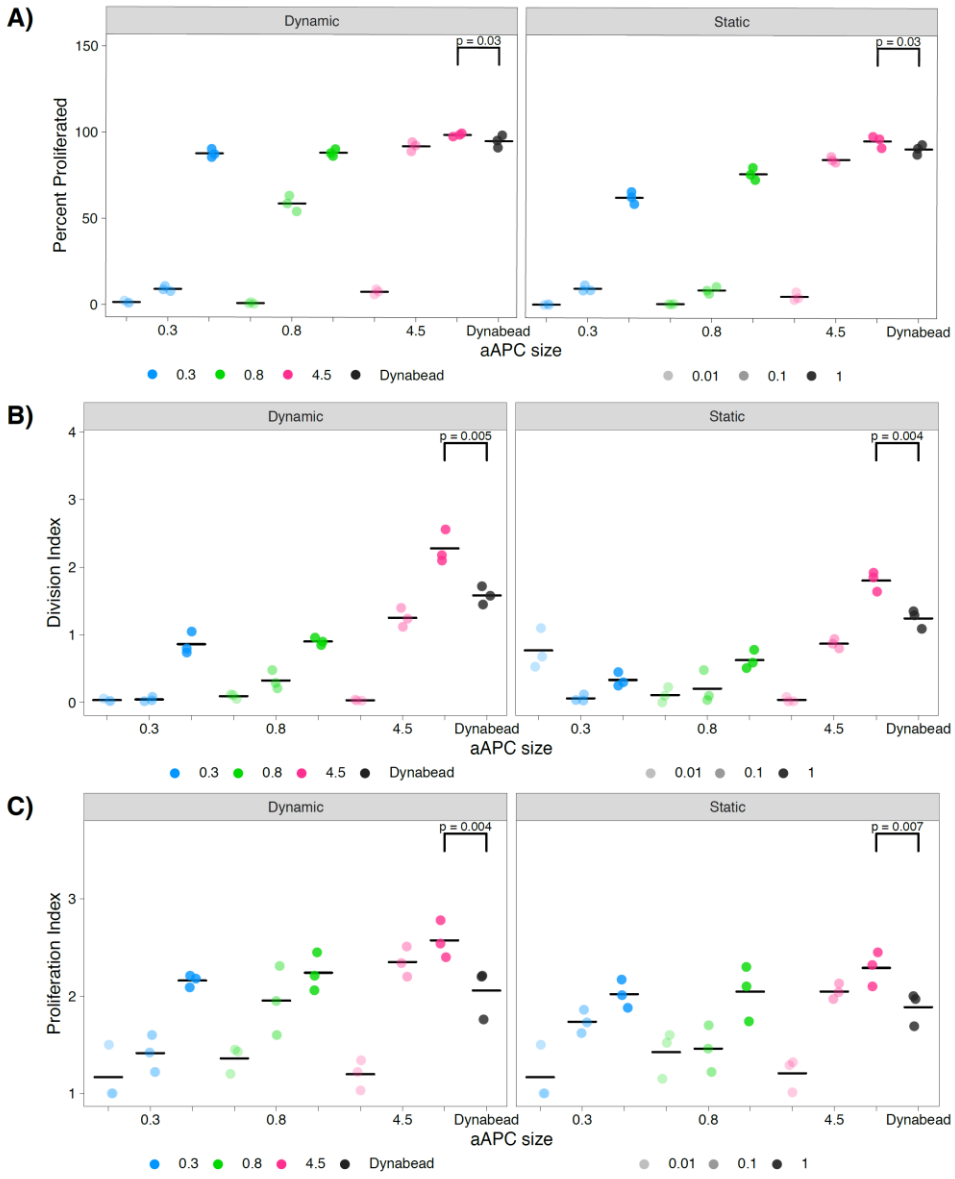

Figure 3.6. accompanies Fig. 3.5B. Proliferation of T cells measured by CFSE dilution and evaluated by FlowJo for **A**) Percent Proliferated, **B**) Division Index, and **C**) Proliferation Index. Each dot represents an independent experiment. Horizontal line shows bootstrapped mean. Comparisons are made by permutation testing (see Methods).

We also examined expression of T-cell activation markers CD25 and CD44 by flow cytometry after activation and found that expression of these markers trended similarly to proliferation (**Fig. 3.5D-G,** statistical comparisons in **Fig. 3.7**). As with absolute expansion, activation and proliferation were greater for larger beads than smaller beads even when antibody

density is held constant. Together these results show that activation and proliferation are proportional to the amount of antigen rather than its density.

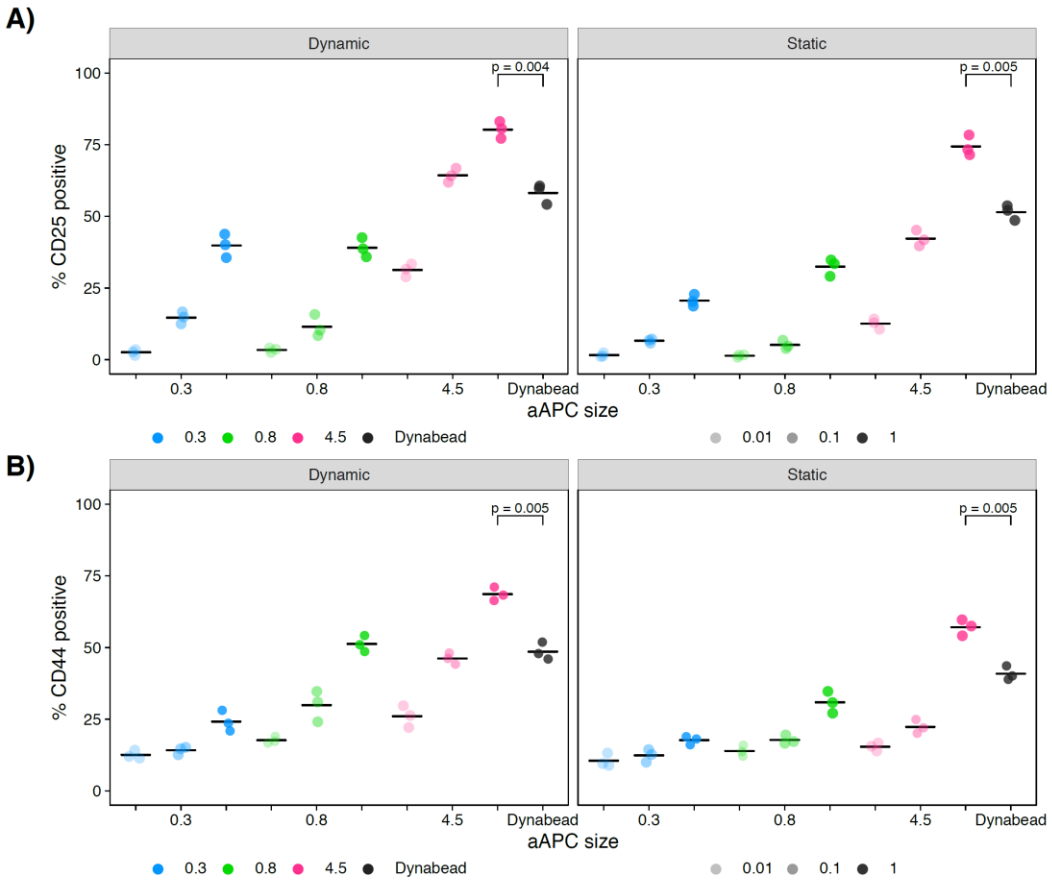

Figure 3.7. accompanies Fig. 3.5E and G. Expression of **A**) CD25+ and **B**) CD44+ T cells after co-culture with aAPCs of various sizes and antibody conjugation densities. Each dot represents an independent experiment. Horizontal line shows bootstrapped mean. Comparisons are made by permutation testing (see Methods).

We showed in prior work that the size of the immune synapse in naive versus effector (recently activated) T cells controls the amount of signal they accumulate in their interactions with APCs.[13] We sought to test the coupling of signal accumulation and synapse size in a reductionist manner. After OT-II T cells were activated with particles, as above, for 24 hours, we purified away the stimulatory particles and co-cultured them with the B cell lymphoma line LB27.4 that was loaded with ovalbumin peptide antigen. We measured the average volume of immune synapses formed between T cells activated in different culture conditions and B cells. based on the accumulation of the integrin leukocyte function–associated antigen 1 (LFA-1) measured by the volume of positive pixels (**Fig. 3.8A**). The average synapse size for T cells co-

cultured with the 4.5 μm particles at high levels of stimulatory antibodies in static conditions (n=3) was 32.8 ± 4.1 μm^2 (**Fig. 3.8B**). The maximum synapse size was observed in the condition where T cells were cultured with 4.5 μm particles with the high level of antibodies in mechanical oscillation conditions (n=3) 36.7 ± 4.1 μm^2 ($p = 0.04$ compared to static). Averaging across all particle sizes and antigen doses, mechanical oscillation increased the size of synapses by 1.3-fold compared to static culture (ANOVA considering movement, size, and dose; movement $p = 2\times10^{-7}$). These results show that the size of the immune synapse is larger when the cells are more activated. Our prior published result compared the size of the synapses for naïve T cells versus effector T cells (lymphoblasts in day 3-5 of culture),[13] and showed that activation of cofilin in effector T cells enabled changes to the cytoskeleton that allowed for larger synapses and a lower threshold of activation than naïve T cells. In other words, the threshold of activation was determined by the size of the synapse and thus the dynamic ability of the cytoskeleton to rearrange when in contact with an APC. The results here go further: we demonstrate here that the dynamic size of the synapse is not just binary, but rather gradated based on signal strength.

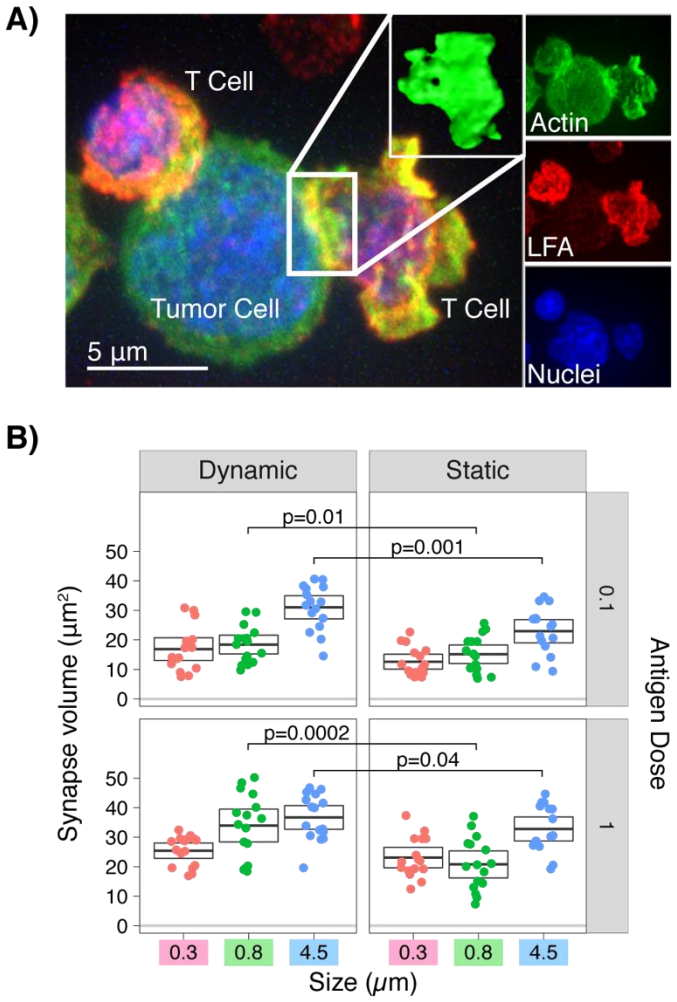

Figure 3.8. (**A**) Immune synapses formed by OT-II T cells activated with 4.5 µm (1) microparticles interacting with (antigen-pulsed) antigen presenting cells (B lymphoma cells) were imaged by confocal microscopy. Images show overlap of confocal slices. Representative cells that had the median immune synapse volume were chosen. (**B**) Analysis of immune synapse volumes (in µm^3) formed by primary naïve T cells activated with various particle sizes with high or low antibody conjugation level cultured at static or dynamic conditions. Each dot represents an immune synapse between a T cell and an antigen presenting cell (n = 16 per condition). Boxes show means and 95% CI values. Results are representative of three independent experiments.

Activating T cells with high signal strength allows for massive expansion, which is needed for transducing chimeric antigen receptors (CARs) and having sufficient transduced cells for a therapeutic dose. The opposite problem arises when expanding T cells in culture for the purposes of generating engineered regulatory T cells. In vivo, regulatory T cells can be elicited to foreign antigens when they are provided at low levels, rather than at high signal strength.[17] Induction of regulatory T cells is improved by provision of TGF-β and IL-2.[18] We recently demonstrated that

alginate microparticles could be loaded with cytokines to skew T cells to iTregs,[19] which served as a motivation to combine that capability with the tunable signal strength of the system presented here. To evaluate the effect of orbital shaking and antigen strength on iTreg formation, we loaded Alg-Hep particles with TGF-β and IL-2. We demonstrated the release of these factors from the particles over time (**Fig. 3.9**). We sorted rigorously naïve CD4+ T cells to eliminate natural regulatory T cells, and then co-cultured these cells with our microparticles. Dynabeads were used for comparison, providing an equivalent amount of soluble TGF-β in the media. We assessed the development of Tregs by intracellular staining for the key transcription factor Foxp3 followed by flow cytometry. The mean fluorescence intensity of the Foxp3 transcript correlates to their regulatory ability,[20] and so Foxp3 expression level was measured as well.

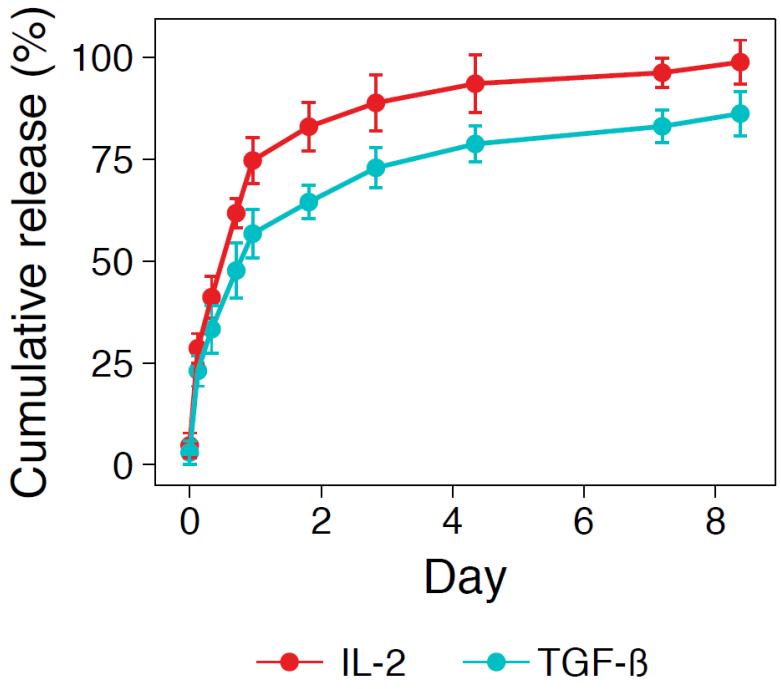

Figure 3.9. Release at 37 °C of TGF-β and IL-2 after loading into Alginate-Heparin particles.

The percentage of iTregs induced in culture with Dynabeads plus TGF-β in static conditions (n=3) was 25.7 +/- 10.1% (mean +/- 95% CI) (**Fig. 3.10A**). The maximum iTreg induction was observed under the condition where T cells were cultured with 4.5 μm particles at the lowest density of antibodies (0.01), resulting in iTreg induction of 71.6 ± 9.6%, almost three-fold higher ($p = 0.005$ compared to static Dynabeads). In general, averaging across all particle

sizes and antigen doses, mechanical oscillation did not alter the rate of iTreg induction at all (1.02-fold difference). Curiously, the lowest amounts of signal strength, as seen in proliferation and activation assays above, were not able to elicit high yields of iTreg induction. In fact, a "sweet spot" of signal was needed, either in the form of larger beads with lower antibody coating or smaller beads with higher antibody coating amounts (**Fig. 3.11A**). The "sweet spot" fell where all three particle sizes could be compared, that is, had comparable numbers of antibodies interacting with T cells (i.e., the largest particles with the lowest antigen density, the medium particles with medium antigen density, and the smallest particles with the highest antigen density). In other words, even as multiple small (300 nm diameter) particles interacted with a single T cell, and offered a comparable antigen amount as a larger particle, the generation of Tregs still favored the situation with the larger particle, i.e., the lower curvature. Thus, in situations where antigen amounts are comparable, larger aAPCs / lower cubature are favored over smaller ones / higher curvature.

The expression of Foxp3 on a per-cell basis was highest in the conditions that elicited the highest induction of iTregs (**Fig. 3.10B**), and again showed a "sweet spot" of signal strength (**Fig. 3.11B**). These results showed that larger immune synapses with low antigen amounts resulted in the highest induction of Tregs.

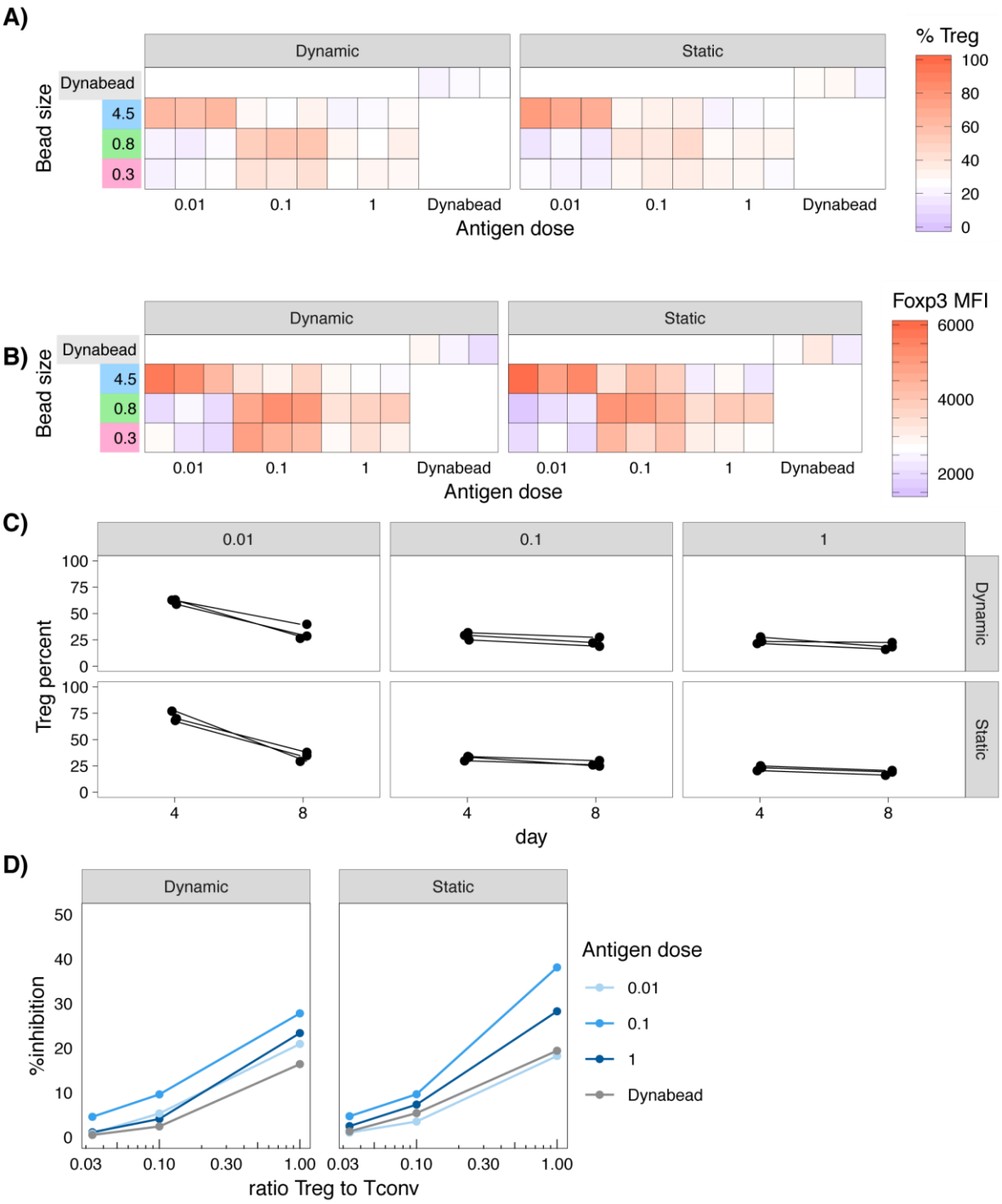

Figure 3.10. Flow cytometric analysis of iTreg development was assessed by flow cytometry for Foxp3 and CD25 co-expression after co-culture of naïve CD4+ T-cells with particles at various formulations either in dynamic or static conditions for 4 d. (**A**) Percentage of induced Tregs and (**B**) mean fluorescence intensity (MFI) of Foxp3 expression in T cells 4 d after activation with various formulation of particles or Dynabeads. (**C**) Stability of formed T-regs as assessed by measuring the change in the population of iTregs (T cells expressing CD4, CD25, and Foxp3+) after 4 and 8 days. (**D**) T-cell suppression assay. Flow sorted Tregs co-cultured with naïve primary CD4+ T-cells (Tconv) at three different ratios of cell counts (1:1,

1:10, and 1:30 of Treg to Tconv) in the presence of surface-coated anti-CD3 and soluble anti-CD28 for 3 d.

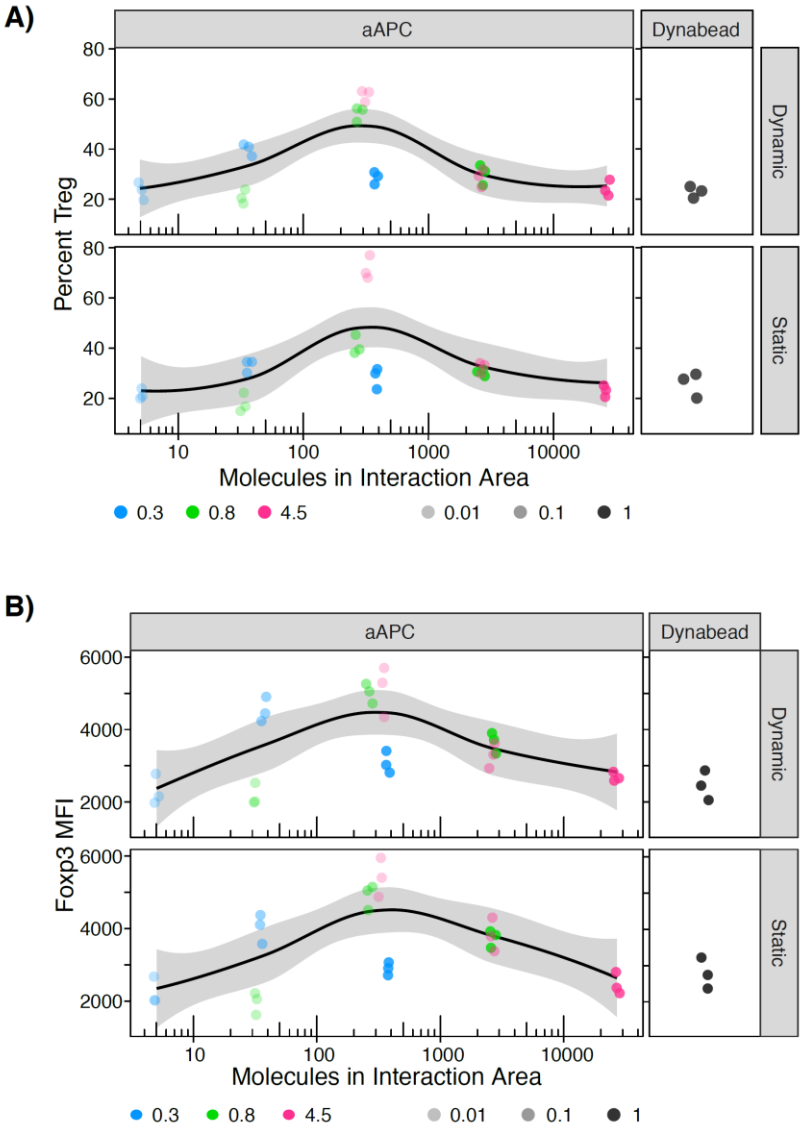

Figure 3.11. Relationship between the number of antibody molecules on the aAPCs and the **A**) development of Tregs, or **B**) activation of conventional T cells. The number of molecules in the interface comes from the text in the Results section and Fig. 1.

We examined the stability of the Foxp3 protein expression, because transient expression of Foxp3 does not yield highly suppressive regulatory T cells.[17] The T cells generated through culture with the 4.5 μm particles were separated from the particles and then maintained in culture with IL-2. We assessed for expression of Foxp3 by flow cytometry at day 4 and at day 8 of culture (**Figure 3.10C**). We found that expression of Foxp3 was dramatically reduced in the condition

where the induction was highest, by the 4.5 μm particles that offered the lowest antigen signal (0.01). Dynamic culture mitigated the loss of Foxp3 expression modestly (29.9 ± 13.1% decrease in dynamic culture versus 37.6 ± 17.7% in static culture). In contrast, the antigenic strengths that were moderate (0.1) and highest (1) had the most stability in culture (4-5% diminishment). Overall, at day 8, the highest expression of Foxp3 was still seen in the co-culture conditions with 4.5 μm particles that offered the lowest antigen signal (0.01), 34 ± 8.8% (n=3).

The ultimate in vitro test of regulatory T-cell function is assessed by their ability to suppress the effector responses of conventional, activated T cells. We co-cultured iTregs induced in a variety of conditions above with conventional T cells at a cellular ratio of 0, 1, 10 and 30 CFSE-labeled conventional, naïve T cells to one iTreg and stimulated with anti-CD3 and anti-CD28. Proliferation of the naïve T cells was assessed without Tregs, and % inhibition was measured by subtracting the proliferation as seen when Tregs were co-cultured. We found that maximal inhibition, and thus maximal regulatory function, was enacted by the iTregs that were generated in the "sweet spot" condition of culture with 4.5 μm particles at medium levels of activating antibodies (0.1) (**Figure 3.10D**). Together these results show that activation and generation of regulatory T cells can be optimized by culturing with particles of large size but low to medium antigenic strength, resulting in the highest stability of regulatory T cells and the most inhibition of effector T-cell proliferation.

3.4. Conclusion

T cells form an interface with antigen presenting cells (APCs) called the "immune synapse" that allows for triggering of TCRs by pMHCs. Artificial antigen presenting cells (aAPCs) can be fabricated to emulate this response and allow for productive expansion of T cells in vitro. By manipulating the size and density of stimulatory signals on aAPCs, we can learn about what is required in the TCR-pMHC interface to reach the threshold for T-cell activation and thus improve cultivation of engineered T-cell therapies. No other work, to our knowledge, has harnessed advanced materials to provide mechanically soft artificial antigen presenting cells combined with mechanical stimulation as we did here.

Orbital shaking provides a mixture of mechanical cues, including oscillatory forces on the immune synapse, stirring of the media to promote T-aAPC engagement, and potentially even shear forces upon the T cells. We showed in prior work that the oscillatory mechanical forces needed to trigger the TCR are in the piconewton range.[1,2] In their engagement with APCs, T cells

generate these forces themselves through actin-dependent pushing and myosin-dependent pulling[3]. The cellular pushing forces occur first, last for about one minute, and through cofilin-mediated cleavage of actin filaments promote the rapid expansion of the lamellipodium to engage the APC.[11,13,21,22] Then T cells pull against the engaged TCR-pMHC bonds, generating the mechanically-induced conformational changes of the TCR and initiation of the biochemical cascade that represents triggering of the TCR.[23,24] By providing exogenous mechanical forces here by an orbital shaker, we showed that T cell triggering can be amplified above and beyond their own capabilities. Specifically, we showed overall that gentle mechanical stimulation of the TCR offers an approximately 2-fold increase in signal strength to T cells as compared to conventional static cultures.

Other work in the use of aAPCs has demonstrated an ability to optimize T-cell signaling and proliferation, akin to the work presented in the first part of this paper. AAPCs fabricated from biomimetic scaffolds, namely mesoporous silica nanorods coated with a lipid bilayers, allowed for maximizing signal strength and an allowed for impressive expansion of T cells *in vitro* [25], but did not allow for obviously tuning down the signal as we did here. Another aAPC system was demonstrated recently with the conjugation of pMHC onto the surface of yeast cells, and this work revealed that density of pMHC was correlated to activation of T cells.[26] Conversely, our work here and other reductionist approaches[15] demonstrated that absolute amount of antigenic signal, rather than density, is more important. Nano-aAPCs of 100 nm diameter coated with anti-CD3 and CD28 were able to elicit modest proliferation *in vitro* but in the *in vivo* context could traffic down lymphatics to draining lymph nodes more readily than micron scaled particles.[27] Recent work with aAPCs comprising polyisocyanopeptide polymers 100-1000 nm long, functionalized with anti-CD3 and IL-2, showed that closer spacing of the anti-CD3 and IL-2 contributed to T-cell activation.[28] These aAPCs together reveal that tuning the amount of antigenic signals and their spatial separations has utility and offers an advantage over biological antigen presenting cells when developing engineering solutions to scaling the production of T cells for therapeutic purposes.

Others have shown that the mechanical stiffness of the surface where antigens or antibodies are tethered has a significant impact on the proliferation and effector responses of T cells. In response to polyacrylamide (PA) surfaces of different stiffness coated with anti-CD3 antibodies, T cells appear to activate strongly in the context of stiff PA surfaces rather than very soft ones,[29] and demonstrate peak spreading on soft surfaces of around 20 kPa.[11] Our work utilized mechanically soft particles (alginate) as well as extremely stiff, commercially available ones (Dynabeads) and found that culture with softer particles could actually outperform stiffer ones,

though the stiffness axes was not directly probed in our work and could be explored in future work as alginate is quite tunable for mechanical stiffness.[19] The ability of conventional Dynabeads or stiff microparticles to serve as a source of cytokines is inherently limited, as shown by recent work demonstrating that IL-2 activity is abrogated when immobilized on very rigid aAPCs.[28] Our aAPCs, on the other hand, demonstrated the ability to enhance regulatory T cell development through gradual secretion of IL-2 and TGF-β. In summary, we demonstrate many advantages of utilizing the advanced material properties of tunable, cytokine-secreting microparticle aAPCs to both control the activation and engineer the differentiation of T cells.

3.5. Materials and Methods

3.5.1. Chemicals and Biologicals:

Unless noted otherwise, all chemicals were purchased from Sigma-Aldrich, Inc. (St. Louis, MO). All glassware was cleaned overnight using concentrated sulfuric acid and then thoroughly rinsed with Milli-Q water. All the other cell culture reagents, solutions, and dishes were obtained from Thermo Fisher Scientific (Waltham, MA), except as indicated otherwise.

3.5.2. Preparation and characterization of cell-mimicking microparticles:

The alginate was charcoal treated, and sterile filtered (0.22 μm filters, Millipore, Billerica, MA) prior to the particle formation. A hydrophobic glass microfluidic droplet junction chip (channel depth 100 μm; Dolomite Microfluidics, Charlestown, MA) was utilized to make monodispersed hydrogel droplets as microparticle substrates. A mixture of alginate solution (1% w/v) and 4-arm PEG hydrazide (MW 5 kDa, Creative PEG work, Chapel Hill, NC) (5 mM) was used as the inner aqueous phase. Mineral oil containing 10 wt% surfactant Span 80 was used as the continuous phase. Several flow rates were applied using two syringe pumps (Fusion 200, Chemyx, Stafford, TX) for the alginate and oil flows to control formation of alginate-based droplets. Images were taken at various time points using a Leica DMIL inverted fluorescence microscope fitted with appropriate filters and connected to a camera. Once particles were formed, they were collected in a bath containing calcium ions (100 mM $CaCl_2$) and left at room temperature for 45 min for ionic crosslinking. The microgels were extensively washed with 10 mM NaCl solution and centrifuged (15,000 rpm for 10 min) twice before further incubation in a solution containing hydroxybenzotriazole (HOBt) and 1-ethyl-3-(3-dimethylaminopropyl)carbodi-imide (EDC). After 2 h, particles were dialyzed against deionized water for three days extensively to remove any residual reagents, then frozen at -20 °C and lyophilized. Particles were then resuspended either in deionized water or phosphate-buffered

saline (PBS) for further use. Magnetic microparticles were fabricated with the addition of super paramagnetic iron oxide nanoparticles (SPION; 50 nm, carboxylated, Chemicell GmbH, Berlin, Germany) to the alginate/PEG mixture. The solution was (bath) sonicated for 10 min at 4 °C prior to use.

For the preparation of antibody-conjugated alginate particles, EDC/NHS chemistry was used to covalently conjugate anti-CD3 (2C11; Bio X Cell) and anti-CD28 (37.51; Bio X Cell) to the surface of particles. After activation of particles' carboxylic groups for 10 min and washing them with PBS (1×) twice, these proteins were added to the particles and vortexed briefly before stirring overnight at 4 °C. The protein-functionalized microparticles were then magnetically separated from unbound proteins and washed several times with PBS (1×). Unreacted functional groups were quenched by washing samples in Tris buffer (100 mM, pH 8).

The antibody density that is commonly used for conventional plate-bound stimulation (10 μg/mL) was used as the "high" amount of antibody ("1" in **Figure 1E**). Dilutions of 10- and 100-fold were made as "medium" (or "moderate") and "low" conjugation densities. As mentioned in the text, the number of particles of different sizes employed in stimulation experiments were adjusted so that their total surface areas were equivalent across conditions order to provide the same surface area for protein conjugation and also for co-culturing with T cells. The amount of antibody (protein) that was used is summarized in **Table 3.3**.

Quantification of the total amount of anti-CD3 and anti-CD28 presented on functionalized particles was analyzed using micro-BCA assay according to the manufacturer's protocol. Dynamic light scattering (DLS) and zeta potential measurements were performed using a Zetasizer (Zetasizer 3000HS, Malvern Instruments Ltd., Worcestershire, UK) in backscattering mode at 173° for the diluted suspensions in water. The iron content of the particles was measured by ICP-OES (Inductively Coupled Plasma – Optical Emission Spectrometry) after digestion with alginate lyase.

To prepare microparticles loaded with IL-2 and TGF-β, crosslinked particles were incubated with the proteins in PBS buffer containing bovine serum albumin (BSA; 0.1 %w/v) and were gently shaken overnight at 4 °C. The particles were then centrifuged and washed several times to remove unabsorbed proteins. The concentrations of IL-2 and TGF-β in the removed supernatant were measured using enzyme-linked immunosorbent assay (ELISA) to estimate the binding capacity of particles. To study the in vitro release profile, protein-loaded particles were dispersed in PBS (pH 7.4) and 500 μL of particles were placed in Eppendorf tubes, gently shaken,

and incubated at 37 °C. At predetermined time points, samples were collected using centrifugation and the supernatant was replaced with an equivalent volume of fresh PBS solution.

Mechanical properties of microparticles were measured using Piuma Nanoindenter (Optics11, Netherlands) with indentation performed by latex beads fixed to the end of cantilevers. The spring constant of the cantilever used in this work was 0.47 N/m. Measurements were performed in liquid mode (ultrapure water) at room temperature. The force-displacement curves were recorded with the vertical ramp size of 10 μm.

3.5.3. Co-culture of particles and immune cells

3.5.3.1. T-cell isolation and activation

Five- to eight-week-old wild-type (C57Bl/6) mice were purchased from the Jackson Labs and maintained in specific pathogen-free facilities at UCLA. All experiments on mice and cells collected from mice were performed under an approved protocol of the Animal Research Committee and in accordance with UCLA's institutional policy on humane and ethical treatment of animals. T-cell culture media was RPMI supplemented with 10% heat-inactivated FBS, 1% penicillin/streptomycin, 1% sodium pyruvate, 1% HEPES buffer, 0.1% μM beta-mercaptoethanol. Total T cells, CD4+ T cells or CD8+ T cells were purified using magnetic-based, negative enrichment kits (Stem Cell Technologies). Cells were counted by hemocytometer using trypan blue exclusion (Calbiochem).

Standard Dynabeads (ThermoFisher) or aAPC-assisted *in vitro* activation of purified T cells was done by culturing cells at a concentration of 1.5×10^6/mL in 24-well plate. Antibodies employed included anti-CD3 (2C11; Bio X Cell) at a concentration of 10 μg/mL followed by addition of 2 μg/mL soluble anti-CD28 (37.51; Bio X Cell). In indicated conditions, 20 IU/mL of human IL-2 was added. The 4.5 μm microparticle aAPCs or Dynabeads were added to the cells at a 1:1 ratio of particles to cells and other particles (0.8 μm, and 0.3 μm) were added in appropriate concentrations to provide the same surface area (see Table above).

For flow cytometric analyses, antibodies to mouse CD4, CD8 (53-6.7), CD25 (PC61.5), CD44 (IM7), FoxP3 and CD16/CD32 ("Fc block") were purchased from eBioscience, BioLegend, or BD Biosciences. To study T-cell proliferative responses in various culture conditions, T-cell expansion was measured by dilution of 5-(and-6)-carboxyfluorescein diacetate, succinimidyl ester (CFSE). For CFSE-dilution experiments, 5×10^5 cells were labeled with 2 μM CFSE for 13 min at 37 °C, washed, and co-cultured with various particles formulations. After the indicated number of days, cells were analyzed by flow cytometry. Flow cytometry was performed on a Cytek

DXP 10. FACS data, including calculations regarding proliferation, were analyzed using FlowJo software (Treestar). Gating for the various analyses is shown in **Figure S7**.

For experiments to induce regulatory T cells (iTreg), CD4+ T cells were purified from mouse spleens by EasySep immunomagnetic negative selection (Stem Cell Technologies). Cells were then activated on anti-CD3e antibody (10 μg/mL)-coated plates with media supplemented with anti-CD28 antibody (2 μg/mL). At the same time particles loaded with TGF-β and IL-2 were added to the media. After four days regulatory T cells were removed from wells coated with anti-CD3e and fixed, permeabilized, and stained with antibodies for flow cytometry analysis. Stability of formed iTregs were also tested after 4 and 8 days of culture by flow cytometry in a similar fashion.

In vitro Treg suppression assay. iTregs were generated using the above approach and flow sorted by expression of CD4+CD25^{hi} cells. To prepare naïve, conventional T cells (Tconv), CD4+ T cells from mouse spleens underwent flow sorting to eliminate all CD25-positive cells, which eliminated activated and natural Tregs (nTregs). We then combined iTreg and CFSE-labeled naïve Tconv at three different ratios of iTreg:Tconv (1:1, 1:10, and 1:30) while being stimulated with plate-coated anti-CD3 and soluble anti-CD28 in 24-well plates as above. As a control, T-cell cultures without iTregs were stimulated in the same manner, and %inhibition was calculated by comparing these cultures to those containing iTregs. Activation markers for iTregs and CD4+ T cells were tested as mentioned before. Flow sorting was performed on a Sony SH800 sorter.

3.5.4. Statistical analysis

All graphs and statistical analyses were performed in R (version 3.5.1). All presented data are expressed as average ± 95% confidence interval, unless otherwise indicated. All averages and confidence intervals were calculated by permuted methods (bootstrap) in R, and all comparisons between groups were performed using permutation testing using the “resample” package in R (version 0.4). Graphs were prepared with ggplot2 in R.

3.6. References

1. Liu, B., Chen, W., Evavold, B. D. & Zhu, C. Accumulation of dynamic catch bonds between TCR and agonist peptide-MHC triggers T cell signaling. *Cell* **157**, 357–368 (2014).
2. Kim, S. T. *et al.* The alphabeta T cell receptor is an anisotropic mechanosensor. *J. Biol. Chem.* **284**, 31028–37 (2009).

3. Hu, K. H. & Butte, M. J. T cell activation r force generation. *J. Cell Biol.* **213**, 535–542 (2016).

4. Xu, J., Melenhorst, J. J. & Fraietta, J. A. Toward precision manufacturing of immunogene T-cell therapies. *Cytotherapy* **20**, 623–638 (2018).

5. Perica, K., Kosmides, A. K. & Schneck, J. P. Linking form to function: Biophysical aspects of artificial antigen presenting cell design. *Biochim. Biophys. Acta - Mol. Cell Res.* **1853**, 781–790 (2015).

6. Deeg, J. *et al.* T cell activation is determined by the number of presented antigens. *Nano Lett* **13**, 5619–5626 (2013).

7. Matic, J., Deeg, J., Scheffold, A., Goldstein, I. & Spatz, J. P. Fine tuning and efficient T cell activation with stimulatory aCD3 nanoarrays. *Nano Lett.* **13**, 5090–5097 (2013).

8. He, H.-T. & Bongrand, P. Membrane dynamics shape TCR-generated signaling. *Front. Immunol.* **3**, 90 (2012).

9. Rossy, J., Laufer, J. M. & Legler, D. F. Role of Mechanotransduction and Tension in T Cell Function. *Front. Immunol.* **9**, 1–11 (2018).

10. Hasani-Sadrabadi, M. M. *et al.* Mechanobiological Mimicry of Helper T Lymphocytes to Evaluate Cell–Biomaterials Crosstalk. *Adv. Mater.* **30**, 1–10 (2018).

11. Wahl, A. *et al.* Biphasic mechanosensitivity of T cell receptor-mediated spreading of lymphocytes. *Proc. Natl. Acad. Sci. U. S. A.* 1–6 (2019) doi:10.1073/pnas.1811516116.

12. Reth, M. Matching cellular dimensions with molecular sizes. *Nat. Immunol.* **14**, 765–7 (2013).

13. Thauland, T. J., Hu, K. H., Bruce, M. A. & Butte, M. J. Cytoskeletal adaptivity regulates T cell receptor signaling. *Sci. Signal.* **3737**, 1–11 (2017).

14. Irvine, D. J., Purbhoo, M. A., Krogsgaard, M. & Davis, M. M. Direct observation of ligand recognition by T cells. *Nature* **419**, 845–9 (2002).

15. Manz, B. N., Jackson, B. L., Petit, R. S., Dustin, M. L. & Groves, J. T-cell triggering thresholds are modulated by the number of antigen within individual T-cell receptor clusters. *Proc. Natl. Acad. Sci. U. S. A.* **108**, 9089–9094 (2011).

16. Guo, M. *et al.* Cell volume change through water efflux impacts cell stiffness and stem cell fate. *Proc. Natl. Acad. Sci. U. S. A.* **114**, E8618–E8627 (2017).

17. Rubtsov, Y. P. *et al.* Stability of the regulatory T cell lineage in vivo. *Science* **329**, 1667–71 (2010).

18. Zheng, S. G., Wang, P., Gray, J. D., Wang, J. & Horwitz, D. A. IL-2 Is Essential for TGF- to Convert Naive CD4+CD25- Cells to CD25+Foxp3+ Regulatory T Cells and for Expansion of These Cells. *J. Immunol.* **178**, 2018–2027 (2014).

19. Majedi, F. S. *et al.* Cytokine Secreting Microparticles Engineer the Fate and the Effector Functions of T-Cells. *Adv. Mater.* **30**, 1703178 (2018).

20. Chauhan, S. K., Saban, D. R., Lee, H. K. & Dana, R. Levels of Foxp3 in Regulatory T Cells Reflect Their Functional Status in Transplantation. *J. Immunol.* **182**, 148–153 (2014).

21. Negulescu, P. A., Krasieva, T. B., Khan, A., Kerschbaum, H. H. & Cahalan, M. D. Polarity of T cell shape, motility, and sensitivity to antigen. *Immunity* **4**, 421–30 (1996).

22. Fritzsche, M. *et al.* Cytoskeletal actin dynamics shape a ramifying actin network underpinning immunological synapse formation. *Sci. Adv.* **3**, e1603032 (2017).

23. Ma, Z., Discher, D. E. & Finkel, T. H. Mechanical force in T cell receptor signal initiation. *Front. Immunol.* **3**, 2–4 (2012).

24. Basu, R. & Huse, M. Mechanical Communication at the Immunological Synapse. *Trends Cell Biol.* **27**, 241–254 (2017).

25. Cheung, A. S., Zhang, D. K. Y., Koshy, S. T. & Mooney, D. J. Scaffolds that mimic antigen-presenting cells enable ex vivo expansion of primary T cells. *Nat. Biotechnol.* **36**, 160–169 (2018).

26. Smith, M. R., Tolbert, S. V. & Wen, F. Protein-Scaffold Directed Nanoscale Assembly of T Cell Ligands: Artificial Antigen Presentation with Defined Valency, Density, and Ratio. *ACS Synth. Biol.* **7**, 1629–1639 (2018).

27. Rhodes, K. R. & Green, J. J. Nanoscale artificial antigen presenting cells for cancer immunotherapy. *Mol. Immunol.* **98**, 13–18 (2018).

28. Hammink, R. *et al.* Cytokine-Functionalized Synthetic Dendritic Cells for T Cell Targeted Immunotherapies. *Adv. Ther.* **1**, 1800021 (2018).

29. Saitakis, M. *et al.* Different TCR-induced T lymphocyte responses are potentiated by stiffness with variable sensitivity. *Elife* **6**, e23190 (2017).

Chapter 4.

T-cell activation is modulated by the 3D mechanical microenvironment [3]

Abstract

T cells recognize mechanical forces through a variety of cellular pathways, including mechanical triggering of both the T-cell receptor (TCR) and integrin LFA-1. Here we show that T cells can recognize forces arising from the mechanical rigidity of the microenvironment. We fabricated 3D scaffold matrices with mechanical stiffness tuned to the range 4-40 kPa and engineered them to be microporous, independently of stiffness. We cultured T cells and antigen presenting cells within the matrices and studied T-cell activation by flow cytometry and live-cell imaging. We found that there was an augmentation of T-cell activation, proliferation, and migration speed in the context of mechanically stiffer 3D matrices as compared to softer materials. These results show that T cells can sense their 3D mechanical environment and alter both their potential for activation and their effector responses in different mechanical environments. A 3D scaffold of tunable stiffness and consistent microporosity offers a biomaterial advancement for both translational applications and reductionist studies on the impact of tissue microenvironmental factors on cellular behavior.

[3] This Chapter is published as: Majedi F.S., Hasani M.M., Thauland T.J., Li S., Bouchard L.S., Butte M.J., T-cell activation is modulated by the 3D mechanical microenvironment. *Biomaterials* 252 (2020) 120058.

4.1. Introduction

When T cells recognize their cognate antigen on the surface of antigen presenting cells (APCs), they form a complex three-dimensional structure known as the immune synapse (IS) [1]. The IS, which facilitates communication between T cells and APCs via receptor-ligand interactions, is critical for T-cell activation, and constitutes a platform for the delivery of effector molecules (e.g. the contents of cytolytic granules). At the molecular level, receptor-ligand interactions at the IS trigger a series of signaling cascades. These TCR-proximal signals initiate transcriptional programs controlling T-cell proliferation, differentiation, and effector function.

The actin cytoskeleton is critical for T-cell biology, and pharmacological disruption of F-actin severely cripples T-cell motility, IS formation, and T-cell activation [2]. While cytoskeletal rearrangement is crucial for IS formation, the state of the cytoskeleton prior to T cell-APC conjugation is also important. We have previously shown that naive T cells are mechanically stiffer than activated effector T cells [3]. This difference in stiffness allows the more pliable effector T cells to form larger IS with APCs upon initial triggering, increasing the number of receptor-ligand interactions and enhancing activation. Thus, the T-cell cytoskeleton acts as a layer of regulation, allowing effector cells to sensitively respond to APCs. The stiffness of the antigen-presenting surface that T cells interact with also plays a role in activation. Experiments examining the interaction of T cells with stimulatory 2D surfaces of varying stiffnesses have demonstrated that relatively stiffer surfaces provide a stronger stimulus [4–9]. Elastic moduli around 15-20 kPa enable maximal spreading of T cells and optimal activation [10]. The cytotoxicity of T cells is also affected by substrate stiffness [11]. All these experiments have been performed in 2D, i.e., on surfaces.

While the mechanical properties of the T cell and the antigen-presenting surface have been investigated, the effect of the mechanical properties of the 3D microenvironment on actin-dependent T-cell functions such as motility, IS formation, and activation has barely been examined. The properties of 3D scaffolds can be manipulated by altering the density of polymers

and crosslinkers. As cells migrate through scaffolds, they interact with functional groups that act as ligands for cell surface receptors, presented by the polymer. Thus, increasing polymer density results in a concomitant increase in ligand density and a decrease in mesh size, which alters cell-polymer interactions. On the other hand, keeping polymer content constant and varying the crosslinker density also alters the mesh size of the gel, which directly impacts molecular diffusion and cell motility [12]. While stiffness and ligand density can be modulated independently of polymer content with some synthetic polymers, the direct relationship between crosslinker density and mesh size has made it difficult at best to relate cell behavior to pure stiffness. Fortunately, in the case of the biodegradable polymer alginate gelation is induced by calcium ions. Due to the formation of G-blocks that provide pockets for calcium entrapment, the stiffness of the gel can be altered by varying the concentration of calcium ions without altering the ligand density or pore size.

Here we sought to mimic a range of biologically relevant stiffnesses that T cells experience while patrolling secondary lymphoid organs and peripheral tissues. We developed 3D porous alginate-based scaffolds that had similar rigidities to lymph nodes. Due to the unique characteristics that the alginate biopolymer possesses, we were able to modulate the rigidity of our scaffolds without affecting their porosity or ligand density. We used these scaffolds to study motility, proliferation, morphology, and immune synapse formation by T cells. We found that mechanically stiffer scaffolds enhanced T-cell activation in 3D cultures, akin to what has been observed for 2D substrates. Our morphological studies of T cells in hard and soft scaffolds revealed increased cell spreading in hard scaffolds. This effect likely contributes to the enhanced immune synapse size, activation, and proliferation we observed for cells cultured in stiff scaffolds.

4.2. Results and Discussion

4.2.1 Alginate-based matrix with constant microporosity with tunable elasticity.

To study how the mechanical stiffness of a 3D environment affects T-cell activation, proliferation, and IS formation, we developed a microporous, alginate-based, 3D scaffold (see Methods). To improve cell adhesion within these scaffolds, the alginate polymer was modified with RGD peptides. We screened polymers with a wide range of mechanical properties by titrating polymer and calcium concentration. Measurements of polymer stiffness demonstrated that we could modulate stiffness over two orders of magnitude by varying alginate density from 0.5% to 2.5% and calcium concentration from 10 mM to 60 mM (**Fig. 4.1a**). Gels with an order-of-magnitude difference in stiffness (4 and 40 kPa) in the range of biologically relevant tissues [13] were chosen for further study. To assess whether changing the stiffness altered the pore size, we acquired images of the microporous structure of our 3D gels by scanning electron microscopy (SEM) (**Fig. 4.1b,c**). We found that both the 40 and 4 kPa gels had a pore size of approximately 130 μm (**Fig. 4.1d**). These results reveal an ability to prepare 3D scaffolds of tunable stiffness and consistent microporosity.

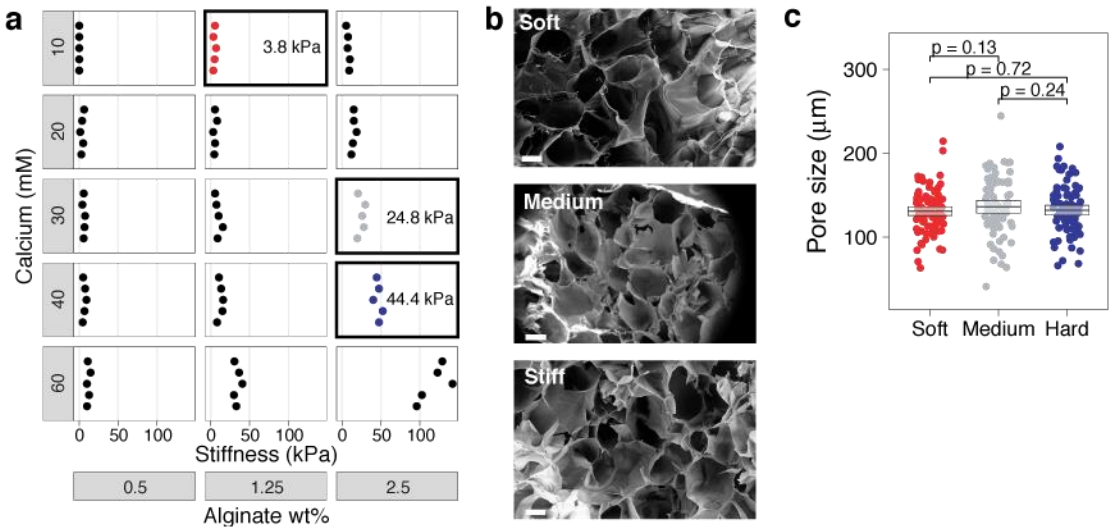

Figure 4.1. Modulation of alginate gel stiffness without affecting porosity. a, Different formulations of materials were screened by changing the concentration of the alginate polymer or calcium crosslinker. Stiffness values (Young's modulus) were measured on an Instron mechanical tester. Boxes are the soft, medium, and stiff conditions chosen for experiments in this paper. **b,** SEM images of three scaffolds with an order of magnitude difference in mechanical stiffness. Hard scaffolds were ~40 kPa, Medium scaffolds were ~25 kPa, and soft scaffolds were ~4 kPa. Images were taken from a region within the bulk of the scaffold. Scale bar is 100 µm. **c,** The size of at least 75 pores in each scaffold were measured from SEM images. Average pore sizes were 131.9 ± 6.1 µm for hard scaffolds, 136.1 ± 8.1 µm for medium scaffolds, and 130.9 ± 5.5 µm for soft scaffolds and were not significantly different. Bootstrap mean ± 95% CI shown (box).

4.2.2 T-cell motility within matrices

Given the importance of motility for T-cell function, we tracked T-cell migration in hard (40 kPa) and soft (4 kPa) gels using live-cell confocal microscopy. Fluorescently-labeled cells were seeded into gels and imaged over time crawling within the 3D scaffolds (**Fig. 4.2a**). Our analyses revealed that the average speed of T cells crawling within hard scaffolds (4.7 ± 0.3 µm/min, average ± 95% CI), was higher than within soft scaffolds (4.0 ± 0.2 µm/min) ($p < 1\text{x}10^{-5}$) (**Fig. 4.2b**). These speeds are in a biologically relevant range for T cells as seen in prior works.[14,15] The

~20% higher speed of cells within stiffer scaffolds affords a higher probability of interaction between T cells and APCs. Thus, these findings are consistent with the fact that T cells were more activated and proliferative in the stiffer gels.

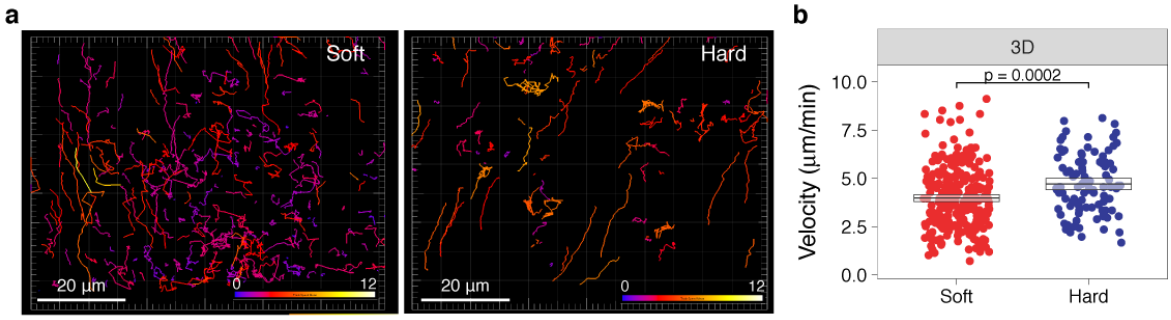

Figure 4.2. T-cell motility is enhanced in stiff 3D scaffolds. a, T cells crawling through microporous alginate scaffolds were imaged for 10 min. T-cell migration in soft (left) and stiff 3D scaffolds (right) were tracked with Imaris. Tracks are color-coded for average track velocity ranging from 0 to 12 µm/min. **b**, Mean velocity of cells crawling through soft and hard scaffolds. Each dot is the average track velocity of a single T cell. Bootstrapped mean and 95% CI are boxed.

4.2.3 T-cell activation and effector functions within matrices

To examine the effect of 3D scaffold stiffness on CD4+ T-cell activation, we cultured T cells and monitored their proliferation. We seeded naïve, CFSE-labeled CD4+ T cells purified from OT-II TCR transgenic mice plus peptide-loaded APCs into hard (40 kPa) and soft (4 kPa) 3D alginate scaffolds. To contrast 3D culture with conventional approaches, we prepared 2D alginate-RGD gels with same mechanical stiffnesses as the 3D scaffolds (**Fig. 4.3**).

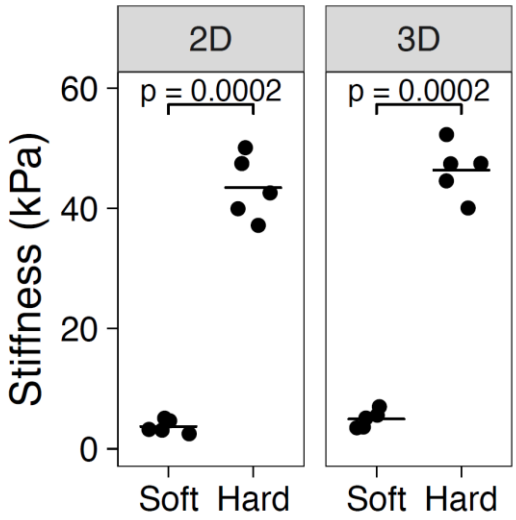

Figure 4.3. Stiffness of scaffolds is not affected by lyophilization and introduction of microporosity. Measurement of the mechanical stiffness by Instron of scaffolds in 2D and 3D.

T cells and peptide-loaded APCs were placed onto these 2D substrates. Sequential generations of daughter cells result in roughly two-fold dilution of the CFSE dye when analyzed by flow cytometry. We also monitored the expression of the activation marker CD25 on the T cells. The stiffer substrate induced more proliferation in both 2D and 3D conditions than the softer substrate (**Fig. 4.4a and b**). Interestingly, the effect of stiffness on proliferation was greater in 3D scaffolds than on 2D surfaces (**Fig. 4.4c and d**). There were slightly more undivided cells in 3D conditions. We hypothesize that the increased degrees of freedom experienced by cells in a 3D matrix makes successful T cell-APC conjugation less frequent, and thus some T cells remained unactivated, as compared with crawling on a 2D surface. However, the proliferation index (a measure of the proliferative response of the cells that divided at least once) was higher in the stiff 3D environment (**Fig. 4.4d**). This result suggests that there is enhanced activation when T cells encounter an APC in 3D. In agreement with the proliferation data, upregulation of CD25, a cell-surface marker of T-cell activation, was more robust on stiffer substrates (**Fig. 4.4e**).

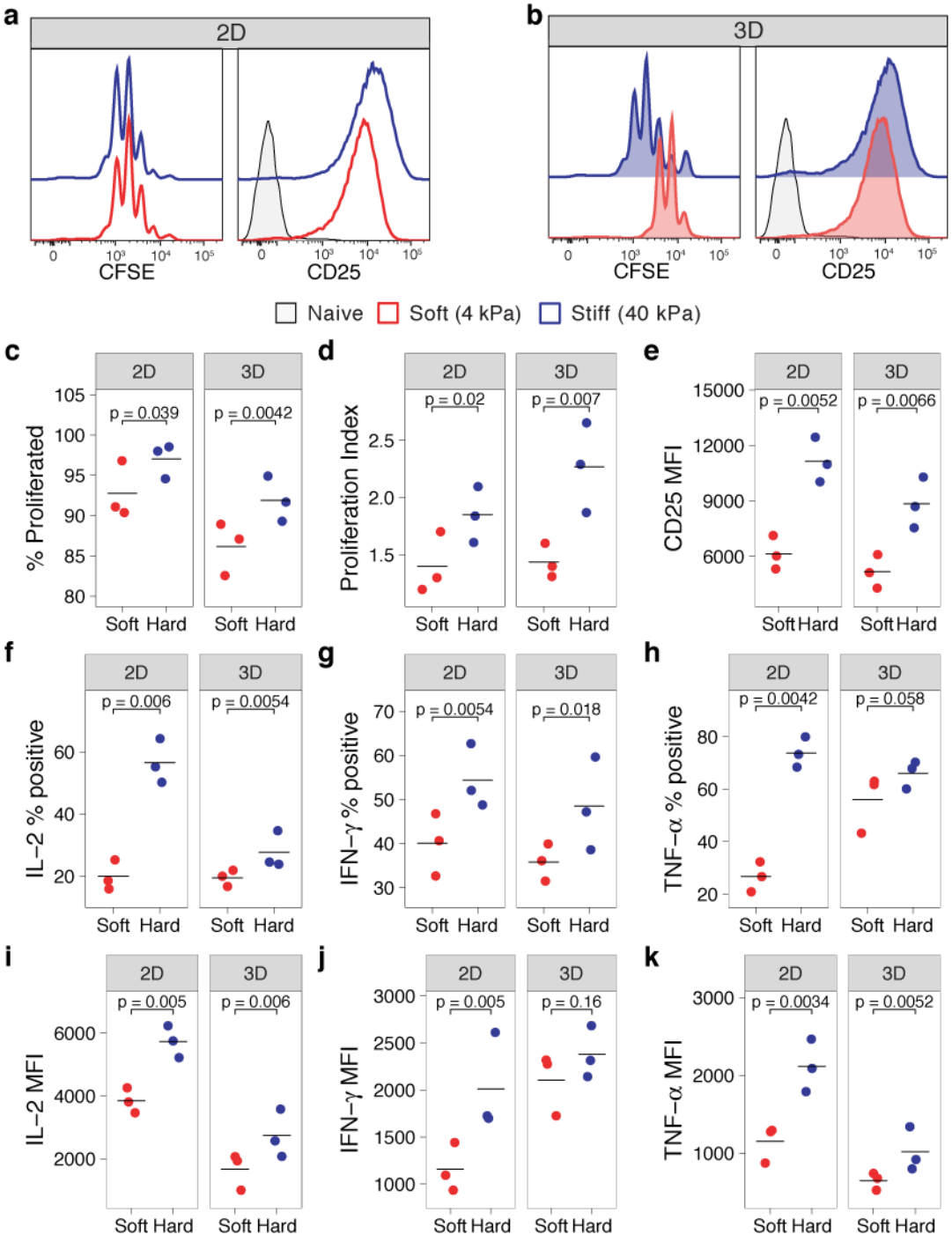

Figure 4.4. T-cell activation is modulated by the stiffness of 3D scaffolds. (a and **b)** FACS analysis of CD25 expression and cell division (CFSE dilution) of CD4+ T cells co-cultured with peptide-pulsed APCs on 2D **(a)** or 3D **(b)** scaffolds with different stiffnesses. Cells were assayed at three days post-stimulation. **(c-e)** Percentage of cells that divided at least once **(c)**, proliferation index of divided cells **(d)**, and mean fluorescence intensity (MFI)

of CD25 **(e)** are plotted for cells activated on 2D or 3D and stiff or soft scaffolds. **(f-h)** Percentage of T cells expressing the effector cytokines IL-2, IFN-γ, or TNF-α. **(i-k)** Expression amount (MFI) of cytokines for those T cells making cytokines. Each dot represents one experiment.

Effector responses of T cells can be assayed not only by proliferation and upregulation of activation markers like CD25, but also by production of key cytokines. To study whether cytokine expression is modulated by the mechanical microenvironment, we monitored the expression of IL-2, IFN-γ, and TNF-α in T cells cultured with peptide-pulsed APCs in 3D scaffolds of hard or soft stiffness by intracellular cytokine staining. We found that the percentage of cells that expressed these cytokines was higher in hard 3D scaffolds than those in softer scaffolds (**Fig. 4.4f-h,** isotype controls shown in **Fig. 4.5**, example data in **Fig. 4.6**). Moreover, in examining the single-cell amount of cytokine expressed in these responsive cells, the T cells responding to antigen in the stiffer matrix produced more effector cytokines than those in a softer matrix (**Fig. 4.4i-k,** example data in **Fig. 4.6**). Some minor differences were noted in comparing cytokines elicited in 3D versus 2D. Notably, the expression of both TNF-α and IL-2 were higher in 2D than 3D. These results show that effector functions of T cells are augmented in stiffer 3D microenvironments as compared to softer environments.

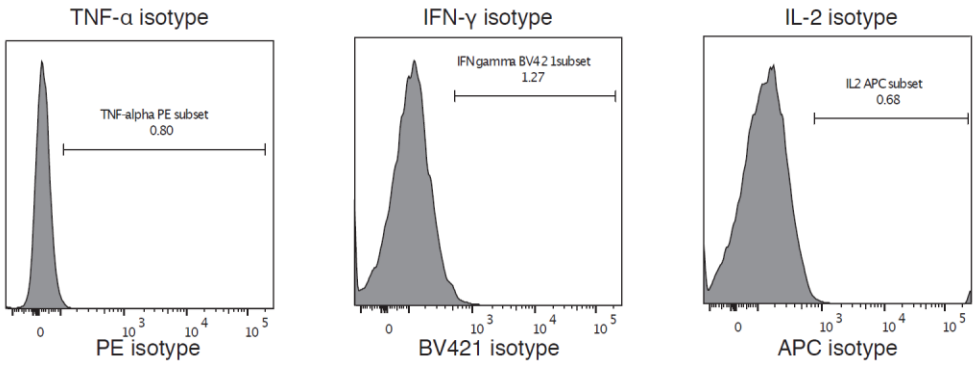

Figure 4.5. Isotype controls for intracellular cytokine staining used to define gating for "positives". Isotype controls for TNF-α, IFN-γ, and IL-2 were stained on CD4+ T cells and used to define positive gates for each cytokine, respectively.

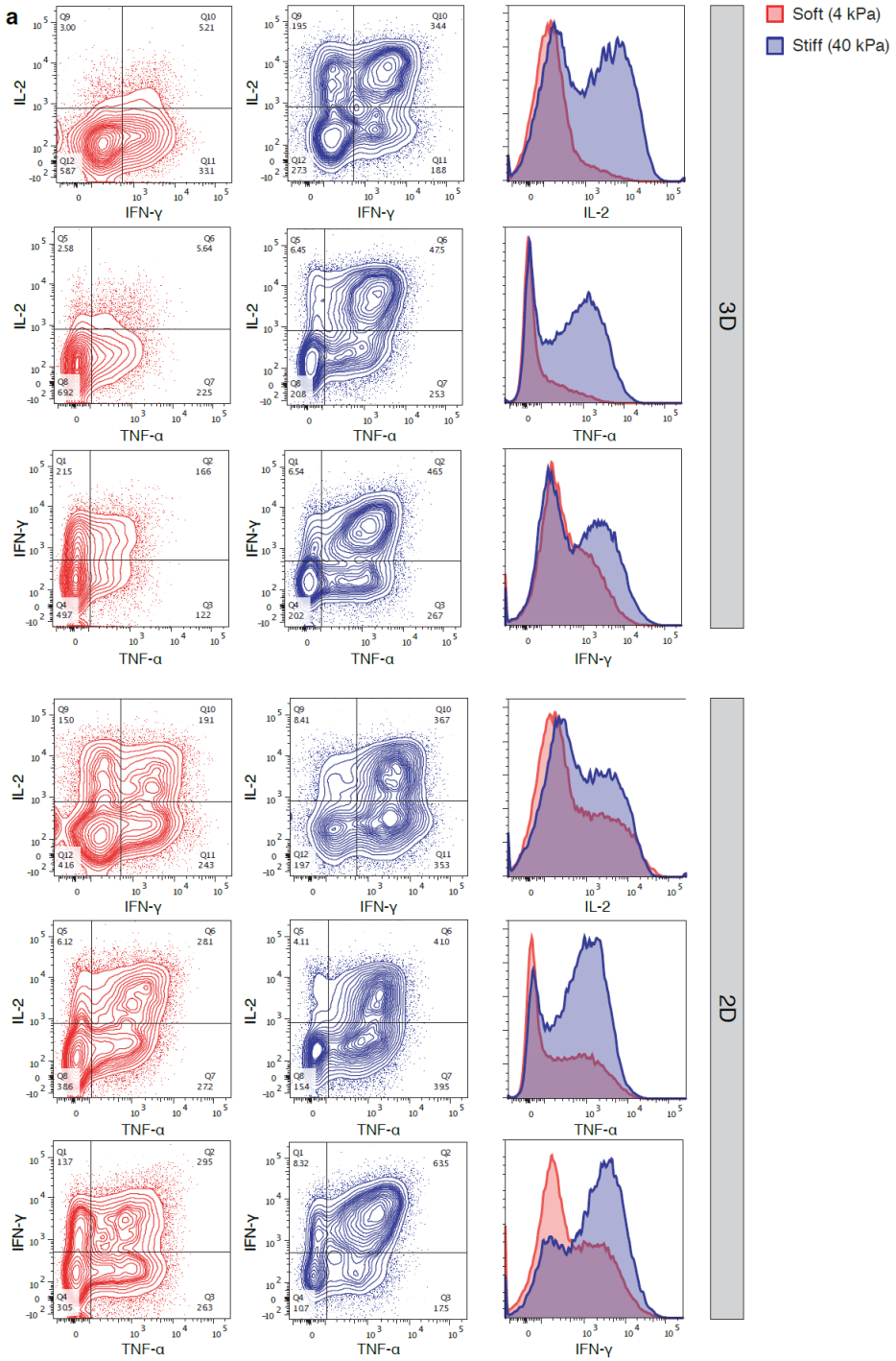

Figure 4.6. Effector responses of T cells upon co-culture with real antigen presenting cells is modulated by mechanical microenvironment. Effector cytokine responses of T cells in presence of real antigen-pulsed APCs was assayed by measuring production of key cytokines in 3D scaffolds (a) and 2D cultures (b) in soft *vs*. hard matrices. Accompanies Fig. 4.

4.2.4 T-cell activation with artificial APC microparticles within matrices

To better understand if the differential activation of T cells cultured in stiff and soft scaffolds above could have been indirect, i.e., arisen from the effects of stiffness upon the antigen presenting cells, we next examined the activation of T cells using artificial APC beads as the stimulus, which are unsusceptible to local micromechanics. We seeded microparticles fabricated from alginate and coated with anti-CD3 and anti-CD28 antibodies, as previously described [16], into the 3D scaffolds. As before we prepared 2D alginate-RGD gels with mechanical stiffnesses like the 3D scaffolds. We introduced naïve, CFSE-labeled CD4+ T cells into the 3D scaffolds or onto the 2D substrates. For a few experiments, we introduced a third "medium" mechanical stiffness to offer an intermediate condition of 25 kPa. The stiffer substrate induced more proliferation and induced more of the activation marker CD25 than the softer one; the intermediate substrate was essentially the same as stiff (**Fig. 4.7a-e**). This result shows that there the enhanced activation of T cells encounter in stiff 3D scaffolds is independent of any mechanical effect of the APC.

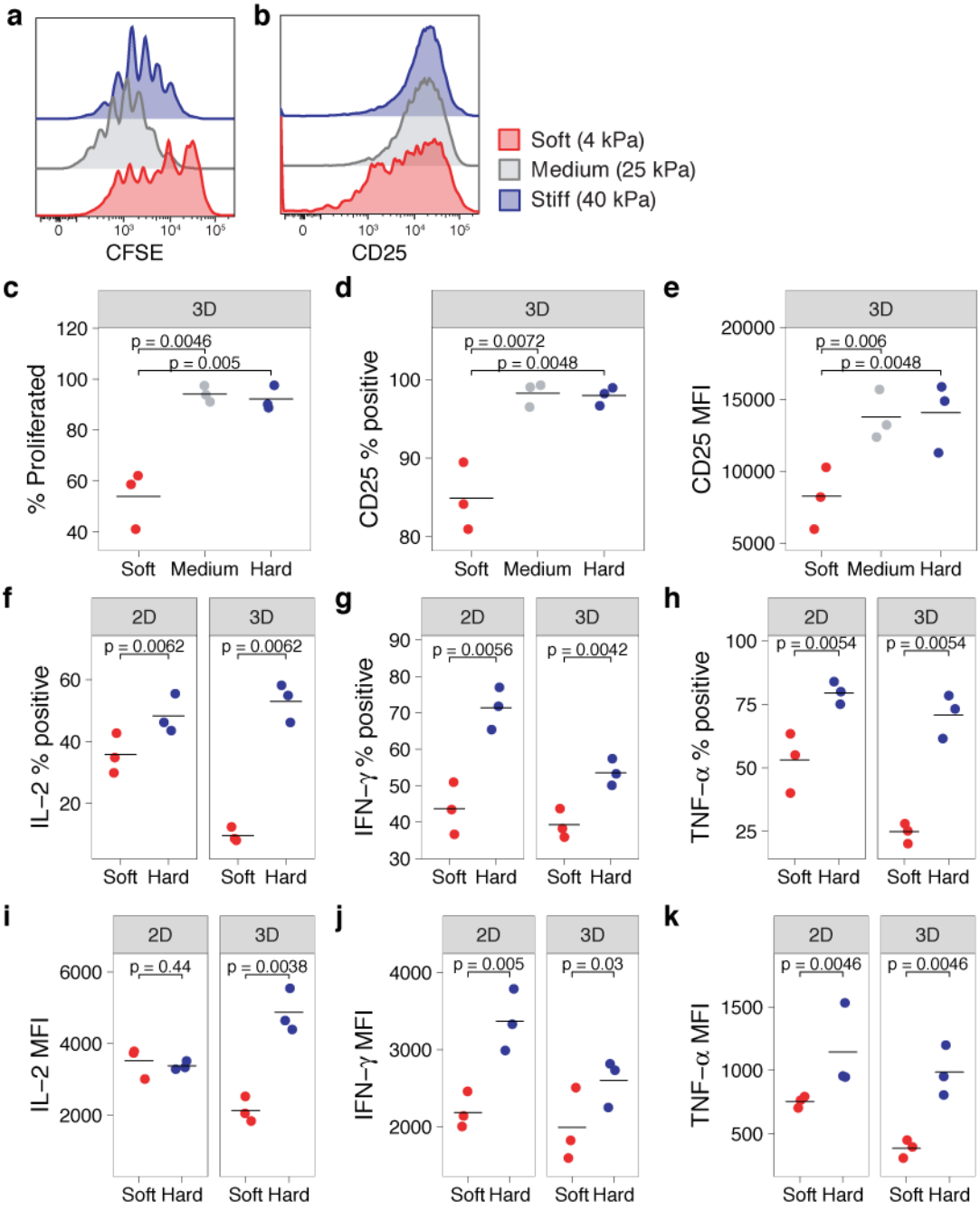

Figure 4.7. T-cell activation by microparticles is modulated by the stiffness of 3D scaffolds. CD4+ T cells co-cultured with artificial APC microparticles on 2D **(a)** or in 3D **(b)** scaffolds with different stiffnesses. **(a** and **b)** FACS analysis of cell division (CFSE dilution) and CD25 expression assayed at three days post-stimulation. **(c)** Percentage of cells that divided at least once**. (d)** Percentage of T cells upregulating CD25 and **(e)** mean fluorescence intensity (MFI) of CD25. **(f-h)** Percentage of T cells expressing the effector cytokines IL-2, IFN-γ, or TNF-

α. **(i-k)** Expression amount (MFI) of cytokines for those T cells making cytokines. Each dot represents one experiment.

As we did with real APCs, we studied whether cytokine expression by T cells is modulated by the mechanical microenvironment using the artificial APC microparticle beads. We found that the percentage of naïve T cells that expressed the effector cytokines was higher when activated in hard 3D scaffolds than those in softer scaffolds (**Fig. 4.7f-h,** example data in **Fig. 4.8**). The single-cell amount of cytokines expressed in these T cells was greater in the stiffer matrix than in a softer matrix (**Fig. 4.7i-k,** example data in **Fig. 4.8**) These results confirm that the augmentation of effector functions of T cells in stiffer 3D microenvironments as compared to softer environments is intrinsic to the T cell itself.

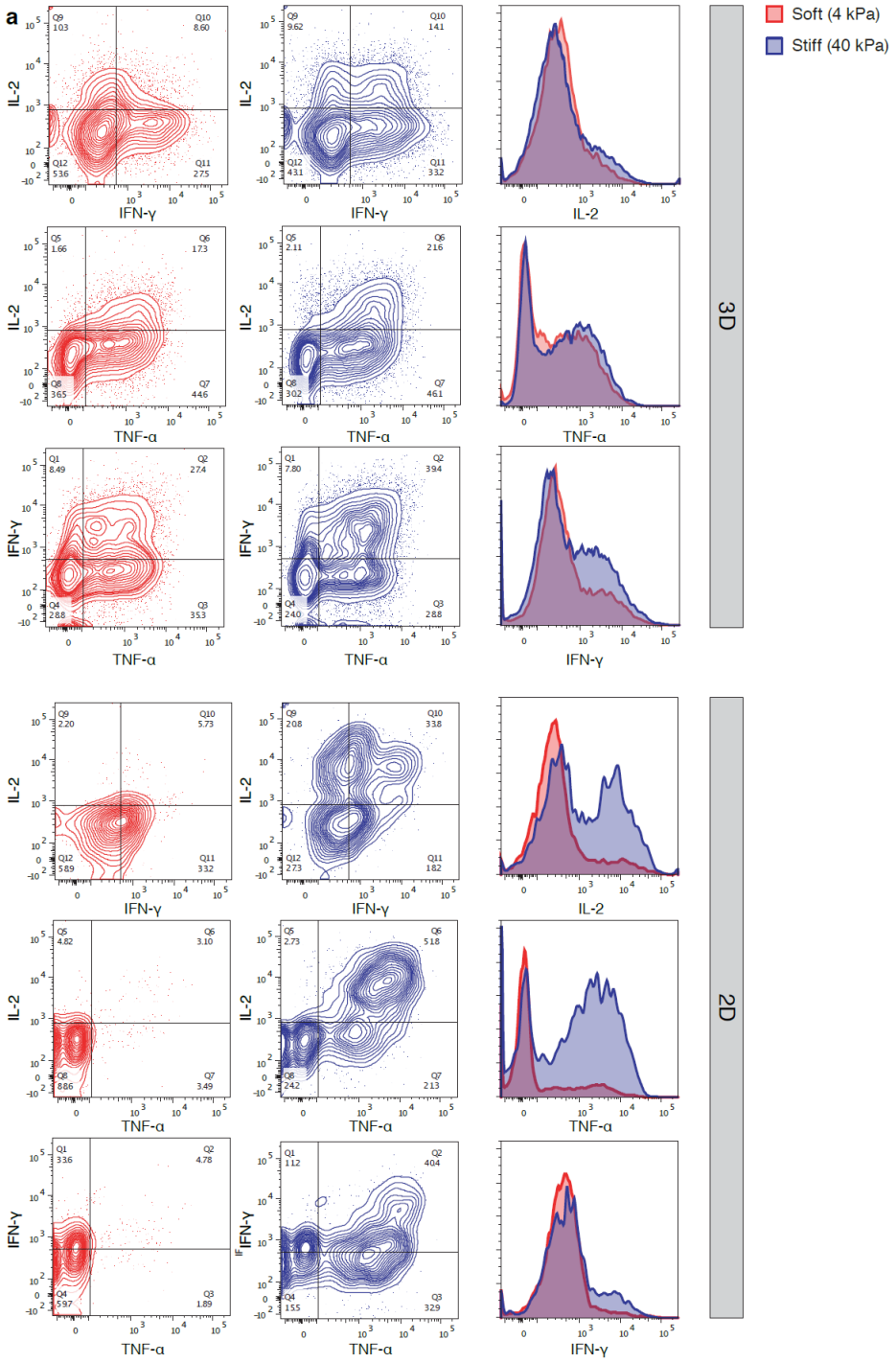

Figure 4.8. Effector responses of T cells upon co-culture with artificial antigen presenting cells is modulated by mechanical microenvironment. Effector responses of T cells upon co-culture with artificial antigen presenting cells was tested by measuring production of key cytokines in 3D scaffolds (a) and 2D cultures (b) in soft *vs.* hard matrices. Accompanies Fig. 7.

4.2.5 Immune synapses

Next, we studied the IS formed by T cells in our 3D alginate scaffolds and compared them to synapses formed on 2D hydrogels. We have previously shown that the size of the IS with antigen presenting cells correlates with T-cell activation [3]. The same has been shown when T cells interact with antibody-coated surfaces [10]. We seeded effector CD4+ T cells purified from spleens of OT-II TCR transgenic mice plus ovalbumin-loaded APCs into hard (40 kPa) and soft (4 kPa) 3D alginate scaffolds. To compare synapses formed in 3D with 2D, we prepared 2D alginate-RGD gels of the same mechanical stiffnesses. T cells and peptide-loaded APCs were placed onto these 2D substrates. As a control, we generated T cell-APC synapses by co-culturing them in pellet in a microtainer tube (see Methods). As a proxy for IS size, we measured the volume of the adhesion molecule LFA-1 that accumulated at the T cell-APC interface [3,17]. LFA-1 plays a crucial role in IS formation [17], and is not expressed on the B cells that we used as APCs in these experiments, making it an ideal protein to define the extent of the T-cell IS [3]. We also stained the T cell-APC conjugates for the cytoskeletal protein F-actin. We found that immune synapses of T cells formed in stiff matrices (**Fig. 4.9a-c**) were significantly larger than those formed in soft matrices (**Fig. 4.9d-f**). There were no notable differences in the ultra-structural organization of actin and LFA-1 in the region of the IS in comparing T cells encountering APCs in stiff (**Fig. 4.9g-i**) and soft matrices (**Fig. 4.9j-l**).

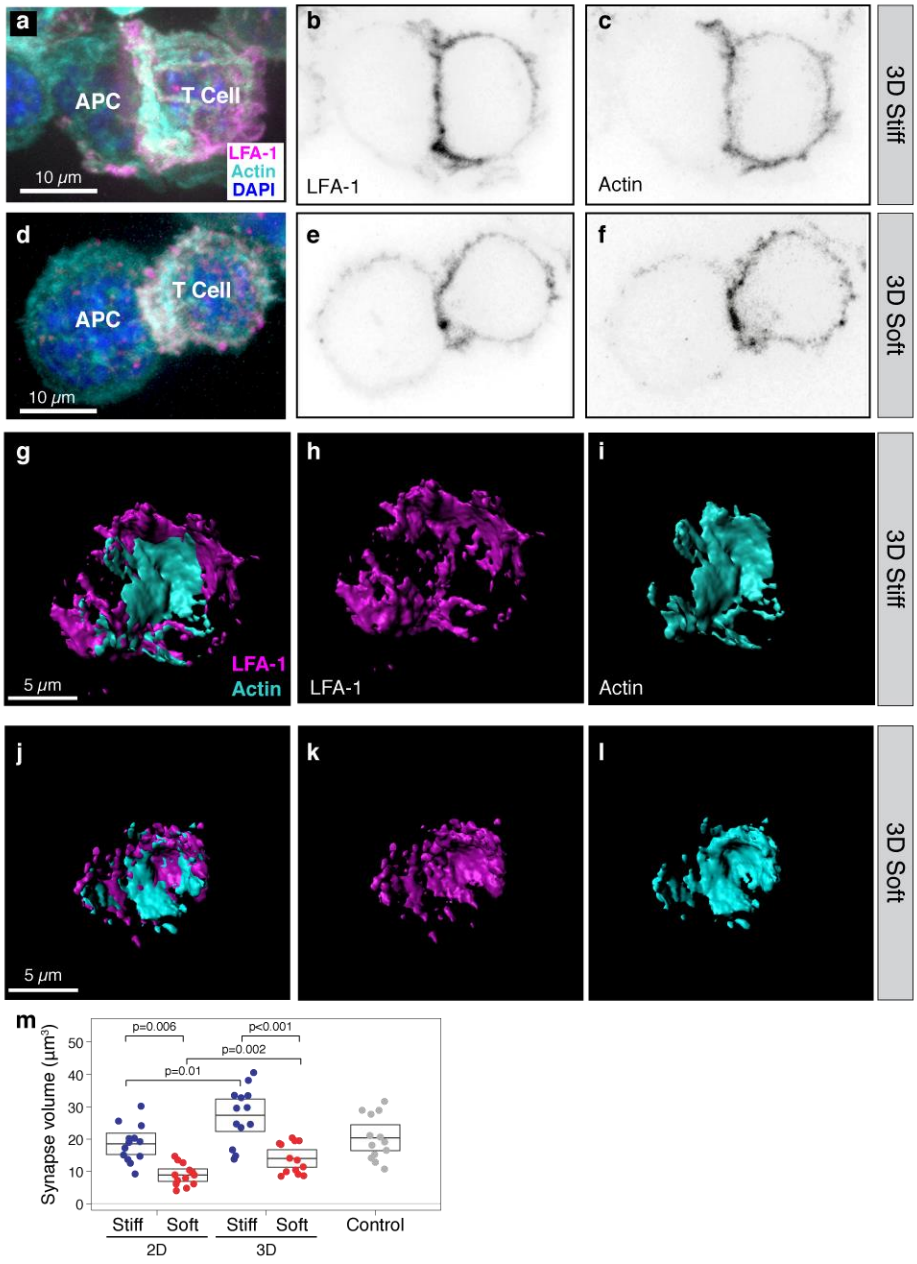

Figure 4.9. Immune synapse size is governed by the stiffness of 3D scaffolds. (a-f) 3D confocal fluorescence microscopy examples of immune synapses formed by T cells and APCs seeded into **(a-c)** stiff (40 kPa) or **(b-f)** soft (4 kPa) 3D scaffolds. LFA-1 is magenta and F-actin is cyan. Cell nuclei were stained with DAPI (blue). Scale bar is 10 μm (for **a-f**). **(g-l)** Reconstructed 3D surfaces in Imaris showing images of LFA-1 and Actin in the formed IS in stiff **(g-i)** and soft **(j-l)** scaffolds. Colocalization of reconstructed 3D surfaces given in **(g)** and **(j)**. **(m)** The volumes of LFA-1-positive voxels at T cell-APC interfaces were measured for IS formed under 2D or 3D conditions or control.

This finding held for T cells activated in 3D matrices or upon 2D substrates (2D and control synapses shown in **Fig. 4.9**). However, the IS formed under 3D conditions were significantly larger than those formed on 2D gels, offering a mechanistic explanation for the greater activation and proliferation seen in the prior experiments.

Because mechanosignaling through integrins has been the subject of many studies in lymphocytes and other cells, we sought to understand if the RGD peptide serving as an integrin ligand in our biomaterials was influencing T-cell activation. We prepared new stiff 3D matrices (~40 kPa) lacking RGD peptide and compared with those bearing RGD peptide. To eliminate any influence from integrin ligands on APCs, we used artificial APC beads as the stimulus for T cells, as above. We found that T cells were more activated in substrates bearing RGD peptide than those without (**Fig. 4.10**).

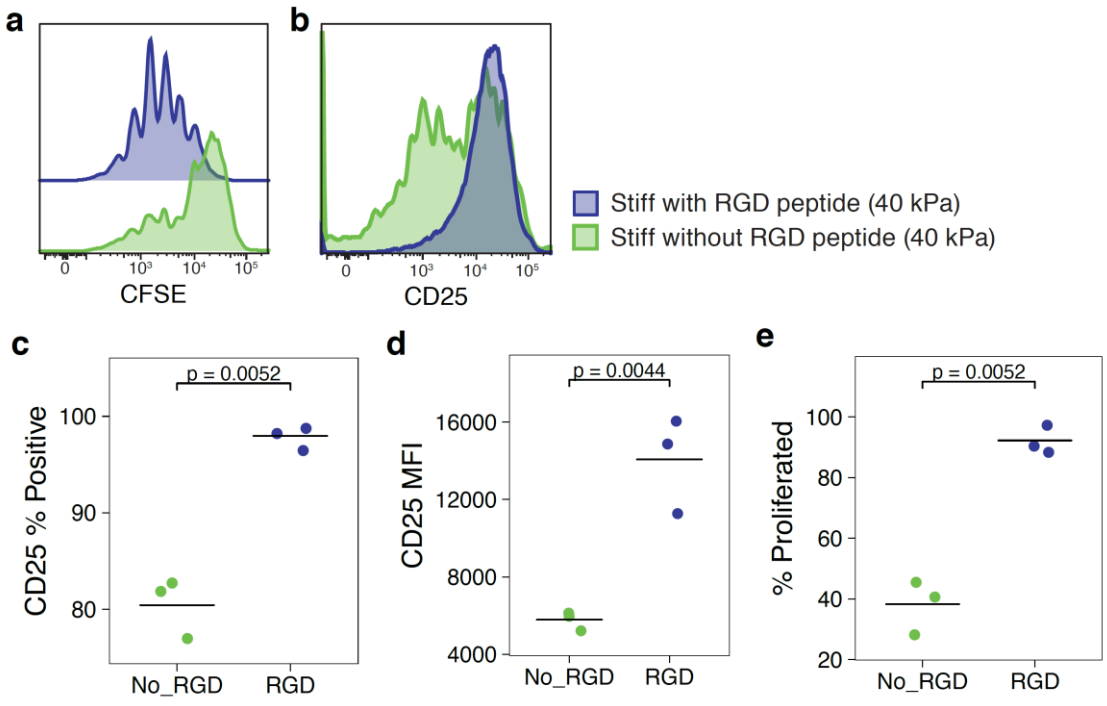

Figure 4.10. RGD presence affects T cell proliferation and activation. FACS analysis of cell division (CFSE dilution) **(a)** and CD25 expression **(b)** of CD4+ T cells co-cultured with artificial APC beads as stimulus in presence or absence of RGD peptide in the 3D hard scaffold.

(c) Percentage of CD25 positive cells **(d)** mean fluorescence intensity (MFI) of CD25 and **(e)** percentage of cells that divided at least once. Cells were assayed at three days post-stimulation.

The T cells in an environment lacking RGD were even less activated than those cultured in soft 2D or 3D environments with RGD (c.f. **Fig. 4.10b**), despite the ample presence of stimulatory beads. This experiment suggests that T cell responses in 3D environments may lost if there is no tethering and/or ligation of integrins. Notably, the integrin signal provided by RGD here is coming in *trans* from the activation signal on beads, suggesting that T cells can integrate signals from multiple distinct spatial sources. Mechanical tethering of ICAM-1, a major integrin ligand on APCs, has been shown to augment T cell activation through adhesive maturation of the integrin LFA-1 and signaling [18]. In addition, the impact of LFA-1 ligation has been well established as an important signal for polarization, clustering, activation, and effector activities of T cells [19–22], but disentangling the effects of these other signaling pathways versus mechanics was not attempted here.

Taken together, these results show that T cells have larger immune synapses with APCs, become more activated, and show more proliferation when encountering antigen in a mechanically stiff 3D microenvironment. Notably, the effector T cells in these experiments were previously, commonly activated before seeding into the various environments, and thus any differences in the subsequent interactions with APCs captured in these synapses were not due to differences in activation. Rather, we speculate these differences represent changes to the cytoskeletal adaptivity of T cells [3] due to the micromechanical environment.

4.3. Conclusion

In vivo, T cells are activated and carry out their effector functions in a 3D tissue environment comprising cells as well as polymeric matrices of collagen, hyaluronan and other polymers. However, the vast majority of *in vitro* experiments - which form the basis for much of

our knowledge of T-cell biology - are carried out on plastic plates that are orders of magnitude stiffer than any biologically relevant substance. This practice continues even though it is accepted that the stiffness of the extracellular substrate affects the function of many different cell types [23]. Moreover, recent work has established that slow-moving cells like fibroblasts can sense time-dependent viscoelasticity independently from the elastic modulus of a substrate [24] and can even exploit viscoelasticity of materials to facilitate migration [25]. Whether this level of time-dependent mechanosensing occurs in highly motile cells like T cells has not been demonstrated.

Recently, several groups have demonstrated that the T-cell receptor itself senses mechanical forces through the development of a catch bond between the TCR and the pMHC [26]. Our group and others have further detailed the mechanical forces acting on the TCR to trigger activation [27,28]. We showed that the forces needed to trigger the TCR arise from the stereotypical pushing and pulling movements of the T cell itself after initial triggering. The pushing forces, when visualized at the cellular scale, are seen as an early, transient spreading of the contact area, allowing for greater contact between the T cell and APC in the immune synapse and enabling engagement of more TCRs [28,29]. When measured by AFM [28], micropillars [30], or traction force microscopy [8], the subsequent pulling forces generated by single T cells range from 100 pN to 1 nN. On the single-TCR level, these forces were found by DNA tension probes to range from 10-20 pN [31], which allows for identification of potent ligands and, subsequently, activation of the mechanosensing capability of the TCR. Mechanical contacts between the TCR the MHC, in addition to other key molecules like integrins and their ligands, support a nuanced view of TCR triggering that goes well beyond simple ligation and entails the actin cytoskeleton and a variety of signals [32].

The TCR is embedded in a fluid membrane buttressed by a complex cytoskeletal scaffold. Thus, anchoring of pMHC on a stiff substrate allows the TCR to experience a greater force when these molecules interact. Indeed a number of groups have investigated the role of anchoring TCR

ligands on various substrate stiffnesses using 2D synthetic polymers such as PDMS and polyacrylamide [4,5,9]. Across many experimental modalities, the finding has been consistent: within the physiological range, the stiffer the anchoring, the greater the T-cell activation. Our work here is distinguished from these prior papers because our T cells were activated by antigen borne on antigen presenting cells rather than by antigen anchored directly to the stiff or soft substrate. These data could support the notion that the APC may convey some microenvironmental environmental information to T cells. Thus, to discern whether APC's role is paramount, we tested T-cell activation here using soft, artificial APC beads that are not influenced by the microenvironment, and T-cell activation was still augmented in the mechanically stiff 3D context as compared to the soft regime. Taken together, T cells can sense 3D environmental micromechanical stiffness whether the stimulatory signal comes from APC or artificial APC beads.

The mechanism by which T cells sense mechanics is as yet unclear; however, recent work supports a role for integrin signaling. Artificially increasing the tethering of the integrin ligand ICAM-1 on the APC side of the synapse facilitates activation of T cells, matures LFA-1, and influences the T cell cytoskeleton [18,33]. Our own work here supports that integrin binding is important to mechanosensing in 3D. It is well known that the integrin LFA-1 on T cells binds to its ligand ICAM-1 on APCs. Anchoring of ICAM-1 to the APC cytoskeleton enhances the molecular forces acting on LFA-1, leading to the unfolding and "maturation" of the LFA-1 receptor into a higher affinity state for its ligand. Thus, forces acting on the T cell through the ICAM-1-LFA-1 system offer a route to co-stimulation that is independent of TCR triggering [18,34]. Another mechanism has been proposed to explain how mechanical stiffness is sensed through anchoring of LFA-1 by ICAM-1. Constrained, mature LFA-1 reduces the catalytic activity of the inhibitory phosphatase SHP-1 through interactions with the actin cytoskeleton and its centripetal flow [35]. Whether integrin signaling is paramount in mechanosensing is still unclear. Another route by which T cells could sense forces is through microenvironmental stiffness acting on their

cytoskeleton or nuclear envelope [23,36]. This kind of mechanosensing would not act through the TCR or LFA-1, but rather through other intracellular sensors or through the cytoskeleton itself [37].

Optimal methods to exploit the mechanical properties of the 3D microenvironment on T-cell activation are lacking. A recent work showed that T cells sense differences between 2D and 3D collagen gels as well as high and low density 3D collagen gels, but this biomaterial unfortunately couples changes in stiffness with changes in porosity [38]. Another recent work compared 3D polystyrene mesh and Matrigel (a heterogeneous, nanoporous 3D matrix comprising collagens, laminin, proteoglycans and other ECM proteins) to 2D culture and found an enhancement in T-cell proliferation in 3D cultures [39]. 3D porosity has a major impact on motility and cytoskeletal regulation, and thus the use of Matrigel or collagen confounds studies of highly motile cells like T cells. Difficulties in tuning the stiffness of 3D biomaterials without dramatically altering their porosity has been a roadblock in pursuing a reductionistic understanding of the role of tissue mechanics [12]. Regardless, the potential scientific and clinical applications are compelling: encapsulation and therapeutic delivery of T cells in hydrogels offers much potential for cancer immunotherapy and other adoptive cell therapies [40–42].

The development here of scaffolds of tunable stiffness and consistent microporosity thus represents an advance for T-cell biology. In summary, this work shows that T cells can sense their 3D mechanical environment.

4.4. Experimental Materials and Methods

4.4.1 Chemicals and Biologicals

Unless noted otherwise, all chemicals were purchased from Sigma-Aldrich, Inc. (St. Louis, MO). All glassware was cleaned overnight using concentrated sulfuric acid and then thoroughly rinsed with Milli-Q water. All the other cell culture reagents, solutions, and dishes were obtained from Thermo Fisher Scientific (Waltham, MA), except as indicated otherwise.

4.4.2 Scaffolds

To form the scaffolds, we first oxidized the alginate (Mw ~250 kDa, high G blocks; Novamatrix UP MVG, FMC Biopolymer, Rockland, Maine) with sodium periodate (1.5 %), overnight at room temperature, then quenched the reaction by dropwise addition of ethylene glycol for 45 min. We then dialyzed the solution (MWCO 3.5 kDa) against deionized water for 3 d followed by lyophilization. Afterward, the alginate was dissolved in MES (MES 150 mM, NaCl 250 mM, pH 6.5) and covalently conjugated to RGD-containing peptide (GGGGRGDY; GenScript USA Inc., Piscataway, NJ) using carbodiimide chemistry (NHS/EDC). The reaction was continued for 24 h followed by dialysis (MWCO 20 kDa) and lyophilization. This alginate-RGD complex in PBS was then cross-linked via calcium sulfate solution. The gels were casted in desired 24- or 96-well plates followed by two overnight washes to get rid of extra calcium ions and then used as 2D matrices. For 3D structures these same scaffolds were frozen at -80 °C, lyophilized for 3 d, and stored at 4 °C before cellular studies.

We prepared an array of different alginate formulations by varying either the polymer content or the amount of crosslinker (here $CaSO_4$). To measure the mechanical stiffness of our gels we used Instron 5542 mechanical tester and all the samples were tested at a rate of 1 mm/min. The Young's modulus was then calculated from the slope of the linear region that corresponds with 0–10% strain. The softer gel comprised alginate 1.25% with 10 mM $CaSO_4$. The medium gel comprised alginate 2.5%- and 30-mM calcium. The stiffer gel comprised alginate 2.5% with 40 mM $CaSO_4$.

Scanning electron microscopy (SEM) images of the gels were taken to see the cross-sectional microstructure and porosity of the alginate-RGD scaffolds. The lyophilized scaffolds were freeze-fractured (using liquid nitrogen) for cross-sectional images. The scaffolds were sputtered with iridium (South Bay Technology Ion Beam Sputtering) prior to imaging with a ZEISS Supra 40VP scanning electron microscope (Carl Zeiss Microscopy GmbH). The sizes of

pores from different parts of the SEM images were then measured and analyzed using ImageJ software (NIH).

Preparation and characterization of artificial APC microparticles

Alginate microparticles were formed using microfluidic platform according to our previous report [16]. Briefly, a mixture of alginate solution (1% w/v) and 4-arm PEG hydrazide (5 kDa, Creative PEG work, Chapel Hill, NC) (5 mM) was used as the inner aqueous phase. Mineral oil (plus 10 wt% Span 80) was used as the continuous phase. To form 4.5 μm alginate-based microparticles, 2 and 28 μL/min were used for the alginate and oil flows, respectively. Formed droplets were collected in a calcium bath (100 mM $CaCl_2$) and left at room temperature for 45 min for ionic crosslinking. The microgels were washed and centrifuged twice at 15,000 rpm for 10 min before further incubation in a solution containing hydroxybenzotriazole (HOBt) and 1-ethyl-3-(3-dimethylaminopropyl) carbodi-imide (EDC) for 2 h. Microparticles were then dialyzed against deionized water for three days to remove any residual and unreacted reagents, followed by freezing at -20 °C and lyophilization. Particles were then resuspended in deionized water for further use.

For the preparation of antibody-conjugated microparticles, anti-CD3 (clone 2C11; Bio-X-Cell) and anti-CD28 (clone 37.51; Bio-X-Cell) were covalently conjugated to the surface of particles using EDC/NHS chemistry. After activation of particle's carboxylic groups for 10 min, microparticles were washed with PBS twice and then antibodies were added to the particles and incubated under gentle stirring at 4 °C overnight. The protein-functionalized microparticles were then separated from the solution and washed several times. Unreacted functional groups were quenched by washing samples in Tris buffer (100 mM, pH 8). A 10-fold dilution of the conjugation density that is used in conventional plate-bound stimulation method for T-cell activation was picked as the final conjugation density for beads. Micro-BCA assay was used to quantify total amount of surface conjugated antibodies according to the manufacturer's protocol.

To immobilize beads to the scaffolds, the freeze-dried scaffolds were activated with EDC/NHS for 15 min. Then the scaffolds were washed twice with PBS (supplemented with 0.42 mM $CaCl_2$) before addition of 5×10^6 artificial APC microparticles. APC microparticles and scaffolds were then incubated at 4 °C for 4 h. Unbound microparticles were then washed away and 5×10^6 T cells were added to the scaffolds and cultured for 5 days to study their effector functions.

4.4.3 T-cell isolation and activation

All *in vitro* experiments were conducted in accordance with UCLA's institutional policy on humane and ethical treatment of animals following protocols approved by the Animal Research Committee. Five- to eight-week-old OT-II TCR transgenic mice (Jackson Labs) were used for all experiments. Cell-culture media was RPMI supplemented with 10% heat-inactivated FBS, 1% penicillin/streptomycin, 1% sodium pyruvate, 1% HEPES buffer, 0.1% μM 2-mercaptoethanol. CD4+ T cells were purified using negative selection enrichment kits (Stem Cell Technologies).

In vitro activation of CD4+ T cells was performed by culturing 1×10^6 cells/mL in tissue culture-treated 24-well plates that were pre-coated with anti-CD3 (clone 2C11; Bio X Cell) at a concentration of 10 μg/mL plus addition of 2 μg/mL soluble anti-CD28 (clone 37.51; Bio X Cell).

4.4.4 Immune synapses

To form *in vitro*, 2D or 3D immune synapses we used T cells from OT-II TCR transgenic mice (Jackson Labs) as above. T cells were extracted from spleens and CD4+ T cells were then purified using EasySep immunomagnetic negative selection (Stem Cell Technologies). Cells were then activated on plates as above. Effector T cells were then collected from wells and allowed to proliferate in interleukin-2 (IL-2, BRB Preclinical Repository, NCI, NIH)-containing medium (50 U/mL), prior to being used for experiments on days 3 to 5 of incubation. The I-A^b-bearing B-cell lymphoma line LB27.4 was purchased from the American Type Culture Collection and used as

APCs for immune synapses. LB 27.4 cells were incubated with Ova peptide (1 μM) for several hours prior to co-culture with T cells.

For synapse formation on 2D or 3D hard vs. soft substrates. Effector CD4+ T cells were mixed with antigen-pulsed APCs and then immediately seeded into 2D or 3D matrices. Then, for experiments in a 3D context, a mild centrifugation was performed to help with dispersion of the cells within the scaffolds and incubated at 37 °C for 30 min. Afterward, to evaluate just the synapses that were formed within the scaffold and not the ones that have been formed on the plastic bottom of the wells we physically transferred the scaffolds into new wells. Following transfer, they were fixed immediately with 4% PFA for 30 min. Then the gels were lysed using EDTA (50 mM) and alginate lyase (porcine, Sigma Aldrich, 3.4 mg/mL). After digestion of the scaffold and recovery of the cells, followed by three centrifugation rounds to remove the dissolved polymer. Cells then were seeded on 8 well-plate Labtek II chamber pre-modified with Poly-D-lysine. The rest of staining and imaging are detailed below.

Control experiments. A ratio of one peptide-pulsed LB27.4 APC cell to one T cell were mixed, followed by centrifugation for 1.5 min at 500 x *g* in a 1.5 mL Eppendorf microfuge tube. This pellet was then incubated at 37 °C for 15 min. Afterwards the pellet was gently pipetted and plated into 8-well Poly-D-lysine-coated Labtek II chambers. The chamber was then centrifuged for 1 min at 50 x *g*.

Staining and imaging. The supernatant was removed from Labtek chambers, wells were washed once with PBS and fixed with 4% PFA. Then to permeabilize cells for intracellular staining, 0.1% Triton X-100 in PBS was incubated with cells for 5 min and blocked in 5% donkey serum for at least an hour. To stain the cells we used antibodies against LFA-1 (clone I21/7) and 4G10 with Alexa Fluor 568–conjugated phalloidin (Life Technologies) and DAPI. After several washes, wells were incubated with fluorescently conjugated secondary antibodies (Jackson ImmunoResearch). Eventually, samples were covered with Fluoromount-G with DAPI (eBioscience) and stored at 4

°C before imaging. For confocal imaging we used a 100× Plan Apo numerical aperture (NA) 1.4 objective (Nikon). Synapses were measured based on LFA-1 and actin accumulation at the T cell–APC interface as calculated in ImageJ/Fiji.

4.4.5 Flow cytometry

For flow cytometry analysis, antibodies to mouse CD4, CD25 (clone PC61.5), CD44 (clone IM7), were purchased from eBioscience, BioLegend, or BD Biosciences. To study proliferation behavior of T-cell responses during various treatments their expansion was measured by 5-(and-6)-carboxyfluorescein diacetate, succinimidyl ester (CFSE) dilution. For CFSE dilution experiments, 5×10^5 naive CD4+ T cells were labeled with 2 μM CFSE for 13 min, followed by two washes and then incubation with splenocytes. Splenocytes were extracted from the spleen of wild type C57Bl/6 mice. Then the cells were incubated in ACK lysis buffer (Gibco) for 5 min at room temperature to remove red blood cells. The remaining cells were then treated with ova peptide as above to present to T cells. Trypan Blue was purchased from Calbiochem. Cells were analyzed on a Cytek DxP10 flow cytometer using FlowJo software (Treestar/BD).

For intracellular cytokine staining (ICCS), cells were fixed with cold 4% paraformaldehyde (PFA) for 20 min at room temperature and then permeabilized with 0.5% saponin for 10 min before blocking with PBS + 1% BSA + 5% donkey serum and staining with appropriate antibodies at 1:100 dilution. Cells were washed and analyzed by flow cytometry as above. The following antibodies were used for ICCS from Biolegend: IL-2 (clone JES6-5H3, APC, Cat #503808); TNF-α (clone MP6-XT22, PE, Cat #506313), IFN-ɣ (clone XMG1.2, BV421, Cat #505814); mouse IgG1 isotype control (clone MOPC-21, Cat #400112, Cat #400135); mouse IgG2a isotype control (clone MOPC-173, Cat #558055, Cat #558053).

4.4.6 Live-cell imaging

For the experiments regarding to the velocity measurement of T-cell migration on 2D gels or within 3D scaffolds, CD4+ T cells were stained with CellTrace CFSE (1 μM) as per the

manufacturer's protocol (Life Technologies). The scaffold was mounted in a Delta T dishes (Bioptechs), which kept the media warmed to 37 °C. For experiments in presence of LB 27.4 cells as APCs, B cells were loaded with ovalbumin peptide prior to introduction to T cells and then seeded in matrices. Fields were imaged every 12 or 15 s for 10-20 min with a 40× Plan Fluor NA 0.6 extra-long working distance objective (Nikon). Imaris software (Bitplane/Oxford Instruments) was used to track CellTrace CFSE-loaded T cells over time. Velocities and other statistics were exported from Imaris and analyzed in R.

4.4.7 Statistical analysis

We employed permutation testing for all statistical comparisons including synapse size, proliferation, and activation markers. We used the permutationTest2 function of the "resample" package of R to calculate p values and determine the 95% confidence intervals, performing 50 to 100,000 permutations. Horizonal lines in all figures show the bootstrapped mean and boxes show the 95% confidence interval calculated from bootstrapping using the CI.t function of the "resample" package.

4.5. References:

1. Dustin, M. L. Visualization of cell-cell interaction contacts: Synapses and kinapses. *Self. Nonself.* **2**, 85–97 (2011).
2. Burkhardt, J. K., Carrizosa, E. & Shaffer, M. H. The actin cytoskeleton in T cell activation. *Annu. Rev. Immunol.* **26**, 233–59 (2008).
3. Thauland, T. J., Hu, K. H., Bruce, M. A. & Butte, M. J. Cytoskeletal adaptivity regulates T cell receptor signaling. *Sci. Signal.* **3737**, 1–11 (2017).
4. Judokusumo, E., Tabdanov, E., Kumari, S., Dustin, M. L. & Kam, L. C. Mechanosensing in T lymphocyte activation. *Biophys. J.* **102**, L5-7 (2012).
5. O'Connor, R. S. *et al.* Substrate rigidity regulates human T cell activation and proliferation. *J. Immunol.* **189**, 1330–9 (2012).

6. Tabdanov, E. *et al.* Micropatterning of TCR and LFA-1 ligands reveals complementary effects on cytoskeleton mechanics in T cells. *Integr. Biol. (Camb).* **7**, 1272–84 (2015).

7. Husson, J., Chemin, K., Bohineust, A., Hivroz, C. & Henry, N. Force generation upon T cell receptor engagement. *PLoS One* **6**, e19680 (2011).

8. Hui, K. L., Balagopalan, L., Samelson, L. E. & Upadhyaya, A. Cytoskeletal forces during signaling activation in Jurkat T-cells. *Mol. Biol. Cell* **26**, 685–95 (2015).

9. Saitakis, M. *et al.* Different TCR-induced T lymphocyte responses are potentiated by stiffness with variable sensitivity. *Elife* **6**, e23190 (2017).

10. Wahl, A. *et al.* Biphasic mechanosensitivity of T cell receptor-mediated spreading of lymphocytes. *Proc. Natl. Acad. Sci. U. S. A.* 1–6 (2019) doi:10.1073/pnas.1811516116.

11. Basu, R. *et al.* Cytotoxic T Cells Use Mechanical Force to Potentiate Target Cell Killing. *Cell* **165**, 100–110 (2016).

12. Vining, K. H. & Mooney, D. J. Mechanical forces direct stem cell behaviour in development and regeneration. *Nat. Rev. Mol. Cell Biol.* **18**, 728–742 (2017).

13. Buxboim, A., Ivanovska, I. L. & Discher, D. E. Matrix elasticity, cytoskeletal forces and physics of the nucleus: how deeply do cells 'feel' outside and in? *J. Cell Sci.* **123**, 297–308 (2010).

14. Bauer, C. A. *et al.* Dynamic Treg interactions with intratumoral APCs promote local CTL dysfunction. *J. Clin. Invest.* **124**, 2425–2440 (2014).

15. Martinez, G. J. *et al.* The Transcription Factor NFAT Promotes Exhaustion of Activated CD8+ T Cells. *Immunity* **42**, 265–278 (2015).

16. Majedi, F. S. *et al.* Augmentation of T-Cell Activation by Oscillatory Forces and Engineered Antigen-Presenting Cells. *Nano Lett.* 580704 (2019) doi:10.1021/acs.nanolett.9b02252.

17. Grakoui, A. *et al.* The immunological synapse: a molecular machine controlling T cell activation. *Science* **285**, 221–7 (1999).

18. Comrie, W. A., Li, S., Boyle, S. & Burkhardt, J. K. The dendritic cell cytoskeleton promotes T cell adhesion and activation by constraining ICAM-1 mobility. *J. Cell Biol.* **208**, 457–473 (2015).

19. Dustin, M. L. & Springer, T. A. Lymphocyte function-associated antigen-1 (LFA-1)

interaction with intercellular adhesion molecule-1 (ICAM-1) is one of at least three mechanisms for lymphocyte adhesion to cultured endothelial cells. *J. Cell Biol.* **107**, 321–31 (1988).

20. Suzuki, J. I., Yamasaki, S., Wu, J., Koretzky, G. A. & Saito, T. The actin cloud induced by LFA-1-mediated outside-in signals lowers the threshold for T-cell activation. *Blood* **109**, 168–175 (2007).

21. Contento, R. L. *et al.* Adhesion shapes T cells for prompt and sustained T-cell receptor signalling. *EMBO J.* **29**, 4035–4047 (2010).

22. Sabatos, C. A. *et al.* A synaptic basis for paracrine interleukin-2 signaling during homotypic T cell interaction. *Immunity* **29**, 238–48 (2008).

23. Discher, D. E., Janmey, P. & Wang, Y.-L. Tissue cells feel and respond to the stiffness of their substrate. *Science* **310**, 1139–43 (2005).

24. Chaudhuri, O. *et al.* Hydrogels with tunable stress relaxation regulate stem cell fate and activity. *Nat. Mater.* **15**, 326–334 (2016).

25. Wisdom, K. M. *et al.* Matrix mechanical plasticity regulates cancer cell migration through confining microenvironments. *Nat. Commun.* **9**, (2018).

26. Liu, B., Chen, W., Evavold, B. D. & Zhu, C. Accumulation of dynamic catch bonds between TCR and agonist peptide-MHC triggers T cell signaling. *Cell* **157**, 357–368 (2014).

27. Kim, S. T. *et al.* The alphabeta T cell receptor is an anisotropic mechanosensor. *J. Biol. Chem.* **284**, 31028–37 (2009).

28. Hu, K. H. & Butte, M. J. T cell activation requires force generation. *J. Cell Biol.* **213**, 535–542 (2016).

29. Negulescu, P. A., Krasieva, T. B., Khan, A., Kerschbaum, H. H. & Cahalan, M. D. Polarity of T cell shape, motility, and sensitivity to antigen. *Immunity* **4**, 421–30 (1996).

30. Bashour, K. T. *et al.* CD28 and CD3 have complementary roles in T-cell traction forces. *Proc. Natl. Acad. Sci. U. S. A.* **111**, 2241–6 (2014).

31. Liu, Y. *et al.* DNA-based nanoparticle tension sensors reveal that T-cell receptors transmit defined pN forces to their antigens for enhanced fidelity. *Proc. Natl. Acad. Sci. U. S. A.* **113**, 5610–5 (2016).

32. Blumenthal, D. & Burkhardt, J. K. Multiple actin networks coordinate

mechanotransduction at the immunological synapse. *J. Cell Biol.* **219**, 1–12 (2020).

33. Jankowska, K. I. *et al.* Integrins modulate T cell receptor signaling by constraining actin flow at the immunological synapse. *Front. Immunol.* **9**, 1–19 (2018).

34. Comrie, W. A. & Burkhardt, J. K. Action and Traction: Cytoskeletal Control of Receptor Triggering at the Immunological Synapse. *Front. Immunol.* **7**, 1–25 (2016).

35. Ben-Shmuel, A., Joseph, N., Sabag, B. & Barda-Saad, M. Lymphocyte mechanotransduction: The regulatory role of cytoskeletal dynamics in signaling cascades and effector functions. *J. Leukoc. Biol.* 1–13 (2019) doi:10.1002/JLB.MR0718-267R.

36. Buxboim, A. *et al.* Coordinated increase of nuclear tension and lamin-A with matrix stiffness outcompetes lamin-B receptor that favors soft tissue phenotypes. *Mol. Biol. Cell* **28**, 3333–3348 (2017).

37. Totaro, A., Panciera, T. & Piccolo, S. YAP/TAZ upstream signals and downstream responses. *Nat. Cell Biol.* **20**, 888–899 (2018).

38. Wang, P. *et al.* WDR5 modulates cell motility and morphology and controls nuclear changes induced by a 3D environment. *Proc. Natl. Acad. Sci. U. S. A.* **115**, 8581–8586 (2018).

39. Pérez Del Río, E., Martinez Miguel, M., Veciana, J., Ratera, I. & Guasch, J. Artificial 3D Culture Systems for T Cell Expansion. *ACS Omega* **3**, 5273–5280 (2018).

40. Monette, A., Ceccaldi, C., Assaad, E., Lerouge, S. & Lapointe, R. Chitosan thermogels for local expansion and delivery of tumor-specific T lymphocytes towards enhanced cancer immunotherapies. *Biomaterials* **75**, 237–249 (2016).

41. Stephan, S. B. *et al.* Biopolymer implants enhance the efficacy of adoptive T-cell therapy. *Nat. Biotechnol.* (2015) doi:10.1038/nbt.3104.

42. Smith, T. T. *et al.* Biopolymers codelivering engineered T cells and STING agonists can eliminate heterogeneous tumors. *J. Clin. Invest.* **127**, 2176–2191 (2017).

Chapter 5.

Bioengineered 3D Scaffolds to Educate and Expand Tumor Fighting T cells

5.1. Introduction

Despite recent successes in cancer immunotherapies that emphasize high therapeutic potency in treating patients with progressive tumors, significant challenges, including insufficient activation and eventual exhaustion of effector T cells as well as suppression of their effector responses in the tumor microenvironment; and inadequate ability to expand tumor-specific T cell ex vivo hinder the potential of T cell therapies, especially in solid tumors. Most of the current immunotherapy approaches aim to facilitate T cells to fight tumors and provoke their infiltration. Some of the commonly used strategies include blocking inhibitory receptors such as anti PD-1 and anti CTLA-4 while others include evoking cytotoxic T lymphocyte (CTL) responses such as chimeric antigen receptor (CAR)-T cell therapies and adoptive cell transfer (ACT) approaches. Despite their revolutionary approaches for hematopoietic cancers, potency of these methods and the need for expanding tumor-specific T cells is a need not yet satisfactorily met for solid tumor therapy. One of the major flaws associated with checkpoint inhibitor therapies (CPI) and chemokine therapies such as IL-2 or IL-12 that hampers their clinical translation is their administration route and all the immune-related adverse events that are affiliated with it. In this regard few attempts have been made towards making the deliveries more targeted. Nanogel "backpacks" have demonstrated the release of cytokines to T cells.[1] However, the continual release of cytokines risks systemic exposure, side effects, and compromise of a limited supply of cytokine. Collagen-binding domain fused to IL-12 is another example that emphasizes the impact of tumor targeting and prolongation of cytokine release in the tumor stroma.[2] Though, the IV administration in this case especially puts patients with cardiovascular disease at risk. The other

matter in these systems is that the rate of release of cytokines is not well controlled. We have previously shown that the rate at which cytokines are delivered to CD8+ T cells impacts their differentiation and effector functionality.[3,4] To tackle the issues related to ACT and improve *ex vivo* activation and expansion of tumor-reactive T cells several groups have developed antigen-presenting cell (APC) mimetic scaffolds [4–6] that has proven to be two to ten folds more potent in the polyclonal expansion of T cells compared to the commercial Dynabeads. Yet they lack the ability to manipulate tumor microenvironment so that it favors formation of tumor fighting T cells.

Another major challenge that cold tumors face is poor infiltration of effector T cells and a high ratio of T regulatory cells (Tregs) to effector CD8+ T cells. Transforming growth factor b (TGF-b) is known to be the key factor in the induction of T regs from helper T cells drawn to the tumor, which then promotes cancer growth and metastasis. TGF-β also potently inhibits cytotoxic T cells in the tumor microenvironment[7] and has, therefore, become an exciting target in the enhancement of immunotherapy.[8] However, systemic TGF-β inhibition in preclinical models has shown major adverse effects on the cardiovascular, gastrointestinal, and skeletal systems, owing to the pleiotropic effects that TGF-β plays across the body.[9] The release of TGF-β inhibitors by injected nanoliposomes was shown to reduce metastases[10] but did not show a local impact in regulatory T cells.

Moreover, mechanical stiffness of the niche in which T cells home and face antigens makes a difference on their fate (our biomaterials paper) which is a missing piece in most of the in vivo studies. Here we focused our attempts on developing a platform that holds the key to solve the above-mentioned challenges by offering a “synthetic lymph node” niche proximally to the tumor for supporting transferred T cells while enhancing their infiltration and cytotoxic capabilities. Our implantable, porous synthetic lymph node serves as a home for the recruitment of endogenous tumor resident T cells and serves them with the activation clues while juicing them up with

necessary cytokines/chemokines at controlled rates. The mechanical stiffness of our biomaterial is optimized to mimic that of lymph nodes. We believe the provided niche offers a home to T cells either for ACT purposes or for tumor resident T cells to get the required training against tumor cells and facilitates their fight by increasing their number via proliferation signals and blocking the formation of suppressor T cells locally. This flexible platform holds high promises for localized immunomodulation and treatment of cancer.

5.2. **Results and Discussion**

5.2.1. **Artificial antigen presenting cells (aAPCs).**

Recently we have shown that presence of heparin can significantly increase the affinity of positively charged proteins, isoelectric point (pI) >7.5.[11,12] Here, heparin-functionalized mesoporous silica microparticles (5 μm in diameter) are synthesized and optimized to encapsulate and deliver IL-2 (**Fig. 5.1**). Monodisperse mesoporous silica microparticles (5 to 20 μm) are produced *via* a microfluidic jet spray-drying route, using cetyltrimethylammonium bromide (CTAB) and/or Pluronic F127 as templating agents, and tetraethylorthosilicate (TEOS) for silica as reported before.[13,14] Carbodiimide chemistry (NHS/EDC) was utilized to modify silica conjugates with heparin after treating the silica with (3-Aminopropyl)triethoxysilane (APTES) to provide primary amine groups (**Fig. 5.1A**).

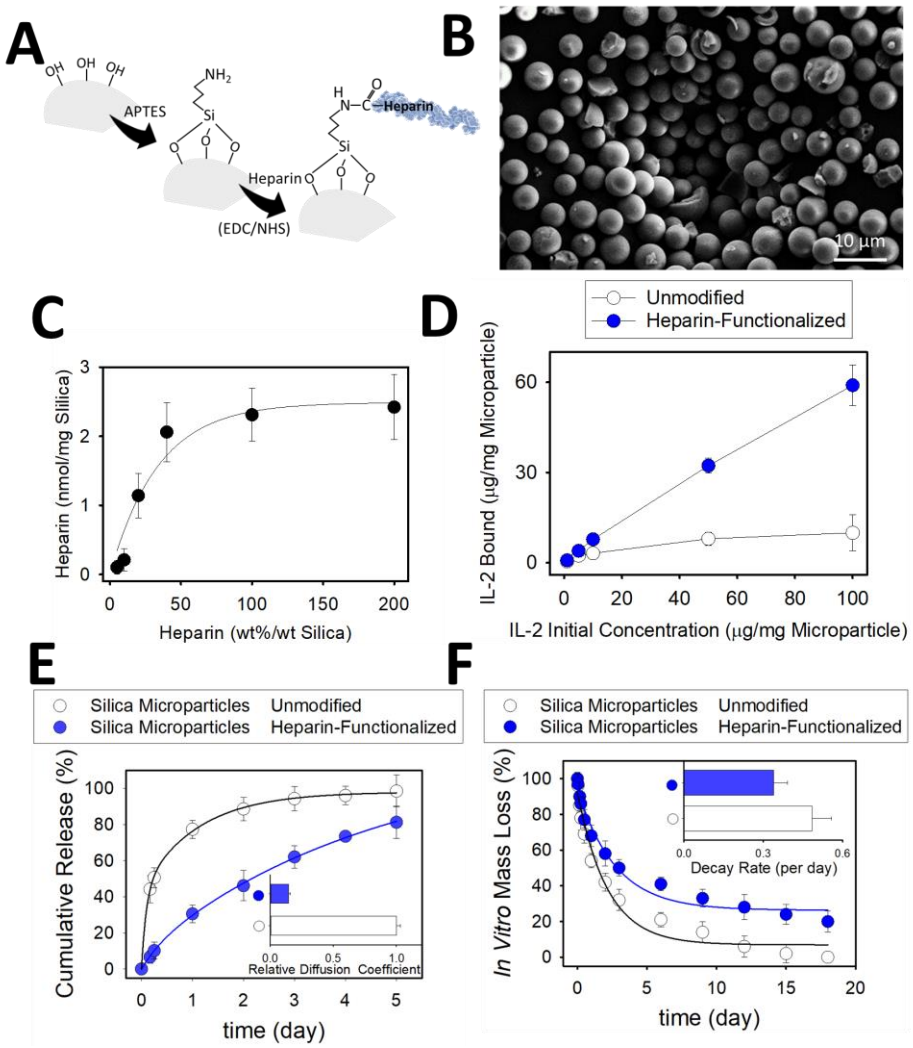

Figure 5.1. (A) Surface chemistry and (B) SEM image of synthesized mesoporous microparticles. (C) The degree of heparin-conjugation of silica particles with various initial amounts of heparin in the reaction mixture. (D) Binding efficiency of IL-2 to the microparticles. (E) Cumulative release of IL-2 from heparin-functionalized and unmodified silica microparticles at 37C. (inset) calculated diffusion coefficients. (F) In vitro degradation of silica-based microparticles over time.

Change in physical properties of silica particles summarized in **Table 5.1**. Heparin-based conjugates (silica-heparin) was developed at several conjugation densities (**Fig. 1C**). Heparin presence provides enhanced efficiency and stability of cytokine binding that enables precise spatiotemporal control over the release profile of target proteins (here IL-2) (**Fig. 5.1D, Fig. 2**). Heparin modification has delayed the rate of release by about 5 folds compared to the unmodified

silica (**Fig. 1E**). *In vitro* degradation of mesoporous silica (MES) beads indicates that these particles are mostly gone in two weeks and heparin modification accelerates the degradation as it will increase the hydrophilicity of particles (**Fig. 5.1F**).

Table 5.1. Change is physical characteristics of mesoporous silica microparticles after surface functionalization with APTES and heparin.

Diameter (µm)	Pore Diameter (nm)	Surface Area (m^2/g)	Pore Volume (ml/g)
5	**11.5**	**384**	**1.1**
15	9	430	0.97

	Pore Diameter (nm)	Surface Area (m^2/g)	Volume (ml/g)
Unmodified	11.5	384	1.1
Anime-modified	10.4	250	0.65
Heparin-functionalized	**7.9**	**119**	**0.23**

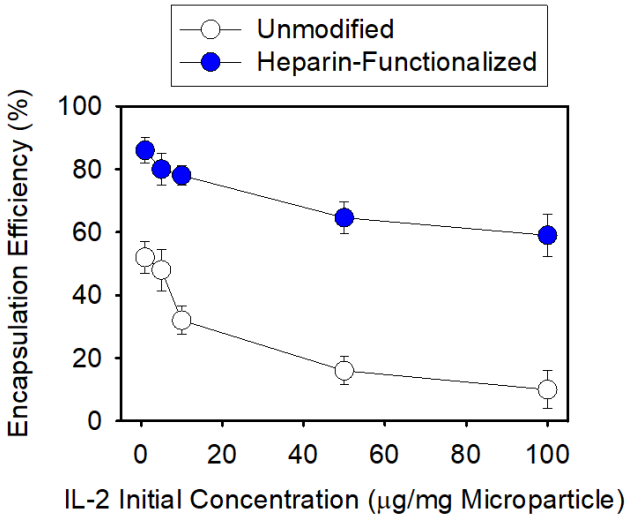

Figure 5.2. Encapsulation efficiency of IL-2 in unmodified (open circles) compared to heparin modified (blue-filled circles) microparticles as a function of initial IL-2 concentration.

Modified Silica-heparin particles are potent aAPCs for *in vitro* T cell expansion. To serve as aAPCs we then decorated the surface of IL-2 loaded silica-heparin beads

with aCD3/aCD28 to provide the anchor for T cells through which they can engage with the beads and get activated as a result (**Fig. 5.3**).

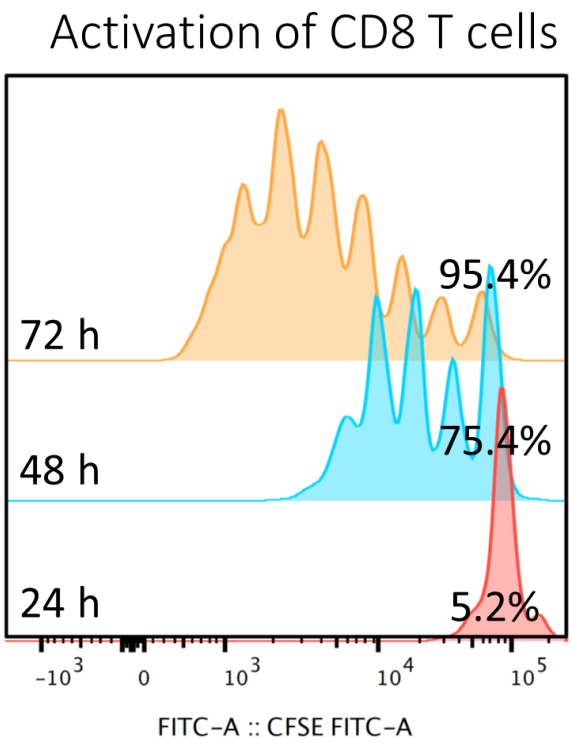

Figure 5.3. Incubation of naive CD8+ T cells in presence of silica-based APCs can induce activation of T cells, measured by tracking the proliferation of T cells as a function of time using CFSE dilution assay.

To evaluate the efficiency of these aAPCs *in vitro* we co-cultured them with CD8+ and CD4+ T cells under different conditions. Plain silica-heparin particles, IL-2 loaded silica-heparin particles, aCD3/aCD28 decorated silica-heparin particles free of IL-2, and Dynabeads supplemented with free IL-2 were compared with IL-2 loaded, aCD3/aCD28 decorated silica-heparin particles (**Fig. 5.4**). Antibody conjugated beads with/-out IL-2 loading were tested as aAPCs and T cell's proliferation and activation were tracked upon a 3 day co-culture with beads (**Fig 5.4a**).

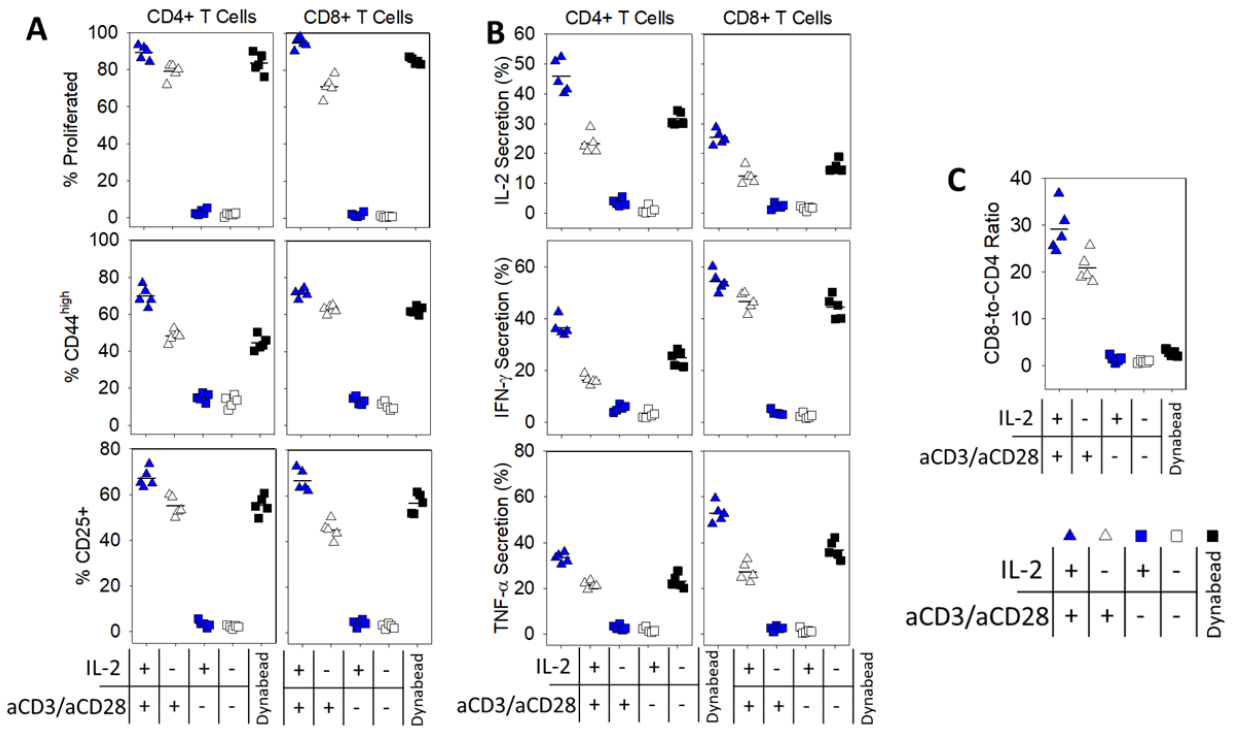

Figure 5.4. T-cell activation is modulated by aAPCs. Naive CD4+ and CD8+ T cells co-cultured with various formulations of aAPCs in 2D. (A) Flow cytometry analysis of cell division (CFSE dilution) and percentage of T cells with high expression of CD44 and of T cells upregulating CD25 assayed three days post-stimulation. (B) Percentage of T cells expressing the effector cytokines IL-2, IFN-γ, or TNF-α. Each dot represents one experiment. (C) FACS quantification of CD8-to-CD4 ratio of T cells cultured with varying formulations of particles, compared to Dynabeads. The starting ratio for all conditions was 0.5.

These particles can strongly interact with T cells and induce activation and proliferation of naive T cells. Presence of IL-2 helped reduce the population of undivided cells and resulted in increased expression of activation markers such as CD25 on activated T cells (**Fig. 5.4a** and **Fig. 5.5**). It should be noted that IL-2 releasing, surface conjugated silica beads performed better than Dynabeads supplemented with soluble IL-2 in terms of activation (**Fig. 5.4a**) and induction of cytokine secretion by T cells (**Fig. 5.4b**). Unique features of MES beads such as high loading capacities for cytokines and securing prolonged release while offering biodegradability renders them to be superior to Dynabeads. We have previously shown that prolonged release of IL-2 favors formation of effector cells.[3] These engineered silica-based aAPCs are easier to produce at higher

quantities (gram scale) compared to the hydrogel-based aAPCs that we reported before.[4] Moreover, the biodegradability of these silica will make them superior compared to Dynabead for *ex vivo* and *in vivo* use. On the other hand, it has been reported that increasing the strength of activation signal favored formation of CD8+ in the case of co-culture of both CD8+ and CD4+ T cells with beads, our beads favored CD8+ population by 30 folds compared to Dynabeads making them suitable for in vivo cancer models (**Fig. 5.4c**). Similar trends have been reported while using silica nanorods.[6]

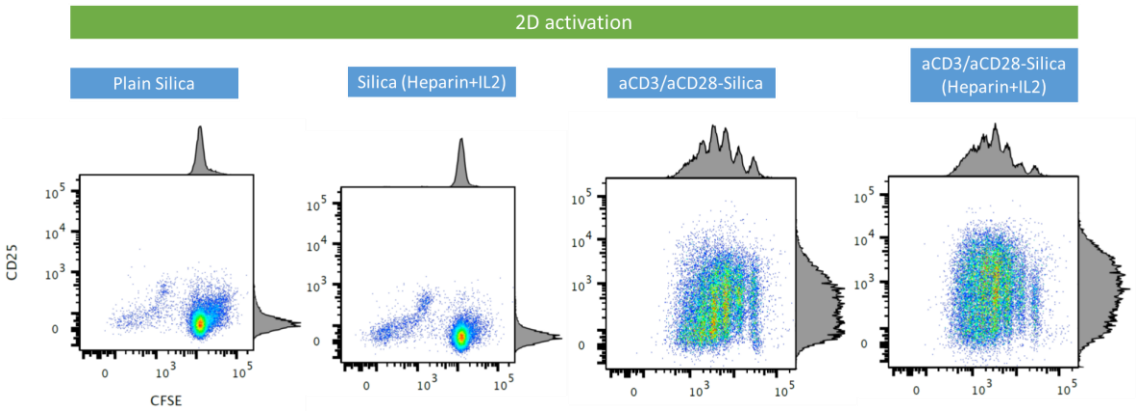

Figure 5.5. Flow cytometry analysis of cell division (CFSE dilution) in x-axis and CD25 expression in y-axis assayed on day 3 post-stimulation of naive T cells with different formulations of developed aAPCs in 2D culture.

5.2.2. 3D scaffolds for T cell expansion

Although, these particles can provide activation cues for cultured T cells but in order to mimic the natural niche that T cells experience during their activation we transformed our activation platform to a 3D matrix. Here we engineer a biocompatible Alginate scaffold which was further decorated with 0.06 µmole RGD per mg alginate RGD peptides to facilitate T cell attachment and trafficking. To achieve the optimal physical properties we tune the stiffness of our hydrogel similar to the stiffness that T cells will experience in lymph nodes during the activation.[15] Here, 40 mM calcium sulfate ($CaSO_4$) was used as a crosslinker which resulted in relatively stiff (40 kPa) gels.[16] The 3D porosity was then created by lyophilization to let the cells experience 3D trafficking while receiving the activation signals (**Fig. 5.6A**). Arrangement of the cells alongside

the pore walls of the scaffolds was then confirmed by scanning electron microscopy (SEM) (**Fig 5.6B**). To provide antigen presentation, developed aAPCs were embedded within the scaffolds and their activation capability were monitored after 5 days of seeding naive CD8+ T cells within them (**Fig. 5.6C**). Solely embedding of the beads within the scaffolds failed to activate T cells in short term time periods. We hypothesize that antibody conjugated beads were coated with a layer of Alginate polymer, making them buried and unavailable for T cells to anchor to (**Fig. 5.6C**).

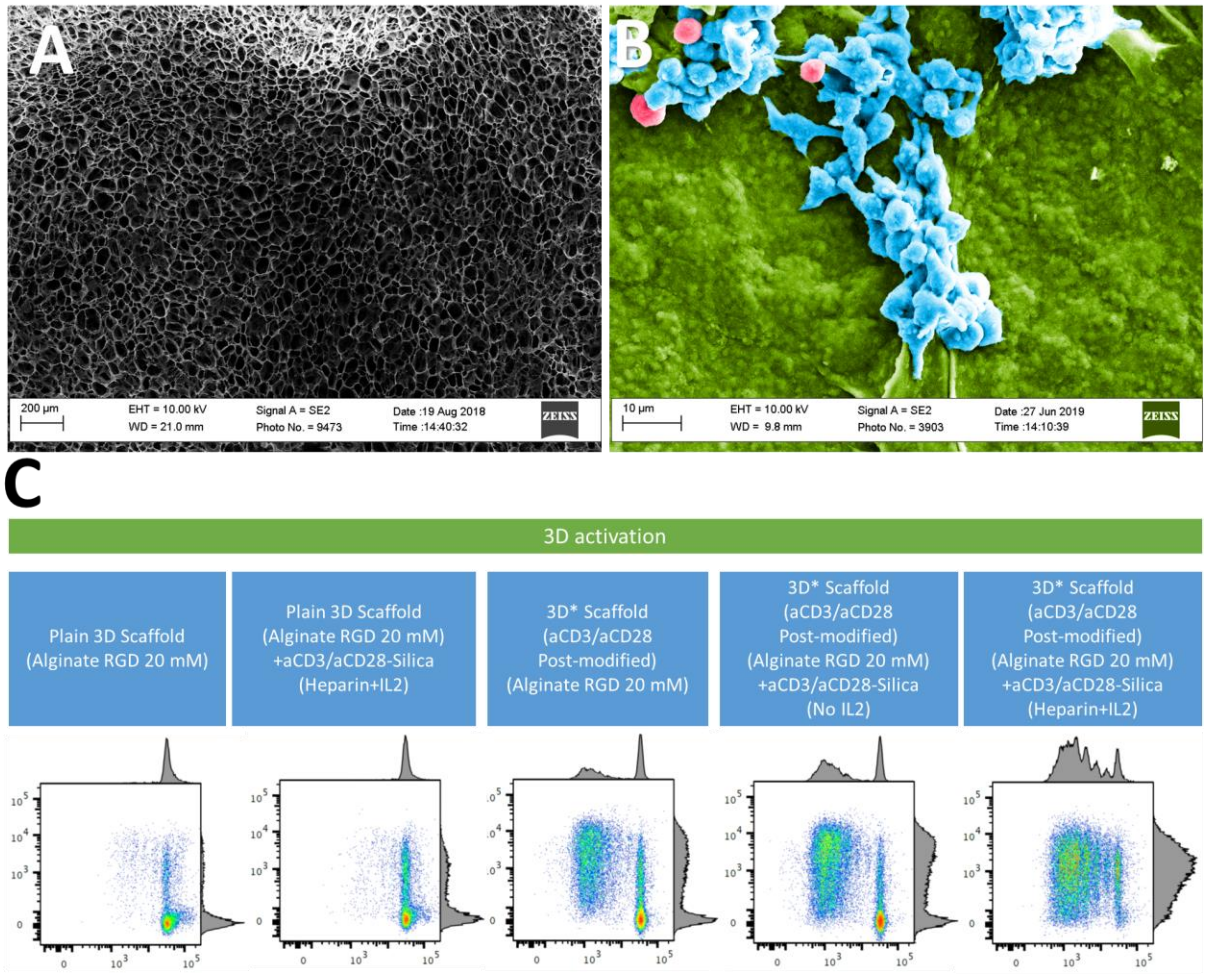

Figure 5.6. (A) SEM images of macroporous 3D scaffolds. Images were taken from a region within the bulk of the scaffold. Scale bar is 200 µm. (B) Colored SEM images demonstrating association of T cells with the alginate-based scaffolds. Images were taken from a pore wall of the scaffold where T cells were aligned. Scale bar is 10 µm. (C) Flow cytometry analysis of cell division

(CFSE dilution) in x-axis and CD25 expression in y-axis assayed three days post-stimulation of naive T cells with different formulations in our 3D scaffold.

To overcome this issue, we post-conjugated our 3D scaffolds with anti-CD3/28 antibodies to ensure the availability of these antibodies to T cells. As for longer term *in vivo* experiments where the scaffold starts to degrade embedded aAPC beads can also become available to cells. (**Fig. 5.7**).

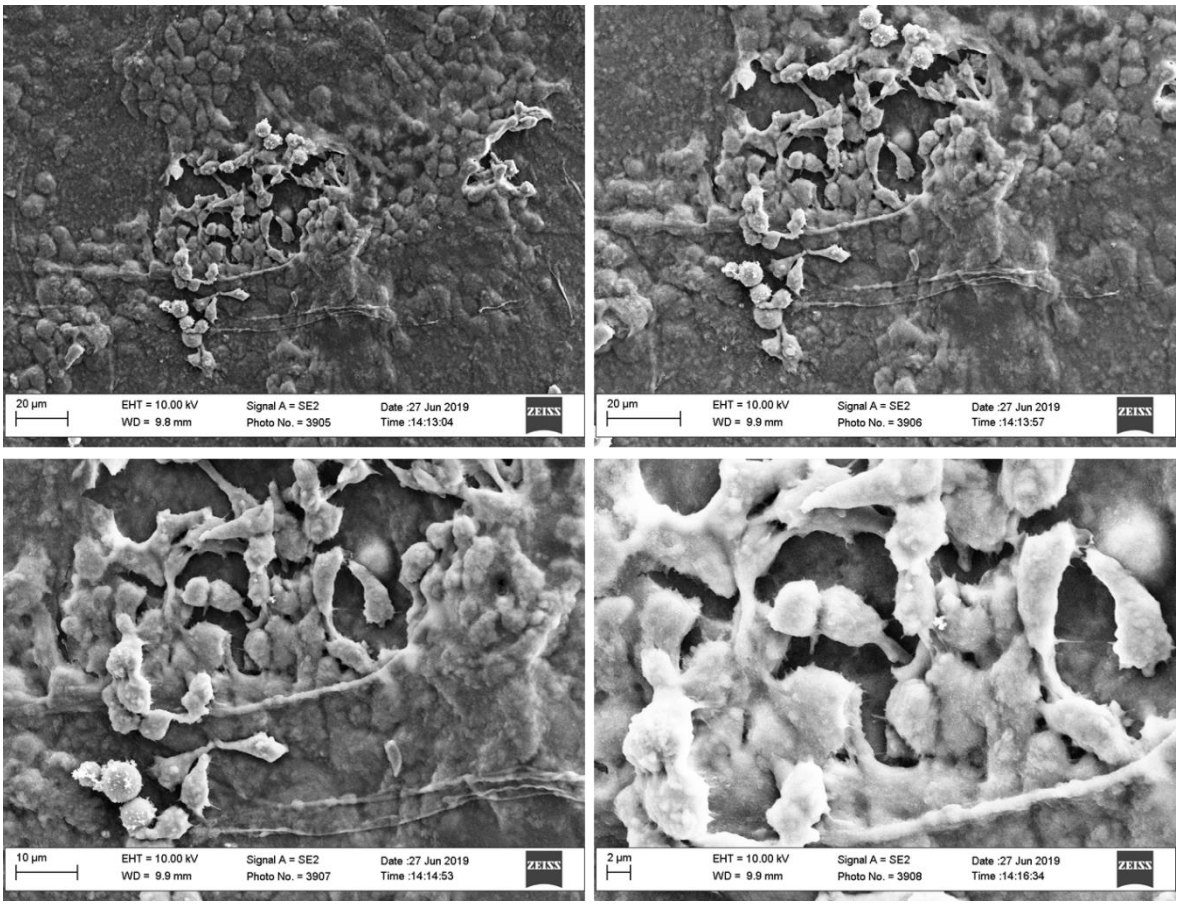

Figure 5.7. SEM images demonstrating associates of T cells with the alginate-based scaffolds. Images were taken from a region within the pores of the scaffold where T cells engaged. Scale bars indicated in each panel.

Proliferation, activation, and cytokine secretion of both CD8+ and CD4+ T cells was compared in the designed 3D scaffolds under different conditions (**Fig. 5.8**). To keep a fair comparison control particle were embedded within the scaffolds for IL-2 release so the release rate would not be a variant in our experiments (**Fig. 5.8**).

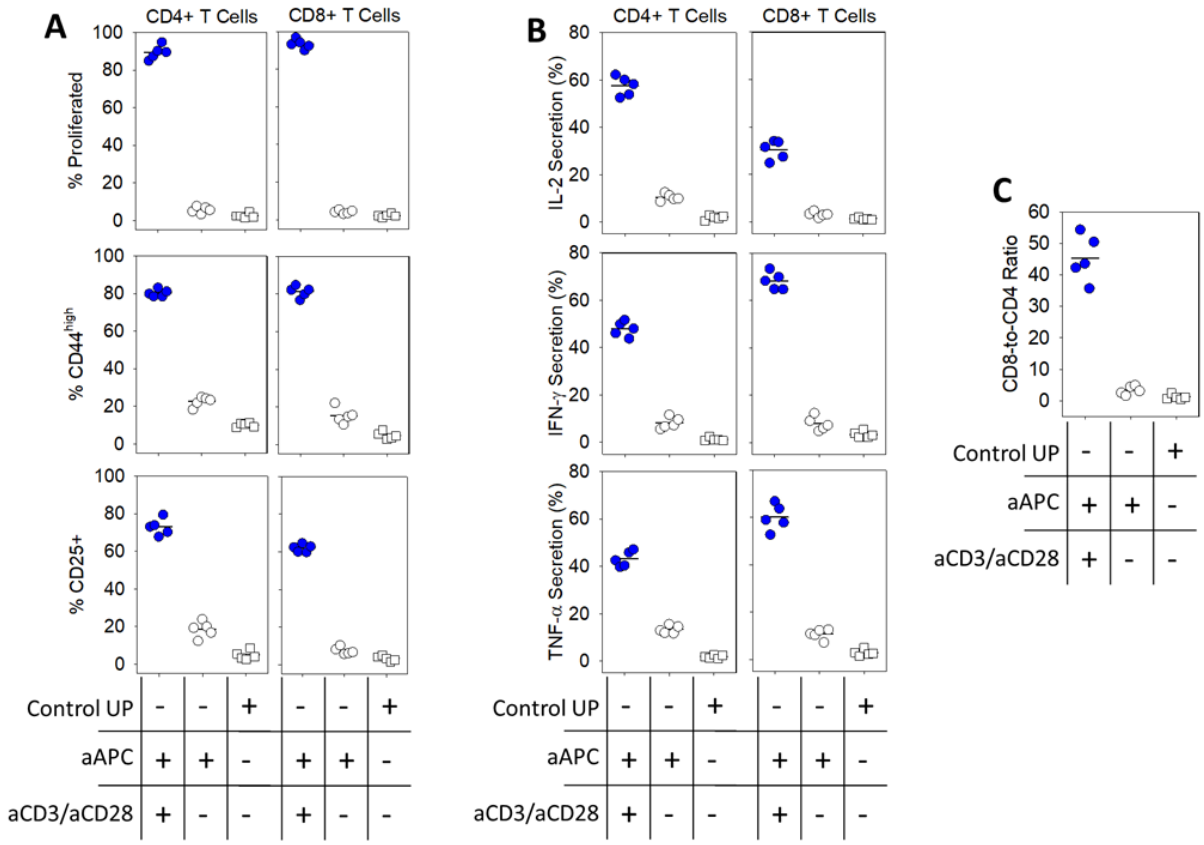

Figure 5.8. T-cell activation is modulated by aAPCs-loaded 3D scaffolds. Naive CD4+ and CD8+ T cells co-cultured with various formulations of 3D scaffolds. (A) Flow cytometry analysis of cell division (CFSE dilution) and CD25/CD44 expression assayed three days post-stimulation. Percentage of cells that divided at least once. Percentage of T cells with high expression of CD44 and percentage of T cells upregulating CD25. (B) Percentage of T cells expressing the effector cytokines IL-2, IFN-γ, or TNF-α. Each dot represents one experiment. (C) FACS quantification of CD8-to-CD4 ratio of T cells cultured with varying formulations of particles, compared to Dynabeads. The starting ratio for all conditions was 0.5.

The release rate of IL-2 from the 3D Alginate-RGD scaffold loaded with aAPCs was measured over time using ELISA (**Fig. 5.9**). Post conjugated 3D scaffolds loaded with antibody decorated, aAPC beads showed the highest proliferation and activation level (**Fig. 5.8A**) and similar to 2D upon co-seeding of both CD8+ and CD4+ T cells in the scaffolds CD8+ population was favored (**Fig. 5.8C**).

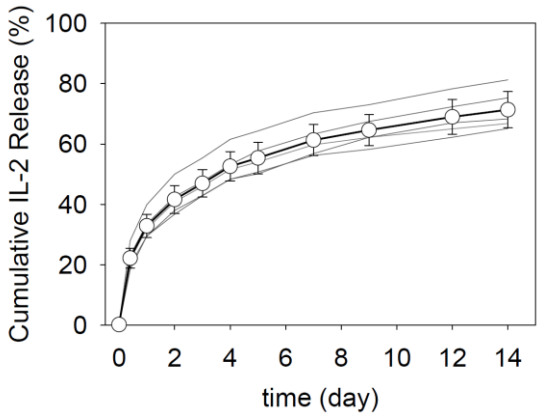

Figure 5.9. Release of IL-2 encapsulated within aAPCs in Alginate-based 3D scaffold. The released IL-2 was measured using ELISA kit over time under gentle shaking (50 rpm) at 37 °C.

Due to the huge surface area that our microporous scaffold offers, T cell's expansion was improved by up to 9 folds upon scaffold post conjugation (**Fig. 5.10**).

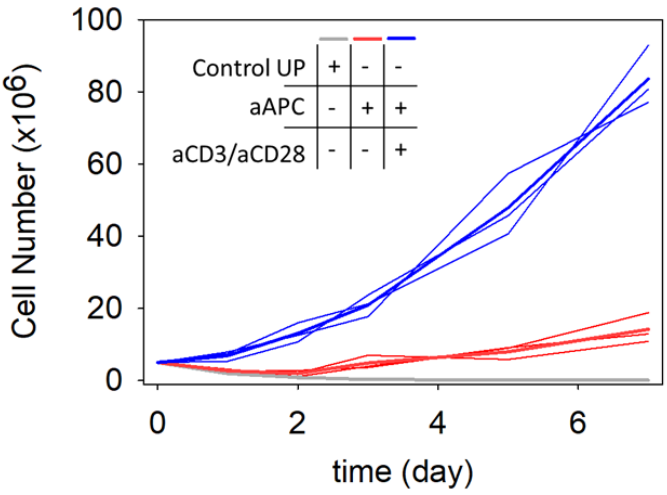

Figure 5.10. Porous scaffolds support robust expansion of T cells. Absolute counts of viable T cells in scaffolds fabricated with different formulations.

As one of the features we sought to optimize in our 3D niche was its mechanical stiffness to be similar to that of lymph nodes we tested whether this feature was drastically affected by particle dispersion within the scaffolds or not. While post conjugation of scaffolds did not change their stiffness, loading of aAPCs within them slightly increased their stiffness (**Fig. 5.11A**) yet kept it in the reasonable range as lymph node's stiffness in case of infection.[15] Another feature we seek to test was shelf-life of our scaffolds over time. Being able to store the scaffold for a long time

without altering its properties is highly favorable for clinical translation of such a product. We noticed no significant changes over time in the stiffness and functionality of our scaffolds (**Fig 5.11B,C**).

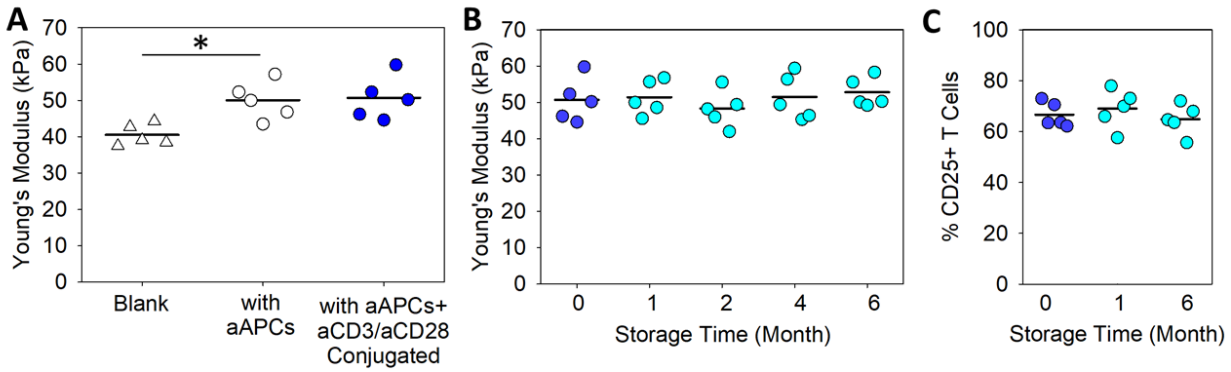

Figure 5.11. Mechanical characteristics of the 3D hydrogels. (A) Change in mechanical properties of freeze-dried scaffolds in absence or presence of silica-based aAPCs with or without post-conjugation with anti-CD3/ anti-CD28 antibodies. **Shelf-life evaluation of scaffolds.** Freeze-dried hydrogel batches were stored at 4°C for different durations up to six months and changes in (B) mechanical properties and (C) level of activated CD8 T Cells were used to assess their shelf-life stability. The individual data are presented (n=5). The results were statistically analyzed using one-way ANOVA with post-hoc analysis. For all the tests, the threshold was set to $P < 0.05$ for statistically significant. Results showed no statistically significant ($p>0.05$) change in elastic modulus or T cell activation.

As for sterilization of scaffolds X-ray irradiation (Gulmay Medical RS320 x-ray unit) was used to irradiate the fabricated scaffolds before *in vitro* or *in vivo* functional tests, following ISO 11137-2:2013 recommended protocols.[17,18] A sterilization dose of 25 kGy (2.5 Mrads) was used, since it has been reported this dose does not alter the properties of pharmaceuticals.[19] Physical and biological properties, including changes in mechanical stiffness or change in T cell activation after sterilization process was tested. Our results showed non-significant changes in mechanical properties of scaffolds after receiving three cycles of 25 kGy sterilization dose (**Fig. 5.12**).

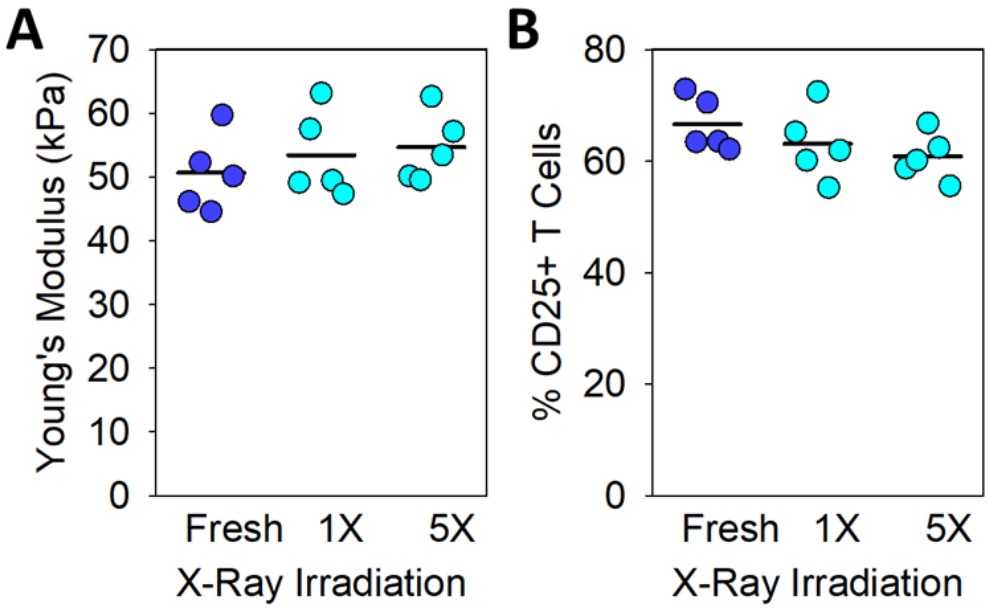

Figure 5.12. Change in mechanical properties and T cell activation of scaffolds after 1 or 5 cycles of x-ray irradiation at 25 kGy dose compared to freshly prepared samples. The individual data are presented (n=5). The results were statistically analyzed using one-way ANOVA with post-hoc analysis. For all the tests, the threshold was set to $P < 0.05$ for statistically significant. Results showed no statistically significant ($p>0.05$) changes in elastic modulus or T cell activation.

Another hurdle that is normally faced in most solid tumors is the abundance of TGF-β which plays a key role in induction of Tregs in tumor microenvironment and leads to immune suppression.[10] TGF-β abundance and activity has been well documented in a number of murine tumor models[10,20–22] and suspected to be a key counteracting player in IL-2 therapies where they seek to enhance CTLs activity. The pivotal role of TGF-β in tumor cell growth and maintaining an immunologically cold tumor microenvironment renders it an ideal area to tackle.[22,23]

Although our insight is quite limited on the exact source of TGF-β in tumor microenvironment and the immunoprotective pathways behind its signaling blockade, studies on combinatorial delivery of a TGF-β receptor-I inhibitor SB505124[10,24] plus an immunostimulant such as IL-2 has shown promising results in mouse melanoma model.[10] Considering all the toxicity reports on systemic administration of immunostimulants which blocks their true

therapeutic benefits, our approach allows for efficient, overtime, local delivery of these agents in the tumor bed.

Here we tested two of the commercially available TGF-β inhibitors, SB505124 and LY2157299 (Galunisertib)[9,25,26], at different doses (**Fig. 5.13**) and tested their potency in suppressing Treg formation. We found LY2157299 to be about two times more potent than the SB505124 at 1 μM concentration in suppressing Treg formation.

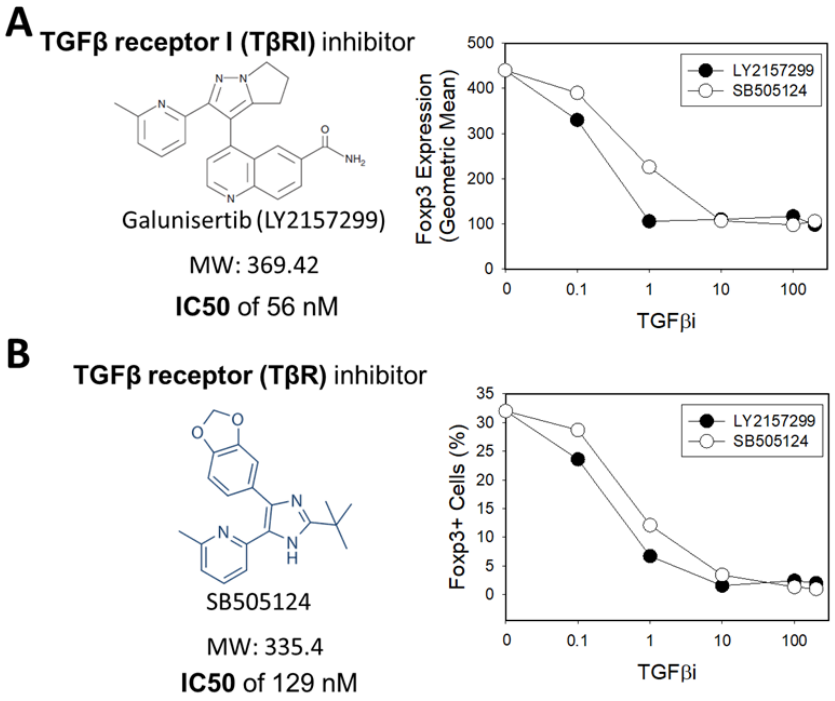

Figure 5.13. Chemical structure, molecular weight and reported IC50 values of the two tested TGFb inhibitors. *In vitro* inhibition assay was used to determine effectiveness of these two molecules to inhibit formation of Treg. Concentrations are in μM.

Due to the hydrophobic nature of this drug, we choose to use poly(lactic-co-glycolic acid (PLGA) as a carrier to load and release the selected TGF-β inhibitors. PLGA renders a slow, controlled biodegradation due to its compact structure. TGF-βi encapsulated PLGA nanoparticles with the size of about 200 nm were then fabricated and tested for their suppression capability against Treg formation (**Fig. 5.14**). Soluble TGF-βi was used as a control to check whether use of

PLGA alters the activity of TGF-β inhibitors or not. Treg formation was suppressed by about 40 percent *via* both soluble administration of TGF-βi or upon coculture with TGF-βi releasing PLGA nanoparticles (**Fig. 5.14C,D**).

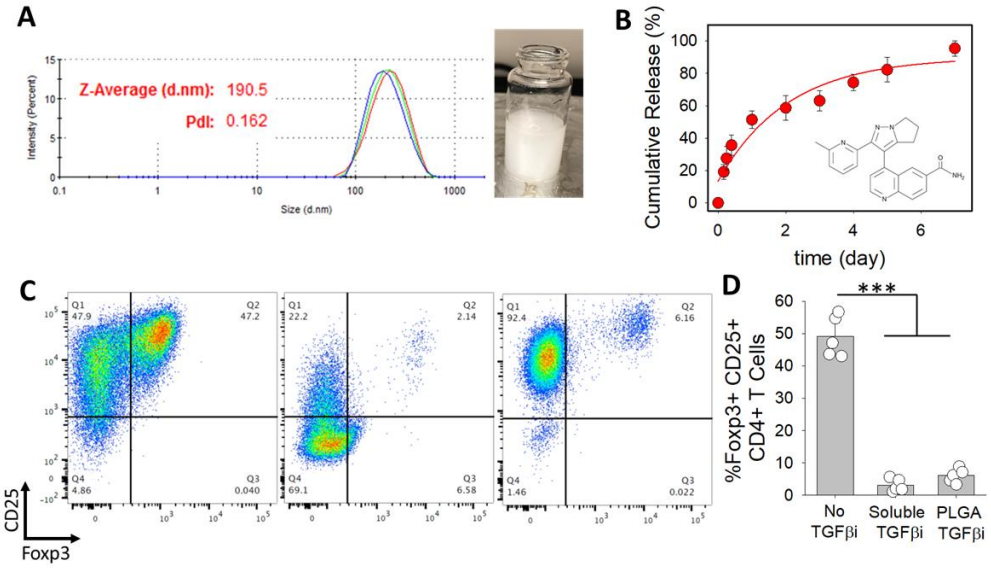

Figure 5.14. (A) Dynamic light scattering (DLS) showing monodisperse formation of TGFbi-loaded PLGA nanoparticles. Inset showing stable suspension of formed nanoparticles in water 24h after dispersion. (B) Release of TGFbi from nanoparticles over time at 37 °C. Chemical structure of selected TGFbi, LY2157299, was also shown. (C) 2D activation and Treg formation using aAPCs in the presence of soluble TGFb. Inhibition using Soluble TGFbi (10 uM) or PLGA NPs loaded with equivalent amounts of TGFbi. (D) Quantified percentages of formed Tregs in 2D.

Once we confirmed their functionality *in vitro* we then loaded these particles within our 3D scaffolds along with IL-2 releasing silica-heparin micro particles (**Fig. 5.15**). In all of the conditions soluble TGF-β was supplemented in the media to induce formation of Tregs. In the 3D model PLGA loaded TGF-βi had a superior inhibitory effect compared to its soluble administration (**Fig. 5.15D**). In our 3D formulation Treg formation was inhibited by about 20 percent due to sustained, local release of TGF-βi on the adjacent cells.

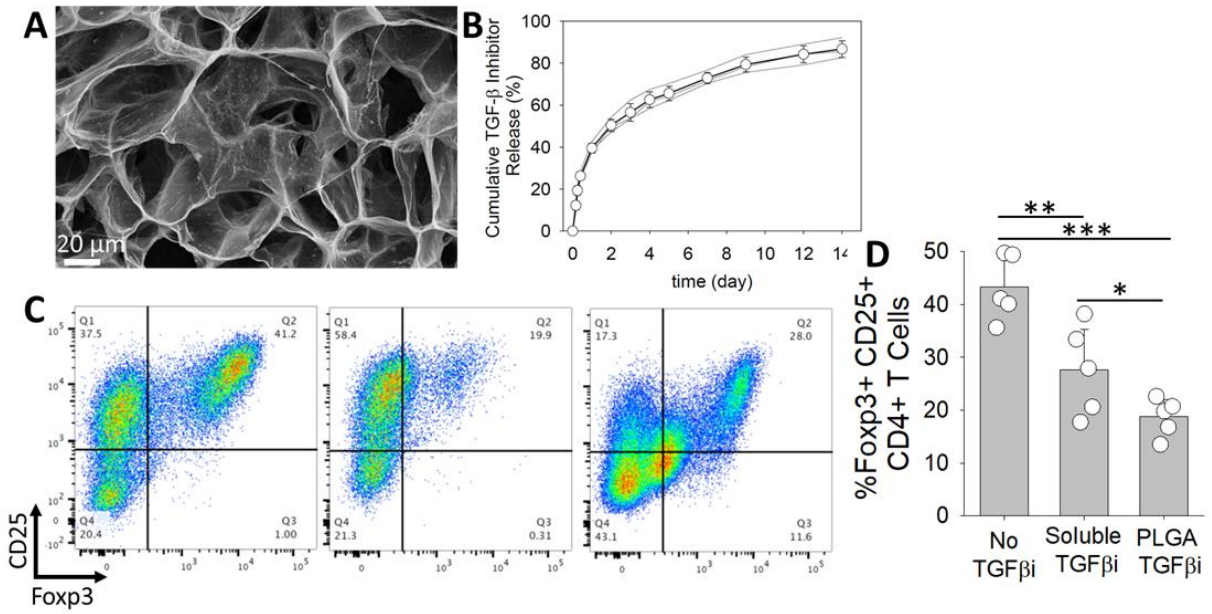

Figure 5.15. 3D Treg inhibition. (A) encapsulation of TGFbi-loaded PLGA nanoparticles in 3D scaffold. (B) Release of TGFbi from scaffolds as a function of time at 37 °C. (C) 3D activation and Treg formation using antigen-presenting scaffolds in the presence of soluble TGFb. Inhibition using Soluble TGFbi (10 uM) or PLGA NPs loaded with equivalent amounts of TGFbi. (D) Quantified percentages of formed Tregs in 2D.

Once we confirmed the capability of our 3D formulation for T cell activation, proliferation, and Treg suppression the next step to make them suitable for *in vivo* functionality was to advertise them for the tissue resident T cells. To this end we juiced our scaffolds with Chemokine (C-C motif) ligand 21 (CCL21) as a chemoattractant to guide naive and active T cells[27,28] towards our synthetic lymph node. Different concentrations of CCL21 were mixed with Alginate-RGD scaffold and were tested for both active and naive, CD8+ or CD4+ T cell's recruitment using a transwell setup (**Fig. 5.16**).

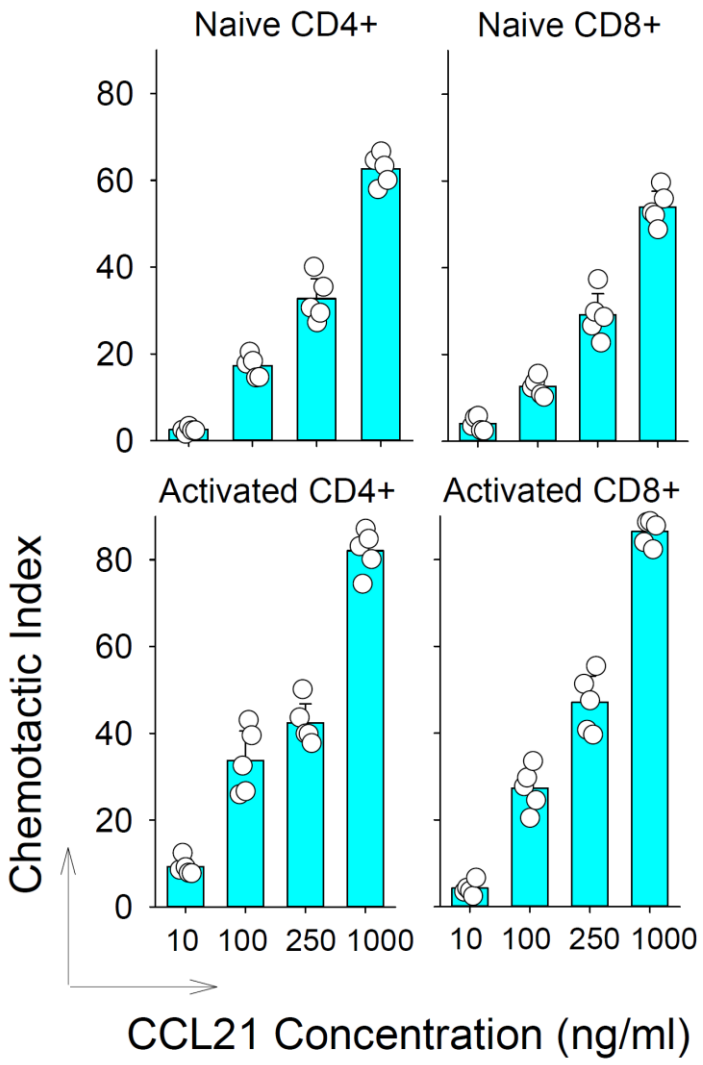

Figure 5.16. Assessment of CCL21 chemotaxis in recruitment of naive and activated CD4+ and CD8+ T cells *in vitro*. 5×105 naive or activated T cells were loaded on the top filter of the transwell chamber. Hydrogels containing various concentrations of CCL21 were placed in the bottom wells at the indicated concentrations. Viable cells migrating to the lower chamber after 4 h were quantified after digesting the scaffold. Chemotactic Index: fold migration over background (empty scaffolds).

Since these scaffolds were designed to be implanted adjacent to the tumor tissue, we also tested recruitment B16F10-OVA cells as a control to show CCL21 have no significant effect on tested tumor cells (**Fig. 5.17**).

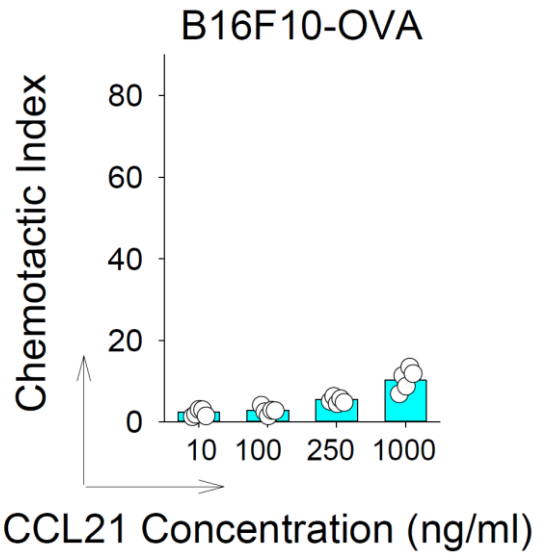

Figure 5.17. Assessment of CCL21 chemotaxis in recruitment of B16F10-OVA tumor cells. 5×105 cells were loaded on the top filter of the transwell chamber. Hydrogels containing various concentrations of CCL21 were placed in the bottom wells at the indicated concentrations. Viable cells migrating to the lower chamber after 8 h were quantified after digesting the scaffold. Chemotactic Index: fold migration over background (empty scaffolds). 5 μm pore size was selected for Transwell migration assay.

5.2.3. **Implanting synthetic lymph nodes for in vivo T cell training**

Upon demonstrating the scaffolds to be successful in vitro in terms of T cell recruitment, activation, expansion, and Treg suppression (**Fig. 5.18**) we then implanted them in the melanoma tumor-bearing wild-type C57/BL6 mice to evaluate their tumor clearance potency.

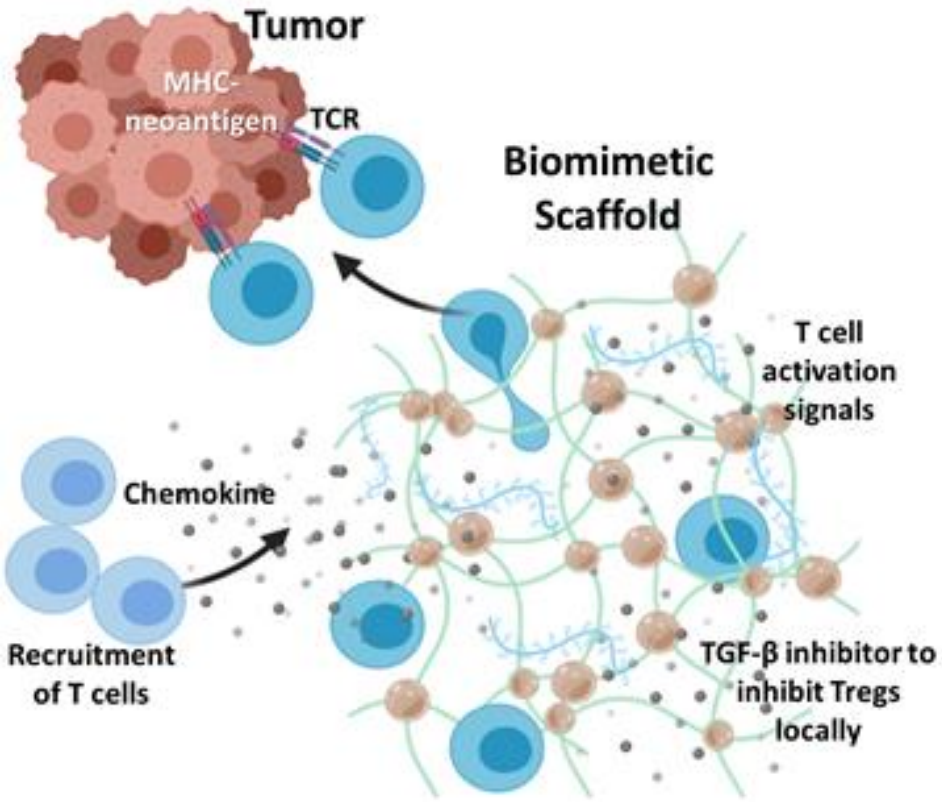

Figure 5.18. Schematic representation of proposed in vivo mechanism of action. Sustained release of CCL21 helps recruitment of endogenous T cells while presentation of surface conjugated activation cues (anti-CD3 and anti-CD28) and sustained release of IL-2 will activate recruited T cells. Sustained release of TGFb inhibitor will prevent formation of Tregs both in scaffolds and tumors.

Typically, mice received subcutaneous injections of B16-F10 cells to their right flank followed by the scaffold implantation adjacent to the tumor once it was palpable. Without any further treatment animal's health was monitored and 17 days after were euthanized. Implanted scaffolds, tumors, tumors' draining lymph nodes, and spleens were then retrieved for further studies (**Fig. 5.19**).

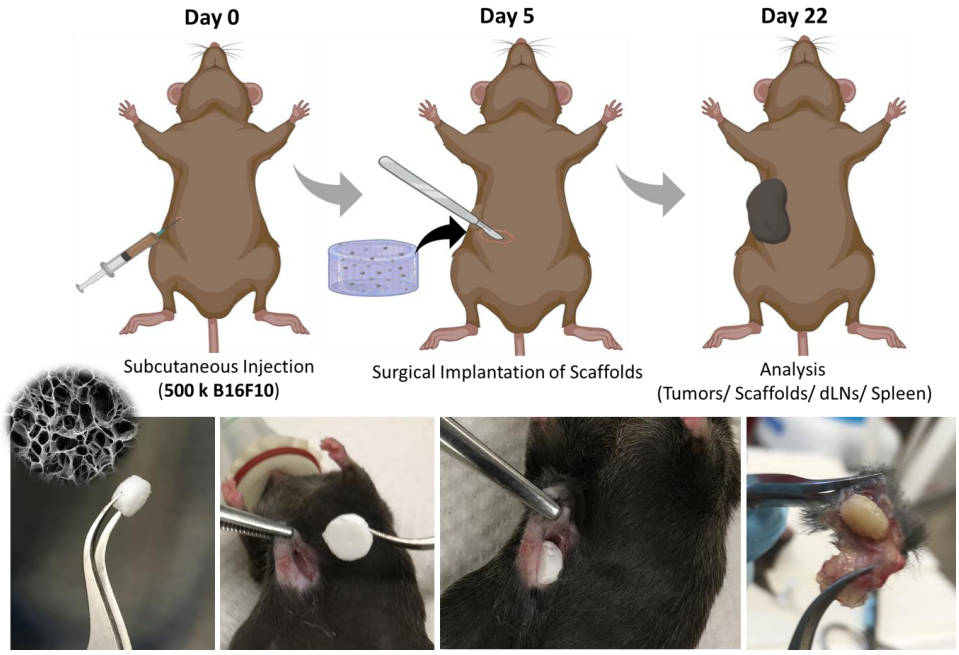

Figure 5.19. Implementation approach: The top panel shows timing of tumor inoculation and follow up surgical implantation of the biomaterial scaffold. The engineered device is surgically implanted in a B16-F10-ova bearing mice.

H&E staining of the scaffold adjacent to the tumor showed successful tissue integration and recruitment of T cells *via* the implanted microporous scaffolds (**Fig. 5.20**).

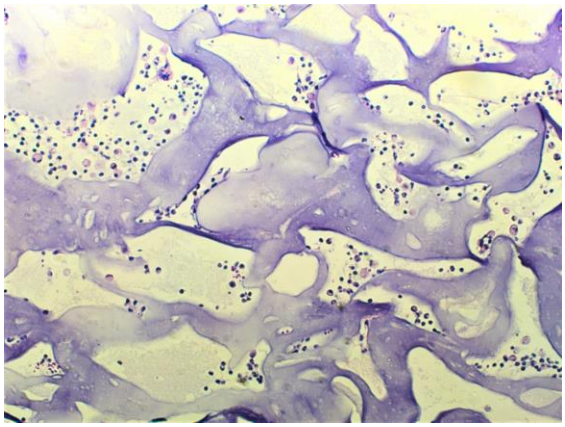

Figure 5.20. H&E staining of the cross sections of the subcutaneously implanted scaffolds that originated from the alginate biopolymer, 7 days after implantation.

In this set of studies, blank scaffolds free of any particles or chemokines were used as controls along with PBS control. Tumor representative images were taken at the end of the

experiments, their masses were measured (**Fig. 5.21** and **Fig. 5.22**) and tumor sizes were tracked overtime as an indicator of the tumor growth rate (**Fig. 5.22**). While for this aggressive tumor if left untreated (PBS control) or implanted control scaffold tumor will triple in size in 7 days, our scaffold suppressed tumor growth drastically (**Fig. 5.22**).

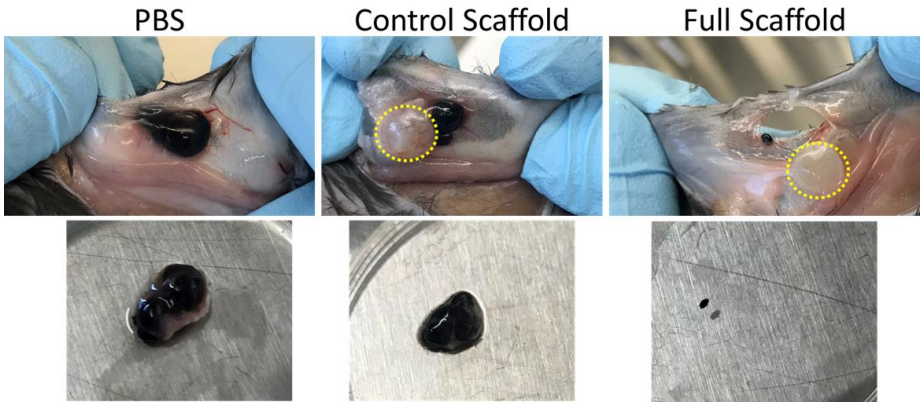

Figure 5.21. Clearance of melanoma tumors. Representative image of tumors extracted from wild-type mice 22 days after tumor inoculation. Local recruitments and activation of endogenous T cells plus Treg suppression via the implanted alginate-based scaffold successfully eliminated the aggressive melanoma tumor in mice.

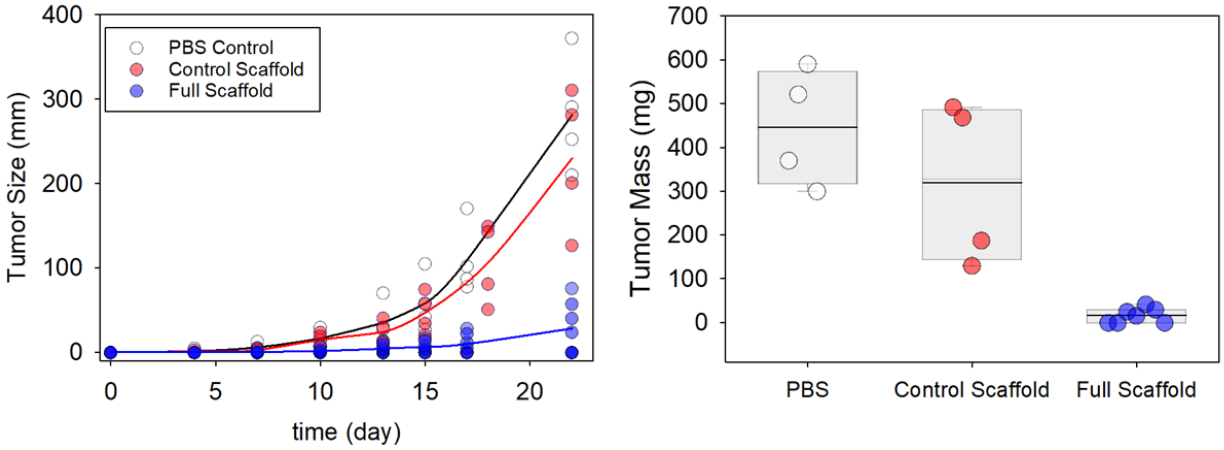

Figure 5.22. Engineered scaffolds can suppress melanoma tumors. Melanoma (B16-F10-Ova) tumor growth and final tumor mass in wild-type mice implanted with either full (n = 7) or control scaffolds (n = 4) compared to PBS (n = 4). Each point represents one mouse.

We then assessed the status of recruited cells by our implanted synthetic lymph nodes (ISL) (**Fig. 5.23**). Due to the successful and prolonged release of the CCL21, T cells, CD8+ T cells in particular, constituted the majority of recruited lymphocytes in our full scaffolds (**Fig. 5.23A**) while no difference seemed to happen in the population of recruited CD4+ T cells in full *vs*. control scaffolds. Thus, CD8+ to CD4+ ratio of T cells were about 7 times higher in the full scaffold compared to the control one (**Fig. 5.23B**).

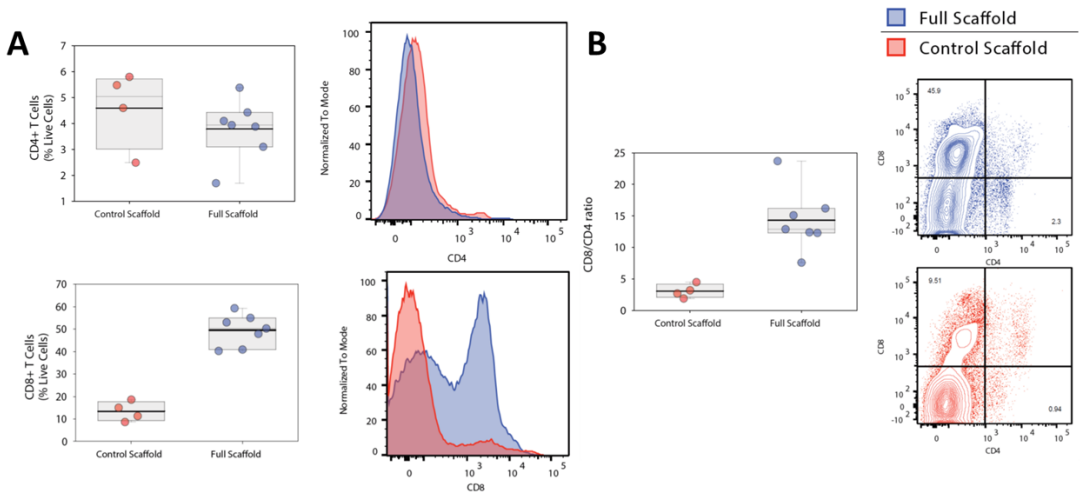

Figure 5.23. ***Status of Recruited T Cells in scaffolds.*** (A) Flow cytometry analysis of CD4+ and CD8+ T cells recruited and expanded in the scaffolds 17 days after subcutaneous implantation of cell-free scaffolds. (B) FACS quantification of CD8-to-CD4 ratio of recruited T cells extracted from full and control scaffolds.

Tumor clearance potency of our implanted synthetic lymph nodes (ISL) was pretty interesting as our scaffold only offers polyclonal activation and expansion of endogenous T cells *via* conjugated anti-CD3/CD28 antibodies while providing IL-2 cytokine. Despite the lack of tumor specific training, T cells that got recruited and trained in our ISL recognized the tumor and were capable of clearing it. This led us towards suspecting about any changes that might have happened to the population of endogenous tumor reactive T cells. We hypothesize that recruiting endogenous T cells in our ISL adjacent to the tumor allows for dual exposure of them to both anti-CD3/28 antibodies which is provided by our ISL and antigens presented on the tumor simultaneously. As a result, T cells will have higher chances of recognizing tumor cells and killing

them. Another possible explanation is our ISL is merely recruiting and expanding tissue resident T cells which along the way results in activation and expansion of tumor-specific resident T cells and this alone plus suppression of Treg population is enough to suppress the tumor growth and clear it. In order to confirm activation of the recruited T cells by our ISL we checked for the level of CD44 expression as an activation marker (**Fig. 5.24A**) and the GZMB expression was measured as an indicator of cytotoxicity tumor fighting T cells (**Fig. 5.24B**). Here, around 80 percent of the recruited CD8+ T cells got activated (**Fig. 5.24A**) from which 20% showed cytotoxic potency (**Fig. 5.24B,C**). No difference amongst the population of programmed-death-1 (PD-1) positive T cells was noticed in our ISLs compared to control (**Fig. 5.24D**).

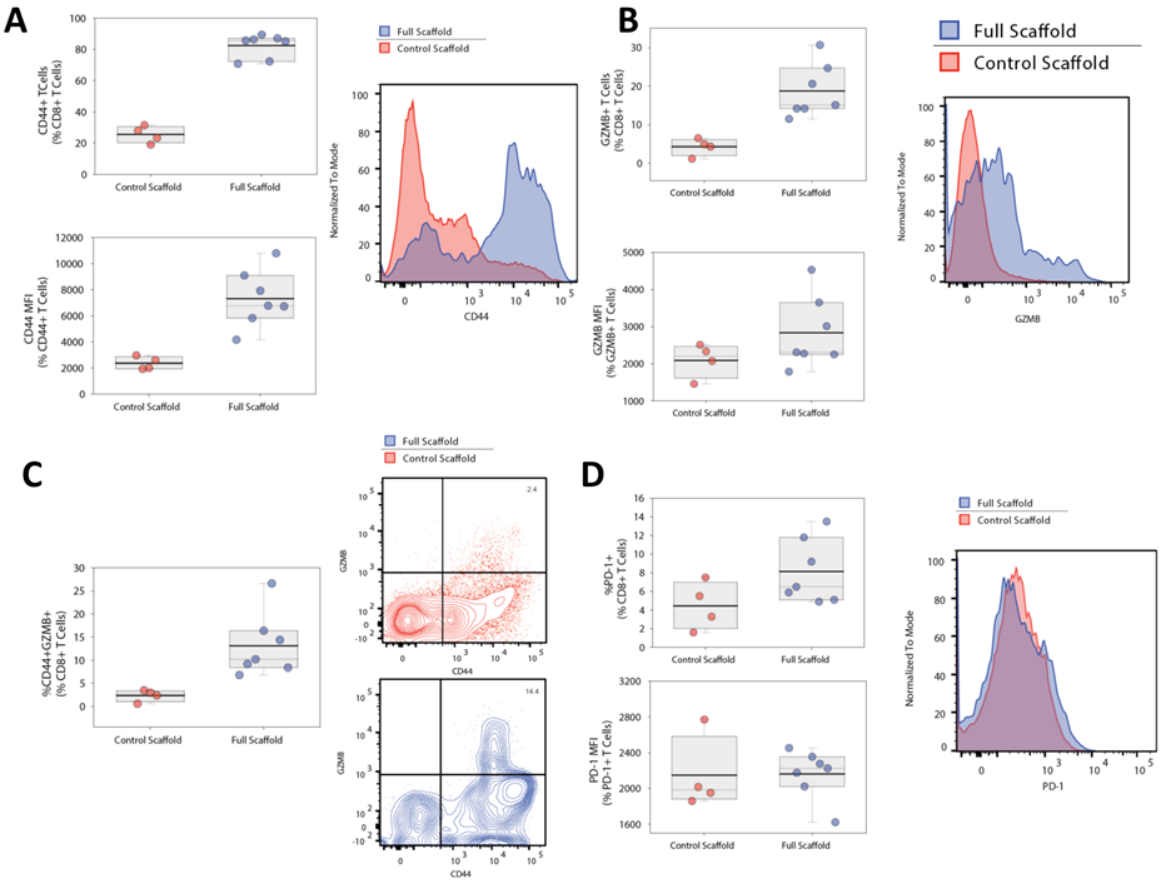

Figure 5.24. ***Activation of Recruited T Cells inside scaffolds.*** Flow cytometry analysis of T cell activation is studied 17 days after subcutaneous implantation of scaffolds. Activation of recruited CD8+ T cells was monitored by measuring surface expression of CD44 as well as

intracellular measurement of Granzyme B (GZMB) expression. (A) Percentage of T cells with high expression of CD44 and mean fluorescence intensity (MFI) of T cells upregulating CD44 were plotted alongside with representative flow cytometry graphs. (B) Percentage of T cells with high intracellular expression of GZMB and MFI of GZMB secreting T cells were plotted. Representative flow cytometry graphs also presented. (C) Percentage of T cells with high expression of CD44 activation marker and GZMB effector cytokine were plotted. Representative flow cytometry graphs also presented. (D) Percentage of PD-1 expressing T cells and their MFIs gated on PD-1+ T cells were plotted. Representative flow cytometry graphs also presented.

Moreover, the population of endogenous OTI T cells within the scaffold were no different from the control scaffold (**Fig. 5.25**).

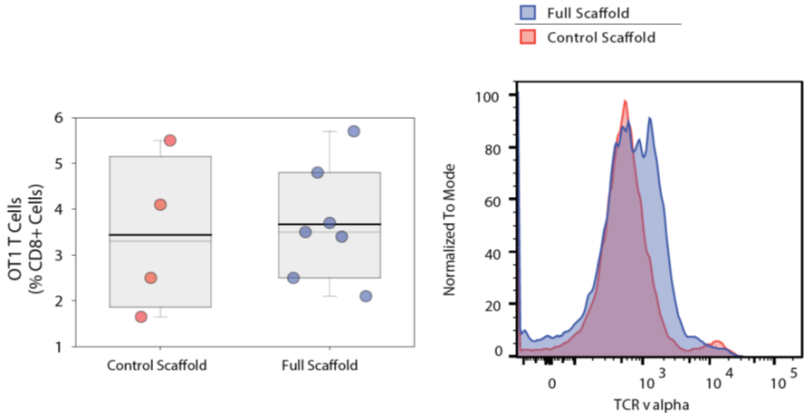

Figure 5.25. ***Status of Recruited Endogenous OTI T Cells in scaffolds.*** Flow cytometry analysis of OTI CD8+ T cells recruitment and expansion in scaffolds 17 days after subcutaneous implantation of cell-free Full and control scaffolds.

5.2.4. Characterization of Tumor infiltrated T cells

Mice bearing B16-F10-Ova tumors were euthanized 22 days after tumor injection. Three out of the seven mice that received the ISL had absolutely no tumor. Detectable tumors in the remainder of mice were the lysed and checked for the presence of polyclonal or tumor specific T cells (**Fig. 5.26**). Percentage of tumor infiltrated CD8+ T cells was increased significantly along with more than two times increase in the population of tumor specific OTIs (**Fig. 5.26B**) confirming the fact that population of tumor specific T cells is improved in our ISL due to adjacency to tumor antigens plus a homing niche for activation and proliferation.

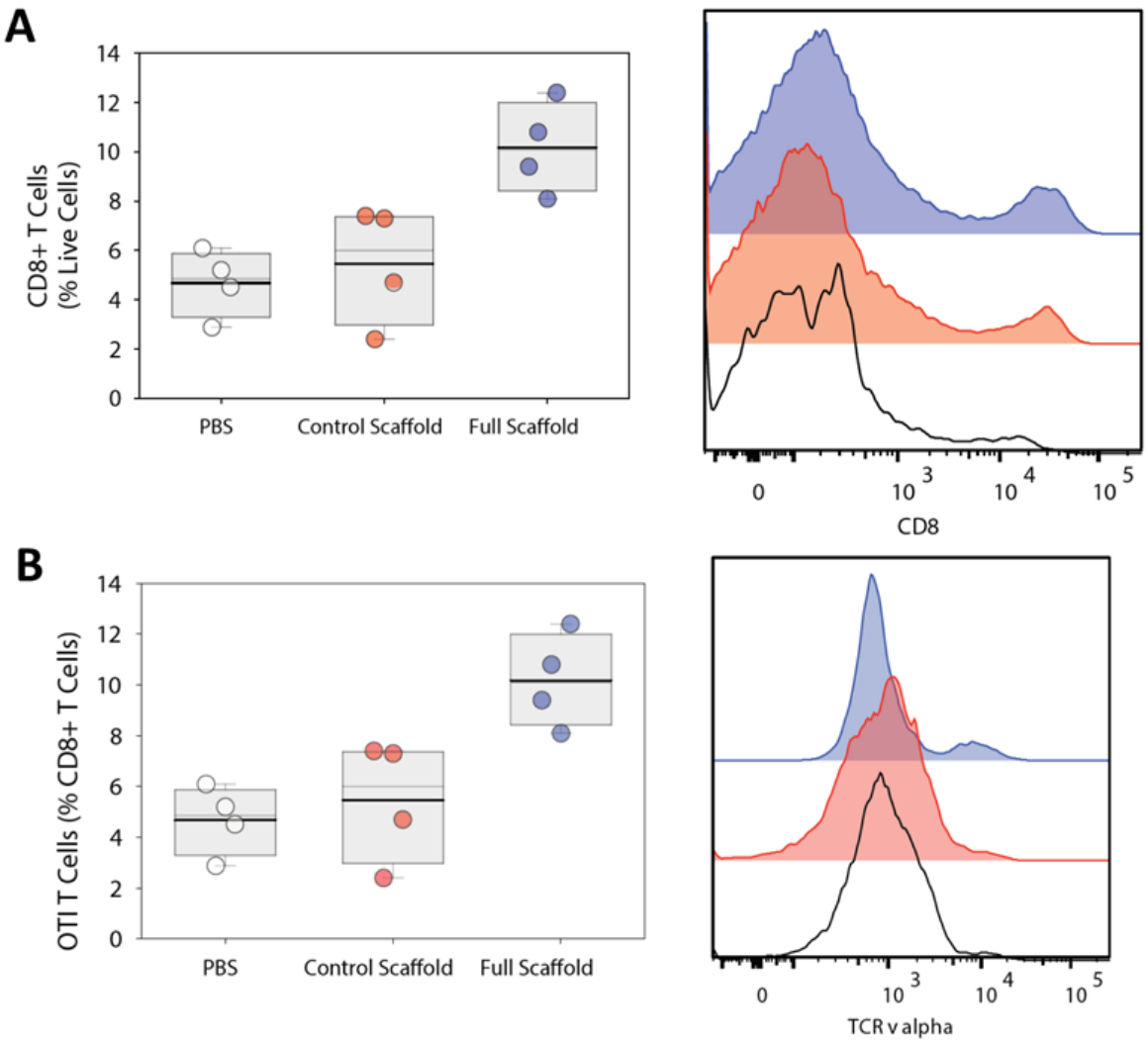

Figure 5.26. ***Presence of CD8+ T cells and OTI T Cells in tumors.*** Flow cytometry analysis of the percentage of (A) CD8+ and (B) OTI CD8+ T cells in tumor 22 days after subcutaneous injection of B16F10-ova cells.

We then assessed the level of GZMB expression of tumor infiltrating T cells in our ISL and we found a 40 percent increase in activated GZMB+ T cells (**Fig. 5.27A,B**). We found no significant difference in the levels of PD-1 expression on day 22 between the examined groups (**Fig. 5.27C**).

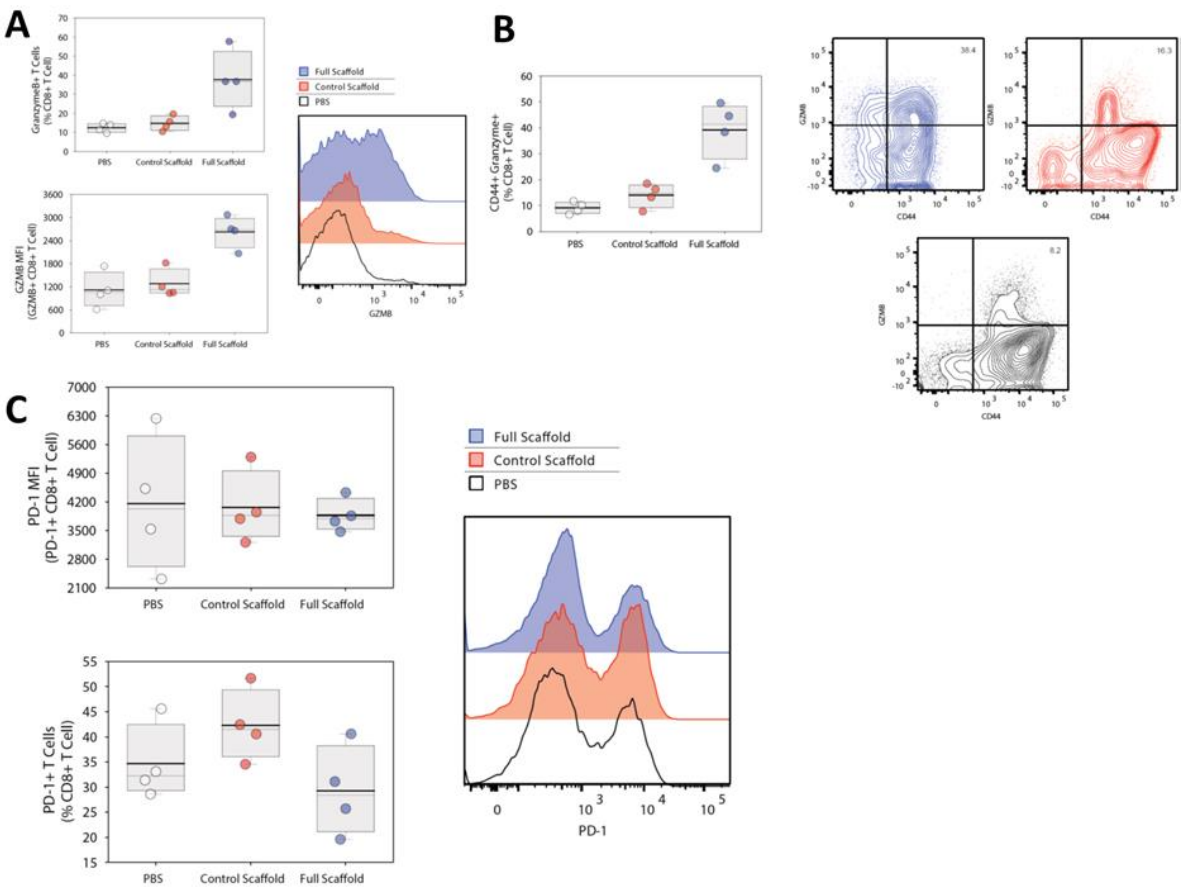

Figure 5.27. ***Presence of Activated CD8+ T Cells inside tumors.*** Flow cytometry analysis of T cell activation is studied 22 days after inoculation of tumor cells. Activated CD8+ T cells in the tumor microenvironment were monitored by measuring their surface CD44 expression as well as Granzyme B (GZMB) intracellular expression. (A) Percentage of T cells with high intracellular expression of GZMB and mean fluorescence intensity (MFI) of T cells upregulating GZMB were plotted alongside with representative flow cytometry graphs. (B) Percentage of T cells with high expression of CD44 activation marker and GZMB effector cytokine were plotted. Representative flow cytometry graphs also presented. (C) Percentage of PD-1 expressing T cells and their MFIs gated on PD-1+ T cells were plotted. Representative flow cytometry graphs also presented.

As mentioned earlier, one of the major hurdles in most solid tumors, such as melanoma, is the immunosuppressive environment which tumor cells promote by inducing formation of Treg. In our platform, TGF-βi (LY2157299) releasing PLGA nanoparticles are designated to reverse tumor's immunosuppressive environment to an immunostimulant one. We were

interested in seeing the effects that our ISL puts in rearranging T cell population around the tumor microenvironment. Treg population was suppressed by about 30 percent with the formulation that carries TGF-βi (**Fig. 5.28**).

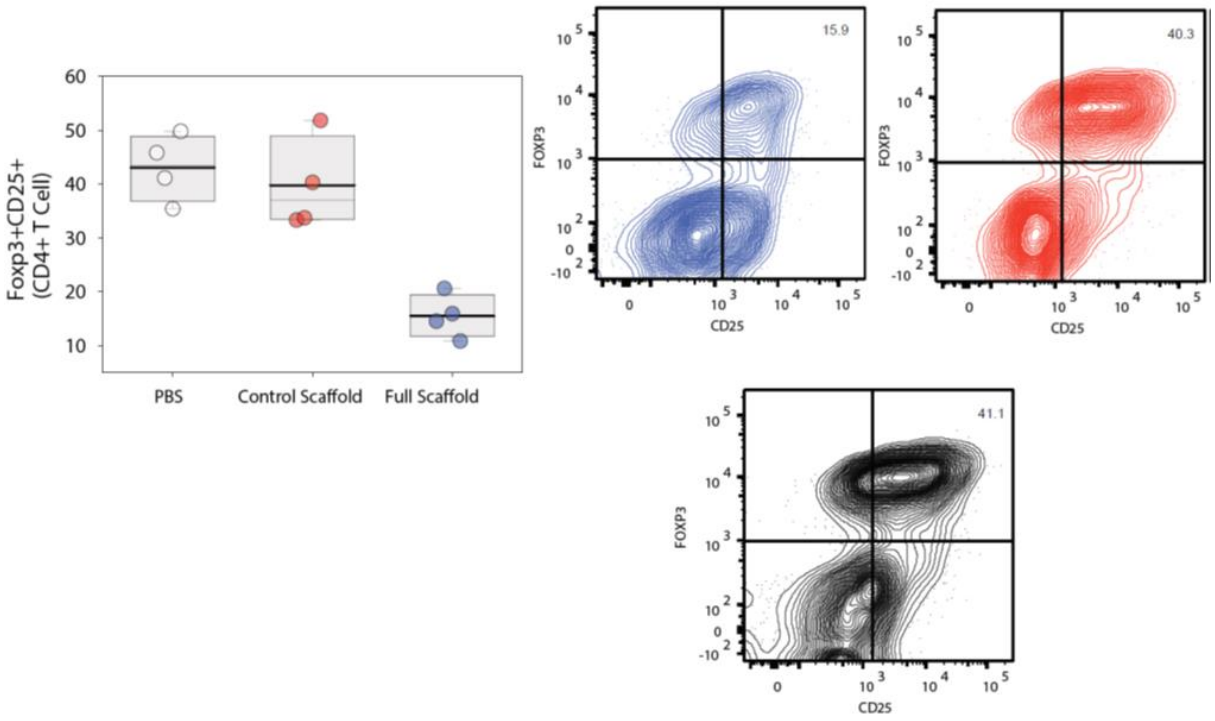

Figure 5.28. The frequency of Foxp3+CD25+CD4+ Tregs in tumor bearing mice. Representative flow cytometry graphs are shown for mice treated with Full Scaffolds (Blue), Control Scaffolds (Red), and PBS (Black).

Furthermore, to see whether our local treatment causes any changes in the population of activated T cells elsewhere we looked into the CD8+ T cells in the draining lymph node (**Fig. 5.29**). Our results showed no significant difference in the population of activated CD8+ T cells (**Fig. 5.29A**) or OT-Is as representative sub populations in the tumor draining lymph nodes (**Fig. 5.29B**).

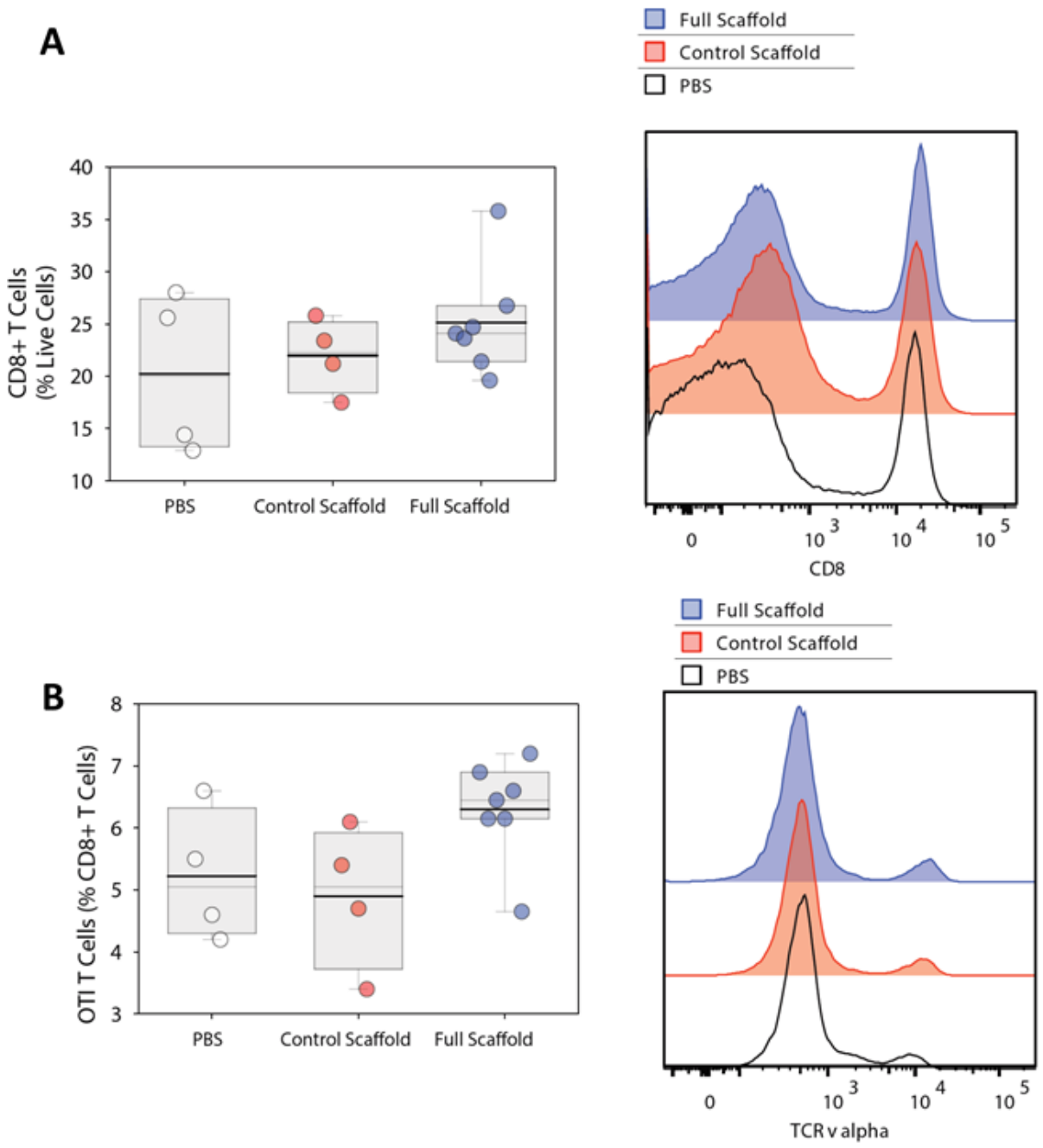

Figure 5.29. ***Presence of CD8+ T cells and OTI T Cells in Tumor Draining Lymph Nodes.*** Flow cytometry analysis of percentage of (A) CD8+ and (B) OTI CD8+ T cells in tumor draining lymph nodes 22 days after subcutaneous injection of B16F10-ova cells in mice receiving different treatment.

Moreover, we did not notice the occurrence of any meaningful changes in the percentage of GZMB+ or PD-1 expressing T cells in our ISL *vs.* control scaffold or PBS control (**Fig. 5.30**).

As mentioned before, one of the major challenges that hampers the therapeutic efficacy of systemic administration of small molecules is the side effects that come with them due to their off-target distribution in other tissues.

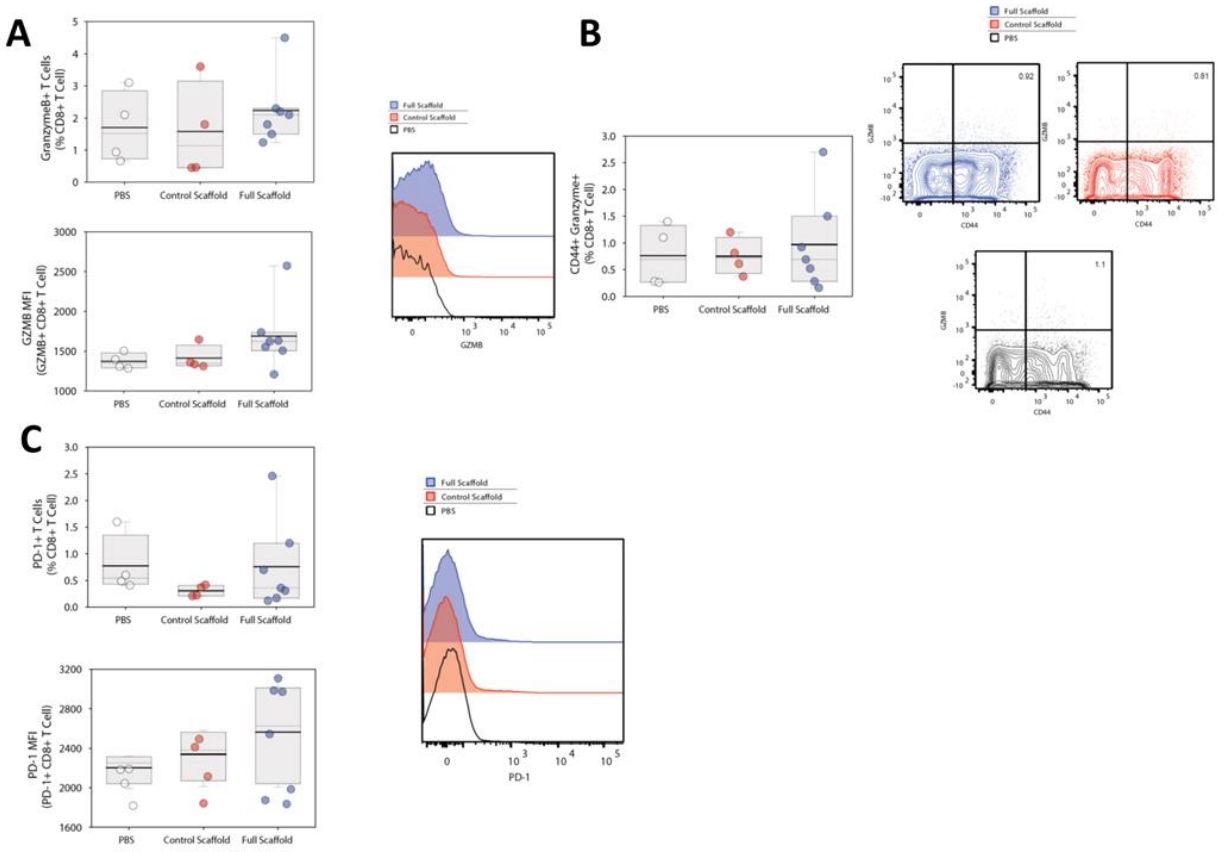

Figure 5.30. Presence of activated CD8+ T cells in tumors draining lymph nodes. Flow cytometry analysis of T cell activation is studied 22 days after inoculation of tumor cells. Activation of CD8+ T cells in the tumor draining lymph nodes was monitored by measuring their surface CD44 expression as well as Granzyme B (GZMB) intracellular expression. (A) Percentage of T cells with high intracellular expression of GZMB and mean fluorescence intensity (MFI) of T cells upregulating GZMB were plotted alongside with representative flow cytometry graphs. (B) Percentage of T cells with high expression of CD44 activation marker and GZMB effector cytokine were plotted. Representative flow cytometry graphs also presented. (C) Percentage of PD-1 expressing T cells and their MFIs gated on PD-1+ T cells were plotted. Representative flow cytometry graphs also presented.

As systemic administration of TGF-βi can result in autoimmune disease[29], we were most interested in studying whether the local release of TGF-βi adjacent to the tumor will result in

suppression of Tregs in the draining lymph not or not. Interestingly our results showed no significant changes in Treg populations in the draining lymph node (**Fig. 5.31**).

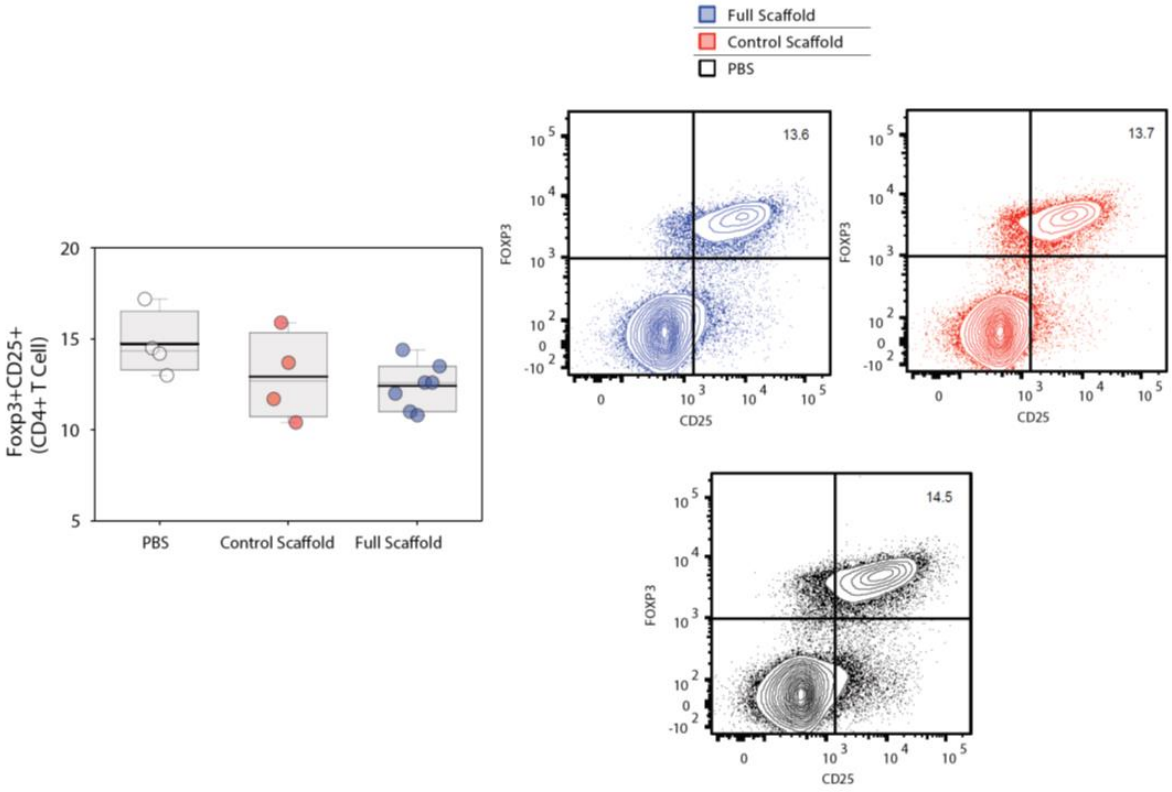

Figure 5.31. The frequency of Foxp3+CD25+CD4+ Tregs in tumor draining lymph nodes. Representative flow cytometry graphs are shown for mice treated with Full Scaffolds (Blue), Control Scaffolds (Red), and PBS (Black).

Additionally, we looked into the changes in the population of T cells in the spleen and found that activated CD8+ T cells were slightly (about 6%) increased using our ISL compared to control scaffold (**Fig. 5.32A**) while the changes in the population of TCR V-alpha positive T cells as a representative population was not meaningful (**Fig. 5.32B**).

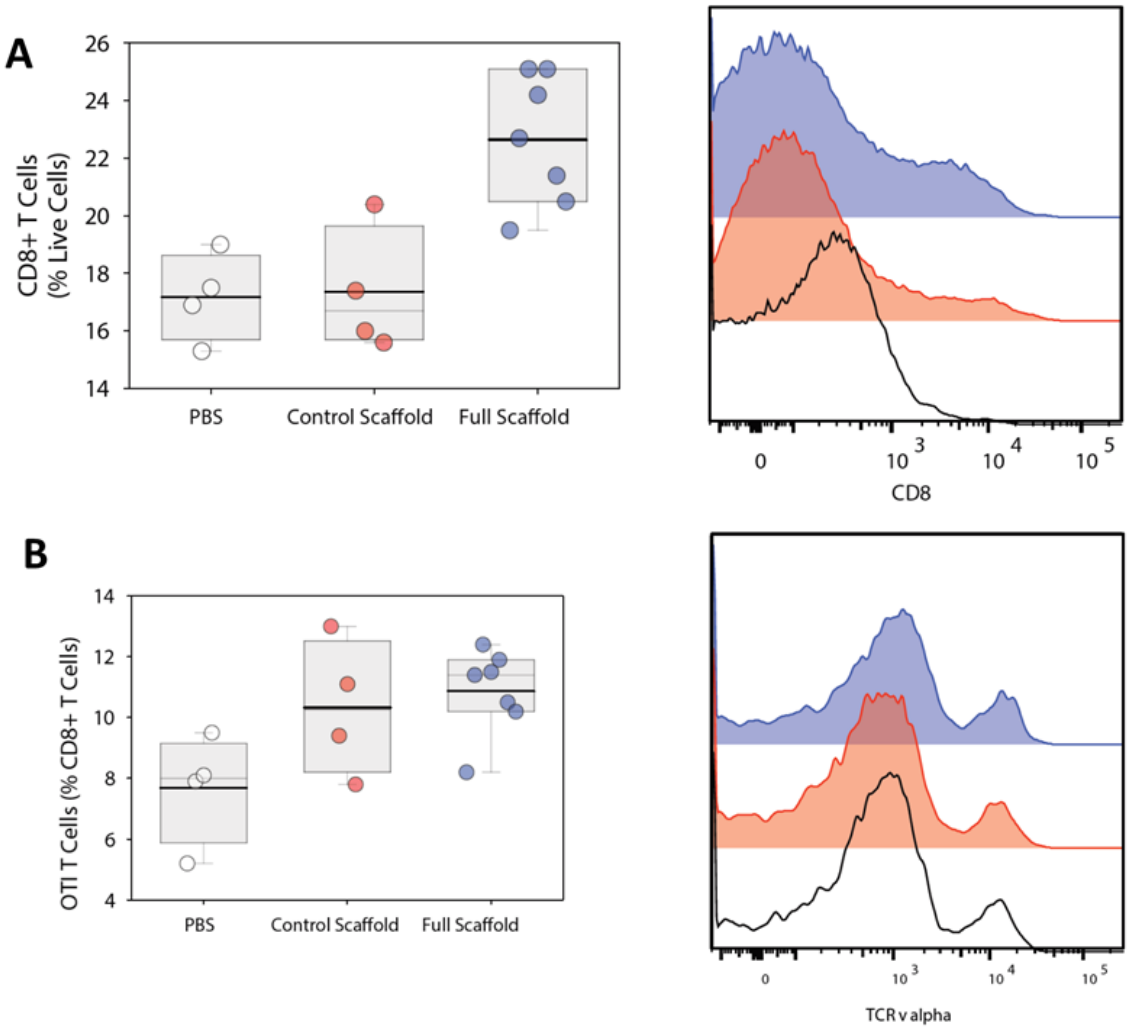

Figure 5.32. Presence of CD8+ T cells and OTI T Cells in Spleen. Flow cytometry analysis of the percentage of (A) CD8+ and (B) OTI CD8+ T cells in the spleen of tumor-bearing mice 22 days after subcutaneous injection of B16F10-ova cells for mice with different treatments.

Moreover, no significant changes in the population of activated, GZMB+ T cells or PD-I expressing CD8+ T cells was observed in the spleen using our ISL *vs.* control conditions (**Fig. 5.33**).

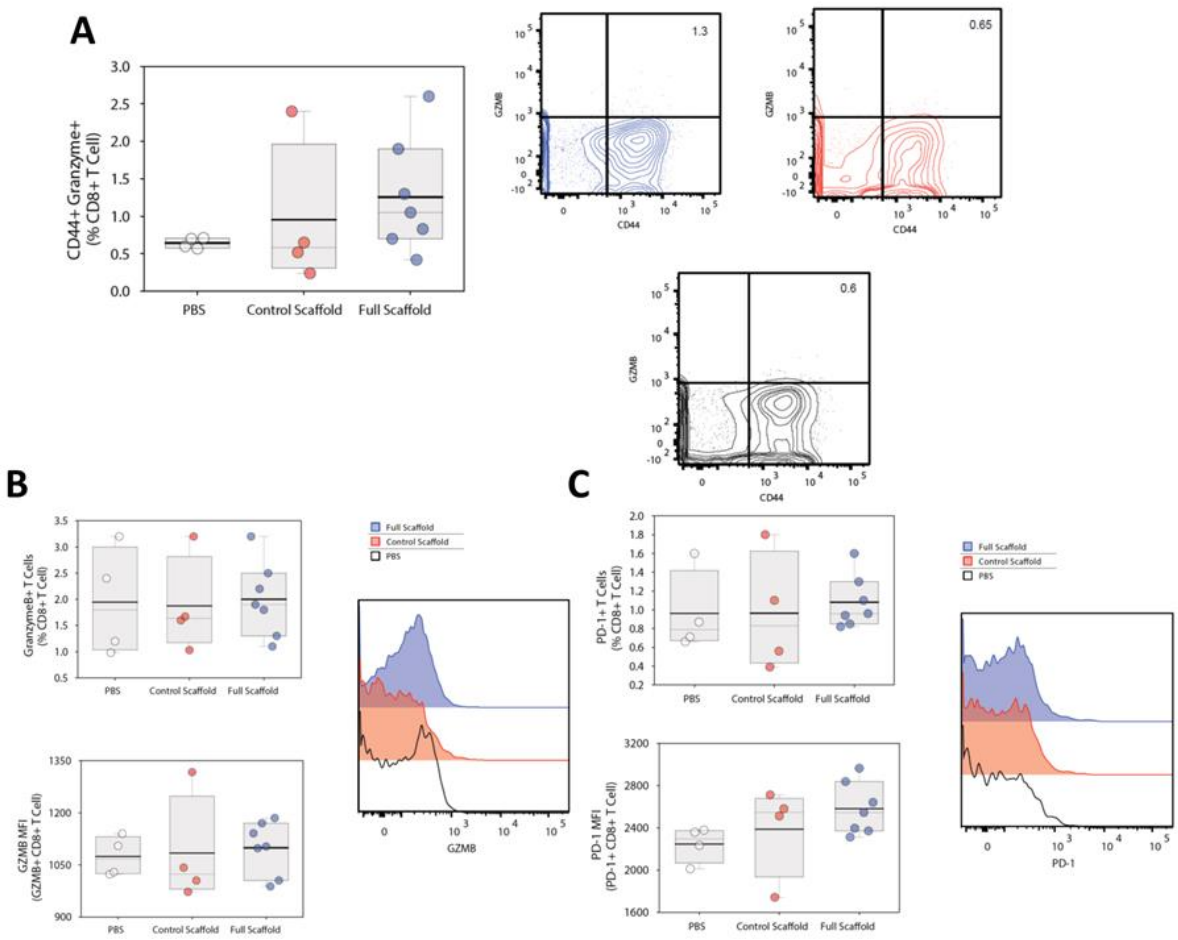

Figure 5.33. Presence of activated CD8+ T cells in spleen. Flow cytometry analysis of T cell activation is studied 22 days after inoculation of tumor cells. Percentage of GZMB+CD44+ T cells was similar in treated vs untreated conditions accompanied with their FACS representatives (A) Percentage of T cells with high intracellular expression of GZMB and mean fluorescence intensity (MFI) of T cells upregulating GZMB were plotted alongside with representative flow cytometry graphs (B). (C) Percentage of PD-1 expressing T cells and their MFIs gated on PD-1+ T cells were plotted. Representative flow cytometry graphs also presented.

In order to advertise our scaffolds specifically for T cells we picked CCL21 as our chemokine. CCL21 as one of the major ligands of CCR7 is considered as the principal integrin activating chemokine. There are some reports on the possible role of CCL21 in recruitment of effector cells.[30,31] On the other hand, stromal cell-derived factor 1 alpha (SDF-1α) is another common chemokine known to regulate migration of many types of cells, especially progenitor cells.[32,33] To verify which chemokine serves our purpose best we kept all the components of the

scaffolds the same except for the chemokine. As shown in **Fig. 34** and **Fig. 35** no significant difference in terms of tumor size or mass was noticed.

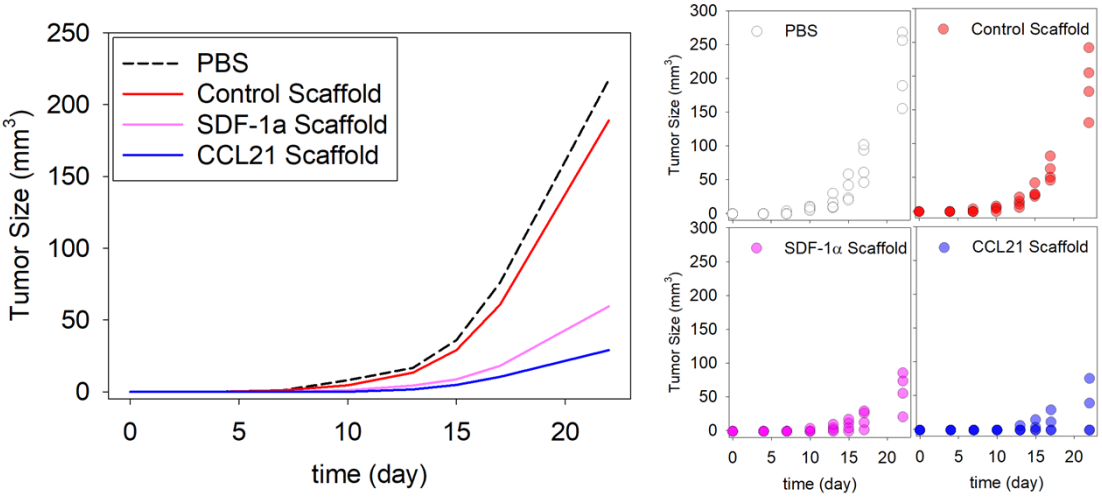

Figure 5.34. Engineered scaffolds can suppress growth of melanoma tumors via recruitment of endogenous T cells. Melanoma (B16-F10-Ova) tumor growth in wild-type mice with full, control scaffolds or PBS treatment (n= 4-7). Here the therapeutic effects of two chemokines (CCL21 and SDF-1a) was studied. Each point represents a mouse.

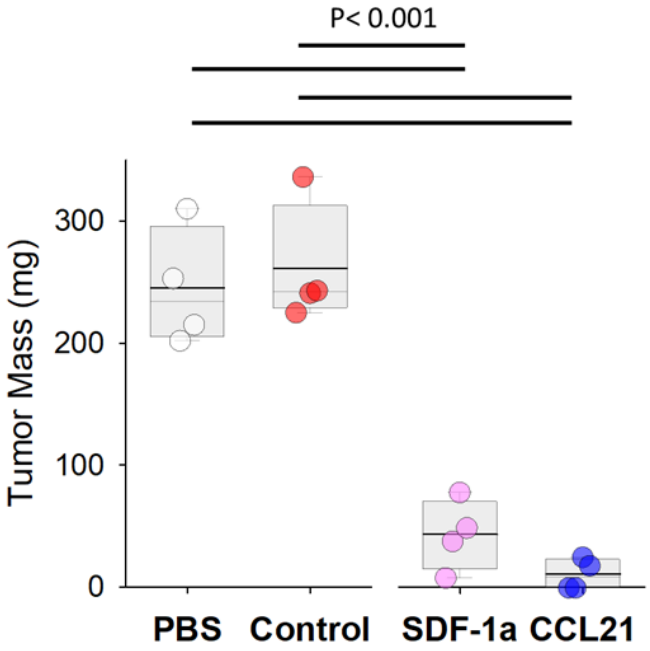

Figure 5.35. Engineered scaffolds can suppress growth of melanoma tumors via recruitment of endogenous T cells. Melanoma (B16-F10-Ova) tumor masses were measured

22 days after tumor inoculation in wild-type mice treated with Full or control scaffolds or PBS treatment (n= 4-7). Here the therapeutic effects of two chemokines (CCL21 and SDF-1a) was studied. Each point represents a mouse.

However, the percentage of recruited CD8+ *via* CCL21 was slightly higher and the population of non-CD8+ cells recruited in the scaffolds containing SDF-1α were visibly higher (**Fig. 5.36**).

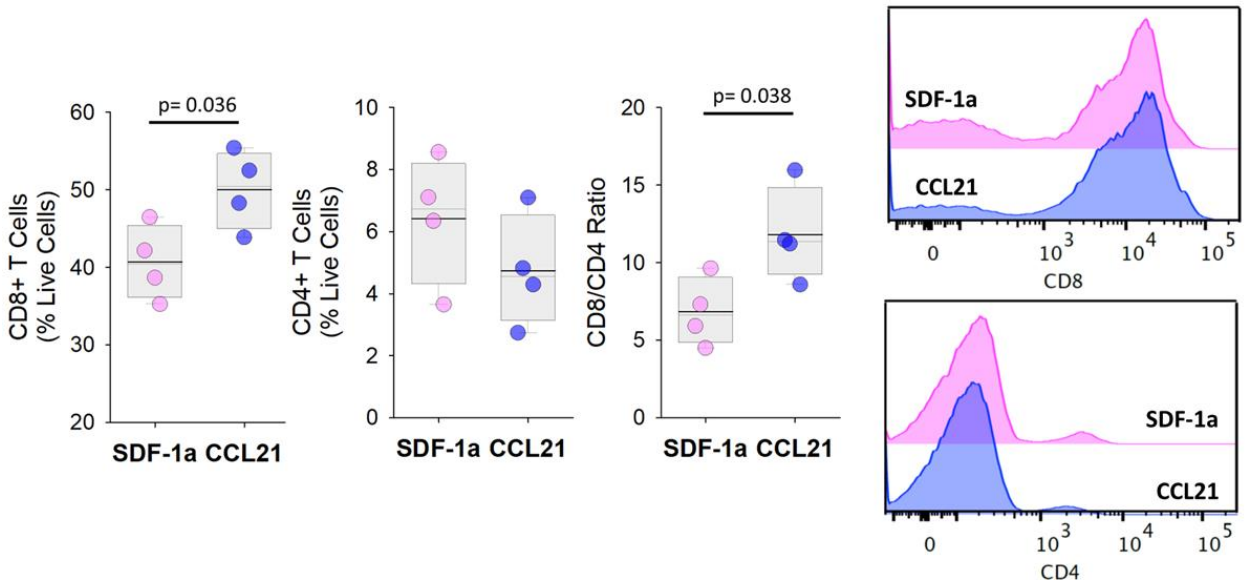

Figure 5.36. Status of Recruited T Cells in scaffolds. (A) Flow cytometry analysis of CD4+ and CD8+ T cells recruited by the scaffolds 17 days after subcutaneous implantation of cell-free (Full) scaffolds releasing either CCL21 or SDF-1a chemokines (n=4). FACS quantification of CD8-to-CD4 ratio of recruited T cells extracted from full and control scaffolds.

Additionally, more activated CD8+ T cells were found in scaffolds with CCL21 (**Fig. 5.37**) while GZMB secreting populations were pretty similar in both conditions. Together these data convinced us that CCL21 favors recruitment of CD8+ T cells more than SDF-1α.

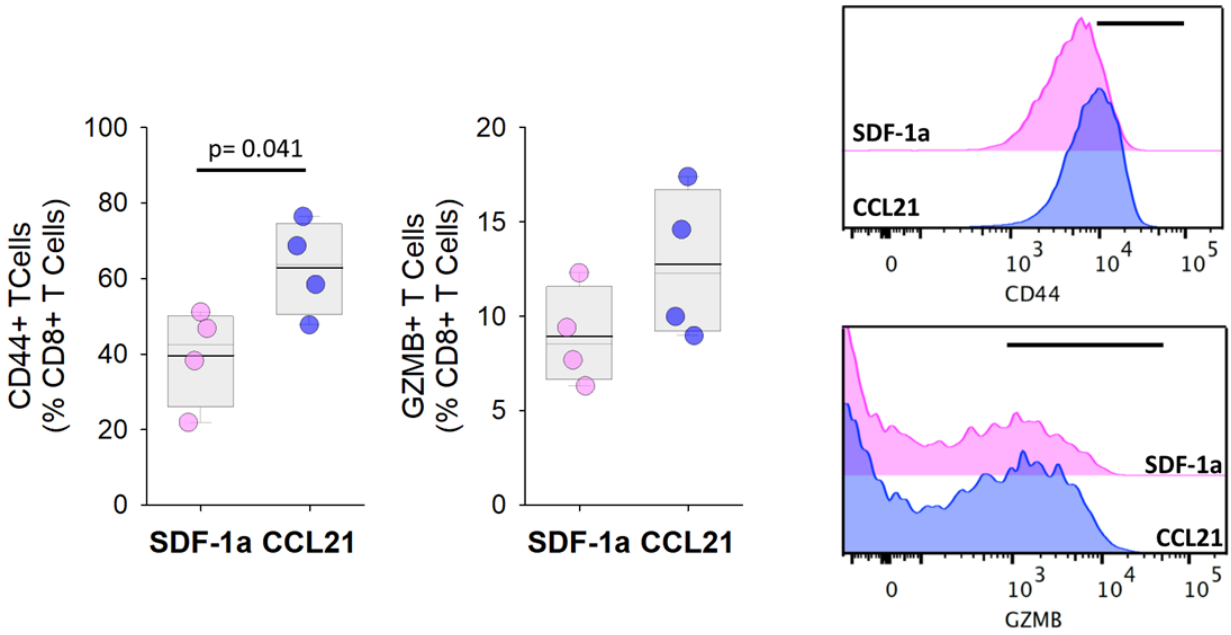

Figure 5.37. The frequency of activated CD44+CD8+ and GZMB+CD8+ in scaffolds after treating mice with Full Scaffolds releasing either CCL21 or SDF-1a chemokines (n=4). Representative flow cytometry data were provided.

5.2.5. Stability and shelf-life evaluation of the scaffolds

In order to test the stability and shelf-life of lyophilized scaffolds after 6-months in 4°C both fresh and 6-months old scaffolds were implanted in mice and checked for their capability of T cell recruitment and activation (**Fig. 5.38A**). In terms of tumor suppression both the freshly made and 6-months old scaffolds did pretty well (**Fig. 5.38**).

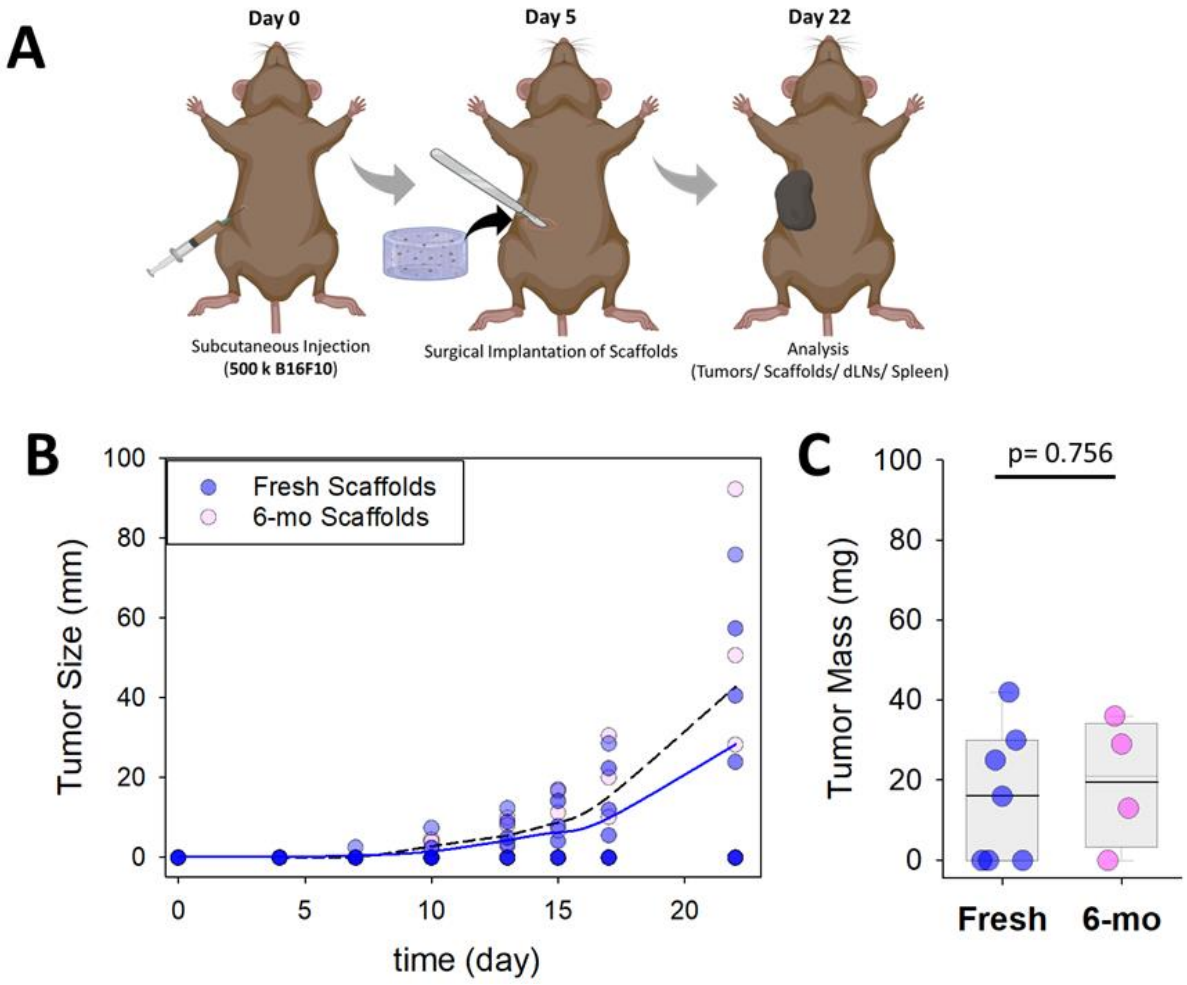

Figure 5.38. Engineered scaffolds can preserve their therapeutic function several months after fabrication. (A) Timing of tumor inoculation and follow up surgical implantation of cells-free scaffolds. (B) Melanoma (B16-F10-Ova) tumor growth and (C) final tumor masses were measured 22 days after tumor inoculation in wild-type mice treated with fresh or 6-months old (Full) scaffolds (n= 4-7). Each point represents a mouse.

As shown in **Fig. 5.39**, percentage of recruited, activated and GZMB+ T cells were pretty identical in old *vs*. fresh scaffolds.

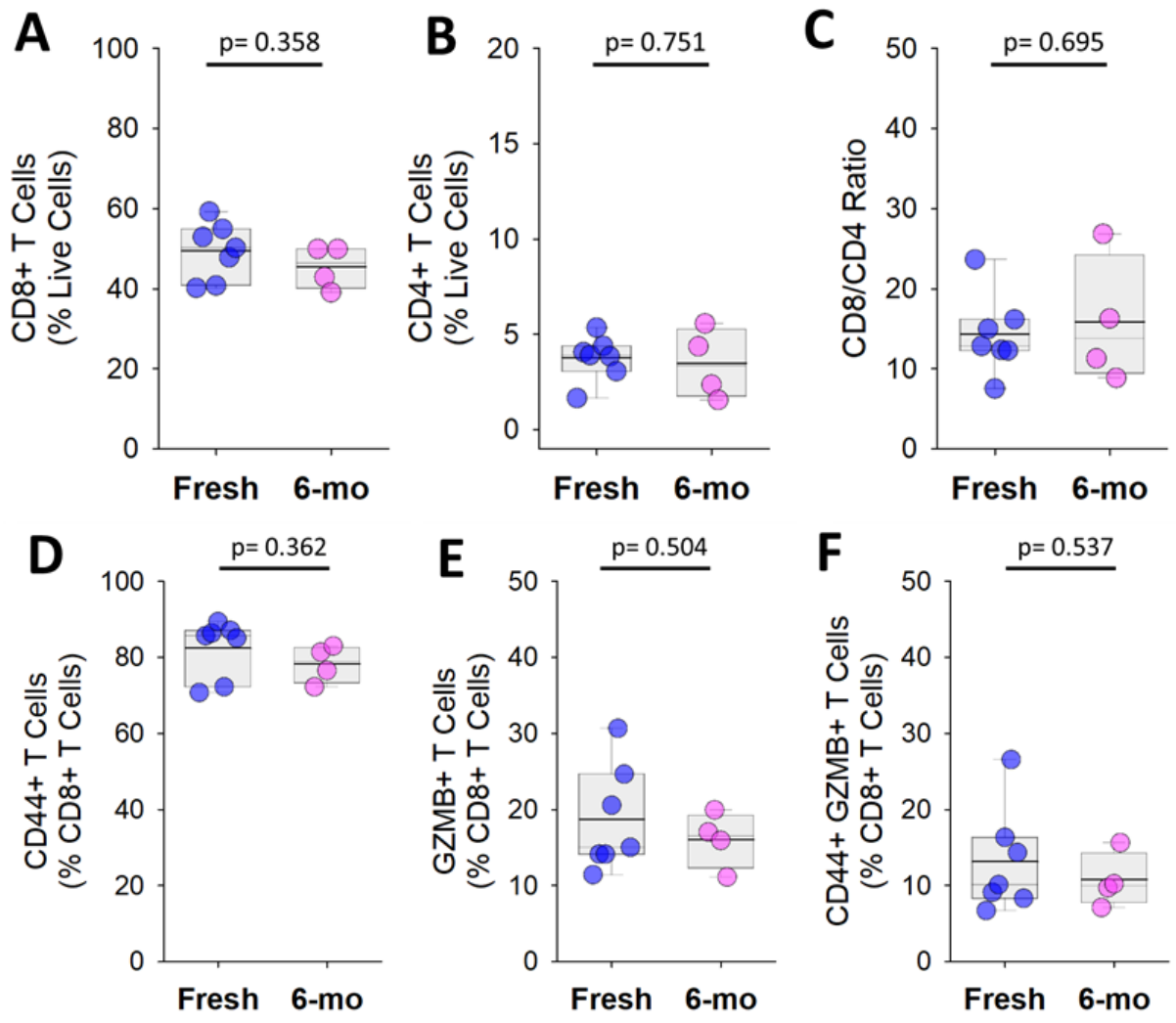

Figure 5.39. Recruitment and activation of endogenous CD8+ and CD4+ T cells in freshly prepared and 6-Month Old Scaffolds. Flow cytometry analysis of percentage of (A) CD8+, and (B) CD4+, (C) ratio of CD8+/CD4+ T cells in the scaffolds. The frequency of activated CD8+ T cells in the scaffolds assessed by (D) CD44, (E) GZMB, as well as (F) co-expression of CD44 and GZMB T cells in freshly prepared or 6-months old Full Scaffolds.

The fact that the percentage of activated GZMB+ T cells and Tregs in the tumors were similar in old *vs*. fresh scaffolds confirms that scaffolds preserve the functionality of loaded drugs and chemokines to good extends (**Fig. 5.40**).

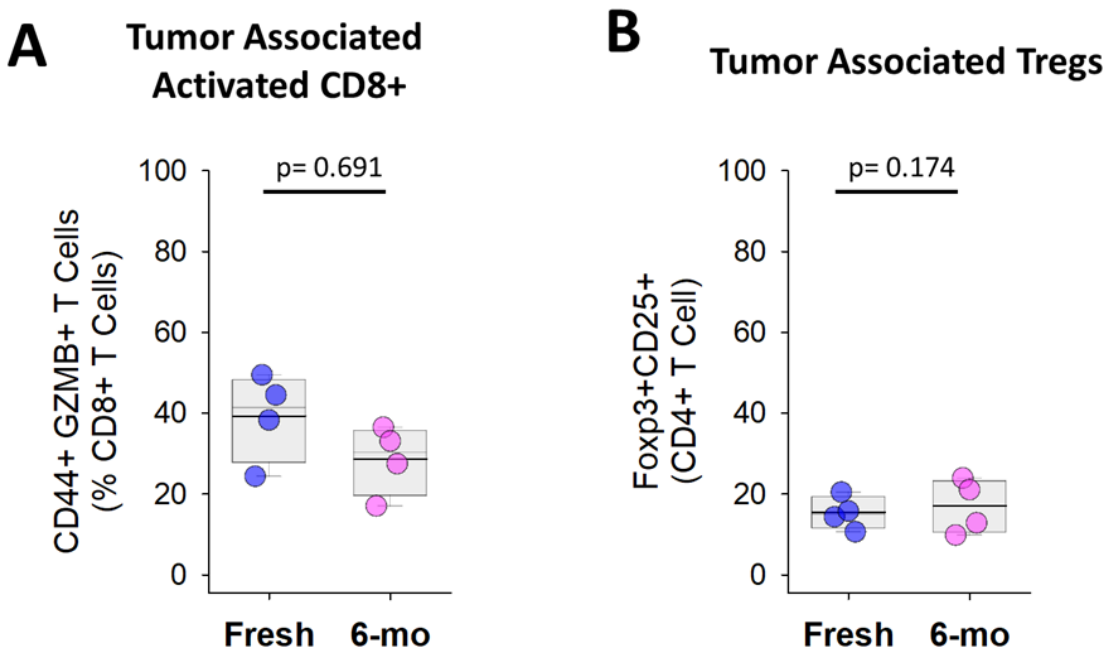

Figure 5.40. The frequency of (A) activated CD44+GZMB+CD8+ (B) Foxp3+CD25+CD4+ Tregs in tumors after being treated with fresh or 6-months old Full Scaffolds.

5.2.6. Treatment of distal tumor through local boosting of T cells

In order to assess the impact of local boosting of T cells adjacent to the primary tumor on formation of systemic immunity we inoculated mice with a second tumor contralateral to the primary one on the same day that we implanted the scaffolds (**Fig. 5.41A,B**). We then monitored tumor growth on both sides and measured the tumor mass at the end of the experiments (**Fig. 5.41C,D**).

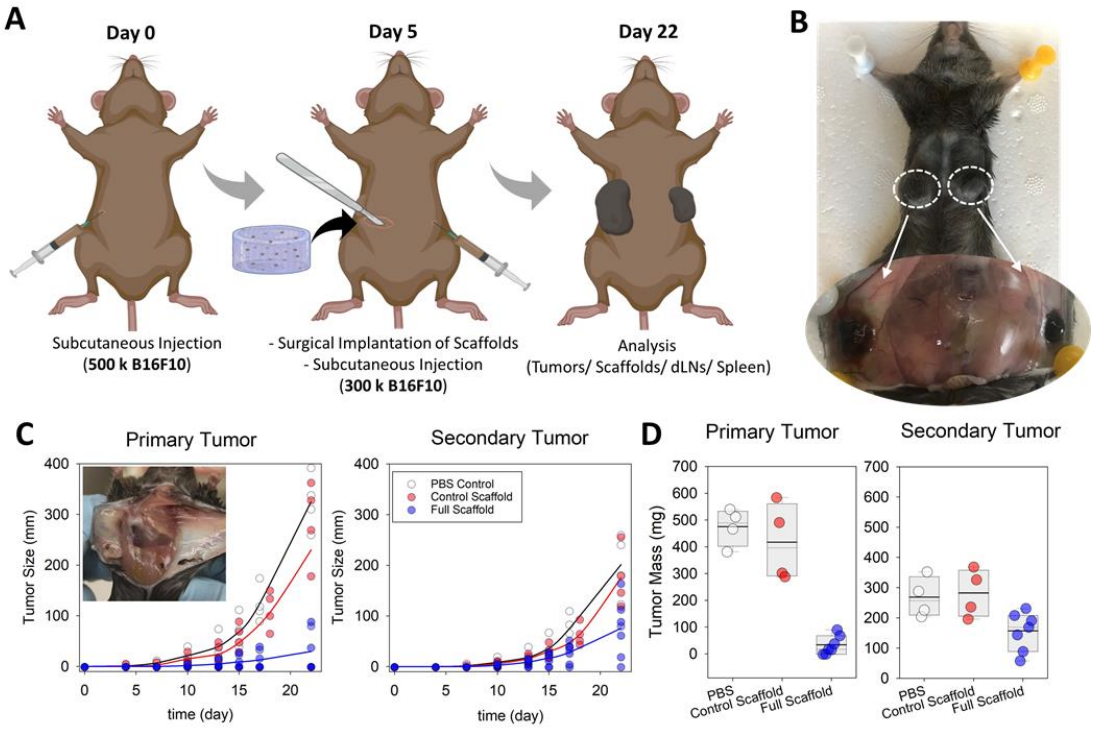

Figure 5.41. Engineered scaffolds not only can suppress the growth of local tumors but they can also affect the distant tumors. (A) Timing of inoculation of primary and secondary tumors and follow up surgical implantation of the cell-free scaffolds. (B) Growth of primary and secondary tumors in the control mouse. (C) Melanoma (B16-F10-Ova) tumor growth and (D) final tumor masses were measured 22 days after inoculation of primary tumors in wild-type mice treated with Full or control scaffolds (n= 4-7). Each point represents a mouse.

Strikingly tumor growth in the secondary tumor was suppressed by about 40 percent upon local treatment of the primary tumor with scaffolds. Percentage of tumor infiltrating CD8+ T cells was increased by more than two times in the contralateral tumor of the mice that received scaffold treatment (**Fig. 5.42**).

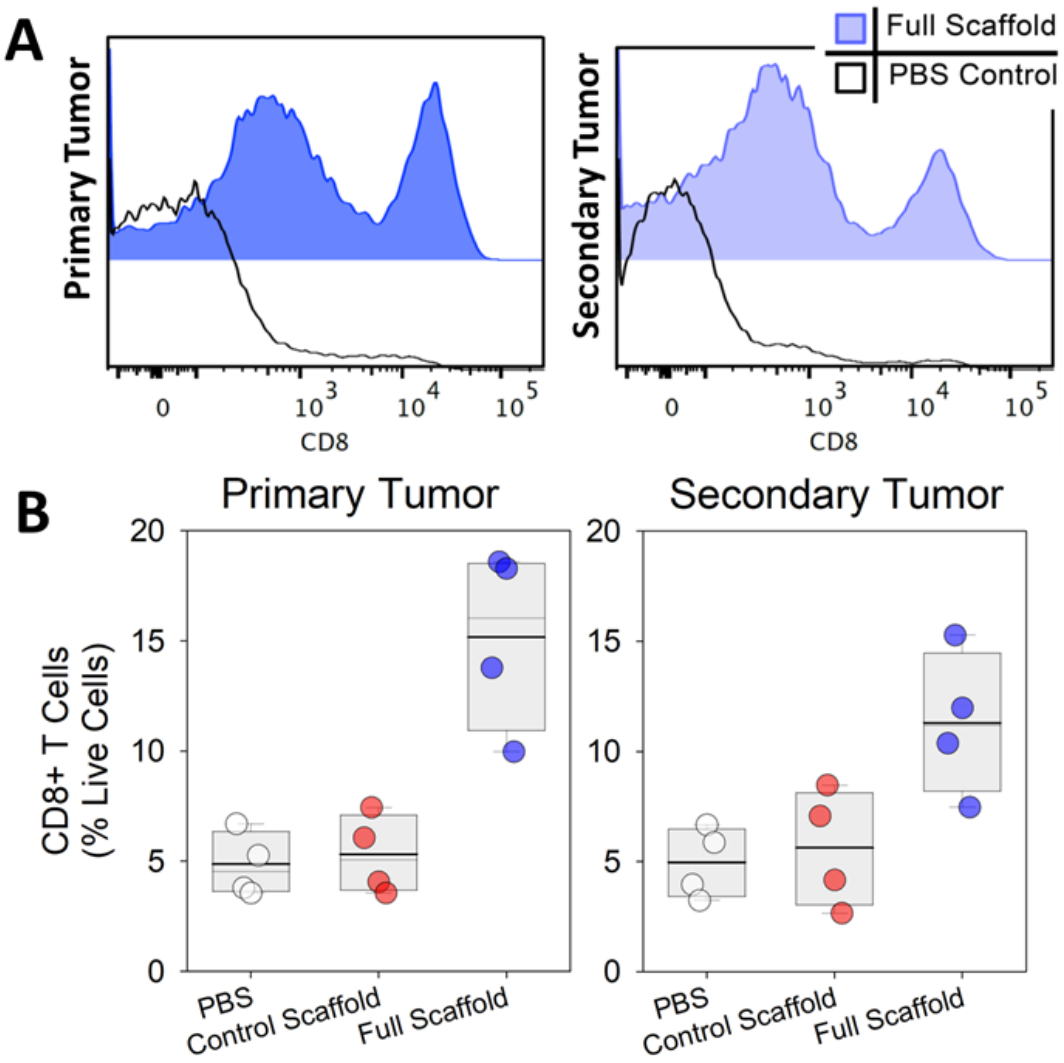

Figure 5.42. (A) Representative flow cytometry study of CD8+ T cells present in the primary and secondary tumors after being treated with Full or control Scaffolds. (B) The frequency of CD8+ T cells in primary and secondary tumors (n=4).

Higher infiltration of CD8+ T cells in both primary and secondary tumors was also confirmed with immunofluorescence staining of tumor sections against CD8 antibodies (**Fig. 5.43**). We did not notice meaningful differences in the population of PD-1+ T cells in either of the tumors (**Fig. 5.44**).

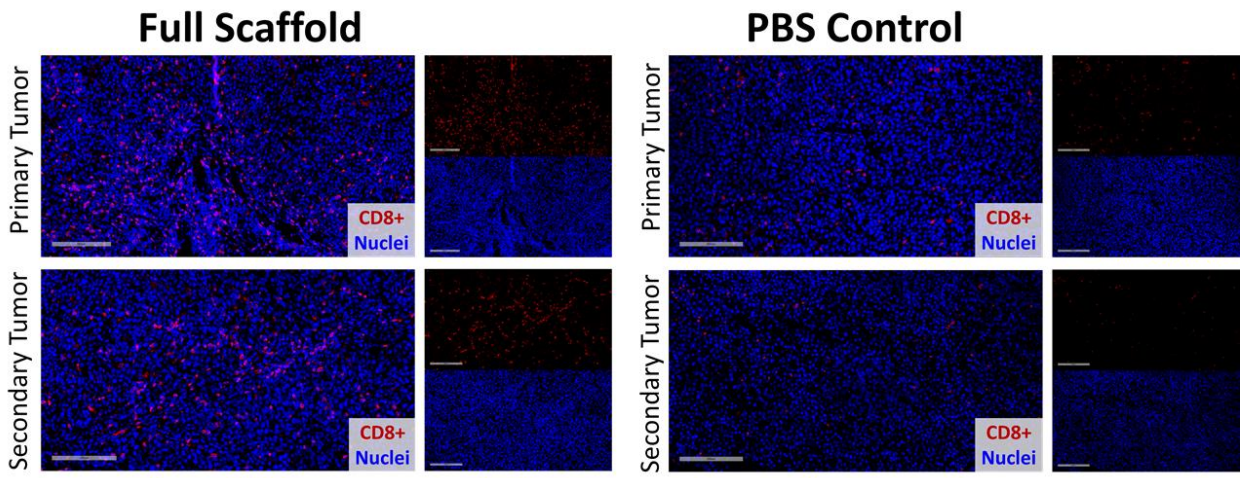

Figure 5.43. Tumor-associated CD8+ T cells were stained in primary and secondary tumors 22 days after tumor inoculation. Note: As 3 out of 7 mice treated with Full scaffold formulation did not grow tumors, these representative sections were only found in the few mice with remaining tumors.

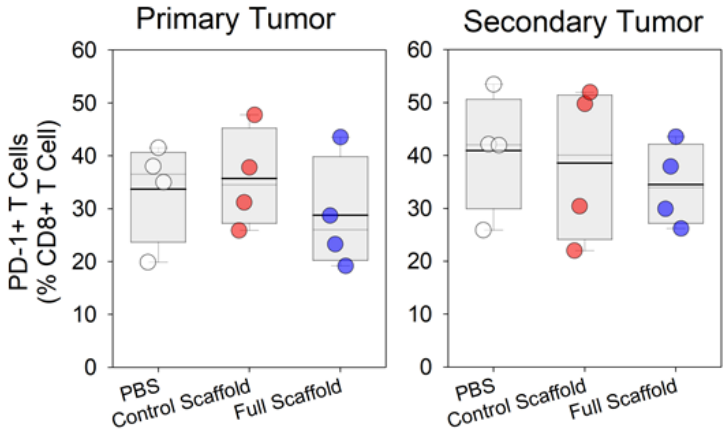

Figure 5.44. Flow cytometry study of PD-1+CD8+ T cells present in primary and secondary tumors after being treated with Full or control Scaffolds. (n=4).

Population of activated GranzymeB secreting CD8+ T cells was considerably improved in the contralateral tumor as well as primary tumor which indicates that some of the tumor recognizing T cells that got trained adjacent to primary tumor were able to make it to the distant tumor (**Fig. 5.45** and **Fig. 5.46**).

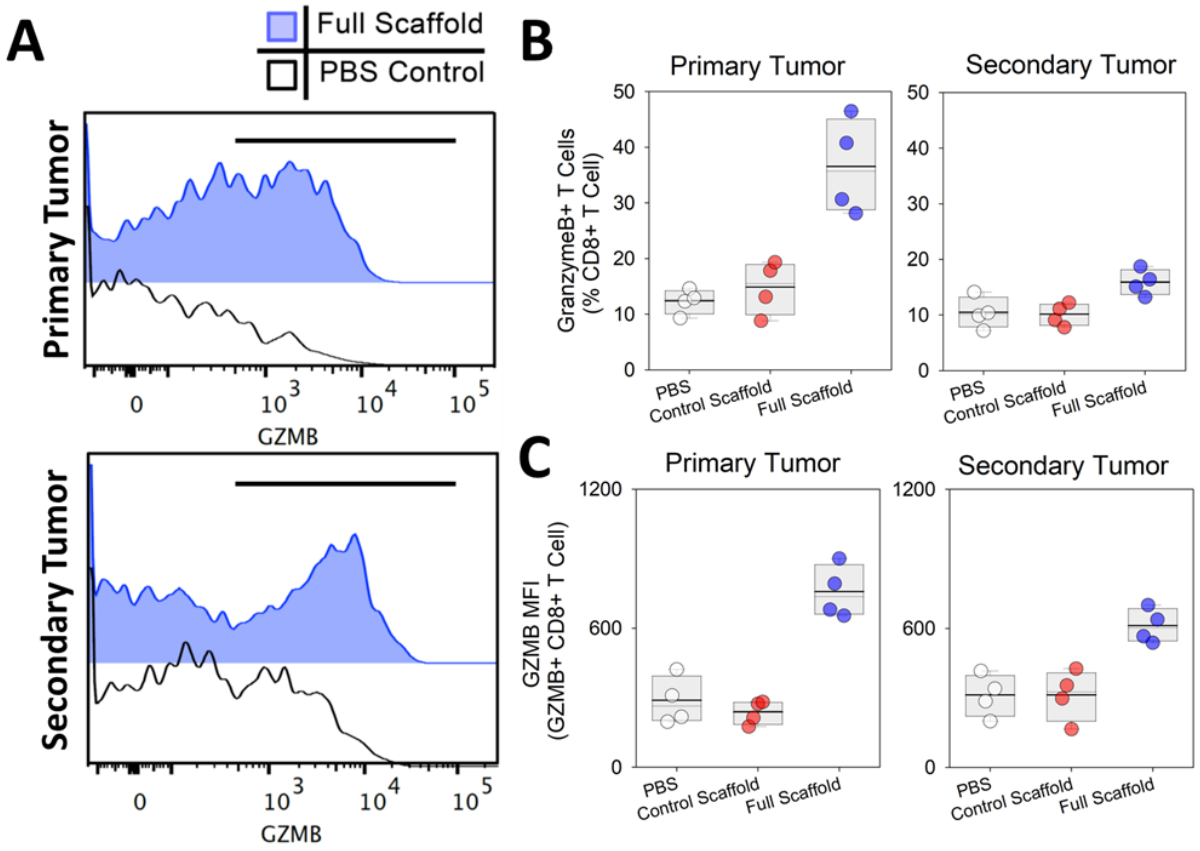

Figure 5.45. (A) Flow cytometry study of GZMB+CD8+ T cell presence in primary and secondary tumors after being treated with Full or control Scaffolds. The frequency (B) and MFI of GZMB+CD8+ T cells in primary and secondary tumors (n=4).

T memory response was induced in mice treated with full scaffolds as it was reflected in the drastic increase in the frequency of endogenous central memory (CD44+CD62L+CD8+) T cells (**Fig. 5.46**).

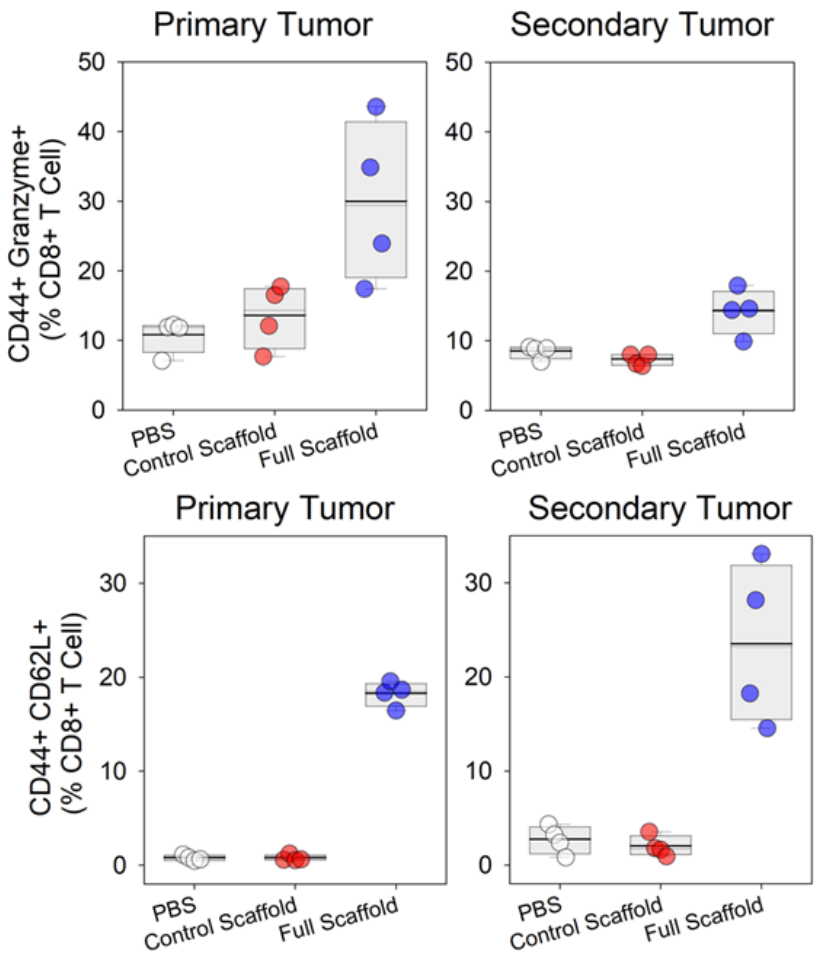

Figure 5.46. Flow cytometry study of the frequency of CD44+GZMB+CD8+ (activated) and CD44+CD62L+CD8+ (central memory) T cells in primary and secondary tumors (n=4).

Additionally, the population of short live effector CD8+ T cells (KLRG1+CD44+) was also considerably improved in both primary and secondary tumor (**Fig. 5.47**).

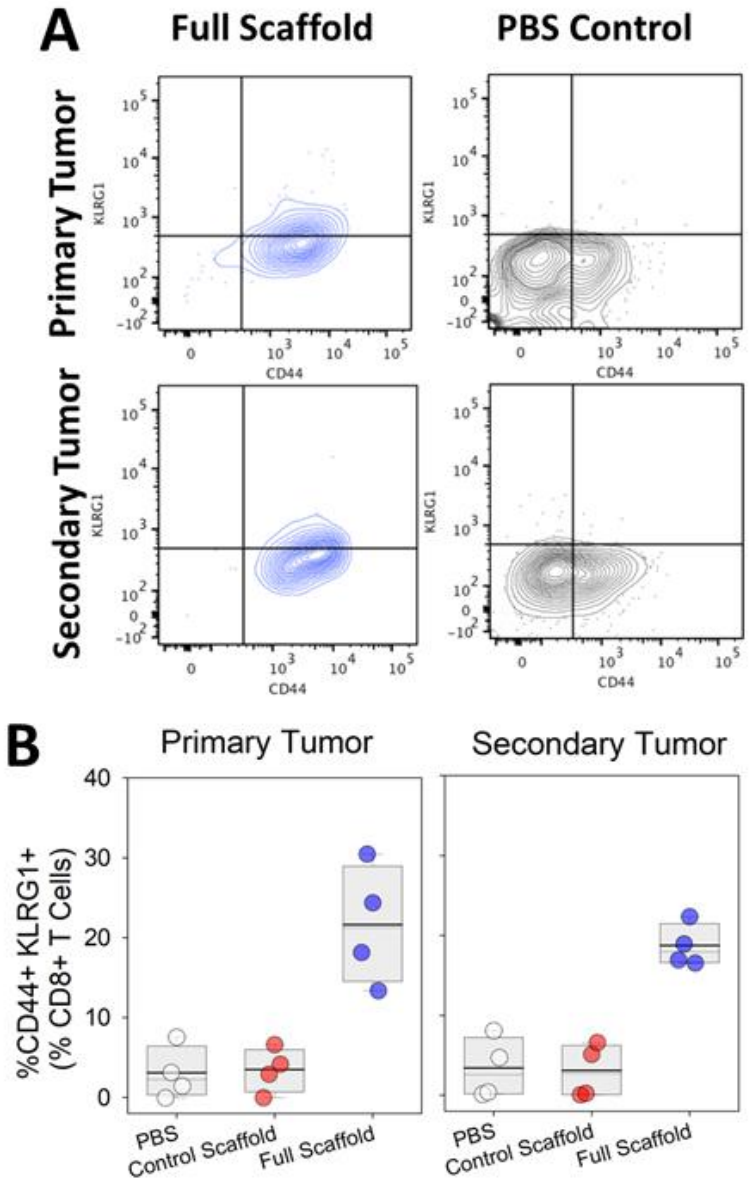

Figure 5.47. Flow cytometry study of CD44+KLRG-1+CD8+ T cell presence in primary and secondary tumors after being treated with Full or control Scaffolds. (A) representative FACS and (B) frequency of (B) CD44+KLRG-1+CD8+ T cells in primary and secondary tumors (n=4).

We also checked for the population of Tregs in both tumors. Since the release of TGFβi is local to the primary tumor where the scaffold is implanted, suppression of regulatory T cells was only observed in the primary tumor and no significant difference was noticed in the secondary tumor (**Fig. 5.48**). The fact that in the primary tumor scaffold is tackling tumor cells from two

angles, one enhancing the population of tumor reactive T cells and the other by suppressing Treg population, compared to secondary tumor where Treg population is undisturbed partially explains the lower suppression of tumor growth in the secondary tumor.

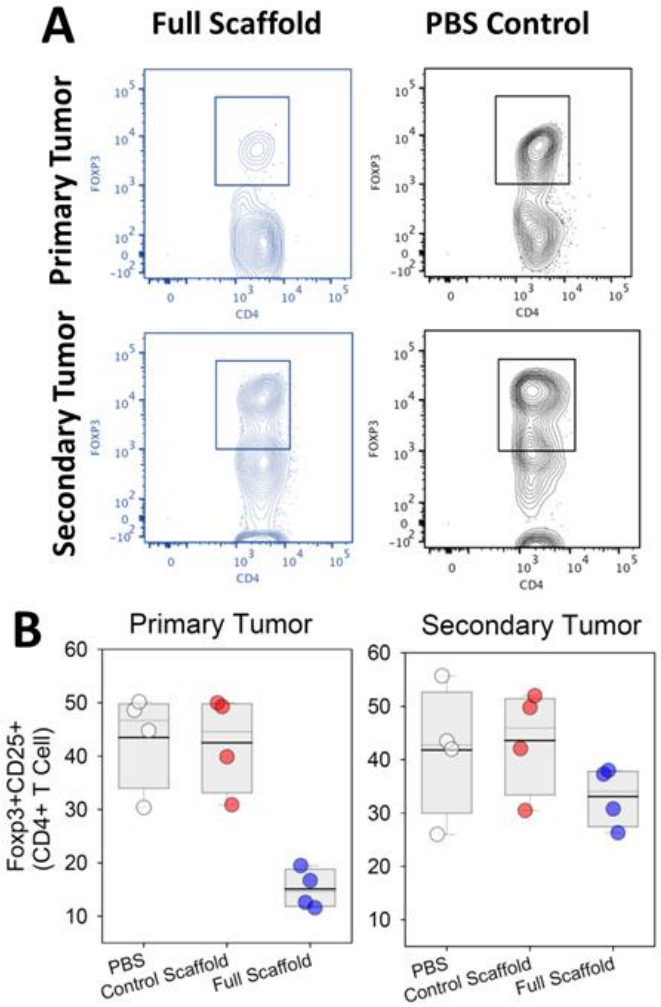

Figure 5.48. (A) Representative flow cytometry of Foxp3+CD25+CD4+ Tregs in primary and secondary tumors for mice treated with Full Scaffolds (Blue) and PBS (Black). (B) The quantified frequency of Foxp3+CD25+CD4+ Tregs in primary and secondary tumors.

We then looked into the T cells recruited by scaffolds (**Fig. 5.49**). Similar to previous results implanted scaffold favored CD8+ T cell recruitment and enhanced CD8 to CD4 ratio in the scaffolds (**Fig. 5.49**).

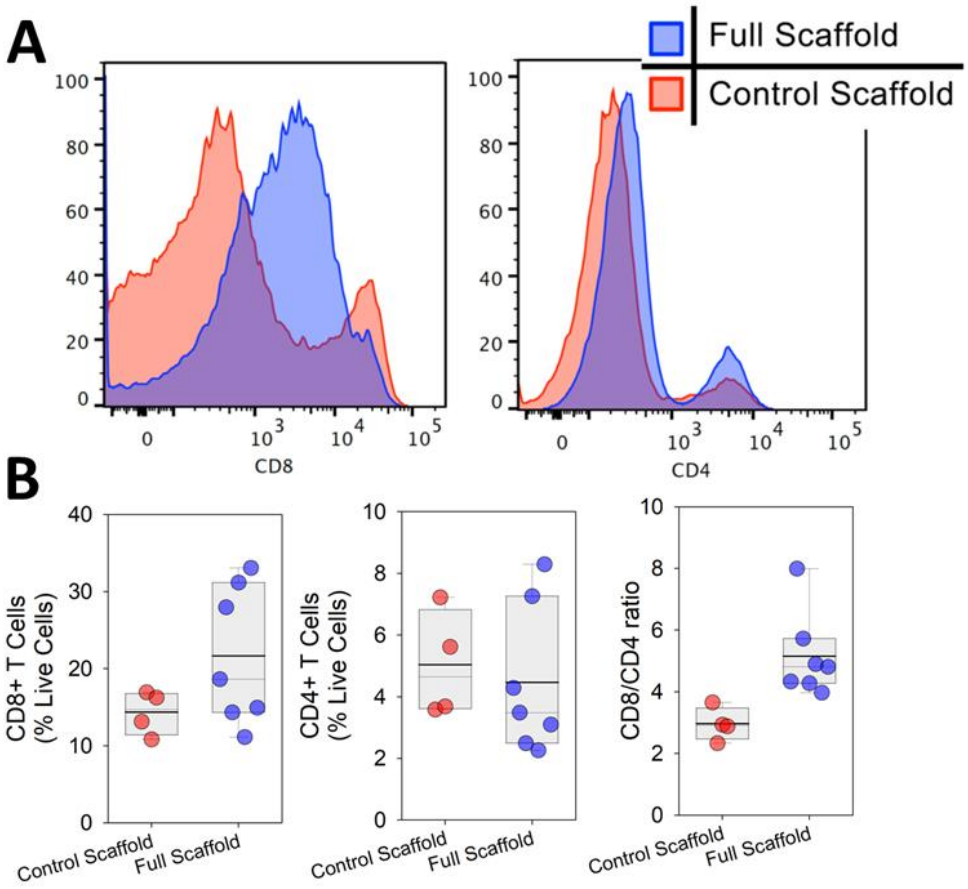

Figure 5.49. (A) Flow cytometry study of CD8+ T cell presence in scaffolds implanted in tumors. (B) The frequency of CD8+ and CD4+ T cells as well as the CD8 to CD4 T cell ratios in Full (n=7) and Control scaffolds (n=4).

Population of both activated and GZMB+ CD8+T cells was also noticeably improved in the full scaffold compared to the control (**Fig. 5.50** and **Fig. 5.51**).

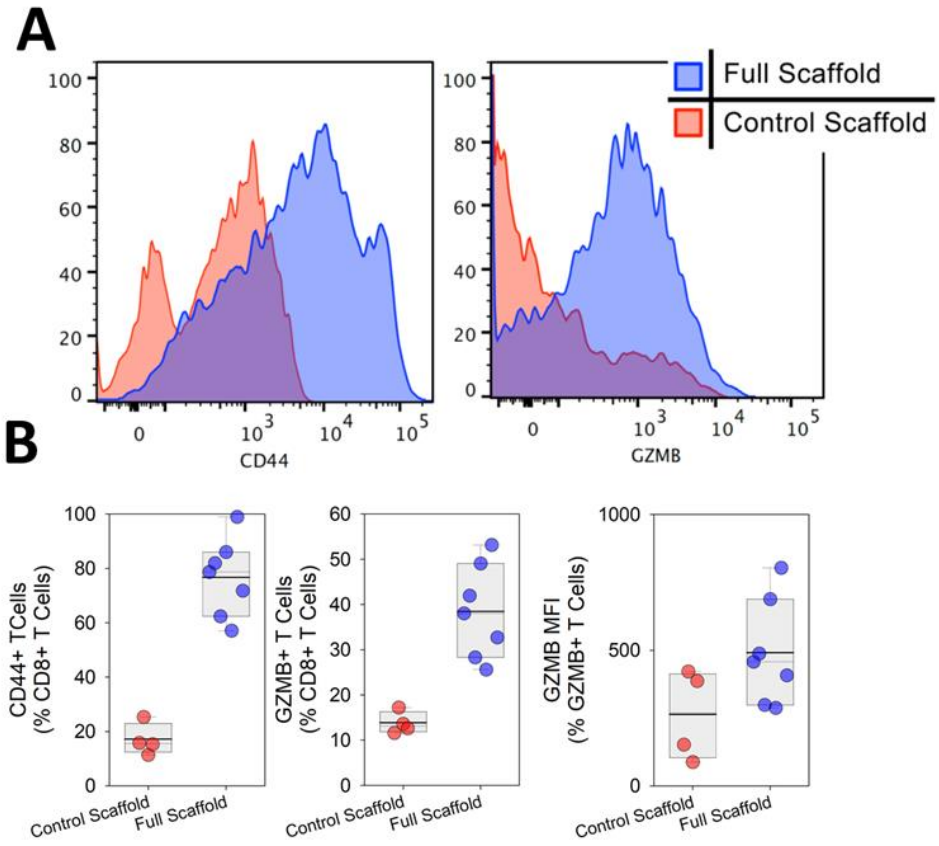

Figure 5.50. Flow cytometry study of CD44+CD8+ and GZMB+CD8+ T cell presence in scaffolds 17 days after being implanted in tumor-bearing mice. (A) representative FACS and (B) frequency of CD44+CD8+ and GZMB+CD8+T cells as well as MFI of GZMB+CD8+ T cells in full (n=7) and control (n=4) scaffolds.

Additionally, short-live effector T cells identified as CD44+KLRG1+ were also improved in the full scaffold (**Fig. 5.51**).

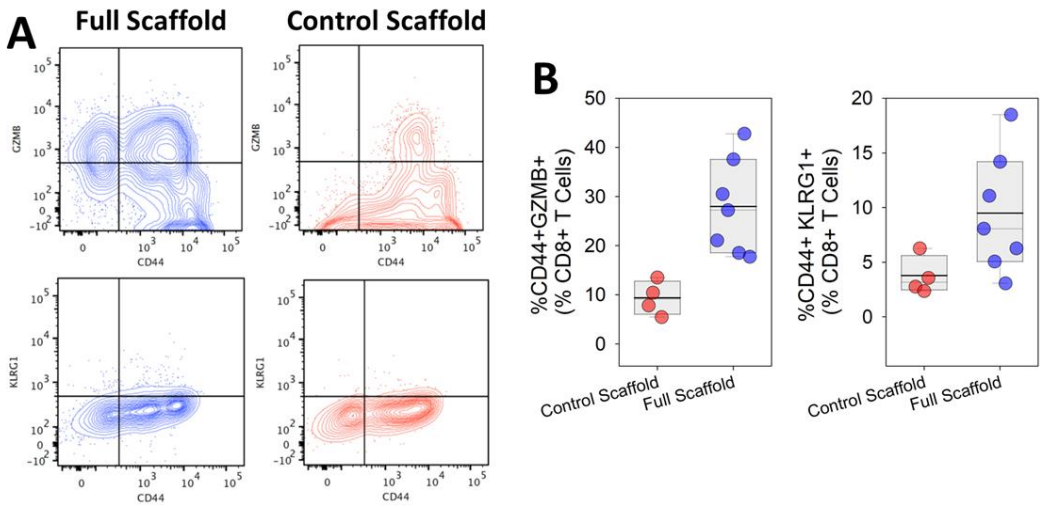

Figure 5.51. Flow cytometry study of CD44+KLRG-1+CD8+ T cell presence in scaffolds 17 days after being implanted in tumor-bearing mice. (A) representative FACS and (B) the frequency of (B) CD44+KLRG-1+CD8+ T cells in Full (n=7) and Control (n=4) scaffolds.

Further we checked the draining lymph nodes of both primary and secondary tumors for the population of CD8+ T cells and GZMB secreting T cells (**Fig. 52**, **Fig. 53**, and **Fig. 54**). Based on these results our local treatment seemed to put no effect on these populations in the draining lymph nodes.

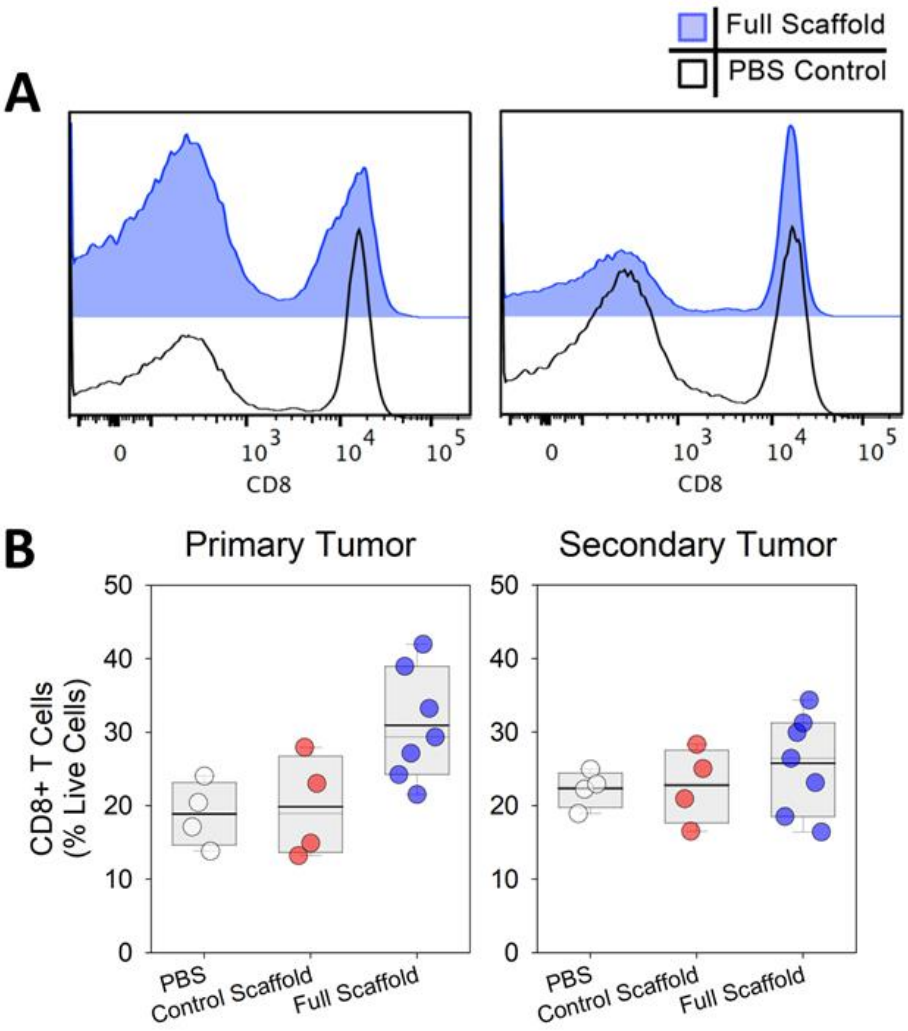

Figure 5.52. Flow cytometry study of CD8+ T cell presence in draining lymph nodes of primary and secondary tumors after being treated with Full (n=7) or Control (n=4) Scaffolds. (A) Representative FACS graphs and (B) The frequency of CD8+ T cells in draining lymph nodes of primary and secondary tumors.

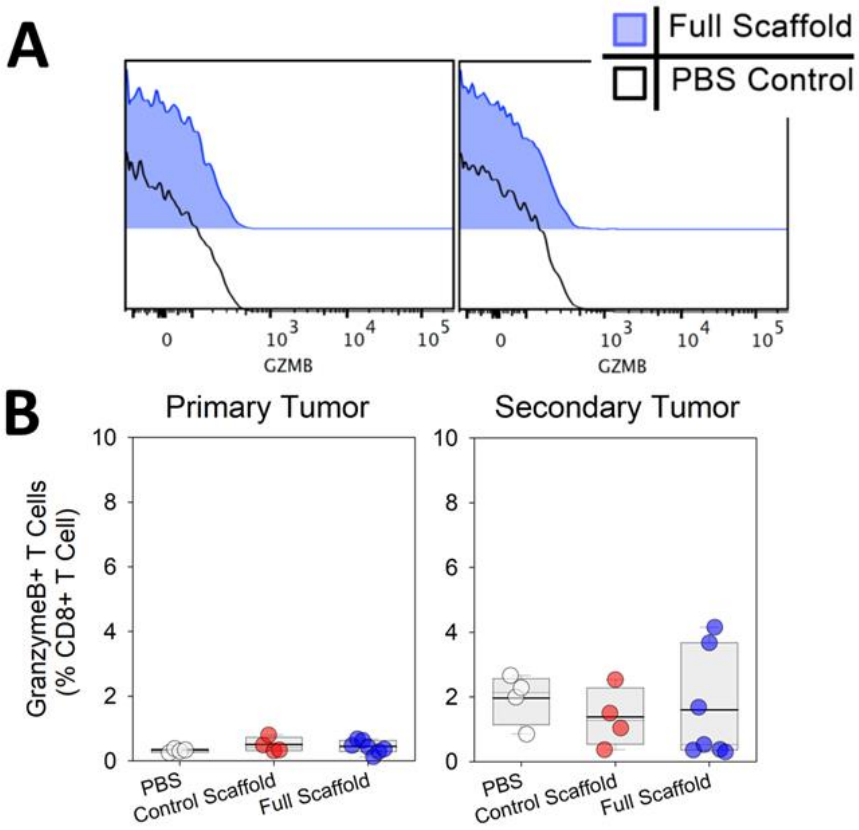

Figure 5.53. Flow cytometry study of GZMB+CD8+ T cell presence in draining lymph nodes of primary and secondary tumors after being treated with Full (n=7) or Control (n=4) Scaffolds. (A) Representative FACS graphs and (B) The frequency of GZMB+CD8+ T cells in draining lymph nodes of primary and secondary tumors.

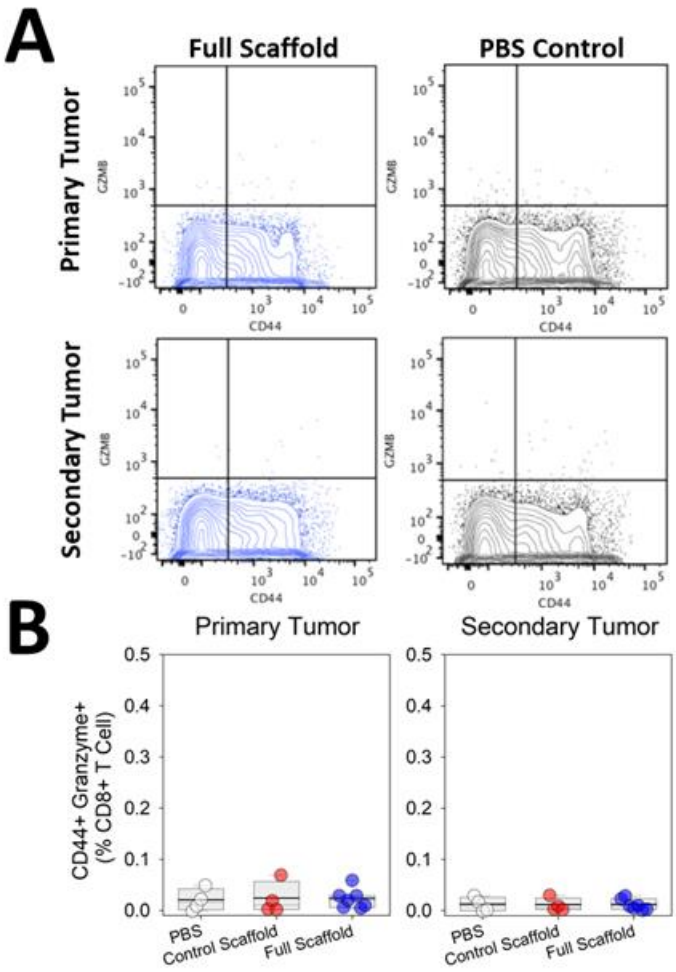

Figure 5.54. Flow cytometry study of CD44+GZMB+CD8+ (effector) T cell presence in draining lymph nodes of primary and secondary tumors after being treated with full (n=7) or control (n=4) Scaffolds. (A) Representative FACS graphs and (B) The frequency of CD44+GZMB+CD8+ T cells in draining lymph nodes of primary and secondary tumors.

Population of central memory T cells were also noticeably higher in the draining lymph nodes of the both primary and secondary confirming the idea that local treatment has partially resulted in systemic immunization against the tumor (**Fig. 55**).

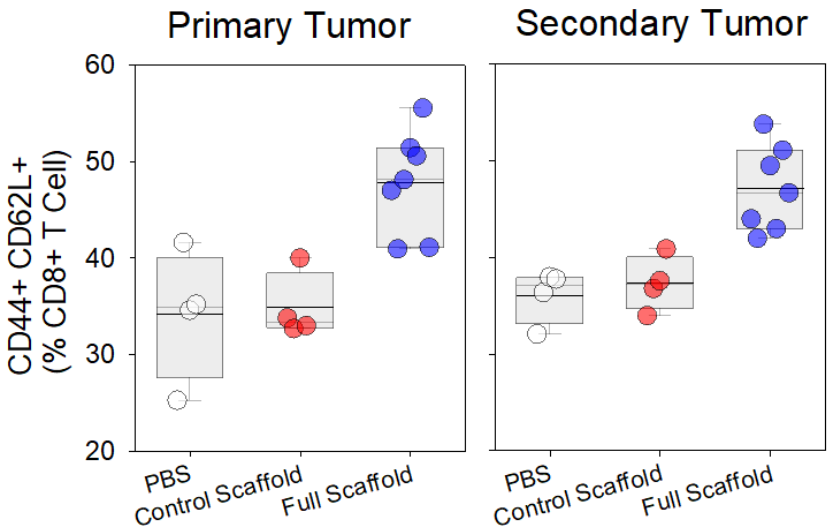

Figure 5.55. Flow cytometry study of the frequency of CD44+CD62L+CD8+ (central memory) T cell presence in draining lymph nodes of primary and secondary tumors after being treated with full (n=7) or control (n=4) Scaffolds.

As demonstrated before, the local release of TGFβi adjacent to the primary tumor showed to have no significant impact on the population of Tregs even in the draining lymph node of the primary tumor (**Fig. 5.56**).

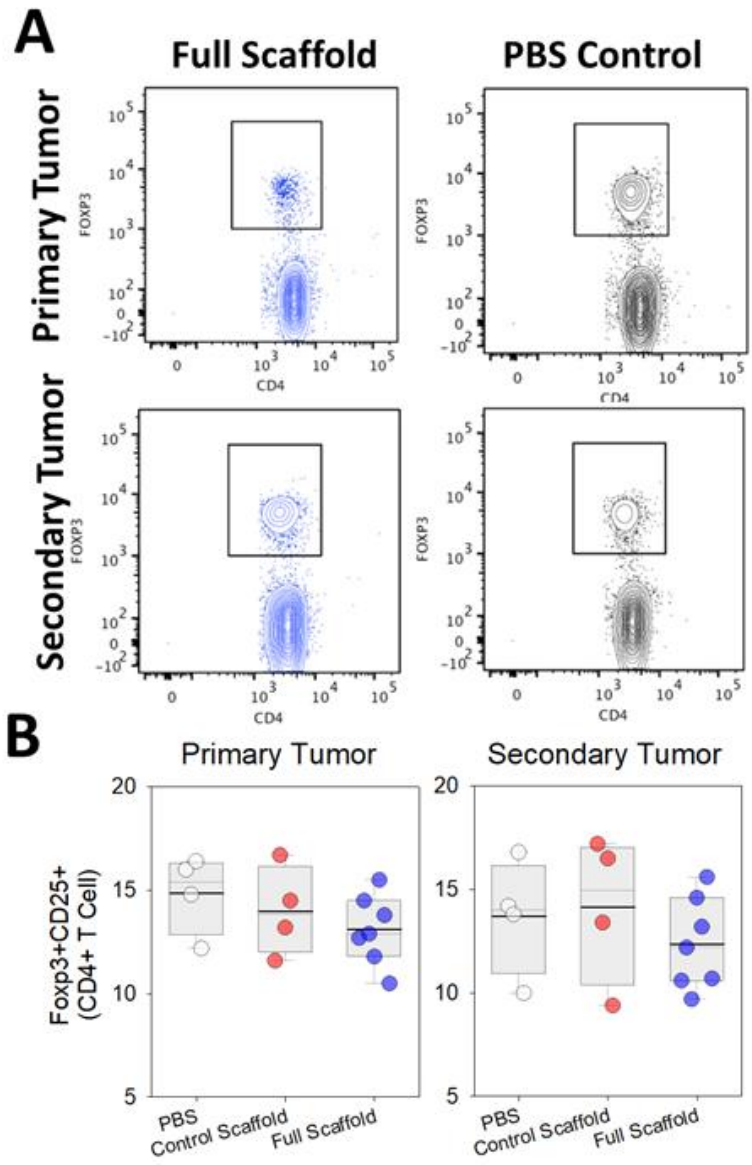

Figure 5.56. (A) Representative flow cytometry of Foxp3+CD25+CD4+ Tregs in primary and secondary tumor draining lymph nodes for mice treated with full Scaffolds (Blue) and PBS (Black). (B) The quantified frequency of Foxp3+CD25+CD4+ Tregs found in tumor draining lymph nodes.

As for the spleen, while the population of CD8+ T cells were improved in the mice treated with full scaffolds (**Fig. 5.57**) frequency of activated or GZMB+ T cells was not affected for the tumor-bearing mice receiving the full scaffold treatment. Though again as a results of full scaffold

implantation increase in the population of central memory T cells were reflected in the spleen as well (**Fig. 5.58**).

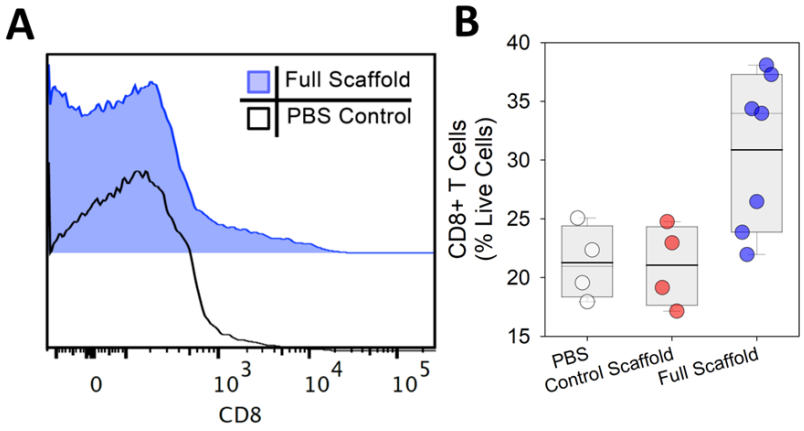

Figure 5.57. Flow cytometry study of CD8+ T cell presence in the spleen of mice after being treated with full (n=7) or control (n=4) Scaffolds. (A) Representative FACS graphs and (B) The frequency of CD8+ T cells.

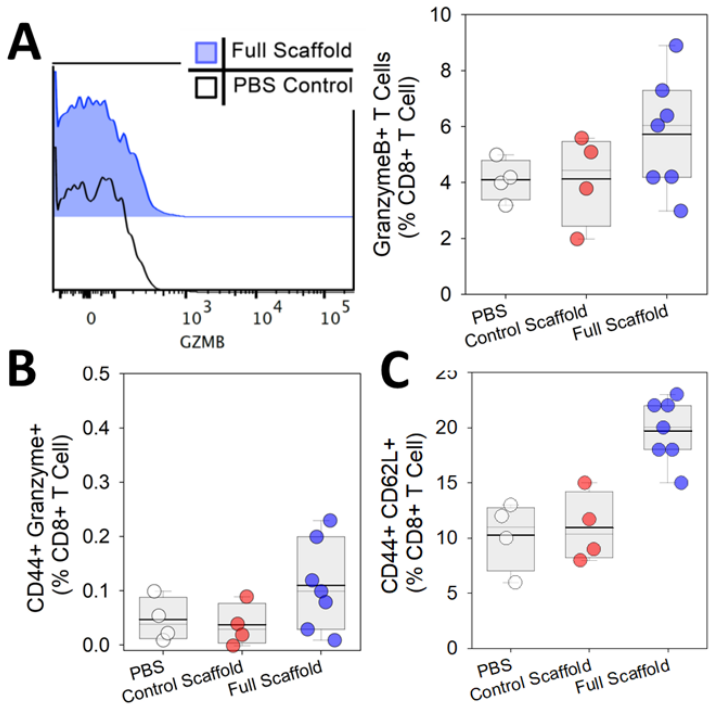

Figure 5.58. Flow cytometry study of effector and memory T cells presence in the spleen of tumor bearing mice after being treated with full (n=7) or control (n=4) scaffolds. (A) Representative FACS graphs and frequency of GZMB+CD8+ T cells in the spleen. The frequency

of (B) CD44+GZMB+CD8+ (effector) and (C) CD44+CD62L+CD8+ (central memory) T cells in the spleen.

5.2.7. Implantable synthetic lymph nodes boost the efficacy of adaptive T cell therapy

As another application for developed ISL we tested its potency in enhancing therapeutic efficacy of adaptive T cell therapy (ACT). ACT has been shown to hold high promises for many cancers including melanoma. Though its potency is limited by the inadequate T cell expansion in the tumor's suppressive microenvironment plus poor trafficking of tumor recognizing T cells to the tumor site. Thus, localization of trained T cells adjacent to the tumor while providing a niche that enhances their proliferation can overcome the main problems associated with ACT. Moreover, suppression of Treg in the tumor microenvironment can boost the therapeutic effects. Application of alginate-based scaffolds as matrices for transplantation of lymphocytes has been reported for mouse breast cancer model[34] where the matrix serves as a T cell delivery depot to support their local expansion. We believe our ISL offers a superiority to the reported works as it offers the capability of not only facilitating T cell's tumor infiltration and expansion but also rendering the possibility of recruiting naïve tissue/tumor resident T cells and activating them while hampering the immunosuppressive microenvironment of the tumor. In our melanoma model mice were injected subcutaneously with Ova peptide expressing B16-F10 cells followed by OTI T cell- loaded ISLs once the tumor was palpable (day 5). Mice were euthanized 22 days after for further analysis (**Fig. 5.59A**). ISLs were made in 96 well plates roughly about the size of a pencil eraser (**Fig. 5.59B,C**) and were then implanted adjacent to the tumor. H&E staining of the scaffolds adjacent to the tumor confirmed tissue engagement, successful delivery and proliferation of OT-Is plus recruitment of endogenous T cells (**Fig 5.59C**).

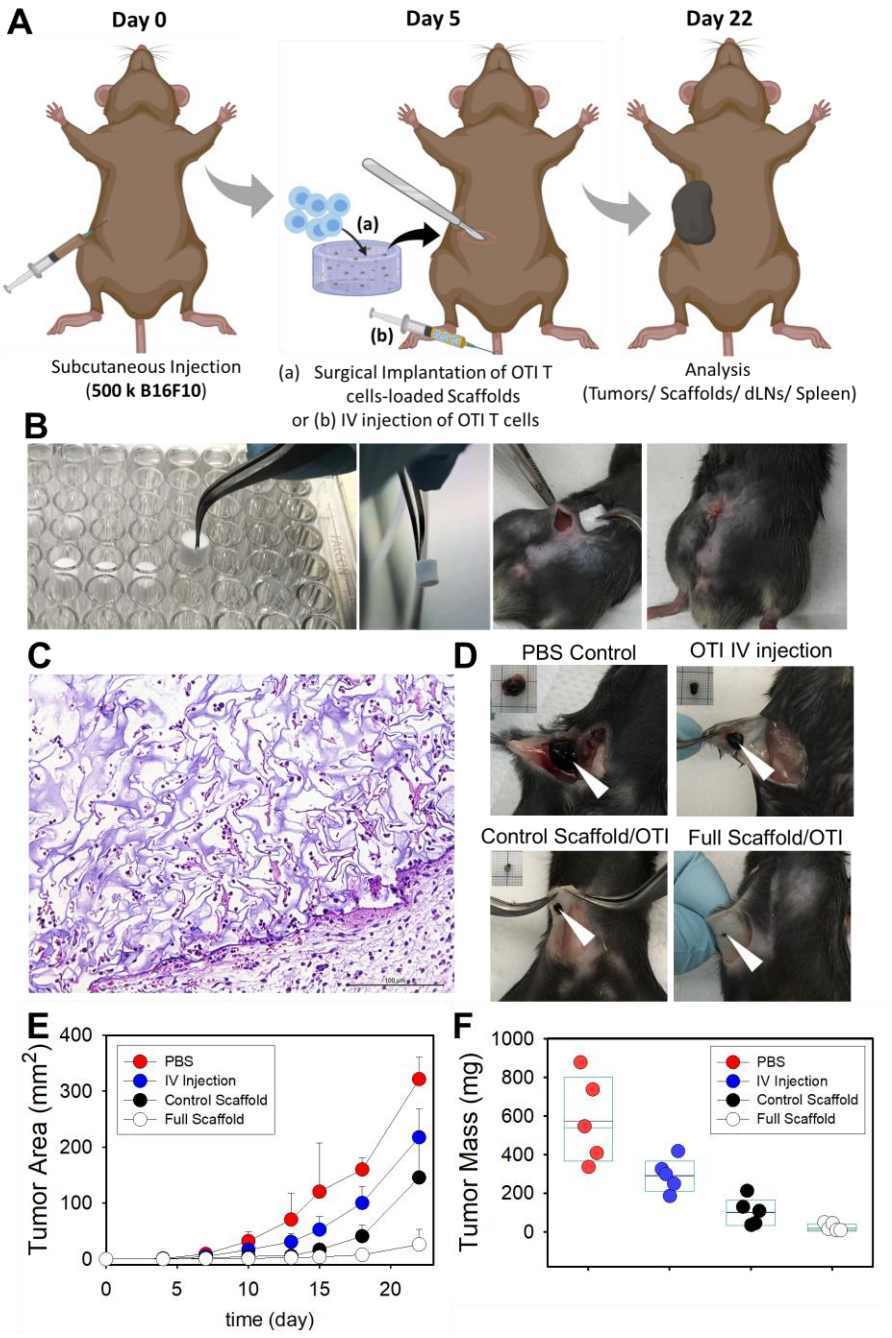

Figure 5.59. Engineered scaffolds can deliver tumor-reactive T cells and suppress growth of melanoma tumors. (A) Timing of tumor inoculation and follow up surgical implantation of the activated OTI cells-loaded biomaterial scaffold. (B) The engineered device is surgically implanted in a B16-F10-ova bearing mice. (C) H&E staining showing connective tissue-like scaffolds. (D) Representative images of subdermal tumors from wild-type mice 22 days after tumor inoculation. Alginate scaffolds carrying tumor reactive T cells and T cell-specific activator cues can eliminate melanoma tumors in mice. (E) Melanoma (B16-F10-Ova) tumor growth and

(F) final tumor mass in wild-type mice with Full or control scaffolds compared to PBS (n=5). Each point represents one mouse.

Area and Mass of the tumors were then tracked while a blank scaffold (loaded with OT-I CD8+ T cells but free of any modification), IV injection of OT-I T cells, and PBS were used as controls (**Fig. 5.59D-F**). Our OT-I loaded ISL suppressed tumor growth by about 16 folds compared to PBS control and improved growth rate by about 10-fold compared to IV injection of OT-Is (**Fig. 5.59E**). The IV injection control here represents the systemic injection of tumor recognizing T cells which due to the poor tumor infiltration loses the fight against cancer cells. On the other hand control scaffolds in here overcomes that issue by local delivery of trained T cells to the tumor but yet fails to be as effective as full scaffolds where besides local delivery of OT-1s enhances ACT by supporting their expansion (**Fig. 5.10**), recruitment of endogenous T cells and shutting down the induction of Tregs (**Fig. 5.59E,F** and **Fig. 5.60**). Histology images of the tumors treated with full scaffold platforms shows significant tumor clearance (**Fig. 5.60**).

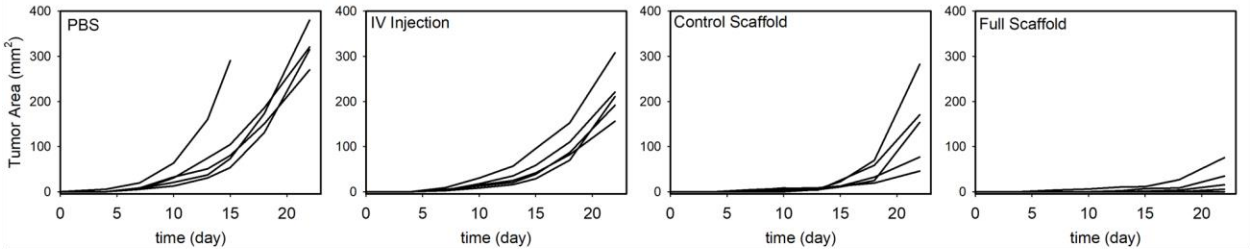

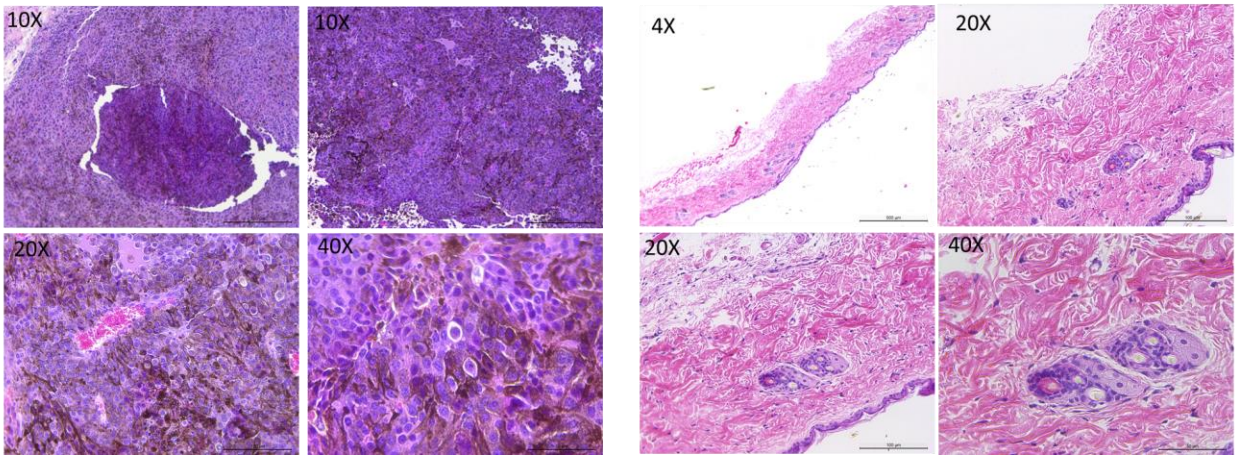

Figure 5.60. (A) Melanoma (B16-F10-Ova) tumor growth for groups with different treatments. Each line represents the tumor size of a single mouse over time. (B) Histologic analysis of the tumor tissues via H&E stain for animals used as PBS control *vs.* OT1-loaded Full Scaffolds.

We then looked into the population of tumor infiltrating T cells (**Fig. 5.61**). We recorded an about 40 percent increase in the population of tumor infiltrated OT-Is in our full scaffold compared to the control scaffold or IV injection. This drastic increase can be due to the higher proliferation of the delivered OT-Is along with suppression of Treg induction that allows for their higher tumor infiltration. Moreover, cytokine releasing GZMB+ T cell's population were also about 20 percent higher in the full scaffold vs the control one (**Fig. 5.61A,B**). The higher population of PD-I+ CD8+ T cells in the control and full scaffold also indicates the fact that more T cells in these conditions have experienced tumor antigens. To check the differences amongst Treg populations we then looked for the presence of FOXP3+CD25+CD4+ T cells in the tumor (**Fig. 5.61C**). As expected, the Treg population was similar to PBS control in mice that received IV injection of OTIs or in control scaffolds where the scaffold served only as a cell transfer platform. On the other hand, regulatory T cells were suppressed by about 40 percent in the full scaffold due to efficient and sustained release of TGFβi. This result proves the importance of tackling tumor from both aspects of empowering tumor fighting T cells as well as weakening the immunosuppressors which can be very promising for ACT therapies. Enhancing the infiltration and delivery of tumor specific T cells has been shown to not be sufficient in many cases due to the high population of Tregs in the tumor. This is where a platform that addresses both needs can be very promising.

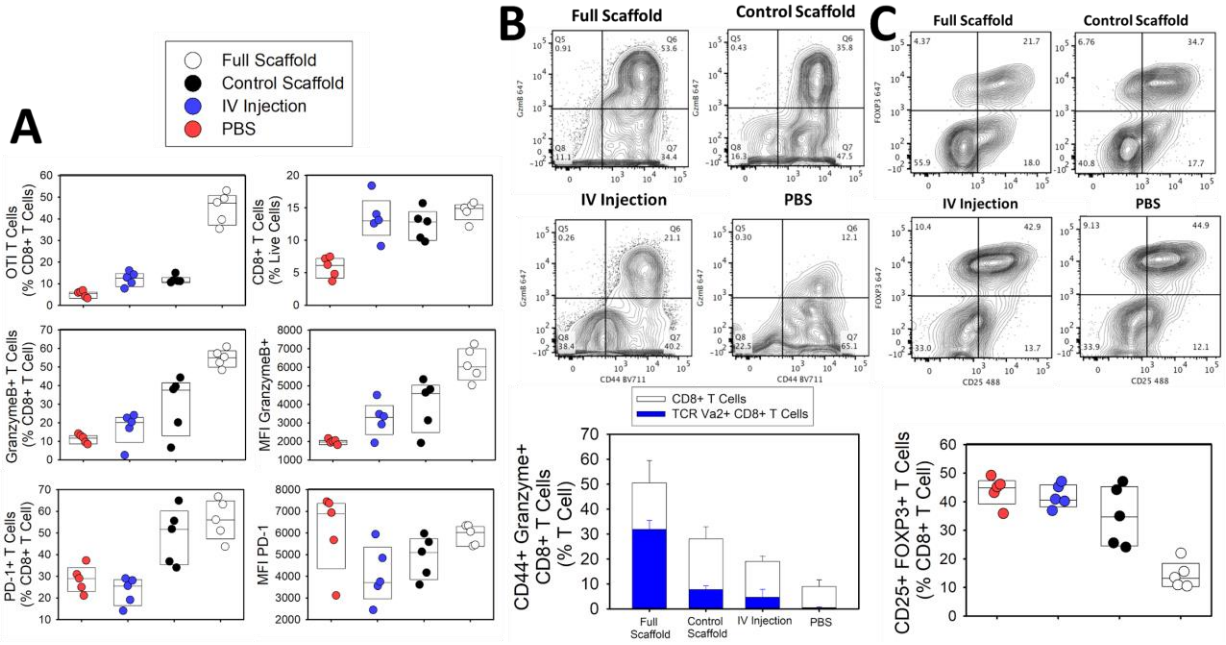

Figure 5.61. Presence of activated CD8+ T cells in tumors. Presence of tumor specific CD8+ T cells (OTI) as well as their level of cytokine secretion and PD-1 expression in tumors was studied 22 days after inoculation of tumor cells using flow cytometry. (A) Percentage of OTI and CD8+ T cells found in tumors. Frequency of CD8+ T cells with high expression of GZMB and PD-1 and mean fluorescence intensity (MFI) of T cells upregulating these two proteins were measured. (B) Percentage of T cells with high co-expression of CD44 activation marker and GZMB effector cytokine were plotted. Representative flow cytometry graphs also presented. (C) The frequency of Foxp3+CD25+CD4+ Tregs in tumor were studied. Representative flow cytometry graphs are shown for mice treated with indicated treatments. (n= 5).

We then checked the population of activated tumor infiltrating CD8+ T cells (**Fig. 5.62**). The FACS representatives clearly demonstrate that considerably a smaller number of activated T cells reached and infiltrated tumor upon IV injection of OT1s compared to their local delivery within scaffolds.

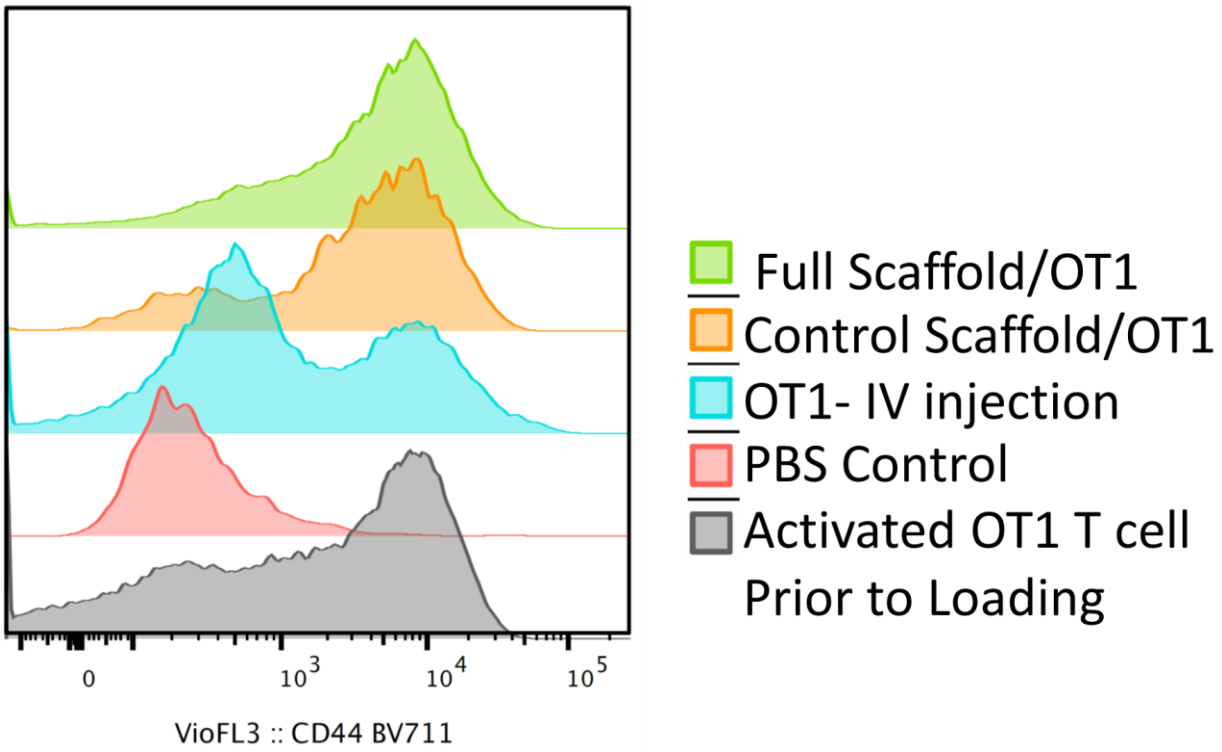

Figure 5.62. Presence of activated CD8+ T cells in tumors. Flow cytometry used to identify the presence of CD44 activated CD8+ T cells in tumors.

Interestingly even when gated only on Vα2+ OTI T cells present in tumor, higher percentage of those preactivated OTI stayed active in the tumor upon local delivery via scaffolds compared to IV injection (**Fig. 5.63**). The similar pattern was recorded for GZMB+ T cells in each of those conditions confirming the superiority of local delivery in terms of persuading higher and more efficient infiltration of tumor fighting T cells. Higher population of antigen experienced T cells upon local delivery of OTIs was also confirmed by levels of PD-1 expression on T cells (**Fig. 5.63**).

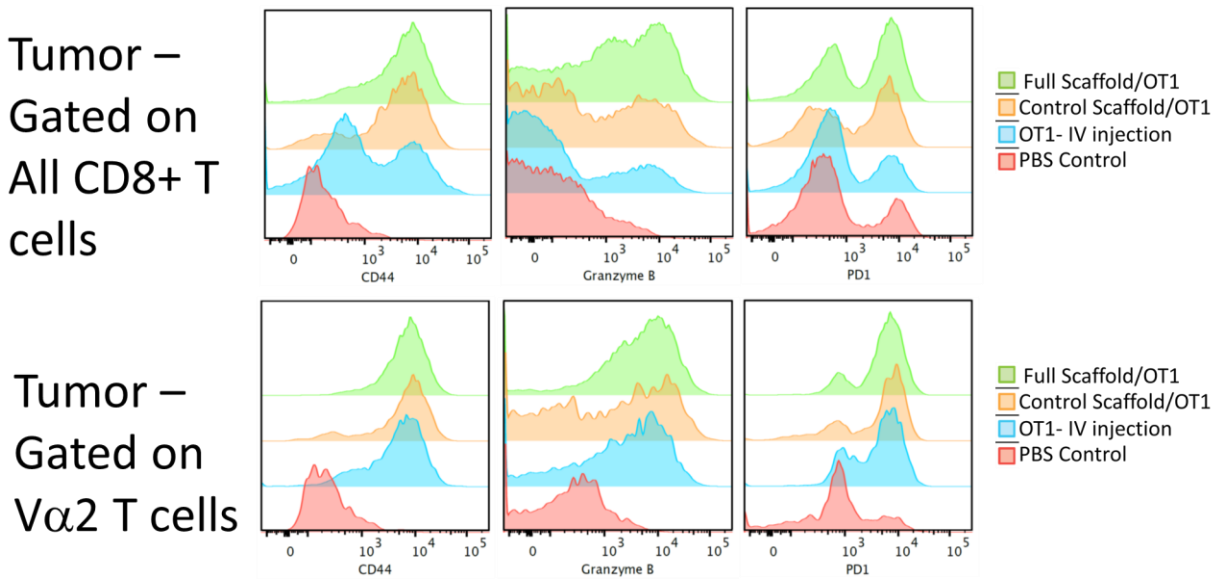

Figure 5.63. Presence of activated CD8+ T cells in tumors. Flow cytometry used to identify the presence of CD44+, Granzyme+, and PD-1+ cells gated on CD8+ T cells (upper panels) and gated on OTIs (lower panels) in tumors. OTI T cells were recognized by staining for Vα2 surface receptors.

As a measure of tumor clearance, we used TUNEL assay to observe DNA degradation in our groups. TUNEL assay was used as a measure of apoptotic tumor cells where the microscopy images showed drastically higher percentage of tumor apoptosis in our Full scaffold that delivered OTIs (**Fig. 5.64**).

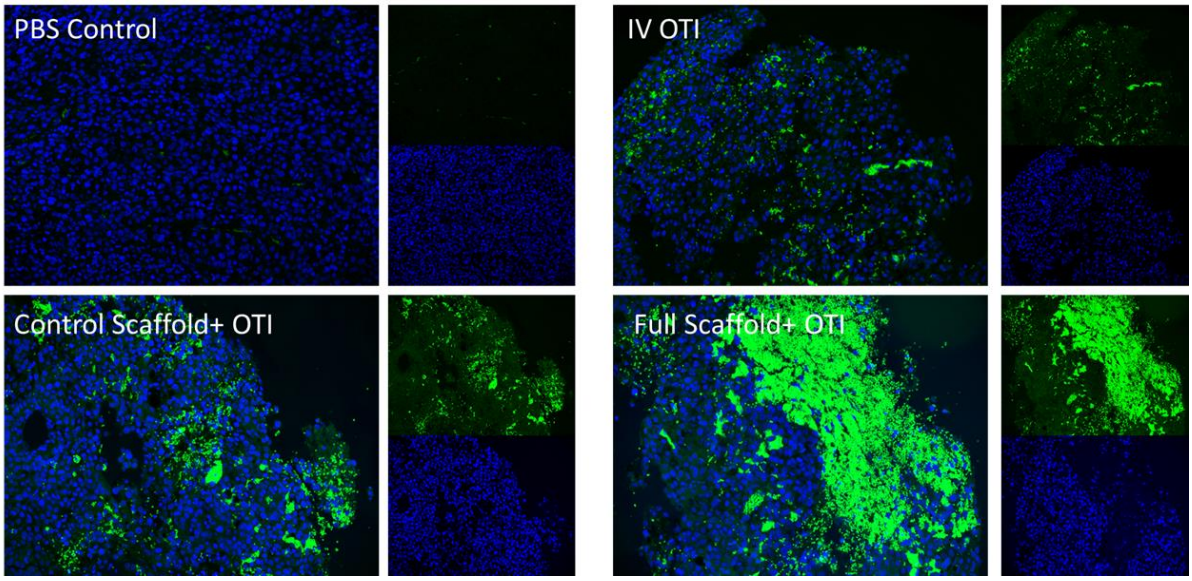

Figure 5.64. Local delivery of tumor-reactive T cells (OT1) can promote tumor apoptosis. Cell apoptosis was detected using TUNEL staining for samples with various treatments.

As a measure of the locality of the effects of our scaffolds we then looked into the tumor draining lymph node (**Fig. 5.65**). Our results showed no difference in the population of OTI T cells or CD8+ T cells in general upon different treatments compared to PBS control. On the contrary GZMB secreting T cells or PD-1+ population were higher in the case of IV injection of OTIs due to unspecific accumulation of OTIs in tissues other than tumor (**Fig. 5.65A**). This data proves the superiority of local delivery as opposed to systemic delivery which can cause several unwanted side effects. The population of CD44+GZMB+ CD8+ T cells were also intact in the draining lymph node of scaffold treated mice (**Fig. 5.65B**). As another important population that we were interested to make sure our local treatment does not affect we compared the percentage of FOXP3+CD25+ CD4+ T cells as a measure of Treg population (**Fig. 5.65C**). Our data showed that the population of Tregs in the tumor draining lymph node was intact compared to PBS control which eliminated the risk of autoimmune side effects that are normally associated with systemic delivery of TGF-βi drugs.

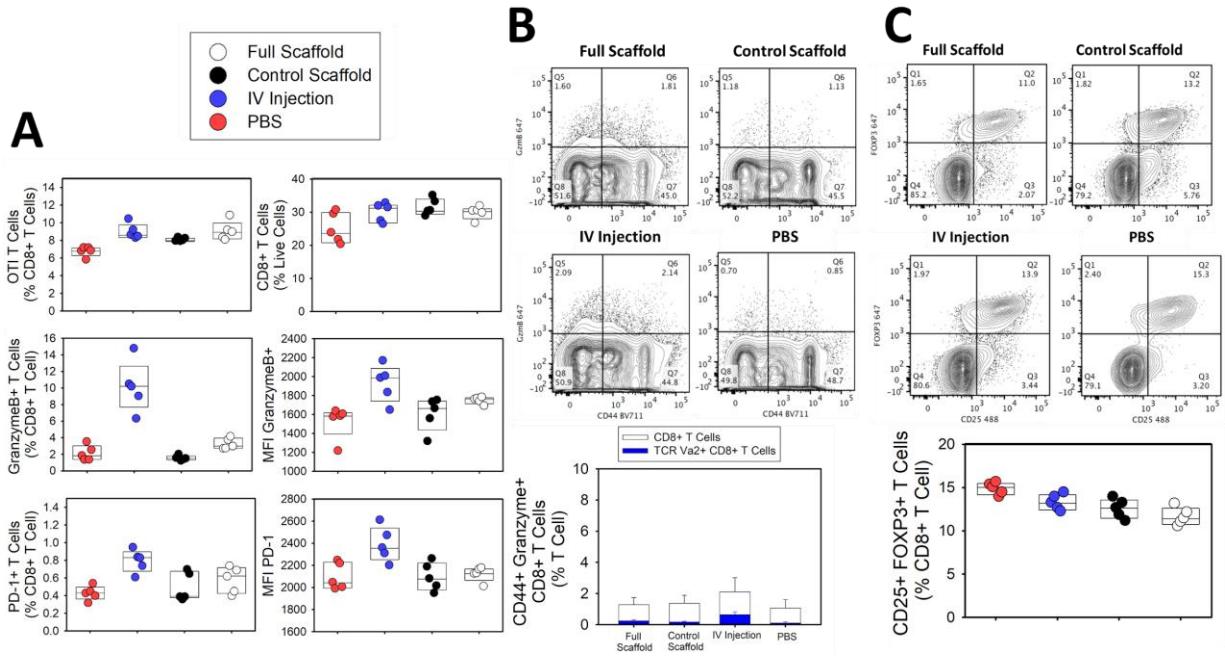

Figure 5.65. Presence of activated CD8+ T cells in tumor draining lymph nodes. Presence of tumor-antigen specific CD8+ T cells (OTI) as well as activation of CD8+ T cells in the tumor draining lymph nodes was studied 22 days after inoculation of tumor cells using flow cytometry. (A) Percentage of OTI and CD8+ T cells found in tumor draining lymph nodes. Frequency of CD8+ T cells with high expression of GZMB and PD-1 and mean fluorescence intensity (MFI) of T cells upregulating these two proteins were measured. (B) Percentage of T cells with high expression of CD44 activation marker and GZMB effector cytokine were plotted. Representative flow cytometry graphs also presented. (n= 5). (C) The frequency of Foxp3+CD25+CD4+ Tregs in tumor were studied. Representative flow cytometry graphs are shown for mice treated with indicated treatments. (n= 5).

We also saw a similar trend in the spleens of mice treated with different formulations where no meaningful differences were noted in the population of CD8+s, GZMB secreting T cells, PD-1+ T cells in the mice treated with scaffolds compared to PBS controls while IV injection of OTIs increased the population of GZMB+ T cells or PD-1 expressing T cells (**Fig. 5.66**).

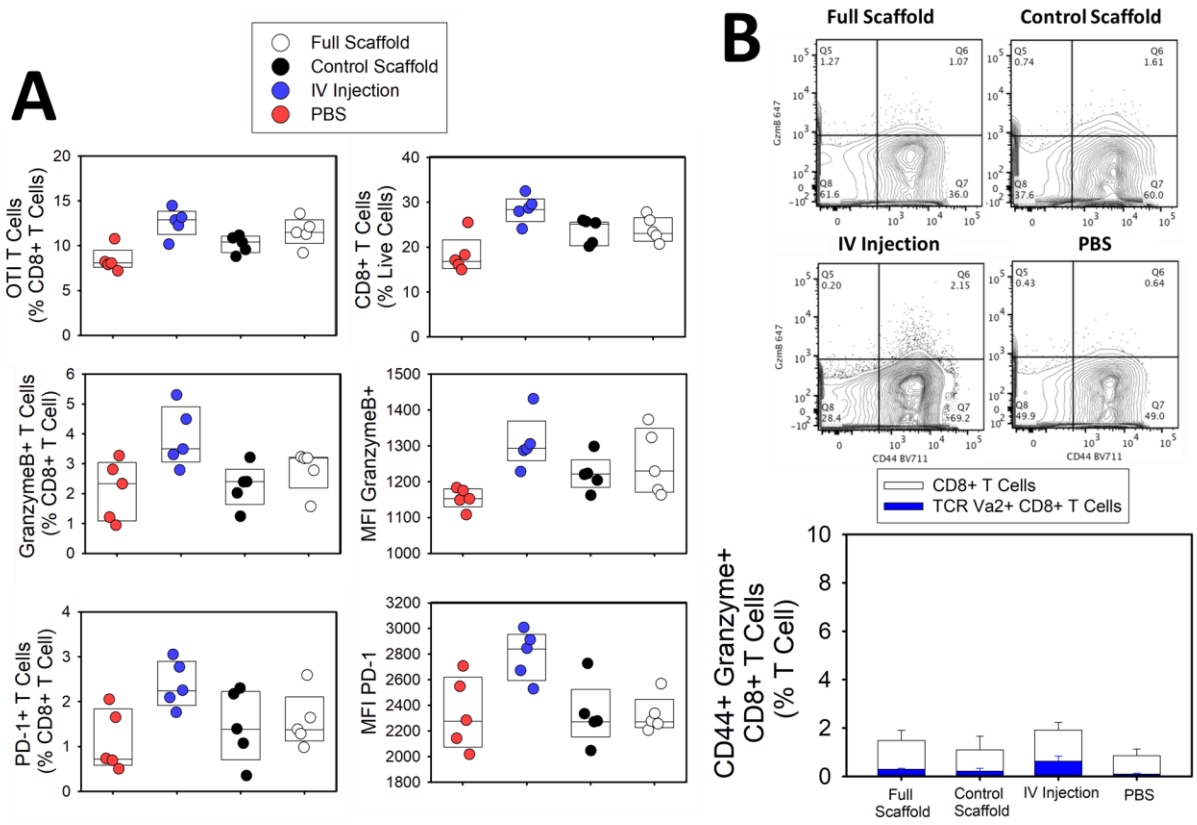

Figure 5.66. Presence of activated CD8+ T cells in spleen. Presence of tumor-antigen specific CD8+ T cells (OTI) as well as activation of CD8+ T cells in the spleen of tumor bearing mice was studied 22 days after inoculation of tumor cells using flow cytometry. (A) Percentage of OTI and CD8+ T cells found in spleen. Frequency of CD8+ T cells with high expression of GZMB and PD-1 and mean fluorescence intensity (MFI) of T cells upregulating these two proteins were measured. (B) Percentage of T cells with high expression of CD44 activation marker and GZMB effector cytokine were plotted. Representative flow cytometry graphs also presented. (n= 5).

5.3. Experimental Materials and Methods

5.3.1. Chemicals and Biologicals

Unless noted otherwise, all chemicals were purchased from Sigma-Aldrich, Inc. (St. Louis, MO). All glassware was cleaned overnight using concentrated sulfuric acid and then thoroughly rinsed with Milli-Q water. All the other cell culture reagents, solutions, and dishes were obtained from Thermo Fisher Scientific (Waltham, MA), except as indicated otherwise.

5.3.2. Preparation and characterization of artificial APC microparticles

Monodisperse mesoporous silica microparticles (5 to 20 μm) were formed using a microfluidic jet spray-drying route, using cetyltrimethylammonium bromide (CTAB) and/or Pluronic F127 as templating agents, and tetraethylorthosilicate (TEOS) for silica as reported before.[13,14] Carbodiimide chemistry (NHS/EDC) was utilized to modify silica conjugates with heparin after treating the silica with (3-Aminopropyl)triethoxysilane (APTES) to provide primary amine groups. Briefly, mesoporous silica microparticles (800 mg) was suspended in dehydrated Methanol (50 ml). Then, APTES (3 ml) was added and the suspension was stirred at room temperature overnight, and the final product was centrifuged (1500 rpm, 3 min) and washed with methanol five times, followed by drying under high vacuum. For the surface functionalization of the aminated-silica particles with heparin, heparin sodium salt (216 mg) was dissolved in deionized water (8 ml) and activated via successive addition of EDC (63 mg) and sulfo-NHS (71.4 mg). After stirring for 5 min, the ethanolic solution of amino-functionalized silica (20 mg in 1.12 ml) was added to the reaction mixture and stirred for 12 h at room temperature. Afterwards the particles were separated by centrifugation and washed several times with deionized water and ethanol to remove unreacted reagents.

For the preparation of antibody-conjugated microparticles, anti-CD3 (clone 2C11; Bio-X-Cell) and anti-CD28 (clone 37.51; Bio-X-Cell) were covalently conjugated to the surface of particles using carbodiimide chemistry. After activation of antibodies' carboxylic groups for 10 min with EDC/NHS, microparticles were added and incubated under gentle stirring at 4°C overnight. The protein-functionalized microparticles (artificial antigen presenting cells, aAPCs) were then separated from the solution and washed several times. Unreacted functional groups were quenched by washing samples in Tris buffer (100 mM, pH 8) for 30 min. A 10-fold dilution of the conjugation density that is used in conventional plate-bound stimulation method for T-cell

activation was picked as the final conjugation density for beads. Micro-BCA assay was used to quantify total amount of surface conjugated antibodies according to the manufacturer's protocol.

5.3.3. Preparation and characterization of scaffolds

To form the scaffolds, we first oxidized the alginate (Mw ~250 kDa, high G blocks; Novamatrix UP MVG, FMC Biopolymer, Rockland, Maine) with sodium periodate (1.5 %), overnight at room temperature, then quenched the reaction by dropwise addition of ethylene glycol for 45 min. We then dialyzed the solution (MWCO 3.5 kDa) against deionized water for 3 days followed by lyophilization. Afterward, the alginate was dissolved in MES (MES 150 mM, NaCl 250 mM, pH 6.5) and covalently conjugated to RGD-containing peptide (GGGGRGDY; GenScript USA Inc., Piscataway, NJ) using carbodiimide chemistry (NHS/EDC). The reaction was continued for 24 h followed by dialysis (MWCO 20 kDa) and lyophilization. This alginate-RGD complex in PBS was then cross-linked via calcium sulfate solution. The gels were casted in desired 24- or 96-well plates followed by two overnight washes to get rid of the extra calcium ions and then used as 2D matrices. For 3D structures these same scaffolds were frozen at -80°C, lyophilized for 3 days, and stored at 4°C before cellular studies. To prepare aAPC loaded scaffolds, 20×10^6 aAPCs were mixed with 1 ml of alginate prior to crosslinking with $CaSO_4$.

We prepared an array of different alginate formulations by varying either the polymer content or the amount of crosslinker (here $CaSO_4$). To measure the mechanical stiffness of our gels we used Instron 5542 mechanical tester and all the samples were tested at a rate of 1 mm/min. The Young's modulus was then calculated from the slope of the linear region that corresponds with 0–10% strain. Here the stiff gel comprised of alginate 2.5% with 40 mM $CaSO_4$ was used.

X-ray irradiation (Gulmay Medical RS320 x-ray unit) was used to irradiate the fabricated scaffolds before *in vitro* or *in vivo* functional assays, following ISO 11137-2:2013 recommended protocols.[17] A 25 kGy (2.5 Mrads) sterilization dose was used. Physical properties, including

changes in morphology and mechanical stiffness of the scaffolds, or T cell activation property change after sterilization was tested.

Scanning electron microscopy (SEM) images of the gels were taken to see the cross-sectional microstructure and porosity of the alginate-based scaffolds. The lyophilized scaffolds were freeze-fractured (using liquid nitrogen) for cross-sectional images. The scaffolds were sputtered with iridium (South Bay Technology Ion Beam Sputtering) prior to imaging with a ZEISS Supra 40VP scanning electron microscope (Carl Zeiss Microscopy GmbH). The sizes of pores from different parts of the SEM images were then measured and analyzed using ImageJ software (NIH). For SEM imaging of cell-loaded scaffolds, the cell-laden hydrogels were fixed with 2.5% glutaraldehyde, followed by post-fixation in osmium tetroxide prior to serial dehydration in increasing concentrations of ethanol (25, 50, 75, 90, and 100%) for 15 min each, and iridium sputtering.

To immobilize anti-CD3 and anti-CD28 to the scaffolds, the freeze-dried scaffolds were activated with EDC/NHS for 15 min. Then the scaffolds were washed twice with PBS (supplemented with 0.42 mM $CaCl_2$) before addition of anti-CD3 and anti-CD28. Then they were incubated at 4°C overnight. Unreacted functional groups were quenched by washing the scaffolds with Tris buffer (100 mM, pH 8) for 30 min. For T cell activation studies, 5×10^6 primary naïve T cells were added to the scaffolds and cultured for 3-5 days to study their effector functions.

To prepare IL-2 loaded aAPCs, microparticles were incubated with cytokine in PBS buffer containing bovine serum albumin (BSA; 0.1 %w/v) and were gently shaken overnight at 4°C. The microparticles were then centrifuged and washed several times to remove unabsorbed cytokines. The concentration of IL-2 in the removed supernatant was measured using enzyme-linked immunosorbant assay (ELISA) to estimate the binding capacity of microparticles.

In vitro release of IL-2 from aAPCs or from aAPCs-loaded scaffolds as well as CCL21 release from the scaffolds were studied by incubating 20×10^6 microparticles or one scaffolds in

2 ml PBS (pH 7.4; supplemented with 1 mM $CaCl_2$) at 37 °C. At different time intervals, 500 μL of the supernatant was collected, and replaced with an equivalent volume of PBS. The concentration of released IL-2 was determined using a human IL-2 and murine CCL21 ELISA kits as a function of time.

TGF-β inhibitor, LY2157299 (Cayman Chemical), loaded poly(lactic-co-glycolic) acid (PLGA) nanoparticles (NPs) were prepared using a nanoprecipitation method as previously reported. Resomer RG 503 PLGA (50:50; molecular weight: 28 kg/mol) was used in this study. LY2157299 and PLGA were dissolved in 5 mL dichloromethane and sonicated into 1% poly vinyl alcohol (PVA) solution (50 ml) by probe sonicator (12 W) for 2 min. The resulting emulsification was then added to 100 ml of 0.5% PVA solution. The solution was agitated, and the dichloromethane was allowed to evaporate for 4 h. The solution was then centrifuged at 3000xg for 5 min to pellet out any non-nano dimensional materials. The supernatant was removed and ultracentrifuged and washed three times at 21,000 g for 20 min to wash away the PVA. The resulting nanoparticle solution was flash frozen in liquid nitrogen and lyophilized for 2 days prior to characterization and use. Hydrodynamic diameter and surface charge of formed PLGA NPs was studied using dynamic light scattering (DLS) and zeta potential measurements (Zetasizer Nano, Malvern, UK). To load these NPs into alginate-based scaffolds, LY2157299-loaded PLGA NPs were mixed with alginate prior to crosslinking *via* calcium. The concentration of released and LY2157299 from nanoparticles before and after loading into alginate scaffolds was determined by measuring the UV absorption of LY2157299.

5.3.4. T cell isolation and activation

All *in vitro* experiments were conducted in accordance with UCLA's institutional policy on humane and ethical treatment of animals following protocols approved by the Animal Research Committee. Five- to eight-week-old wild-type or OT-I/OTII TCR transgenic mice (Jackson Labs) were used for all experiments.

Cell-culture media was RPMI supplemented with 10% heat-inactivated FBS, 1% penicillin/streptomycin, 1% sodium pyruvate, 1% HEPES buffer, 0.1% μM 2-mercaptoethanol. CD4+/CD8+ T cells were purified using EasySep immunomagnetic negative selection enrichment kits (Stem Cell Technologies).

Control *in vitro* activation of CD4+/CD8+ T cells was performed by culturing 1×10^6 cells/mL in tissue culture-treated 24-well plates that were pre-coated with anti-CD3 (clone 2C11; Bio X Cell) at a concentration of 10 μg/mL plus addition of 2 μg/mL soluble anti-CD28 (clone 37.51; Bio X Cell). T cells were then collected from wells and allowed to proliferate in interleukin-2 (IL-2, BRB Preclinical Repository, NCI, NIH)-containing medium (50 U/mL), prior to being used for experiments.

For Treg formation experiments CD4+ T cells were purified from mouse spleen as mentioned above. Cells were then either activated on scaffolds or on anti-CD3e antibody (8 mg/ml) coated plates with the anti-CD28 antibody (2 mg/ml) supplemented medium. At the same time TGF-β (15 ng/ml) was added to the media. After four days regulatory T-cells were removed and stained with antibodies for flow cytometry analysis.

5.3.5. Flow cytometry

For flow cytometry analysis, antibodies to mouse antibodoes, were purchased from eBioscience, BioLegend, or BD Biosciences. To study proliferation behavior of T-cell responses during various treatments their expansion was measured by 5-(and-6)-carboxyfluorescein diacetate, succinimidyl ester (CFSE) dilution. For CFSE dilution experiments, 5×10^5 naive CD4+/CD8+ T cells were labeled with 2 μM CFSE for 13 min, followed by two washes and then incubation with splenocytes. Splenocytes were extracted from the spleen of wild type C57Bl/6 mice. Then the cells were incubated in ACK lysis buffer (Gibco) for 5 min at room temperature to remove red blood cells. The remaining cells were then treated with ova peptide as above to present

to T cells. Trypan Blue was purchased from Calbiochem. Cells were analyzed on a Cytek DxP10 flow cytometer using FlowJo software (Treestar/BD).

For intracellular staining of GranzymeB and Foxp3, the recommended protocol by eBioscienceTM Foxp3 / Transcription Factor Staining Buffer Set was followed. The following antibodies were used for intracellular staining from Biolegend: Foxp3 (clone MF-14, AF647, Cat #126408); GZMB (clone GB11, AF647, Cat #515406), Mouse IgG1, κ Isotype Ctrl (clone MOPC-21, AF647, Cat #400130).

5.3.6. Migration Assay

The migration assay to evaluate the role of chemokines on recruitment of T cells and melanoma cancer in the presence and absence of magnetic particles was performed using regular Transwell migration as we reported before.[11] The number of migrated cells was evaluated after 4 h using an automatic cell counter.

5.3.6. **In vivo Tumor Suppression Assay**

2-5×10^5 B16F10-OVA tumor cells were subcutaneously injected into right or both (in the contralateral tumor model) right and left flanks of C57BL/6J WT mice (6-8 weeks old). These melanoma-derived cells are transfected to express chicken ovalbumin peptide (OVA)[35]. Five days after tumor cell injection, scaffolds were surgically implanted subcutaneously into the same approximate region of the tumors in both flanks. For cell-loaded studies, *ex vivo* activated OT-I T cells were transferred either intravenously using retro-orbital injections (100 μL per animal) or implantable scaffolds at the same day. Tumor size was assessed over time using a digital caliber until day 22 at which animals were sacrificed and the tumor, draining lymph nodes, and spleen were extracted. Tumor mass was measured using a digital balance before digesting the tumor tissue for flow cytometry or fixing it for tissue sectioning. Tumors were digested by incubating in collagenase and DNase I (50 μg/mL) at 37 °C for 15 min. These enzymes were inactivated with EDTA (20 μL/mL of solution). Tissues were then mechanically disaggregated and passed through

a 0.7 μm cell strainer to obtain a single-cell suspension. Cells were then stained with the fluorochrome-conjugated antibodies on ice. For intracellular staining, cells were permeabilized with Granzyme B Fix/Perm buffer according to the manufacturer's instructions (BioLegend) before staining. Detection of apoptotic cells in tumor tissue was achieved using Terminal deoxynucleotidyl transferase-mediated dUTP nick-end labeling (TUNEL) staining following the manufacturer's directions. TUNEL-positive cells indicated as apoptotic melanoma cells. Tissue sections were imaged by a fluorescence microscope (Keyence BZ-X800, Osaka, Japan).

5.3.8. Statistical analysis

The Kruskal-Wallis rank sum test, one-way ANOVA and two-tailed Student's t-test were utilized as appropriate to analyze the data at a significance of α or $p < 0.05$. Quantitative data were expressed as mean ± standard deviation (SD). To determine the number of specimens for the proposed experiments, power analysis was conducted based on our preliminary data.

5.4. References

1. Tang, L. *et al.* Enhancing T cell therapy through TCR-signaling-responsive nanoparticle drug delivery. *Nat. Biotechnol.* (2018) doi:10.1038/nbt.4181.
2. Mansurov, A. *et al.* Collagen-binding IL-12 enhances tumour inflammation and drives the complete remission of established immunologically cold mouse tumours. *Nat. Biomed. Eng.* (2020) doi:10.1038/s41551-020-0549-2.
3. Majedi, F. S. *et al.* Cytokine Secreting Microparticles Engineer the Fate and the Effector Functions of T-Cells. *Adv. Mater.* **30**, 1703178 (2018).
4. Majedi, F. S. *et al.* Augmentation of T-Cell Activation by Oscillatory Forces and Engineered Antigen-Presenting Cells. *Nano Lett.* **19**, (2019).
5. Wang, H. & Mooney, D. J. Biomaterial-assisted targeted modulation of immune cells in cancer treatment. *Nature Materials* (2018) doi:10.1038/s41563-018-0147-9.
6. Cheung, A. S., Zhang, D. K. Y., Koshy, S. T. & Mooney, D. J. Scaffolds that mimic antigen-presenting cells enable ex vivo expansion of primary T cells. *Nat. Biotechnol.* (2018)

doi:10.1038/nbt.4047.

7. Chen, M. L. *et al.* Regulatory T cells suppress tumor-specific CD8 T cell cytotoxicity through TGF-β signals in vivo. *Proc. Natl. Acad. Sci. U. S. A.* (2005) doi:10.1073/pnas.0408197102.

8. Batlle, E. & Massagué, J. Transforming Growth Factor-β Signaling in Immunity and Cancer. *Immunity* (2019) doi:10.1016/j.immuni.2019.03.024.

9. Kelly M Credill, A. J. S. Nonclinical Safety Evaluation of a Transforming Growth Factor β Receptor I Kinase Inhibitor in Fischer 344 Rats and Beagle Dogs. *J. Clin. Toxicol.* (2014) doi:10.4172/2161-0495.196.

10. Park, J. *et al.* Combination delivery of TGF-β inhibitor and IL-2 by nanoscale liposomal polymeric gels enhances tumour immunotherapy. *Nat. Mater.* (2012) doi:10.1038/nmat3355.

11. Majedi, F. S. *et al.* Cytokine Secreting Microparticles Engineer the Fate and the Effector Functions of T-Cells. *Adv. Mater.* **30**, (2018).

12. Hasani-Sadrabadi, M. M. *et al.* Mechanobiological Mimicry of Helper T Lymphocytes to Evaluate Cell–Biomaterials Crosstalk. *Adv. Mater.* **30**, 1706780 (2018).

13. Waldron, K. *et al.* Formation of monodisperse mesoporous silica microparticles via spray-drying. *J. Colloid Interface Sci.* (2014) doi:10.1016/j.jcis.2013.12.027.

14. Liu, W., Chen, X. D. & Selomulya, C. On the spray drying of uniform functional microparticles. *Particuology* (2015) doi:10.1016/j.partic.2015.04.001.

15. Meng, K. P., Majedi, F. S., Thauland, T. J. & Butte, M. J. Mechanosensing through YAP controls T cell activation and metabolism. *J. Exp. Med.* (2020) doi:10.1084/jem.20200053.

16. Majedi, F. S. *et al.* T-cell activation is modulated by the 3D mechanical microenvironment. *Biomaterials* (2020) doi:10.1016/j.biomaterials.2020.120058.

17. Corrigendum, T. Sterilization of health care products — Radiation — Part 2 : Establishing the sterilization dose. *Order A J. Theory Ordered Sets Its Appl.* (2009).

18. EUROPEAN COMMITTEE FOR STANDARDIZATION. *Sterilization of health care products — Radiation. BE EN ISO 11137-2:2013* (2013).

19. Abuhanoglu, G. & Özer, A. Y. Radiation effects on pharmaceuticals. *Fabad Journal of*

Pharmaceutical Sciences (2010).

20. Gorelink, L. & Flavell, R. A. Immune-mediated eradication of tumors through the blockade of transforming growth factor-β signaling in T cells. *Nat. Med.* (2001) doi:10.1038/nm1001-1118.

21. Liu, V. C. *et al.* Tumor Evasion of the Immune System by Converting CD4 + CD25 – T Cells into CD4 + CD25 + T Regulatory Cells: Role of Tumor-Derived TGF-β . *J. Immunol.* (2007) doi:10.4049/jimmunol.178.5.2883.

22. Yingling, J. M., Blanchard, K. L. & Sawyer, J. S. Development of TGF-β signalling inhibitors for cancer therapy. *Nature Reviews Drug Discovery* (2004) doi:10.1038/nrd1580.

23. Kano, M. R. *et al.* Improvement of cancer-targeting therapy, using nanocarriers for intractable solid tumors by inhibition of TGF-β signaling. *Proc. Natl. Acad. Sci. U. S. A.* (2007) doi:10.1073/pnas.0611660104.

24. Town, T. *et al.* Blocking TGF-β-Smad2/3 innate immune signaling mitigates Alzheimer-like pathology. *Nat. Med.* (2008) doi:10.1038/nm1781.

25. Rodón, J. *et al.* Pharmacokinetic, pharmacodynamic and biomarker evaluation of transforming growth factor-β receptor i kinase inhibitor, galunisertib, in phase 1 study in patients with advanced cancer. *Invest. New Drugs* (2015) doi:10.1007/s10637-014-0192-4.

26. Yingling, J. M. *et al.* Preclinical assessment of galunisertib (LY2157299 monohydrate), a first-in-class transforming growth factor-β receptor type I inhibitor. *Oncotarget* (2018) doi:10.18632/oncotarget.23795.

27. Weninger, W. *et al.* Naive T Cell Recruitment to Nonlymphoid Tissues: A Role for Endothelium-Expressed CC Chemokine Ligand 21 in Autoimmune Disease and Lymphoid Neogenesis. *J. Immunol.* (2003) doi:10.4049/jimmunol.170.9.4638.

28. Liu, C. *et al.* The role of CCL21 in recruitment of T-precursor cells to fetal thymi. *Blood* (2005) doi:10.1182/blood-2004-04-1369.

29. Wrzesinski, S. H., Wan, Y. Y. & Flavell, R. A. Transforming growth factor-β and the immune response: Implications for anticancer therapy. *Clinical Cancer Research* (2007) doi:10.1158/1078-0432.CCR-07-1157.

30. Lin, Y., Sharma, S. & John, M. S. CCL21 cancer immunotherapy. *Cancers* (2014)

doi:10.3390/cancers6021098.

31. Novak, L., Igoucheva, O., Cho, S. & Alexeev, V. Characterization of the CCL21-mediated melanoma-specific immune responses and in situ melanoma eradication. *Mol. Cancer Ther.* (2007) doi:10.1158/1535-7163.MCT-06-0709.

32. Cencioni, C., Capogrossi, M. C. & Napolitano, M. The SDF-1/CXCR4 axis in stem cell preconditioning. *Cardiovasc. Res.* **94**, 400–407 (2012).

33. Dunussi-Joannopoulos, K. *et al.* Efficacious immunomodulatory activity of the chemokine stromal cell–derived factor 1 (SDF-1): local secretion of SDF-1 at the tumor site serves as T-cell chemoattractant and mediates T-cell–dependent antitumor responses. *Blood* **100**, 1551–1558 (2002).

34. Stephan, S. B. *et al.* Biopolymer implants enhance the efficacy of adoptive T-cell therapy. *Nat. Biotechnol.* (2015) doi:10.1038/nbt.3104.

35. Bellone, M. *et al.* Relevance of the tumor antigen in the validation of three vaccination strategies for melanoma. *J. Immunol.* **165**, 2651–6 (2000).

Chapter 6.

Conclusion and Future Remarks

Concluding Remarks

In this thesis, we hope to have contributed to the field of immunotherapy by developing a few engineering platforms. The first contribution we hope to have made is by designing platforms that enable controlled release of cytokines from microparticles. These platforms allowed us to study not only the effect of the amount of the released cytokine but also the impact that the rate at which those cytokines are presented to cells can put on cellular fate. We demonstrated how these platforms were able to skew the activation, differentiation, proliferation, and effector responses of T cells. This new capability is easily adaptable to influence the behaviors of other immune cells, including NK cells and B cells.

Our second contribution has been towards engineering formulations for better understanding of the biochemical and biophysical cues that impact the so called “immune synapses”. By manipulating the size and density of stimulatory signals on our artificial APCs, we learned about what is required in the TCR-pMHC interface to reach the threshold for T-cell activation and thus improve cultivation of engineered T-cell therapies. No other work, to our knowledge, has harnessed advanced materials to provide mechanically soft artificial antigen presenting cells combined with mechanical stimulation as we did here. We also offered the application of orbital shaking as a way to study and modulate the strength and frequency of the exchanged forces between T cell and APCs. This approach provides a mixture of mechanical cues, including oscillatory forces on the immune synapse, stirring of the media to promote T-aAPC engagement, and potentially even shear forces upon the T cells. By providing exogenous mechanical forces here by an orbital shaker, we showed that T cell triggering can be amplified

above and beyond their own capabilities. Specifically, we showed overall that gentle mechanical stimulation of the TCR offers an approximately 2-fold increase in signal strength to T cells as compared to conventional static cultures.

There are few other reports where the use of aAPCs has demonstrated an ability to optimize T cell signaling and proliferation. Research groups have shown that aAPCs fabricated from biomimetic scaffolds, namely mesoporous silica nanorods coated with a lipid bilayers, allow for maximizing signal strength and for impressive expansion of T cells *in vitro*,[1] but did not allow for obviously tuning down the signal as we did here. Our work here and other reductionist approaches[2] demonstrated that absolute amount of antigenic signal, rather than density, is more important. Tuning the strength of antigenic signals and their spatial separations has utility and offers an advantage over biological APCs when developing engineering solutions to scaling the production of T cells for therapeutic purposes. Also, considering the urgent need for rapid and efficient *ex vivo* expansion of T cells in personalized therapies, our platform offers an improvement toward addressing these needs. Additionally, based on other reports on the importance of the stiffness of the surface where antigens or antibodies are tethered on the proliferation and effector responses of T cells[3] our work utilized mechanically soft particles (alginate) as well as extremely stiff, commercially available ones (Dynabeads) and found that culture with softer particles could actually outperform stiffer ones. In summary, we demonstrate many advantages of utilizing the advanced material properties of tunable, cytokine-secreting microparticle aAPCs to both control the activation and engineer the differentiation of T cells.

Another improvement that we contributed to in this work was to design platforms that allow for further exploring the effect of substrate stiffness on T cell behavior. The TCR is embedded in a fluid membrane buttressed by a complex cytoskeletal scaffold. Thus, anchoring of pMHC on a stiff substrate allows the TCR to experience a greater force when these molecules interact. Indeed, a number of groups have investigated the role of anchoring TCR ligands on

various substrate stiffnesses using 2D synthetic polymers such as PDMS and polyacrylamide.[3–5] Across many experimental modalities, the finding has been consistent: within the physiological range, the stiffer the anchoring, the greater the T cell activation. Our work here is distinguished from these prior works because our T cells were activated by antigen borne on APCs rather than by antigen anchored directly to the stiff or soft substrate. These data could support the notion that the APC may convey some microenvironmental information to T cells. Thus, to discern whether APC's role is paramount, we tested T cell activation here using soft, artificial APC beads that are not influenced by the microenvironment, and T-cell activation was still augmented in the mechanically stiff 3D con- text as compared to the soft regime. Taken together, T cells can sense 3D environmental micromechanical stiffness whether the stimulatory signal comes from APC or artificial APC beads. The mechanism by which T cells sense mechanics is as yet unclear; however, recent work supports a role for integrin signaling. Artificially increasing the tethering of the integrin ligand ICAM-1 on the APC side of the synapse facilitates activation of T cells, matures LFA-1, and influences the T cell cytoskeleton.[6,7] Our own work here supported that integrin binding is important to mechanosensing in 3D. Optimal methods to exploit the mechanical properties of the 3D microenvironment on T-cell activation are lacking. 3D porosity has a major impact on motility and cytoskeletal regulation, and thus the use of Matrigel or collagen confounds studies of highly motile cells like T cells. Difficulties in tuning the stiffness of 3D biomaterials without dramatically altering their porosity has been a roadblock in pursuing a reductionistic understanding of the role of tissue mechanics[8]. Regardless, the potential scientific and clinical applications are compelling: encapsulation and therapeutic delivery of T cells in hydrogels offers much potential for cancer immunotherapy and other adoptive cell therapies [9–11]. The development here of scaffolds of tunable stiffness and consistent microporosity thus represents an advance for T cell biology. In summary, our work shows that T cells can sense their 3D mechanical environment.

Eventually to gather all the different designs that we developed here in one platform we tailored a polymeric based delivery system that can locally recruit endogenous T cells and train them against the tumor cells. The developed microporous 3D niche here offers a substrate with optimal stiffness for T cell activation and expansion while juicing up these cells with the required cytokines to encourage their cytotoxic potency while suppressing the population of immunosuppressive Tregs. We also tested the capability of our proposed cancer therapy in clearing distant tumors. Our results showed that local training of T cells adjacent to the primary tumor can generate systemic immunity which will renders the potency to fight distant tumors as well. Additionally, the biodegradable and implantable synthetic lymph node technology that we developed here can also be a potent candidate for transfer of activated and patient specific T cells. Beyond the high potency of our technology for cancer immunotherapy we believe that this platform can be inspiring for new local treatments that can benefit from sustained release of biomolecules while providing a 3D substrate for cellular modifications.

Future directions

The 3D bioimplant that we developed here is quite modular and can be applicable for other types of solid cancers. Based on the importance of biophysical cues and our demonstration of how exogenous forces can boost T cell activation, one possibility that can be foreseen for this 3D platform is to embed some magneto responsive elements within the scaffold that enables the application of mechanical forces on the T cell that travel through the scaffold. This will add an additional on demand control over T cell activation. Another area for improvement in these scaffolds would be to add injectability to their features which will then make these platforms more suited for hard to access tumors. Additionally, the non-invasive nature of injection allows for several administrations of the scaffolds during the treatment if needed. Though, some optimization will be needed in terms of injectable scaffolds and specially for T cell transfer applications. Due to the nature of injection and the shear forces associated with it the structure

and viability of injected cells will be affected compared to the implanted scaffolds. So, it will be a trade-off between ease of application and loss of functionality of the therapeutics due to injection. Another bright area for these platforms is to synergize them with combinatorial checkpoint blockade therapies which can be very beneficial especially for tumors that are in late stages. Moreover, the developed 3D platform can be used for harnessing autoimmune disease with slight modifications so that they can release TGFβ which will then pursue formation of Tregs. Another room for improvement in these platforms is to simplify the fabrication procedure and try to make it a one or two step synthesis. This will help in terms of clinical translation and ease of manufacturing.

References

1. Cheung, A. S., Zhang, D. K. Y., Koshy, S. T. & Mooney, D. J. Scaffolds that mimic antigen-presenting cells enable ex vivo expansion of primary T cells. *Nat. Biotechnol.* (2018) doi:10.1038/nbt.4047.
2. Manz, B. N., Jackson, B. L., Petit, R. S., Dustin, M. L. & Groves, J. T-cell triggering thresholds are modulated by the number of antigen within individual T-cell receptor clusters. *Proc. Natl. Acad. Sci. U. S. A.* **108**, 9089–9094 (2011).
3. Saitakis, M. *et al.* Different TCR-induced T lymphocyte responses are potentiated by stiffness with variable sensitivity. *Elife* **6**, e23190 (2017).
4. Judokusumo, E., Tabdanov, E., Kumari, S., Dustin, M. L. & Kam, L. C. Mechanosensing in T lymphocyte activation. *Biophys. J.* **102**, L5-7 (2012).
5. O'Connor, R. S. *et al.* Substrate rigidity regulates human T cell activation and proliferation. *J. Immunol.* **189**, 1330–9 (2012).
6. Jankowska, K. I. *et al.* Integrins modulate T cell receptor signaling by constraining actin flow at the immunological synapse. *Front. Immunol.* **9**, 1–19 (2018).
7. Comrie, W. A., Li, S., Boyle, S. & Burkhardt, J. K. The dendritic cell cytoskeleton promotes T cell adhesion and activation by constraining ICAM-1 mobility. *J. Cell Biol.* **208**, 457–473 (2015).
8. Vining, K. H. & Mooney, D. J. Mechanical forces direct stem cell behaviour in

development and regeneration. *Nat. Rev. Mol. Cell Biol.* **18**, 728–742 (2017).

9. Monette, A., Ceccaldi, C., Assaad, E., Lerouge, S. & Lapointe, R. Chitosan thermogels for local expansion and delivery of tumor-specific T lymphocytes towards enhanced cancer immunotherapies. *Biomaterials* **75**, 237–249 (2016).

10. Stephan, S. B. *et al.* Biopolymer implants enhance the efficacy of adoptive T-cell therapy. *Nat. Biotechnol.* (2015) doi:10.1038/nbt.3104.

11. Smith, T. T. *et al.* Biopolymers codelivering engineered T cells and STING agonists can eliminate heterogeneous tumors. *J. Clin. Invest.* **127**, 2176–2191 (2017).